The Pennsylvania State University

The Graduate School

John and Willie Leone Family Department of Energy and Mineral Engineering

# EXAMINATION OF UNCONVENTIONAL PHENOMENA IN NATURALLY FRACTURED LIQUID-RICH GAS RESERVOIRS: SINGLE-BLOCK COMPOSITIONAL MODEL

A Dissertation in

Energy and Mineral Engineering

by

Bander Nasser Al Ghamdi



Submitted in Partial Fulfillment
of the Requirements
for the Degree of

Doctor of Philosophy

May 2016

The dissertation of Bander Nasser Al Ghamdi was reviewed and approved* by the following:

Luis Felipe Ayala H.
Professor of Petroleum and Natural Gas Engineering;
Associate Department Head for Graduate Education;
William A. Fustos Family Professor in Energy and Mineral Engineering;
FCMG Chair in Fluid Behavior and Rock Interactions
Dissertation Advisor
Chair of Committee

Turgay Ertekin
Department Head of John and Willie Leone Family Department of Energy and Mineral Engineering;
Professor of Petroleum and Natural Gas Engineering;
George E. Trimble Chair in Earth and Mineral Sciences;
Undergraduate Program Chair of Petroleum and Natural Gas Engineering

Eugene Morgan
Assistant Professor of Petroleum and Natural Gas Engineering

Mathieu Stienon
Professor of Mathematics

***Signatures are on file in the Graduate School**

## ABSTRACT

Liquid-rich gas reservoir development is highly dependent on the thermodynamic behavior of the fluids-in-place. During the depletion of liquid-rich gas reservoirs, the gas condenses as the pressure of the reservoir reduces below the hydrocarbon dew-point pressure, which introduces a liquid phase called retrograde condensate. In such conditions, the productivity experiences a reduction in recovery due to the appearance of condensate near the production channels, which in turn reduces the overall flow of hydrocarbons to the surface.

A numerical compositional reservoir simulation was developed in-house to simulate the productivity of liquid-rich gas reservoirs in tight formations. The capability of the simulator proved to be successful after simulating a hypothetical case of a 2-D tight liquid-rich gas reservoir using the in-house simulator against commercial software CMG. The results of both simulators came into agreement with one producer well being put on production at a constrained bottom-hole flowing pressure of 1500 psia. The validation of the basic framework of the in-house simulator has provided the necessary confidence to extend the development of more complex models.

The impact of capillary pressure on phase behavior was explored using an in-house generated coupled phase behavior model with a capillary pressure equation. The influence of capillary pressure was examined against different sets of composition combinations in different reservoir settings. The capillary forces' extents were highly dependent on composition combinations and pore radiuses. Mixtures with higher volatile concentrations showed the highest capillary forces. The enhancement in condensate propagation, resistance to gas flow, and impact on recovery were explored at 10 nm and 20 nm pore radiuses. The investigation suggested that interfacial tensions implied greater influence on the flow behavior in oil-dominated systems than in gas-dominated conditions. Evaluating the flow performance of unconventional phenomena in liquid-rich gas reservoirs was extended to include diffusion while activating capillary forces. The results showed higher domination of diffusion on reservoir performance which provided additional fluid recovery. Subsequently, the enhanced withdrawal of fluid dismissed the impact of capillary forces on gas flow and the impact of condensate blockage.

# TABLE OF CONTENTS

LIST OF FIGURES ..... vi

LIST OF TABLES ..... xi

NOMENCLATURE ..... xiv

ACKNOWLEDGEMENTS ..... xx

Chapter 1 INTRODUCTION ..... 1

Chapter 2 BACKGROUND ..... 3

2.1 Flow behavior of liquid-rich gas reservoirs ..... 3
2.2 Flow behavior in tight reservoirs ..... 8
2.3 Reservoir modeling techniques ..... 13

Chapter 3 PROBLEM STATEMENT ..... 18

Chapter 4 MODEL FORMULATION ..... 20

4.1 Molar vs mass formulations ..... 23
4.2 Compositional model formulations ..... 30
4.3 Finite difference approximation ..... 35
4.4 Evaluating transmissibility terms ..... 38
4.5 Source term ..... 40
4.6 Solution technique ..... 43
4.7 Internal checks ..... 46
4.8 Production and recoveries at surface conditions ..... 47
4.8.1 Surface facilities for compositional simulator ..... 48
4.8.2 Fluid-in-place ..... 51
4.8.3 Recovery calculations ..... 55

Chapter 5 VALIDATION OF THE MODEL ..... 57

5.1 In-house simulator versus commercial software ..... 57
5.2 System under study ..... 58
5.3 Preliminary results ..... 63

Chapter 6 EFFECT OF CAPILLARY PRESSURE ON DEW POINT IN NANOPORES ..... 74

6.1 Coupling a phase behavior model with a capillary pressure equation ..... 75
6.2 Estimating capillary pressure and dew-point pressure in nanopores ..... 79
6.3 Validating the coupled phase behavior – capillary pressure model ..... 81
6.4 Examining the influence of capillary pressure under different conditions ..... 90

Chapter 7 IMPLEMENTING SINGLE-BLOCK SIMULATION WITH FRACTURES .....99

7.1 Quarter-block representation.....101
7.2 Space discretization.....103

Chapter 8 INVESTIGATING THE INFLUENCE OF CAPILLARY PRESSURE ON NEAR CRITICAL FLUIDS .....106

8.1 Numerical study input.....106
8.2 Reservoir performance without the inclusion of capillary pressure.....109
8.3 Flow behavior with the activation of capillary forces.....117
8.3.1 Interfacial tension based on a fluid-dominant system.....126
8.4 Influence of diffusion while activating capillary pressure inside nanopores .....131

Chapter 9 CONCLUSION AND RECOMMENDATION .....142

9.1 Concluding remarks .....142
9.2 Recommendation .....144

BIBLIOGRAPHY.....146

Appendix A DERIVATION OF FLUID FLOW EQUATION.....153

Appendix B PHASE BEHAVOIR MODEL.....159

B.1 Equation of State .....159
B.2 Vapor-liquid equilibrium flash.....161
B.3 Properties predictions.....165

Appendix C STANDARD PVT PROPERTY CALCULATIONS.....170

C.1 Fluids-in-place calculations.....170
C.2 Productivity analysis .....174

Appendix D MODIFIED BLACK-OIL MODEL.....179

D.1 Definition of composition and saturation using mass formulation .....179
D.2 Formulations of fluid-in-place .....183
D.3 Surface production for MBO.....184

Appendix E RESULT TABLES OF CAPILLARY RELATIONSHIPS.....188

## LIST OF FIGURES

Figure 2.1: A typical phase diagram of a gas-condensate system (after Ahmed, 2000) ..... 4

Figure 2.2: Maximum liquid dropout across different temperatures ..... 5

Figure 2.3: Typical GOR and API of a liquid-rich gas reservoir ..... 6

Figure 2.4: A typical three reservoir regions in a liquid-rich gas system (after Fan *et al.*, 2005) ..... 7

Figure 2.5: Liquid-rich gas distribution in porous media (after Fan *et al*., 2005) ..... 10

Figure 3.1: Arrangement of matrix blocks and fractures ..... 18

Figure 3.2: Flow pattern during condensate drop-out ..... 19

Figure 4.1: Surface separation facility ..... 48

Figure 5.1: Two-dimensional grid system (11x11) with one producer at (6x6) ..... 58

Figure 5.2: Gas pressure after 1000 days (in-house simulator vs. CMG) ..... 64

Figure 5.3: Global composition of P1 after 1000 days (in-house simulator vs. CMG) ..... 65

Figure 5.4: Oil saturation after 1000 days (in-house simulator vs. CMG) ..... 65

Figure 5.5: Gas pressure at the well (in-house simulator vs. CMG) ..... 66

Figure 5.6: Overall composition at the well (in-house simulator vs. CMG) ..... 67

Figure 5.7: Gas saturation at the well (in-house simulator vs. CMG) ..... 68

Figure 5.8: Condensate saturation at the well (in-house simulator vs. CMG) ..... 68

Figure 5.9: Gas rate at reservoir conditions (in-house simulator vs. CMG) ..... 69

Figure 5.10: Condensate rate at reservoir conditions (in-house simulator vs. CMG) ..... 70

Figure 5.11: Gas rate at surface conditions (in-house simulator vs. CMG) ..... 71

Figure 5.12: Cumulative gas production (in-house simulator vs. CMG) ..... 71

Figure 5.13: Incremental material balances per component (in-house simulator) ..... 72

Figure 5.14: Cumulative material balances per component (in-house simulator) ..... 73

Figure 5.15: Maximum change in condensate saturation (in-house simulator) ..... 73

Figure 6.1: Capillary pressure effect on phase envelopes (Nojabaei *et al.*, 2013)..... 75

Figure 6.2: Flow chart to estimate capillary pressure given radius of the pores..... 80

Figure 6.3: Capillary pressure for methane 70% - decane 30%..... 82

Figure 6.4: Capillary pressure for methane 70% - decane 30% (Nojabaei *et al.*, 2013)..... 83

Figure 6.5: Interfacial tension for methane 70% - decane 30%..... 84

Figure 6.6: Interfacial tension for methane 70% - decane 30% (Nojabaei *et al.*, 2013)..... 84

Figure 6.7: Density versus pressure for 70% - decane 30% at 550 $^{o}$F without $P_{cgo}$ ..... 85

Figure 6.8: Dew-point pressure difference for methane 70% - decane 30% ..... 86

Figure 6.9: Sat. pressure difference for methane 70% - decane 30% (Nojabaei *et al.*, 2013) ..... 86

Figure 6.10: $P_{gi}^{(n)}$ effect on capillary pressure for methane 70% - decane 30% ..... 88

Figure 6.11: $P_{gi}^{(n)}$ effect on interfacial tension for methane 70% - decane 30%..... 89

Figure 6.12: $P_{gi}^{(n)}$ effect on dew-point pressure for methane 70% - decane 30% ..... 89

Figure 6.13: Capillary pressure for binary mixtures with different concentrations..... 92

Figure 6.14: Interfacial tension for binary mixtures with different concentrations ..... 93

Figure 6.15: Dew-point pressure difference for mixtures with different concentrations..... 93

Figure 6.16: Capillary pressure for methane-butane: different temperatures ..... 94

Figure 6.17: Capillary pressure for methane-hexane: different temperatures..... 95

Figure 6.18: Capillary pressure for methane-decane: different temperatures..... 95

Figure 6.19: Capillary pressure versus temperature at 10 nm..... 96

Figure 6.20: Vapor and liquid densities versus temperature for different mixtures ..... 97

Figure 6.21: Influence of capillary pressure on phase envelopes ..... 98

Figure 7.1: Single-block representation..... 99

Figure 7.2: Fractures surrounding the matrix from the sides..... 100

Figure 7.3: Representation of the quarter single-block matrix (*after Ayala, 2004*)..... 101

Figure 7.4: Grid refinement toward fractures ..... 102

Figure 7.5: 1D grid discretization toward a fracture ..... 103

Figure 7.6: Reservoir condensate content using different discretization scenarios ..... 105

Figure 8.1: Methane-butane phase envelope using different concentrations ..... 110

Figure 8.2: Condensate at reservoir condition for methane-butane ..... 111

Figure 8.3: Methane-butane oil saturation profile for different concentrations ..... 111

Figure 8.4: Condensate at reservoir condition for methane-hexane ..... 112

Figure 8.5: Condensate at reservoir condition for methane-decane ..... 113

Figure 8.6: Molar recovery for mixtures with the highest condensate ..... 114

Figure 8.7: Condensate recovery for mixtures with the highest condensate ..... 114

Figure 8.8: Oil saturation profile across the single-block for methane-hexane ..... 115

Figure 8.9: Oil saturation evolution for methane-hexane without capillary pressure ..... 116

Figure 8.10: Reservoir pressure profile for methane-hexane with capillary forces ..... 119

Figure 8.11: Oil saturation for methane-hexane with capillary forces in a radius of 10 nm .... 120

Figure 8.12: Oil saturation at the corners for methane-hexane with capillary forces ..... 121

Figure 8.13: Oil saturation at the center for methane-hexane with capillary forces ..... 121

Figure 8.14: Condensate at reservoir condition for methane-butane (70%-30%) with capillary forces ..... 122

Figure 8.15: Condensate at reservoir condition for methane-hexane (85%-15%) with capillary forces ..... 123

Figure 8.16: Condensate at reservoir condition for methane-decane (70%-30%) with capillary forces ..... 123

Figure 8.17: Percent change in gas recovery for methane-hexane (85%-15%) ..... 124

Figure 8.18: Percent change in condensate recovery for methane-hexane (85%-15%) ..... 125

Figure 8.19: IFT values at different temperatures for methane-hexane (70%-30%) ..... 127

Figure 8.20: Phase behavior for methane-decane (70%-30%) ..... 128

Figure 8.21: Phase behavior for methane-hexane (70%-30%) ..... 129

Figure 8.22: IFT ratio of oil-gas dominated systems for methane-decane (70%-30%).....130

Figure 8.23: IFT ratio of oil-gas dominated systems for methane-hexane (70%-30%).....130

Figure 8.24: Oil saturation versus pressure at different temperatures for methane-hexane (85%-15%).....131

Figure 8.25: Pressure at the corners for methane-hexane (85%-15%) with diffusion .....134

Figure 8.26: Pressure at the center for methane-hexane (85%-15%) with diffusion .....135

Figure 8.27: Oil saturation profile for methane-hexane (85%-15%) with diffusion.....136

Figure 8.28: Condensate evolution for methane-hexane (85%-15%) with diffusion .....137

Figure 8.29: Condensate at reservoir for methane-hexane (85%-15%) with diffusion .....138

Figure 8.30: Condensate at reservoir for methane-butane (70%-30%) with diffusion .....139

Figure 8.31: Condensate at reservoir for methane-decane (70%-30%) with diffusion.....139

Figure 8.32: Gas recovery improvement with diffusion .....140

Figure 8.33: Condensate recovery improvement with diffusion.....141

Figure A.1: Rectangular control volume illustration .....153

Figure E.1: Capillary pressure of methane-butane: different concentrations.....196

Figure E.2: Interfacial tension of methane-butane: different concentrations.....196

Figure E.3: Dew-point pressure differences of methane-butane: different concentrations.....196

Figure E.4: Capillary pressure of methane-hexane: different concentrations.....197

Figure E.5: Interfacial tension of methane-hexane: different concentrations .....197

Figure E.6: Dew-point pressure differences of methane-hexane: different concentrations.....197

Figure E.7: Capillary pressure of methane-decane: different concentrations .....198

Figure E.8: Interfacial tension of methane-decane: different concentrations .....198

Figure E.9: Dew-point pressure differences of methane-decane: different concentrations .....198

Figure E.10: Capillary pressure of methane-butane: different temperatures .....199

Figure E.11: Interfacial tension of methane-butane: different temperatures .....199

Figure E.12: Dew-point pressure differences of methane-butane: different temperatures .....199

Figure E.13: Capillary pressure of methane-hexane: different temperatures.....200

Figure E.14: Interfacial tension of methane-hexane: different temperatures.....200

Figure E.15: Dew-point pressure differences of methane-hexane: different temperatures.....200

Figure E.16: Capillary pressure of methane-decane: different temperatures.....201

Figure E.17: Interfacial tension of methane-decane: different temperatures.....201

Figure E.18: Dew-point pressure differences of methane-decane: different temperatures.....201

# LIST OF TABLES

Table 4.1: Component's molar and mass representation ..... 20

Table 4.2: Inventory of unknowns ..... 22

Table 4.3: Inventory of equations ..... 22

Table 4.4: Variables of binary mixture in molar form ..... 23

Table 4.5: Variables of binary mixture in mass form ..... 23

Table 5.1: Constant variables throughout the study ..... 59

Table 5.2: Fluid properties ..... 60

Table 5.3: Hydrocarbon fluid properties ..... 60

Table 5.4: Well information ..... 60

Table 5.5: Surface separation facility information ..... 61

Table 5.6: Oil/gas relative permeability and capillary pressure data ..... 61

Table 5.7: Oil/water relative permeability and capillary pressure data ..... 62

Table 5.8: Numerical tolerance for calculations ..... 63

Table 6.1: Hydrocarbon fluid properties for methane 70% - decane 30% ..... 82

Table 6.2: Stability versus PBM in predicting upper dew-point pressure ..... 87

Table 6.3: Stability versus PBM in predicting lower dew-point pressure ..... 87

Table 6.4: Fluid properties for methane-butane with different concentrations ..... 90

Table 6.5: Fluid properties for methane-hexane with different concentrations ..... 91

Table 6.6: Fluid properties for methane-butane with difference concentrations ..... 98

Table 7.1: Grid discretization testing cases ..... 104

Table 8.1: Grid properties of the matrix and fractures ..... 107

Table 8.2: Fluid properties of the mixtures under study ..... 108

Table 8.3: Composition combinations, and reservoir conditions of the mixtures.....109

Table 8.4: Surface separation conditions.....109

Table 8.5: Simulation cases for methane-butane with the inclusion of capillary forces.....117

Table 8.6: Simulation cases for methane-hexane with the inclusion of capillary forces.....118

Table 8.7: Simulation cases for methane-decane with the inclusion of capillary forces.....118

Table 8.8: Simulation cases for methane-butane with the inclusion of capillary forces and diffusion ($t \leq 150$ days).....132

Table 8.9: Simulation cases for methane-hexane with the inclusion of capillary forces and diffusion ($t \leq 150$ days).....132

Table 8.10: Simulation cases for methane-decane with the inclusion of capillary forces and diffusion ($t \leq 150$ days).....133

Table E.1: Higher and lower dew-point for methane 70% - decane 30%.....188

Table E.2: Effect of changing $P_{gi}^{(n)}$ on dew-point for methane 70% - decane 30%.....188

Table E.3: Capillary, dew-point pressure, and IFT for methane 85% - butane 15%.....189

Table E.4: Capillary, dew-point pressure, and IFT for methane 70% - butane 30%.....189

Table E.5: Capillary, dew-point pressure, and IFT for methane 60% - butane 40%.....189

Table E.6: Capillary, dew-point pressure, and IFT for methane 85% - hexane 15%.....190

Table E.7: Capillary, dew-point pressure, and IFT for methane 70% - hexane 30%.....190

Table E.8: Capillary, dew-point pressure, and IFT for methane 60% - hexane 40%.....190

Table E.9: Capillary, dew-point pressure, and IFT for methane 85% - decane 15%.....191

Table E.10: Capillary, dew-point pressure, and IFT for methane 70% - decane 30%.....191

Table E.11: Capillary, dew-point pressure, and IFT for methane 70% - decane 30% (cont.).....191

Table E.12: Capillary, dew-point pressure, and IFT for methane 60% - decane 40%.....192

Table E.13: Capillary data for higher dew-point at 10 nm for methane 85% - butane 15%....192

Table E.14: Capillary data for lower dew-point at 10 nm for methane 85% - butane 15%.....192

Table E.15: Capillary data for higher dew-point at 10 nm for methane 85% - hexane 15%...193

Table E.16: Capillary data for lower dew-point at 10 nm for methane 85% - hexane 15% ....193

Table E.17: Capillary data for higher dew-point at 10 nm for methane 70% - decane 30% ...193

Table E.18: Capillary data for lower dew-point at 10 nm for methane 70% - decane 30% ....194

Table E.19: Searching for single-phase temp. at 10 nm for methane 85% - butane 15%.....194

Table E.20: Searching for single-phase temp. at 10 nm for methane 85% - hexane 15% .....195

Table E.21: Searching for single-phase temp. at 10 nm for methane 70% - decane 30% .....195

# NOMENCLATURE

$A_x$ = total area perpendicular to the flow in the x-direction, *ft*$^3$

$A_y$ = total area perpendicular to the flow in the y-direction, *ft*$^3$

$A_z$ = total area perpendicular to the flow in the z-direction, *ft*$^3$

$B_g$ = gas formation volume factor, *rb/Mscf*

$B_{gei}$ = initial equivalent gas formation volume factor, *rcf/scf*

$B_o$ = oil formation volume factor, *rb/stb*

$CIP$ = current condensate in place, *stb*

$fs_o$: overall liquid molar fraction at the separation facility

$fs_o^i$: initial overall liquid molar fraction at the separation facility

$G$ = depth measured positive in the downward direction, *ft*

$GIP$ = current gas in place, *scf*

$GHIP$ = total amount of free gas in place, *lbmol*

$g_m$: moles of each component in the free gas, $lbmol$

$G_P$ = cumulative production of surface gas, *scf*

$h$ = thickness, *ft*

$k$ = absolute permeability, *mD*

$k_{rg}$ = relative permeability of the gas phase

$k_{ro}$ = relative permeability of the condensate phase

$k_{rog}$ = relative permeability to oil in the two-phase oil-gas system at irreducible water

$k_{row}$ = relative permeability to oil in a two-phase water-oil system

$k_{rocw}$ : relative permeability to oil at connate water saturation (irreducible water).

$k_{rw}$ = relative permeability of the water phase

$k_x$ = absolute permeability in the x- direction, *mD or perms*

$k_y$= absolute permeability in the y- direction, *mD or perms*

$k_z$= absolute permeability in the z- direction, *mD or perms*

$k_h$ = geometric mean of the permeabilities, *perms*

$K_m$ = vapor-liquid molar equilibrium ratio of the *m*$^{th}$ component in the hydrocarbon mixture

$K_m^\omega$ = vapor-liquid mass equilibrium ratio of the *m*$^{th}$ component in the hydrocarbon mixture

$M_m$ = molar rate of the $m^{th}$ component in the control volume, $\frac{RB\ .\ lbmol}{RCF\ .\ Day}$

$M_m^{\omega}$= mass rate of $m^{th}$ component in the control volume, $\frac{RB\ .\ lbm}{RCF\ .\ Day}$

$M_P$ = cumulative molar production of hydrocarbons, $\frac{RB\ .\ lbmol}{RCF\ .\ Day}$

$M_{Pm}$ = cumulative molar production of $m^{th}$ component, $\frac{RB\ .\ lbmol}{RCF\ .\ Day}$

$MW_m$= molecular weight of the $m^{th}$ component, *lb/lbmol*

$MW_g$= molecular weight of gas, *lb/lbmol*

$MW_o$= molecular weight of oil, *lb/lbmol*

$m_g$ = mass of the gas phase, *lbm*

$m_o$ = mass the condensate phase, l*bm*

$m_T$ = total mass of the mixture, *lbm*

$n_c$ = total number of components of the hydrocarbon mixture

$n_s$ = total number of surface facility stages

$n_x$ = total number of gridblocks in the x-direction

$n_y$ = total number of gridblocks in the y-direction

$n_g$ = number of moles in the gas phase, *mole*

$n_o$ = number of moles in the condensate phase, *mole*

$n_T$ = total number of moles of the mixture, *mole*

$N_P$ = cumulative production of surface oil, *stb*

$N_T$ = total molar rate of hydrocarbon fluids leaving or entering the reservoir, $\frac{RB\ .\ lbmol}{RCF\ .\ Day}$

$N_g$ = molar rate of fluids that is produced as gas on the surface, $\frac{RB\ .\ lbmol}{RCF\ .\ Day}$

$N_o$ = molar rate of fluids that is produced as condensate on the surface, $\frac{RB\ .\ lbmol}{RCF\ .\ Day}$

$N_m$= molar rate of the $m^{th}$ component at the interface, $\frac{RB\ .\ lbmol}{RCF\ .\ Day}$

$N_m^*$ : molar rate of m$^{th}$ component leaving the system, $\frac{lbmol\ .RB}{RCF\ day}$

$OCIP$ = Original condensate in place, *stb*

$OGIP$ = original gas in place, *scf*

$OHIP$ = original hydrocarbons in place as a function of specific density, *lbm*

$OSIP_m$ = original species-in-place of the $m^{th}$ component, *lbm*

$p_{cm}$ = critical pressure of the $m^{th}$ component, *psia*

$p_i$ = initial reservoir pressure, *psia.*

$p_g$ = pressure of the gas phase, *psia*

$p_o$ = pressure of the condensate phase, *psia*

$p_{sc}$ = pressure at standard conditions, taken at the pressure of the stock tank, *psia*

$p_{wf}$ = wellbore bottomhole pressure, *psia*

$p_c$ = Capillary pressure, *psi*

$p_{cgo}$ = gas/oil capillary pressure, *psia*

$p_{cow}$ = oil/water capillary pressure, *psia*

$q_{res,g}$= volumetric rate of gas produced at the reservoir, *rb/day*

$q_{res,o}$ = volumetric rate of condensate produced at the reservoir, *rb/day*

$q_{sc,g}$= volumetric rate of gas produced at the surface, *scf/day*

$q_{sc,o}$ = volumetric rate of condensate produced at the surface, *stb/day*

$Q_m$ = rate of external withdrawal/injection of $m^{th}$ component in molar unit, *lbmol/day*

$Q_m^{\omega}$ = rate of external withdrawal/injection of $m^{th}$ component in mass unit, *lbm/day*

$Q_o^{\omega}$ = condensate rate of external withdrawal/injection in mass unit, *lbm/day*

$Q_g^{\omega}$ = gas rate of external withdrawal/injection in mass unit, *lbm/day*

$r_e$ = equivalent radius of the well, *ft*

$r_w$ = wellbore radius of the well, *ft*

$R$ = universal gas constant, $\frac{10.73 \ \ psia\ ft^3}{lbmol\ .\ R}$

$R_{HC}$= recovery factor of hydrocarbons, *%*

$R_m$ = recovery of the $m^{th}$ component, *%*

$R_g$ = surface gas recovery, *%*

$R_o$= surface condensate recovery, *%*

$R_{so}$ = dissolved gas-oil ratio, *scf/stb*

$R_{vi}$ = initial volatilized oil-gas ratio, *stb/MMscf*

$R_v$ = volatilized oil-gas ratio, *stb/MMscf*

$S_g$ = gas saturation at reservoir conditions

$S_o$ = condensate saturation at reservoir conditions

$S_w$ = water saturation at reservoir conditions

$SIP_m$ = species-in-place of the $m^{th}$ component, *lbmol*

$t$ = time, *days*

$t_i$ = initial time before simulation starts, *days*

$t_f$ = time at the end of the time step, *days*

$T_{cm}$ = critical temperature of the $m^{th}$ component, $^oF$ *or* $^oR$

$T_{gx}$ = gas transmissibility coefficient on the x-direction

$T_{gy}$ = gas transmissibility coefficient on the y-direction

$T_{ox}$ = condensate transmissibility coefficient on the x-direction

$T_{oy}$ = condensate transmissibility coefficient on the y-direction

$T_{pc}$ = pseudo-critical temperature of the mixture, $^oR$

$T_{sc}$ = temperature at standard conditions, taken at the stock tank, $^oR$

$v_{mo}$ = velocity of the $m^{th}$ component in the condensate phase averaged across sectional area, *ft/s*

$v_{mg}$ = velocity of the $m^{th}$ component in the gas phase averaged across sectional area, *ft/s*

$V_g$ = gas volume, $ft^3$

$V_o$= oil volume, $ft^3$

$V_T$= mixture total volume, $ft^3$

$v_g$= gas specific volume, $ft^3/lbm$

$v_g$= oil specific volume, $ft^3/lbm$

$\bar{v}_g$ = gas molar volume, $ft^3/lbmol$

$\bar{v}_o$ = oil molar volume, $ft^3/lbmol$

$\bar{v}_T$ = mixture total molar volume, $ft^3/lbmol$

$v_g^D$ = Darcian velocity of the gas phase due to pressure gradients, *ft/s*

$v_o^D$ = Darcian velocity of the condensate phase due to pressure gradients, *ft/s*

$v_{mg}^F$ = Fickian velocity of the $m^{th}$ component in the gas phase due to concentration gradients, ft/s

$v_{mo}^F$ = Fickian velocity of the $m^{th}$ component in the condensate phase due to concentration gradients, ft/s

$V_b$= bulk volume of the grid block ($\Delta x \Delta y \Delta z$), $ft^3$

$V_P$ = porous volume of the grid block ($\phi \Delta x \Delta y \Delta z$), $ft^3$

$x_m$ = molar composition of the $m^{th}$ component in the condensate phase

$x_m^{sc}$: molar composition of the condensate phase at stock tank of the $m^{th}$ component

$y_m$ = molar composition of the $m^{th}$ component in the gas phase

$y_m^{sc}$: molar composition of the gas phase at stock tank of the $m^{th}$ component

$z_m$ = overall molar composition of the $m^{th}$ component in the hydrocarbon mixture

$z_m^{\omega}$ = overall mass composition of the $m^{th}$ component in the hydrocarbon mixture

$z_m^{ws}$ = overall molar composition of the $m^{th}$ component feeding 1st stage of surface facility

$Z_g$ = compressibility factor of the gas phase

$Z_o$ = compressibility factor of the condensate phase

$Z_{cm}$ = compressibility factor of the $m^{th}$ component at the critical point

$Z_{osc}$: compressibility factor of condensate at standard conditions

$Z_{gsc}$: compressibility factor of gas at standard conditions, which is taken to be 1 always.

Greek

$\alpha_g$= equilibrium vapor molar fraction

$\alpha_o$= equilibrium condensate molar fraction

$\alpha_g^{\omega}$= equilibrium vapor mass fraction

$\alpha_o^{\omega}$= equilibrium condensate mass fraction

$\alpha_{gs}^{\omega}$= equilibrium vapor mass fraction at the separator stage

$\alpha_{os}^{\omega}$= equilibrium condensate mass fraction at the separator stage

$\phi$ = porosity

$\omega_{mo}$ = mass composition of the $m^{th}$ component in the condensate phase

$\omega_{mg}$ = mass composition of the $m^{th}$ component in the gas phase

$\lambda$ = pore-size distribution index

$\mu_g$= viscosity of the gas phase, *cp*

$\mu_o$= viscosity of the condensate phase, *cp*

$\Omega_{am}$ = Peng-Robinson attraction parameter constant for the $m^{th}$ component in the mixture

$\Omega_{bm}$ = Peng-Robinson co-volume parameter constant for the $m^{th}$ component in the mixture

$\rho_{air}$ = air mass density, $lbm/ft^3$

$\rho_g$ = gas mass density, $lbm/ft^3$

$\rho_o$ = condensate mass density, $lbm/ft^3$

$\rho_w$ = water mass density, $lbm/ft^3$

$\rho_{gsc}$= gas specific density at standard conditions, $lbm/ft^3$

$\rho_{osc}$= oil specific density at standard conditions, $lbm/ft^3$

$\bar{\rho}_g$ = gas molar density, *lbmol/ft*$^3$

$\bar{\rho}_o$ = condensate molar density, *lbmol/ft*$^3$

$\bar{\rho}_{gsc}$= gas molar density at standard conditions, *lbmol/ft*$^3$

$\bar{\rho}_{osc}$= oil specific density at standard conditions, *lbmol/ft*$^3$

$\bar{\rho}^i_{o,ST}$= initial oil density at stock tank condition using separator calculations, *lbmol/ft*$^3$

$\bar{\rho}_{o,ST}$= oil density at stock tank condition using separator calculations, *lbmol/ft*$^3$

$\Delta t$ = time discretization, *days*

$\omega_m$ = Pitzer's acentric factor of the $m^{th}$ component

$\Delta x$ = finite difference space discretization in the x-direction, *ft*

$\Delta y$ = finite difference space discretization in the y-direction, *ft*

$\Delta z$ = finite difference space discretization in the z-direction, *ft*

$\Phi_g$ = Hubbert's potential of the gas phase, *psia*

$\Phi_o$ = Hubbert's potential of the condensate phase, *psia*

Subscripts

$i$= running subscript for gridblocks in the x-direction

$j$= running subscript for gridblocks in the y-direction

$m$ = running subscript for components

$g$ = gas

$o$ = condensate

w = water

$s$ = running subscript for the Cartesian direction (x, y, or z)

$f$ = running subscript for the phase type (o, g, or w)

## ACKNOWLEDGEMENTS

The achievement of this project is a result of enormous support of many people who took a great part in helping me attain such accomplishment.

I would like to express my grateful gratitude to my academic advisor, Dr. Luis Ayala for his unlimited support, patient guidance, and valuable friendship throughout my studies here at Pennsylvania State University. My sincere gratitude also goes to the members of the committee, Dr. Turgay Ertekin, Dr. Eugene Morgan, and Dr. Mathieu Stienon, whose knowledge and assistance contributed vastly to the success of my research and to my academic achievement.

Special thanks are conveyed to Saudi Aramco for their sponsorship, advice, and continuous support, which have contributed vastly to my development and success.

My heartfelt gratitude and appreciation is due to my wife, Faten for standing by my side and for the overwhelming love and endless support. Also, I would like to express my gratitude to my children, Jury, Nasser, and Wuard for their love, which awards me with strength and courage.

In Addition, I would like to express my deepest sense of gratitude to my beloved family for their everlasting support, prayers, and encouragement throughout the stages of my life. I dedicate all my success to my parents, Nasser and Rafiah, my grandmother, Fatima, and to my family members, Abdullah, Bader, Budoor, Boshra, and Abdullaziz.

# Chapter 1

# INTRODUCTION

The industrial reliance on hydrocarbon fluids has been continuously rising due to the surge in consumption. Today's market is persistent in developing applications with dependency on petroleum-products, since the alternate solutions found in renewable energies are still developing and are not economically proven. Currently, the total global energy consumed using renewable energies is about 10%, which is forecasted to reach ~15% by the year 2035 (Hilyard, 2012). Hilyard (2012) highlights an increase in demand for oil and natural gas reaching up to 32% and 44% respectively by the year 2035. Thus, with the increase in demand and increase in price of oil, experts and researchers are eager to explore new reserves and acquire the most from existing developments.

Liquid-rich gas reservoirs are one of the important resources of hydrocarbons to compensate for the world's consumption and support forecasted demands. Unlike dry-gas and wet-gas reservoirs, liquid-rich gas reservoirs split into two phases inside the reservoir after the pressure drops below dew point pressure. Dry-gas and wet-gas reservoirs are presented in a single phase state inside the reservoir throughout the entire isothermal depletion. At surface conditions, dry-gas maintains its single phase state because of its low content in heavy components and high concentration of lighter components. Under surface conditions with pressure and temperature lower than the reservoir conditions, condensate with content up to 66 STB/MMSCF will drop out of the wet-gas stream (McCain, 1993). Moreover, gas-condensate reservoirs yield production of gas and condensate with condensate content up to 313 STB/MMSCF (McCain, 1993). Despite the high content of condensate, this type of reservoir is still considered part of the gas family, since the heptane-plus concentration is below 12.5%. The rich content of condensation at surface makes this type of reservoir appealing for economical investment and development. However, extracting fluids from liquid-rich gas reservoirs is not hassle-free; great challenges arise at the pore-scale in the form of flow impairment and loss of fluids to the reservoir.

The retrograde condensation, attendant with the depletion of liquid-rich gas reservoirs, lead to a deficiency in the flow of fluids moving toward the production channels. The impairment is a result of accumulation of condensate near the wellbore region in an immobility state until

reaching a critical saturation point. In such conditions, the reservoir productivity experiences a reduction in recovery, which in turn reduces the overall flow of hydrocarbons to the surface.

Evaluating the productivity of liquid-rich gas reservoirs can be achieved through numerical reservoir simulation, which works as a window for researchers to see inside the reservoir. There are two modeling techniques that can be used to simulate liquid-rich gas performance, compositional simulation and modified black-oil simulation. Compositional simulators evaluate reservoir behavior by accounting for each component making up the fluid mixture. Formulating a compositional simulator requires the knowledge of fluid properties calculated at reservoir conditions. Compositional models capture these changes through the use of a built-in Equation-of-State model, where fluid properties are calculated based on changes of pressure, temperature, and composition. In contrast, modified black-oil simulators treat the reservoir as a two-component system, oil and gas. It predicts the performance of the reservoir based on a PVT model, which is the result of several laboratory experiments. In these experiments, reservoir conditions are reinstated based on the volumes of fluids retrieved at surface conditions to simulate pressure-volume-temperature relationships. Thus, the formulation of a modified black-oil model depends on fluid properties at surface conditions such as formation volume factors, solution gas-oil ratio, and volatile oil-gas ratio.

Inevitable complexity is associated with capturing the thermodynamic behavior of liquid-rich gas reservoirs in tight formations without the use of an Equation-of-State. The aim of the study is to generate an in-house compositional model and a coupled phase-behavior model with a capillary equation, capable of addressing liquid-rich gas reservoir behavior in a naturally fractured tight formation. The study will include investigating the impact of implied higher retention of oil inside the nanopores through activating capillary forces. Great emphases will be placed upon capturing the influence of capillary pressure on phase behavior, dew-point pressure, residence of condensate inside the reservoir, and resistance against gas to flow. Furthermore, this research is expected to map the significance of including diffusion while activating capillary forces on the flow performance of liquid-rich gas reservoirs in tight settings.

# Chapter 2

# BACKGROUND

## 2.1 Flow behavior of liquid-rich gas reservoirs

Petroleum reservoirs are classified into five categories: dry gas, wet gas, gas-condensate, volatile oil, and black oil. Few non-hydrocarbon components and hundreds of hydrocarbon components make up the fluids of these naturally occurring reservoirs. The chemistry of gas-condensate reservoir fluids makes it the most complex among the five categories (Whitson and Brule, 2000). Reservoir physical properties are illustrated through phase behavior relationships as a function of pressure, temperature, and composition. Phase behaviors are demonstrated through phase envelopes to explain reservoir evolution during depletion by highlighting coexistence of fluids at different reservoir states. Figure **2.1** shows a typical pressure-temperature phase diagram for gas-condensate reservoirs. The complexity of gas-condensate reservoirs is related to its existence near critical point, at which the distinguishing physical properties between gas and liquid vanishes. In unconventional formations, gas-condensate reservoirs are best described as liquid-rich gas reservoirs.

Liquid-rich gas reservoirs exhibit reservoir temperatures greater than the critical temperature and less than the cricondentherm. At initial conditions, their mixture of hydrocarbon molecules is presented in the gas form. Generally, reservoir temperature is a weak function of depth and has insignificant aerial variation in a given reservoir (Whitson and Brule, 2000). Thus, isothermal depletion is presumed during fluid extractions from liquid-rich gas reservoirs. As the pressure depletes below saturation pressure, fluids-in-place evolve to exhibit a two-phase system. The split is a result of weak attraction unveiling between the light and heavy molecules of the initial single-phased fluid (Ahmed, 2000). Molecules with higher tendency to be in the liquid phase will drop out, and those with the tendency to be gas will stay in the gas phase until the maximum liquid drop-out is reached. As the pressure depletes further toward the lower dew point pressure, the condensate will start to vaporize until reaching a single gas phase.

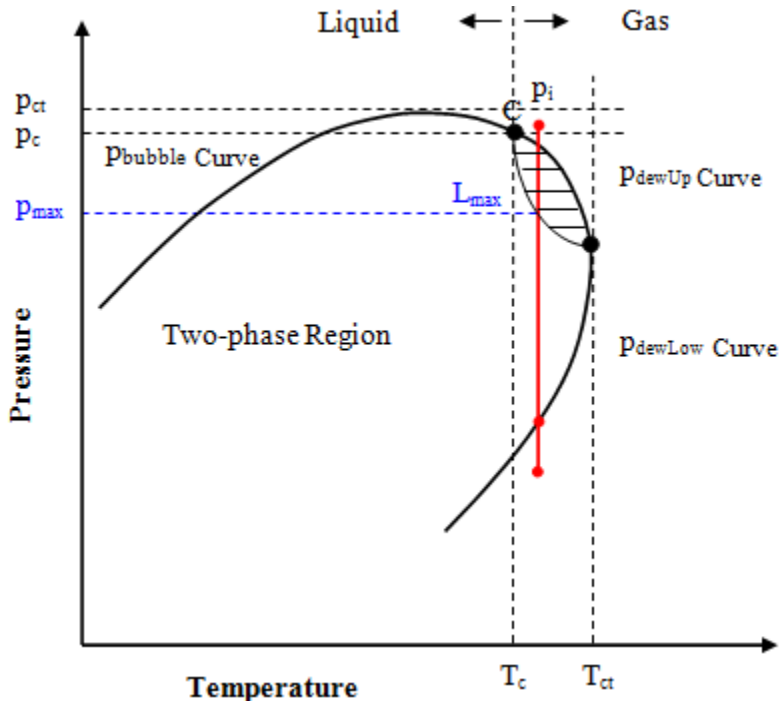


**Figure 2.1: A typical phase diagram of a gas-condensate system (after Ahmed, 2000)**

The complexity that arises in the production of liquid-rich gas systems is in the shaded sub-envelope of the phase envelope shown in Figure **2.1**. As the pressure enters this region, retrograde-condensate will form and continue to accumulate until the maximum liquid drop-out $L_{max}$ is reached. Condensate will be present in the reservoir by occupying the pore-spaces gradually until reaching the critical saturation at which the condensate will start mobilizing. According to Boom *et al.* (1996), even liquid-rich gas reservoirs with liquid drop-out of around 1-2% experience flow impairment near the wellbore region. Figure **2.2** shows the maximum liquid drop-out for liquid-rich gas reservoirs across several temperatures ranging from near-critical and increasing toward the cricondentherm. These curves have been developed for a liquid-rich gas system with moderate condensate content. The magnitude of the liquid drop-out indicates alarming impact to the flow scheme of the fluids-in-place.

Understanding the physical properties of liquid-rich gas reservoirs is certainly important for field development and operational planning. The concentration of lighter components and heavier components control the fluid properties such as saturation pressure, Gas-Oil-Ratio (GOR), and

API gravity. Common compositions found in the fluids stream such as methane and heptanes-plus have a direct relationship and can be used as an identifier for the reservoir type and performance (Craft and Hawkins, 1991). The concentration of light and heavy components has essential relationships with saturation pressure and GOR. Fluid mixtures with higher concentration of heavy components exhibit higher saturation pressure because more molecules have the tendency to be in the liquid phase. Danesh (1998) reports an inverse relationship between the concentration of heavy components and initial GOR. The higher the concentration, the lower the initial GOR would be, because small amounts of gas molecules escape the mixture in place at initial conditions.

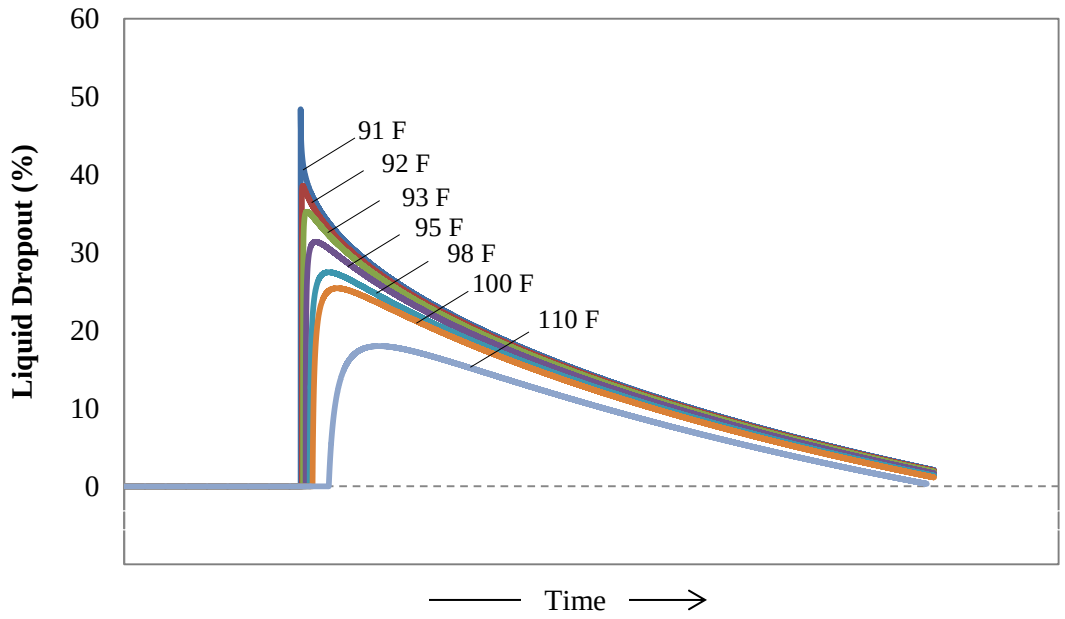


**Figure 2.2: Maximum liquid dropout across different temperatures**

Furthermore, liquid-rich gas fluids have certain characteristics during production which impacts on the trends of the GOR and API gravity. Figure **2.3** illustrates the trend of GOR and API versus time in a typical liquid-rich gas reservoir. The curves represent the compositions of the fluids at surface conditions, which depend on the compositions reaching the wellbore. Before reservoir pressure drops below saturation point, GOR and API maintain a stable trend indicating single phase production from the reservoir, with condensate dropping at a constant rate under surface conditions. Once saturation pressure is reached and condensate starts accumulating in the reservoir, the trend of GOR and API will increase.

The presence of condensate in the reservoir and the rise in GOR indicate that the heavy components have been left behind in the reservoir, and only the gas is allowed to reach the wellbore. According to Craft and Hawkins (1991), the reason GOR increases after the saturation point is related to the fact that condensate becomes attached to the rock pores and persists in mobility. Once the critical saturation point is reached, condensate will mobilize and the GOR will drop as indicated toward the end of the GOR curve. Furthermore, API gravity compares the relative densities of hydrocarbon fluids. It has an inverse relationship with density showing greater API gravity for fluid with less density (Ahmed, 2000). The continuous increase of API can be referred to loosing heavier components to the reservoir more than the recoverable quantities at surface (McCain, 1994). This proves that there is quite an amount of heavy components that will never make it to the surface. Thus, the API curve indicates that the fluid mixture coming from the reservoir will continue to show less of heavy components as time proceeds.

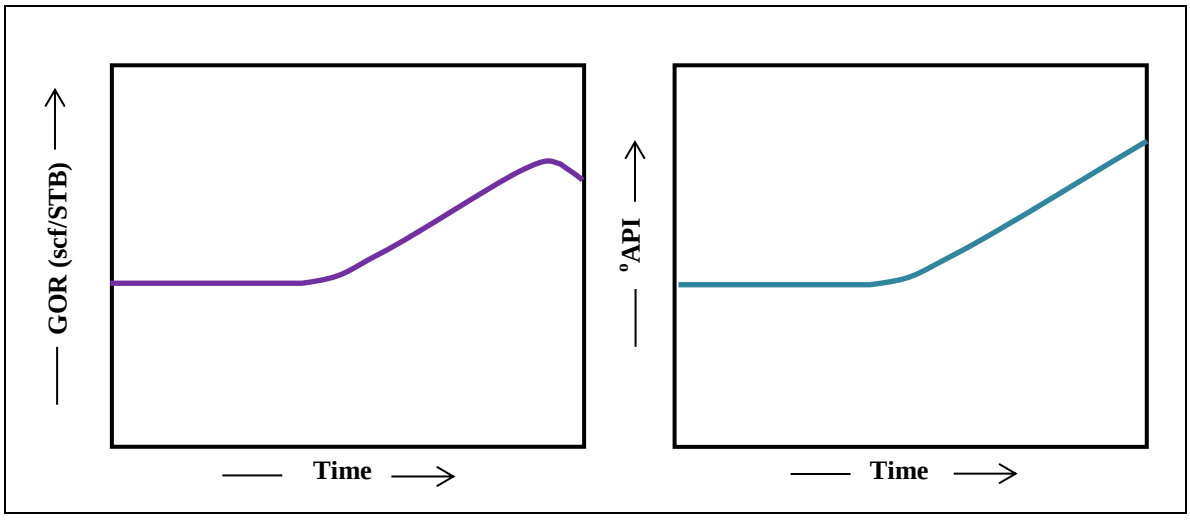


**Figure 2.3: Typical GOR and API of a liquid-rich gas reservoir**

Theoretically, the flow behavior in liquid-rich gas reservoirs is categorized into three regions as described in the work of Fevang and Whitson (1995). Figure **2.4** shows the three regions of liquid-rich gas reservoirs which are the wellbore region (R 1), the accumulation region (R 2), and the reservoir region (R 3). The farthest point from the wellbore is considered region 3, where the fluids-in-place are presented in a single phase. The pressure in this region is maintained above

dew point until the drop in pressure near the wellbore is communicated further in the reservoir. As soon as the pressure depletes below dew point pressure, the single gas phase flowing from region 3 toward the wellbore will split into two phases. The point where the pressure reaches dew point pressure marks the end of region 3 and the start of region 2, where gas and condensate coexist. After a period of time of production and as the reservoir pressure depletes further below the dew point, region 3 will eventually disappear.

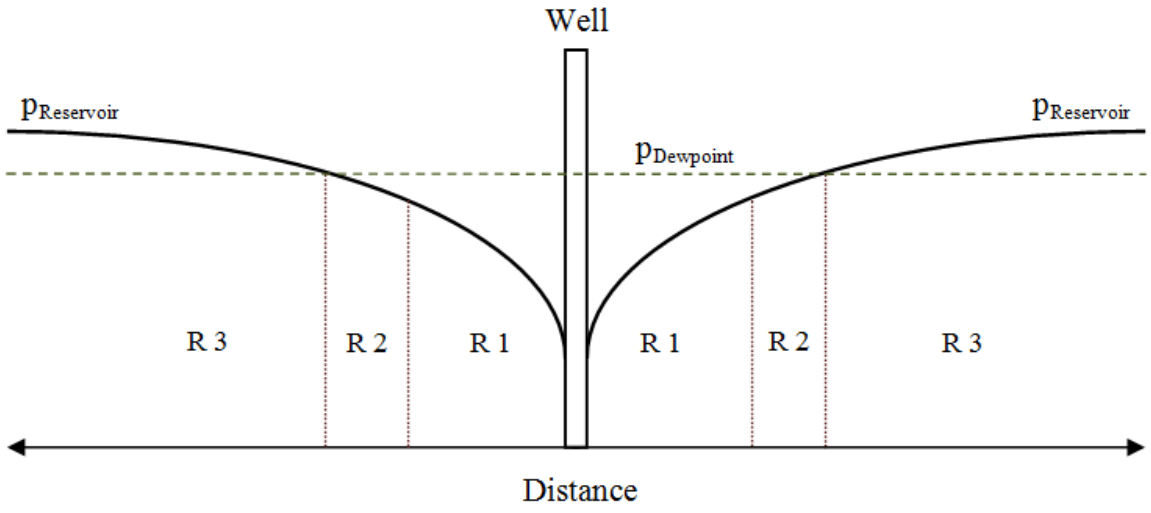


**Figure 2.4: A typical three reservoir regions in a liquid-rich gas system (after Fan *et al.*, 2005)**

The second region represents the condensate build-up section, where the condensate starts to drop out of the gas coming from region 3. The condensate at this section is immobile and only gas continues to flow. Condensate will continue to accumulate until it reaches the maximum liquid drop-out represented by oil saturation. Under these settings, gas flow experiences a great deal of flow impairment due to the increase in condensate presence in the pore spaces that were available previously for the gas. A replica of the fluid behavior in region 2 can be attained through a Constant-Volume-Depletion (CVD) experiment. Basically, it is represented by taking a sample and duplicating the pressure conditions at the boundary of region 2 and region 3, where the pressure is at dew point. The volume at this point is recorded to become the reference point to maintain constant volume at the end of each stage. Then, the pressure is lowered stepwise to allow the fluids to expand in volume. Once equilibrium is reached between the two phases and

the pressure is constant, gas will be expelled by an amount that will return the cell volume to its reference point. The expelled gas represents the gas that was allowed to freely flow from region 2 toward the wellbore region. While the condensate dropped in the cell represents the accumulated condensate in region 2. Valuable information is retrieved from the CVD test for gas and condensate such as: composition, volume, compressibility factor, maximum liquid drop-out, instantaneous recovery, and cumulative recovery.

The first region represents the reservoir behavior at the wellbore once the critical condensate saturation is exceeded. Evidently, region 1 has the highest pressure drop because of the fluid extraction. The fluids that make it to the surface are coming from region 1, which means that the earlier discussion of the behavior of composition, GOR, and API applies here. Two phases exist in this region, and the oil saturation is above critical saturation. According to Fevang and Whitson (1996), in this region both fluids flow and there is no accumulation taking place. In fact, collecting samples from the well-stream and conducting constant-composition-expansion tests (CCE) in the laboratory provides sufficient information about this region in particular. The CCE test is performed to simulate the pressure-volume relations of the hydrocarbon system-in-place. Throughout the test, it maintains the same mass inside the experimental cell, drops the pressure from initial conditions gradually, and records the volumes evolving and the fluid compressibilities. Also, CCE provides the dew point pressure at which condensate drop-out occurs, which marks the point between the accumulation region and region 3. According to Fevang and Whitson (1996), the existence of these regions at all times or in part depend on the composition of the fluids-in-place and reservoir conditions.

### 2.2 Flow behavior in tight reservoirs

The complexity of producing from gas reservoirs is associated with the intricate properties of the fluid, and the flow mechanism in heterogeneous reservoirs with strongly varying rock properties. In general, hydrocarbons occupy the porous spaces in the rock formations, and are trapped by geological structured non-permeable lethologies. The connectivity of the pore-space, known as permeability, allows the fluids to travel according to the drive mechanism. Low permeability is associated with poor connectivity between the pores and subsequently leads to poor flow

performance. Gas formations with permeability less than 1 mD are defined as tight reservoirs, while formations with permeability less than 0.001 mD are referred to as ultra-tight reservoirs (Abaa *et al.,* 2012). Considering the flow phenomenon of liquid-rich gas reservoirs, tight and ultra-tight formations can be inevitably complex hosting environments in which to achieve economical production.

However, Holditch (2006) mentioned that the definition of tight reservoirs is not limited to permeability, and includes other physical factors. Fluids flowing under Darcian law depend on permeability, viscosity, and the pressure gradient. Darcy's law dominates the flow regime in porous media under isothermal conditions as long as the flow is continuous and laminar. In the case where the flow of fluids in the reservoir becomes impaired due to formation tightness or resistance by other fluids, such as with condensate build-up, Fick's law prevails. Fick, in 1855, introduced the idea of the exchange of matters through a porous media by diffusion, where the molecules are exchanged at random motions. His law applies when there is a molecular-to-molecular interaction, or molecular-to-surface interaction. The flow of fluid in this case is a function of the diffusion coefficient and the concentration gradient. In 1986, Ertekin *et al.* introduced the concept of multi-mechanistic flow, where the flow of fluids submits to Darcian and Fickian law. In tight reservoirs with low permeable flow paths, the gas flows in the pressure domain under Darcy's law, and flows by diffusion in the concentration domain under Fick's law.

The multi-mechanistic flow concept was adopted in the work of Ayala *et al.* (2004, 2006, and 2007) to assess the impact of multi-mechanistic flow on naturally fractured retrograde gas reservoirs using a compositional model. The representation of the reservoir was depicting the concept of the "sugar-cube" initiated by Warren and Root (1963) to present the reservoir as a group of matrix blocks separated and surrounded by fractures. The dual permeability system was considered with the fractured permeability being the highest, while assuming constant diffusion coefficients throughout the simulation period. The study evaluated the recovery of gas-condensate in tight formations with permeability ranging from 1 mD to 0.0001 mD, and included the consideration of different diffusion coefficients. It was concluded that the permeability of the reservoir is the controlling factor of the flow mechanism in tight formations. Fickian flow was responsible for the flow of fluids through the reservoir when the permeability of the matrix was less than 0.001 mD, while Darcian flow was dominant when the permeability was 0.1 mD and more. At the conditions where the Darcian and Fickian laws were both responsible for the flow,

ultimate recovery reached up to 4 times larger than the recovery when the flow was obeying Darcian law alone. In this work, a reservoir with dual permeability and single porosity in the presence of natural fractures will be considered to assess the influence of unconventional phenomena on the flow behavior of liquid-rich gas reservoirs.

Under the circumstance where Darcian flow prevails in a single permeability reservoir, the fluids are highly dependent on the transport properties and the capillary forces between the fluids-in-place and the rock itself (Phillip *et al.*, 2010). As a result, permeability, relative permeability, and capillary forces are highly influential on the distribution of fluids and flow mechanism. Capillary pressure is a function of saturation and it controls the initial distribution of fluids in the pore spaces. It is a result of cumulative actions that occur as a consequence of the interfacial tensions (IFT) between rocks and fluids in a hydrocarbon reservoir, grain sizes and geometry of pore spaces, and the wetting characteristics of the fluids (Ahmed, 2000). As two immiscible fluids come in contact with each other, a discontinuity in pressure occurs at the interface resulting in an imbalance of forces (Ahmed, 2000). Figure **2.5** illustrates the distribution of fluids in porous media, where the displacement of fluids is controlled by the capillary forces.

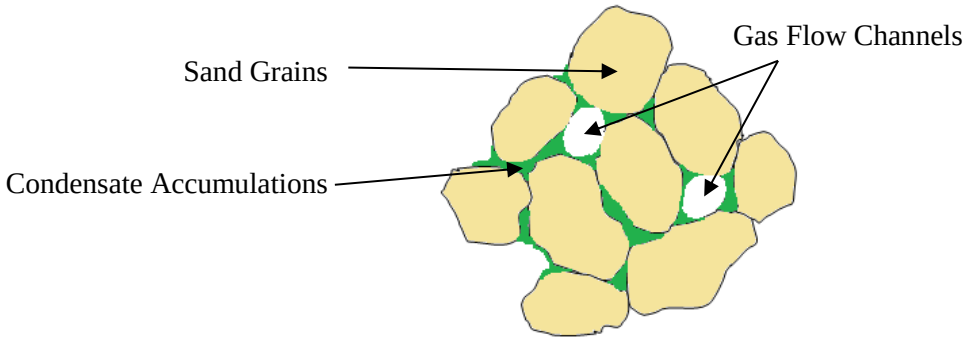


**Figure 2.5: Liquid-rich gas distribution in porous media (after Fan *et al.*, 2005)**

Accurate estimation of the capillary pressure is essential to forecast the productivity and behavior of hydrocarbon reservoirs based on the distribution of fluids. Extensive work has been done throughout the years to develop empirical correlations capable of estimating capillary pressure curves. The first developed relation was introduced by Leverett in 1941 after studying a wide range of rock samples. Leverett (1941) developed the J-function, where he intended to relate the capillary pressure to porosity, interfacial tension, and pore radius, in order to develop a universal capillary curve.

A few years later, research was devoted toward relating the pore-scale properties and the fluid characteristics together to get more precise predictions of the capillary pressure behavior. Corey (1954) found a linear relationship between oil and gas capillary pressure curves and developed an expression capable of characterizing the multiphase fluid flow in a reservoir. Thomeer (1960) introduced a geometrical factor in his analysis of capillary pressure using mercury, in order to classify the capillary pressure curves as functions of pore sizes. Brooks and Corey (1966) carried on the work of Thomeer and modified the capillary pressure function to capture a wide range of geometry classifications. In Brooks and Corey's equation, ($\lambda$) was introduced to represent the pore size distribution in order to indicate the heterogeneity of the porous medium. According to Gang and Kelkar (2007), the most widely used correlation in the petroleum industry for the prediction of capillary pressure curves is the Brooks-Corey equation as shown in equation (2.1).

$$p_c = p_e(S_w^*)^{\frac{-1}{\lambda}} \tag{2.1}$$

Throughout the years, reservoir engineers have always wondered about the vast utilization of Brooks and Corey's model. Li (2004) derived the empirical Brooks-Corey correlation and found that the theoretical development of the correlation has solid theoretical basis. In this correlation, the indication of the heterogeneity relies on the value of the pore size distribution index: the smaller the distribution index, the greater the heterogeneity of the formation and the greater the fractal dimension ($D_f$) value will be (equation 2.2).

$$\lambda = 3 - D_f \tag{2.2}$$

The relationship between surface tension and the physical properties of fluids-in-place was pioneered by Ramsay and Shields (1893), Macleod (1923), Sugden (1924), and Ellis (1932). As temperature increases, liquid density decreases and subsequently surface tension decreases. The findings came in accordance with the assumptions of van der Waals (1910) on the fundamental relationship between cohesion forces and density, where the distance between molecules controls the attraction forces. Thus, as temperature increases, the attraction between molecules decreases causing a split in phases. Macleod (1923) and Sugden (1924) introduced an empirical equation as shown by equation (2.3) relating density and surface tension of pure substances.

$$\sigma = \left[P_{nc}\ \frac{\rho_o - \rho_g}{MW}\right]^4 \quad (2.3)$$

Equation (2.3) is represented as a function of the difference in molar densities and $P_{nc}$, which is the parachor coefficient of the pure substance under study. The changes in IFT are related to the increase in liquid density; high IFT is associated with higher liquid density. Weinaug and Katz (1943) extended the work of Macleod and Sugden and developed an expression for mixtures based on the same fundamentals as presented by equation (2.4).

$$\sigma = \sum_m^{n_c} \left[P_{nc}\ \left(x_m \frac{\rho_o}{MW_o} - y_m \frac{\rho_g}{MW_g}\right)\right]^4 \quad (2.4)$$

Nojabaei *et al.* (2013) investigated the effect of capillary pressure on phase behavior in tight rocks utilizing equation (2.4) and the Laplace equation (2.5). The author has concluded that for oil reservoirs, there is an inverse relationship between capillary pressure and bubble point pressure. It was found that capillary pressure increases with smaller pore sizes and bubble point pressure appeared to be decreasing with smaller pore sizes.

$$P_o - P_g = \frac{2\sigma}{r} \quad (2.5)$$

Relative permeabilities are the most important parameters in determining the productivity of liquid-rich gas reservoirs especially as condensate starts to form when the bottom-hole pressure falls below the dew point (Mott *et al.*, 2000). The determination of the relative permeability, based on the near-well conditions, requires the understanding of the relationship between gas and oil relative permeabilities. Hinchman and Barree (1985) investigated the decline in productivity of liquid-rich gas reservoirs as condensate starts forming near the wellbore. The study related the reduction in flow rate to the condensate build-up near the well, which was highly dependent on the richness of the mixture, the relative permeabilities, and the viscosities. Chopra and Carter (1986) provided sufficient evidence on the validity of the assumption that in a two-phase region, the volumetric flow rates ratio equals the ratio of the volume fractions obtained under constant-composition expansion conditions. The study was conducted through the utilization of the phase equilibrium concept and material balance equations. Chopra and Carter (1986) concluded with

the emphasis that the relationship between gas and oil relative permeabilities illustrated by a ratio is a function of PVT properties and can be expressed as shown in equation (2.6).

$$\frac{k_{rg}}{k_{ro}} = \frac{V_g \mu_g}{V_o \mu_o} \tag{2.6}$$

In the work of Whitson *et al.* (2003), he relates to the work of Chopra and Carter (1986) by indicating that the near-wellbore region experiences gas flowing at high velocity, allowing the viscous forces to be extremely higher than the capillary forces. The ratio of the viscous forces to the capillary forces is referred to as the capillary number. The higher the capillary number, the higher the relative permeability of the gas phase. In relation to the typical three regions of liquid-rich gas reservoirs, Whitson *et al.* (2003) stressed the dominant dependency of well performance on relative permeabilities of region 1. While less importance is given to the relative permeability of region 2; unless the critical saturation is high, then the flow of gas from region 3 toward the wellbore will be impaired.

Hence, the flow of liquid-rich gas reservoirs above saturation pressure is dependent on reservoir permeability, gas viscosity, and the pressure gradient. As the pressure drops below dew point, the flow is dependent on the composition concentration of the mixture, relative permeabilities, and the critical saturation of condensate. In conjunction with the focus of this work, the impact of permeability, capillary forces, and relative permeability on the productivity of a tight liquid-rich gas reservoir will be scrutinized.

## 2.3 Reservoir modeling techniques

Reservoir simulation has gone through several developmental stages to come up with numerical models capable of handling a large number of computations and maintaining numerical stability. Simulation models started consisting of a network of grid blocks partitioned into two- and three-dimensional systems. Generally, the formulation of reservoir simulation consists of differential mass or molar balance equations for each phase in what is known as multi-phase models, and for each component in multi-component simulators. These models incorporate Pressure-Volume-

Temperature (PVT) or Equation-of-State (EOS) models to characterize fluid behavior and properties. Also, they include transport equations to account for the flow of matter inside the porous media. All these equations are combined to form a system of partial differential equations (PDE's). These PDE's are non-linear equations which require integration using finite difference approaches to obtain numerical solutions. The flow equations are discretized by the use of algebraic approximations of the second-order derivatives with respect to space, and first-order derivates with respect to time (Ertekin *et al.*, 2001).

After replacing the derivatives in the differential equation with the algebraic approximation, the PDE's are transformed into finite difference equations. The developed algebraic equations remain non-linear and require further treatment. The non-linearity remains because the coefficients of the equations that are unknown are still functions of the unknown. A part of the finite different equations are constant variables which can be treated with harmonic averaging using minimum numbers of neighboring blocks. Other variables that are functions of the pressure of one-phase, coming from PVT or EOS, such as density, viscosity, and formation volume factors, are considered weak non-linear terms (Ertekin *et al.*, 2001). Strong non-linear terms include variables that are functions of saturation, such as relative permeability and capillary pressures. In a black-oil model, only the weak non-linear terms are arithmetically averaged, and the strong non-linear terms are evaluated with upstream weighting. In the case of compositional simulation, Coats (1980) and Nghiem *et al.* (1981) advocate the use of upstream weighting for all the non-linear terms. Those terms are expressed in compact form which can be referred to as the transmissibility terms. The combination of transmissibility terms, inclusion of external source, and expansion of the accumulation term forms the flow equation.

Solving the flow equation requires using a linearization method, and an organizing technique to form an efficient algorithm (Coats, 1980). One of the commonly used linearization methods is the Newton-Raphson, which is an iterative method known to be used with IMPISC type equations. The method solves for the entire unknown parameters simultaneously at the end of each time step until convergence is achieved. There are other non-Newton-Raphson models which solve for part of the unknowns explicitly, such as IMPES, and IMPESC. With the IMPES method, the pressure is solved implicitly and the saturation is solved explicitly; it is commonly used in black-oil simulation where the fluids system is defined in terms of phases (Ertiken *et al.*, 2001). On the other hand, IMPESC was first formulated in 1978 by Kazemi *et al.* to handle

compositional systems by solving for pressure implicitly, and explicitly for saturation and composition. According to Ayala (2004), the limited stability found with IMPESC gives IMPISC the advantage in terms of stability, but limitation with computational overhead remains an issue.

The advancement in the computation capabilities and development provides versatile applications for engineers to start the utilization of multidimensional simulators in capturing complex reservoir behaviors. Reservoir simulation calculations are classified into three categories: black-oil, modified black-oil, and compositional simulation. Black-oil simulators are designed to capture multiphase flow, where fluid properties are dependent on pressure and independent on composition. The model consists of a system of non-linear differential equations in terms of pressure and saturation. Black-oil simulators treat the reservoir as a two-component system, oil and gas. Volumetric behavior and properties of the reservoir fluids are measured as functions of solution gas-oil-ratio (Rs), formation volume factors of gas and oil, and fluid specific gravities at surface (Whitson *et al.*, 1988). They are capable of simulating gas dissolved in the oil phase, as well as residual oil after the dissolved gas is released below the bubble point pressure. Hepguler and Bard (1997) stress that black-oil simulators only allow for gas to be dissolved into oil and released out of it, but do not accommodate for oil vaporizing into gas phase. This means that the surface gas can exist as free gas in the reservoir or dissolved in the oil, but the surface oil is present in the reservoir as oil only and not volatilized in the gas. Thus, oil and gas phases must maintain a fixed phase composition at all times throughout the simulation process. Thus, the use of black-oil simulators is constrained by the limitation of addressing the phase transfer and change of compositions between gas and oil.

Spivak and Dixon (1973) modified the black-oil formulation to accommodate for the volatized oil in the reservoir gas, which drops out from the gas at the surface. The new formulation defines the oil content in the gas as a function of pressure through the term vaporized oil-gas-ratio (Rv). With the addition of the vaporized oil in the gas reservoir, the formation volume factor for gas and oil is modified to capture the change (Whitson *et al.*, 1988). Modified black-oil simulators became equipped with four functions of pressure: vaporized oil-gas-ratio, solution gas-oil-ratio, and formation volume factors of gas and oil. This has enabled modified black-oil simulators to handle volatile oil and liquid-rich gas reservoirs.

In 1981, Whitson and Torp developed a procedure to calculate PVT properties using the CVD data and composition material balance equations. The gas composition is determined experimentally from the CVD data, while the oil composition is calculated in terms of CVD data and through compositional material balance. Then, each fluid composition is flashed through multi-stage separation to determine PVT properties of the two phases. Their work matched the same results obtained through Peng-Robinson EOS. Coats (1985) developed the same approach using the capabilities of Equation-of-State, which required sophisticated numerical computation. Walsh and Towler (1994) introduced the simplest methods to determine PVT properties from CVD data which they called the Walsh-Towler algorithm. This method can be utilized through simple spreadsheets with its simple dependency on the reported CVD data. Thus, the PVT properties required to utilize a modified black-oil simulator can be attained through either of the methods presented by the Walsh-Towler algorithm, Whitson and Torp (1981), or using an Equation-of-State.

Isothermal depletion in liquid-rich gas reservoirs introduces an additional level of complexity to the analysis due to the fluid's thermodynamic fluid behavior. In this case, fluid properties are highly dependent on changes of pressure and composition. The thermodynamic fluid behavior is addressed through the joint use of Equations-of-State (EOS) and compositional material balances which form what we know today as the compositional simulators. Compositional simulators are capable of appraising the thermodynamic and hydrodynamic behavior of multiphase, multidimensional systems under different reservoir conditions. Kazemi *et al.* (1978) and Coats (1980) pioneered the first formulations of multiphase and multidimensional compositional simulators, which presented the fluid phases as N-component mixtures. Numerically, the compositional simulation computes the compositional changes of the phases of these components using molar conservation and phase equilibrium. With the accuracy of the calculations, compositional simulation provides vast applications for the reservoir engineers to forecast the behavior of complex fluids such as liquid-rich gas.

An Equation-of-State is originally developed through data fitting to existing pressure, volume, and temperature data of pure substances. In 1910, van der Waals developed an understanding of the behavior of real gases which exhibit properties that cannot be explained using the ideal gas law. He introduced an improved EOS by correcting the pressure with an attraction factor and volume with a co-volume factor. Following the vdW milestone, the development for EOS has

been carried on by Redlich-Kwong (1949), Soav-Redlich-Kwong (1972), Peng-Robinson (1976), and others to provide exact descriptions of the critical temperature and pressure which are the end point of vapor-pressure curves. These models are still widely used because of their simplicity, speed, and accuracy for many reservoir engineering applications. Modern Equations-of State are equipped with parameters that adjust for the attraction between the molecules and volume shifts, which makes the Equation-of-State semi-empirical. For binary and multi-component systems, the intricacy of the Equation-of-State increases because of the addition of compositions and obedience to a mixing rule. The higher the intricacy, the heavier the computational overhead, and the more accuracy the results will have.

The performance of compositional simulations in comparison with modified black-oil models was evaluated for gas-condensate reservoirs with different combinations of compositions by Coats (1985), Fevang and Whitson (1996), and Fevang *et al.* (2000). Coats (1985) simulated a cycling case with two components; he reported that both simulators produced the same result above dew point, but with noticeable differences below dew point. Fevang and Whitson (1996) reviewed the work of Coats and recommended extensive care when heptanes-plus is included in the EOS. They reasoned the differences in well deliverability to the oil viscosity which can be improved through proper splitting of heptanes-plus components. Fevang *et al.* (2000) arrived at the same results as Coats (1985) and recommended the use of compositional simulation for rich condensate, and modified black-oil for medium-rich condensate. Nojabaei *et al.* (2014) presented a comparison between modified black-oil simulation and fully compositional models on the bases of the findings from Nojabaei *et al.* (2013). The author examined the productivity of an oil reservoir at a temperature where capillary effect on bubble point pressure was apparent. The inclusion of capillary pressure effect seemed to enhance oil recovery. Overall, the match quality of pressure and production for the various cases examined appeared to depart from each other as time increased in a window of 200 days.

In the present study, great attention will be devoted toward developing a compositional simulator and a coupled phase behavior model with capillary equations, by associating the parameters of the EOS with the radius of the pores. The work will include consistency evaluation, and examining combination of fluid characteristics in tight formations under the influence of transport properties, diffusion, capillary pressure, and the presence of fractures.

# Chapter 3

## PROBLEM STATEMENT

Liquid-rich gas reservoirs are abundant in condensate content despite their classification as part of the gas reservoirs family. Under-saturated liquid-rich gas reservoirs are presented initially in a gaseous phase. Once depletion is undertaken and the pressure drops below dew point, condensate will drop out and accumulate near the production channels. The accumulation continues until the critical saturation is reached to trigger movement. The accumulation period is relevant to the fluid characteristics and depends on the production settings. During the period of accumulation, the productivity declines due to the impairment of flow near the flowing channels. The severity of such experience becomes significant in tighter formations. According to Ayyalasomayajula *et al.* (2003), this phenomenon may cost losses to the production by 40 to 80% of its estimates while flowing in a single phase.

Fractured tight reservoirs are presented numerically as a stack of matrix blocks surrounded by a fracture network as shown by Figure **3.1**, a depiction first presented by Warren and Root (1963). The higher permeability channels provide a sink of low pressure causing the flow of fluid to move from the inner part of the matrix toward the fracture channels. During depletion, condensate starts to form on the edges of the matrix blocks and in the fracture network. As a result, the condensate will accumulate in these areas and starts to hinder the flow of the gas from the inner portion of the matrix to the wellbore, as illustrated by Figure **3.2**.

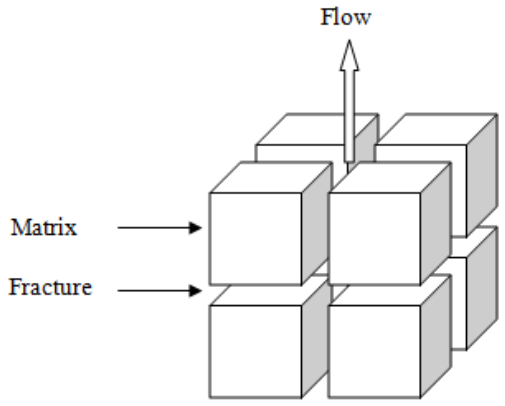


**Figure 3.1: Arrangement of matrix blocks and fractures**

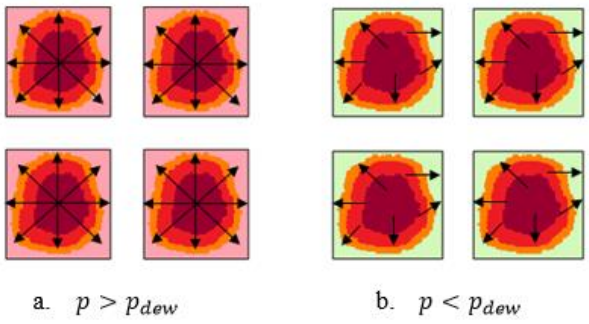


**Figure 3.2: Flow pattern during condensate drop-out**

Understanding the behavior of fractured reservoirs depends on examining the behavior inside the stacked single-matrix blocks under different boundary conditions (Peaceman, 1976). According to Van Golf-Racht (1982), using one single-matrix block to represent the reservoir arrangement illustrated in Figure **3.1** is sufficient since the single block has no communication with the adjacent blocks, which makes it self-governing and a good representative sample for scrutiny. With a single-block system, the inner matrix blocks accumulate most of the fluids in the reservoir, and based on the boundary condition established by the surrounding fractures, the matrix blocks will discharge its fluids into the fractured channels to be transported for production.

Liquid-rich gas reservoir performance relies on the characteristics of the fluids-in-place, rock environment, and boundary conditions. This dependency suggests the use of compositional simulators to evaluate the complexity of the thermodynamic behavior inside the reservoir. In this study, the flow behavior of liquid-rich gas reservoirs will be addressed using single-block simulation by developing a compositional model to examine the evolution of condensate and the productivity performance. More emphases will be placed on providing insight on productivity characteristics of liquid-rich gas systems in unconventional environments, and extend the scrutiny on the propagation of condensate while activating capillary forces and diffusion. The capillary pressure equation will be imbedded inside the phase behavior model through the empirical relationship between density and surface tension of mixtures. For optimum integration and consistent evaluation, it is intended to use a binary mixture varying from light to heavy mixtures. Under different rock environments, the study will consider different composition combinations, tight formations, activation of diffusion, fracture networks, activation of capillary forces, and using various relative permeability constraints.

# Chapter 4

## MODEL FORMULATION

Simulators are aimed at capturing thermodynamic behavior and predicting productivity by accounting for multiphase flow in multidimensional systems. As discussed earlier, there are two modeling techniques that can be used to simulate liquid-rich gas performance, compositional simulation and modified black-oil simulation. This section will emphasize on the compositional model and reference the modified black-oil formulations. In this chapter, the formulations will be expressed to document the assumptions and derivation of the governing equation. For the purpose of this study, the model is built to account for two hydrocarbon phases; gas and condensate that consist of 2-components in a 2-D system with uniform elevation. The general form of the governing differential equations used to represent the hydrocarbon fluid components is illustrated by equation (4.1). The derivation of the equation can be found in Appendix A. Equation (4.1) can be written using molar or mass flow representation based on the definition of variables demonstrated in Table **4.2**.

$$\frac{\partial}{\partial x}\left(C_{mo}A_x\frac{k_x k_{ro}}{\mu_o}\frac{\partial p_o}{\partial x}+C_{mg}A_x\frac{k_x k_{rg}}{\mu_g}\frac{\partial p_g}{\partial x}\right)\Delta x+\frac{\partial}{\partial y}\left(C_{mo}A_y\frac{k_y k_{ro}}{\mu_o}\frac{\partial p_o}{\partial y}+C_{mg}A_y\frac{k_y k_{rg}}{\mu_g}\frac{\partial p_g}{\partial y}\right)\Delta y$$
$$+F_m=\frac{V_b}{5.615}\frac{\partial}{\partial t}\left[\phi\left(S_o C_{mo}\ +S_g C_{mg}\right)\right] \qquad ;\ \ m=1,2 \qquad (4.1)$$

where: $C_{mf}$ : concentration of the $m^{th}$ component in the fluid phase

$F_m$ : flow of the $m^{th}$ component in molar or mass rate

**Table 4.1: Component's molar and mass representation**

| | **Concentration** | | **Flow Rate** |
|---|---|---|---|
| **Representation** | $\boldsymbol{C_{mo}}$ | $\boldsymbol{C_{mg}}$ | $\boldsymbol{F_m}$ |
| Molar | $x_m\bar{\rho}_o$ *(lbmol/ft$^3$)* | $y_m\bar{\rho}_g$ *(lbmol/ft$^3$)* | $M_m\ \left(\frac{lbmol\ .RB}{RCF\ day}\right)$ |
| Mass | $\omega_{mo}\,\rho_o$ *(lbm/ft$^3$)* | $\omega_{mg}\,\rho_g$ *(lbm/ft$^3$)* | $M_m^{\omega}\ \left(\frac{lbm\ .RB}{RCF\ day}\right)$ |

Equations (4.2a) illustrate the differential governing equation in terms of molar flow.

$$\frac{\partial}{\partial x}\left(x_m\bar{\rho}_o A_x \frac{k_x k_{ro}}{\mu_o}\frac{\partial p_o}{\partial x} + y_m\bar{\rho}_g A_x \frac{k_x k_{rg}}{\mu_g}\frac{\partial p_g}{\partial x}\right)\Delta x + \frac{\partial}{\partial y}\left(x_m\bar{\rho}_o A_y \frac{k_y k_{ro}}{\mu_o}\frac{\partial p_o}{\partial y} + y_m\bar{\rho}_g A_y \frac{k_y k_{rg}}{\mu_g}\frac{\partial p_g}{\partial y}\right)\Delta y + M_m = \frac{V_b}{5.615}\frac{\partial}{\partial t}\left[\phi\left(S_o x_m\bar{\rho}_o + S_g y_m\bar{\rho}_g\right)\right] \quad ; \quad m = 1,2 \tag{4.2a}$$

where: $M_m$ : molar flow rate $\left(\frac{lbmol\,.RB}{RCF\ day}\right)$

As discussed in Appendix A, with proper definitions of the concentration term, the governing equation can be written in the mass form as shown in equation (4.2b).

$$\frac{\partial}{\partial x}\left(\omega_{mo}\,\rho_o A_x \frac{k_x k_{ro}}{\mu_o}\frac{\partial p_o}{\partial x} + \omega_{mg}\,\rho_g A_x \frac{k_x k_{rg}}{\mu_g}\frac{\partial p_g}{\partial x}\right)\Delta x + \frac{\partial}{\partial y}\left(\omega_{mo}\,\rho_o A_y \frac{k_y k_{ro}}{\mu_o}\frac{\partial p_o}{\partial y} + \omega_{mg}\,\rho_g A_y \frac{k_y k_{rg}}{\mu_g}\frac{\partial p_g}{\partial y}\right)\Delta y + M_m^{\omega} = \frac{V_b}{5.615}\frac{\partial}{\partial t}\left[\phi\left(S_o\omega_{mo}\,\rho_o + S_g\omega_{mg}\,\rho_g\right)\right] \quad ; \quad m = 1,2 \tag{4.2b}$$

where: $M_m^{\omega}$ : mass flow rate $\left(\frac{lbm\,.RB}{RCF\ day}\right)$

In this work, the porous medium is considered to be wetted by water and condensate. It is assumed to have a natural initial water film in the reservoir. There are neither hydrocarbons dissolved in the water phase nor water can be found in solution with hydrocarbon phases. Thus, since the water is not reacting with the hydrocarbon and its presence is insignificant in the liquid phase, water is treated as an immobile phase.

The model is represented with $3n_c$+4 unknowns as indicated by Table **4.2,** which requires $3n_c$+4 equations as listed in Table **4.3**. Since, the number of components is already defined for this work, the model has 10 unknowns, and requires 10 equations. Moreover, all the other variables of the equations are calculated as a function of the dependent variables. In order to simplify the

calculation of the given equations, the number of unknowns is reduced and the eliminated variables are calculated after the principle unknowns are computed. For this work, the principle unknowns are considered to be the overall molar composition ($z_m$), and gas phase pressure ($p_g$).

**Table 4.2: Inventory of unknowns**

| | |
|---|---|
| Fluid Pressures | $p_o$, $p_g$ |
| Fluid Saturations | $S_o$, $S_g$ |
| Overall Composition | $z_m$ *(m=1, 2,….nc)* |
| Condensate Composition | $x_m$ ,$\omega_{mo}$ *(m=1, 2,….nc)* |
| Gas Composition | $y_m$ , $\omega_{mg}$ *(m=1, 2,….nc)* |
| *Total* | *$3n_c$+4 unknowns* |

**Table 4.3: Inventory of equations**

| | |
|---|---|
| Differential molar/mass balances (4.1) | *nc-equations* |
| Condensate Equilibrium Equation (B.15a) | *nc-equations* |
| Gas Equilibrium Equation (B.15b) | *nc-equations* |
| Vapor fraction/saturation relationship (4.16l) | *1 equation* |
| Saturation constraint (4.14a) | *1 equation* |
| Capillary pressure relationship (4.16p) | *1 equation* |
| Overall composition constraint (4.13) | *1 equation* |
| *Total* | *$3n_c$+4 equations* |

Once all the equations and constraints are defined and presented in a non-linear form, a special iterative procedure is required to solve for the unknowns. Before using the iterative technique, the non-linear equations will be replaced with finite differences approximation derived from Taylor's series as will be shown later in this chapter. The finite difference equations remain non-linear because the coefficients of the equations that are unknown are still functions of the unknown. Solving the flow equation requires using a linearization method; one of the commonly used linearization methods is the Newton-Raphson method. This work utilizes fully implicit formulation of Newton-Raphson to solve the entire unknown parameters simultaneously. The

fully-implicit technique allows all the primary unknowns to be calculated at the same time step, and update the solution using the iterative procedure until convergence is achieved. Once the specified tolerance is met, all the values are updated and can be carried out to the next time step.

### 4.1 Molar vs mass formulations

In this section, molar and mass formulations will be presented to demonstrate their difference to assess the development of the simulation tools for this study. The derivation is based on a binary mixture existing in a two-phase system; condensate and gas. Noteworthy, compositions of the phases can be expressed in molar or mass fraction as functions of fluid properties. Table **4.4** and Table **4.5** define the variables alongside the composition constraints of each phase, where P1 and P2 are pseudo-components standing for a volatile and a non-volatile component. In this development, corresponding definitions of compositions will be substituted into equation (4.2a) and equation (4.2b) to illustrate resemblance and to prove that both methods are expected to yield the same results.

**Table 4.4: Variables of binary mixture in molar form**

| Components | Liquid Composition | Vapor Composition | Liquid Phase—"o" | Vapor Phase—"g" |
|---|---|---|---|---|
| P1: Volatile<br>P2: Non-Volatile | $x_1$<br>$x_2$ | $y_1$<br>$y_2$ | $x_{1_o} + x_{2_o} = 1$ | $y_{1_g} + y_{2_g} = 1$ |

**Table 4.5: Variables of binary mixture in mass form**

| Components | Liquid Composition | Vapor Composition | Liquid Phase—"o" | Vapor Phase—"g" |
|---|---|---|---|---|
| P1: Volatile<br>P2: Non-Volatile | $\omega_{1o}$<br>$\omega_{2o}$ | $\omega_{1g}$<br>$\omega_{2g}$ | $\omega_{1o} + \omega_{2o} = 1$ | $\omega_{1g} + \omega_{2g} = 1$ |

Foremost, the molar flow equation will be developed utilizing the following molar expressions of compositions which are representing the molar concentration of the components in each of the phases.

$$x_1 = \frac{Moles\ of\ P_1\ \ in\ 1\ STB\ of\ oil\left(\frac{lbmol}{stb}\right)}{Moles\ of\ liquid\ phase\ in\ 1\ STB\ of\ oil\left(\frac{lbmol}{stb}\right)} = \frac{R_{so}/379.1\left(\frac{scf}{lbmol}\right)}{5.615\ \left(\frac{ft^3}{rb}\right)\ \rho_l B_l/MW_l}$$

$$= \frac{R_{so}}{(5.615)(379.1)\ \bar{\rho}_l B_l} = \frac{R_{so}}{(5.615)(379.1)\ \bar{\rho}_o B_o} \quad (4.3a)$$

$$x_2 = \frac{Moles\ of\ P_2\ \ in\ 1\ STB\ of\ oil\left(\frac{lbmol}{stb}\right)}{Moles\ of\ liquid\ phase\ in\ 1\ STB\ of\ oil\left(\frac{lbmol}{stb}\right)} = \frac{5.615\ \left(\frac{scf}{stb}\right)\rho_{osc}/MW_o}{5.615\ \left(\frac{ft^3}{rb}\right)\ \rho_l B_l/MW_l}$$

$$= \frac{\rho_{osc}}{MW_o \bar{\rho}_l B_l} = \frac{\rho_{osc}}{MW_o \bar{\rho}_o B_o} \quad (4.3b)$$

$$y_1 = \frac{Moles\ of\ P_1\ \ in\ 1\ SCF\ of\ gas\left(\frac{lbmol}{scf}\right)}{Moles\ of\ vapor\ phase\ in\ 1\ SCF\ of\ gas\left(\frac{lbmol}{scf}\right)} = \frac{1/379.1\left(\frac{scf}{lbmol}\right)}{5.615\ \left(\frac{ft^3}{rb}\right)\ \rho_v B_v/MW_v}$$

$$= \frac{MW_v}{(5.615)(379.1)\rho_v B_v} = \frac{1}{(5.615)(379.1)\ \bar{\rho}_g\ B_g} \quad (4.3c)$$

$$y_2 = \frac{Moles\ of\ P_2\ \ in\ 1\ SCF\ of\ gas\left(\frac{lbmol}{scf}\right)}{Moles\ of vapor\ phase\ in\ 1\ SCF\ of\ gas\left(\frac{lbmol}{scf}\right)} = \frac{5.615\ \left(\frac{scf}{stb}\right)\ R_v\ \rho_{osc}/MW_o}{5.615\ \left(\frac{ft^3}{rb}\right)\ \rho_v B_v/MW_v}$$

$$= \frac{R_v\ \rho_{osc}}{MW_o\ \bar{\rho}_v B_v} = \frac{R_v\ \rho_{osc}}{MW_o\ \bar{\rho}_g\ B_g} \quad (4.3d)$$

Recalling the molar-flow equation (4.2a), the molar-flow equation for each component is represented by equation (4.4) and (4.5) respectively.

$$\frac{\partial}{\partial x}\left(x_1\,\bar{\rho}_o A_x \frac{k_x k_{ro}}{\mu_o}\frac{\partial p_o}{\partial x} + y_1 \bar{\rho}_g A_x \frac{k_x k_{rg}}{\mu_g}\frac{\partial p_g}{\partial x}\right)\Delta x + \frac{\partial}{\partial y}\left(x_1 \bar{\rho}_o A_y \frac{k_y k_{ro}}{\mu_o}\frac{\partial p_o}{\partial y} + y_1 \bar{\rho}_g A_y \frac{k_y k_{rg}}{\mu_g}\frac{\partial p_g}{\partial y}\right)\Delta y + \frac{Q_1}{5.615} = \frac{V_b}{5.615}\frac{\partial}{\partial t}\left[\phi\left(S_o x_1 \bar{\rho}_o + S_g y_1 \bar{\rho}_g\right)\right] \quad ; \quad m = 1 \tag{4.4}$$

In the same form, molar equation for component-2 is illustrates as shown:

$$\frac{\partial}{\partial x}\left(x_2\,\bar{\rho}_o A_x \frac{k_x k_{ro}}{\mu_o}\frac{\partial p_o}{\partial x} + y_2 \bar{\rho}_g A_x \frac{k_x k_{rg}}{\mu_g}\frac{\partial p_g}{\partial x}\right)\Delta x + \frac{\partial}{\partial y}\left(x_2 \bar{\rho}_o A_y \frac{k_y k_{ro}}{\mu_o}\frac{\partial p_o}{\partial y} + y_2 \bar{\rho}_g A_y \frac{k_y k_{rg}}{\mu_g}\frac{\partial p_g}{\partial y}\right)\Delta y + \frac{Q_2}{5.615} = \frac{V_b}{5.615}\frac{\partial}{\partial t}\left[\phi\left(S_o x_2 \bar{\rho}_o + S_g y_2 \bar{\rho}_g\right)\right] \quad ; \quad m = 2 \tag{4.5}$$

Substituting the molar expressions of component-1 into equation (4.4) will yield to the following development:

$$\frac{\partial}{\partial x}\left(\frac{R_{so}}{(5.615)(379.1)\,B_o} A_x \frac{k_x k_{ro}}{\mu_o}\frac{\partial p_o}{\partial x} + \frac{1}{(5.615)(379.1)\,B_g} A_x \frac{k_x k_{rg}}{\mu_g}\frac{\partial p_g}{\partial x}\right)\Delta x + \frac{\partial}{\partial y}\left(\frac{R_{so}}{(5.615)(379.1)\,B_o} A_y \frac{k_y k_{ro}}{\mu_o}\frac{\partial p_o}{\partial y} + \frac{1}{(5.615)(379.1)\,B_g} A_y \frac{k_y k_{rg}}{\mu_g}\frac{\partial p_g}{\partial y}\right)\Delta y + \frac{Q_1}{5.615} = \frac{V_b}{5.615}\frac{\partial}{\partial t}\left[\phi\left(S_o \frac{R_{so}}{(5.615)(379.1)\,B_o} + S_g \frac{1}{(5.615)(379.1)\,B_g}\right)\right] \tag{4.6a}$$

Multiplying equation (4.6a) by [(5.615)(379.1)] will form the final form of the molar differential equation of component-1.

$$\frac{\partial}{\partial x}\left(R_{so}\,A_x \frac{k_x k_{ro}}{\mu_o B_o}\frac{\partial p_o}{\partial x} + A_x \frac{k_x k_{rg}}{\mu_g B_g}\frac{\partial p_g}{\partial x}\right)\Delta x + \frac{\partial}{\partial y}\left(R_{so} A_y \frac{k_y k_{ro}}{\mu_o B_o}\frac{\partial p_o}{\partial y} + A_y \frac{k_y k_{rg}}{\mu_g B_g}\frac{\partial p_g}{\partial y}\right)\Delta y + Q_1(379.1) = \frac{V_b}{5.615}\frac{\partial}{\partial t}\left[\phi\left(\frac{S_o}{B_o}R_{so} + \frac{S_g}{B_g}\right)\right] \tag{4.6b}$$

Since equation (4.6b) is written in molar form, $Q_1$ is the molar rate per day (*lbmol/day*). Equation (4.6b) resembles the gas-phase flow equation in the black-oil approaches since the term $[Q_1(379.1)]$ is now transformed to gas surface rate (*scf/day*). The final representation is shown by equation (4.6c).

$$\frac{\partial}{\partial x}\left(R_{so}\,A_x\frac{k_x k_{ro}}{\mu_o B_o}\frac{\partial p_o}{\partial x}+A_x\frac{k_x k_{rg}}{\mu_g B_g}\frac{\partial p_g}{\partial x}\right)\Delta x\;+\frac{\partial}{\partial y}\left(R_{so}A_y\frac{k_y k_{ro}}{\mu_o B_o}\frac{\partial p_o}{\partial y}+A_y\frac{k_y k_{rg}}{\mu_g B_g}\frac{\partial p_g}{\partial y}\right)\Delta y$$
$$+q_{sc,g}=\frac{V_b}{5.615}\frac{\partial}{\partial t}\left[\phi\left(\frac{S_o}{B_o}R_{so}\;+\frac{S_g}{B_g}\right)\right] \qquad (4.6c)$$

The next step is to substitute the molar expressions of component-2 into equation (4.5) which will lead to the following development:

$$\frac{\partial}{\partial x}\left(\frac{\rho_{osc}}{MW_o\,B_o}\,A_x\frac{k_x k_{ro}}{\mu_o}\frac{\partial p_o}{\partial x}+\frac{\rho_{osc}\,R_v}{MW_o B_g}A_x\frac{k_x k_{rg}}{\mu_g}\frac{\partial p_g}{\partial x}\right)\Delta x$$
$$+\frac{\partial}{\partial y}\left(\frac{\rho_{osc}}{MW_o\,B_o}A_y\frac{k_y k_{ro}}{\mu_o}\frac{\partial p_o}{\partial y}+\frac{\rho_{osc}\,R_v}{MW_o B_g}A_y\frac{k_y k_{rg}}{\mu_g}\frac{\partial p_g}{\partial y}\right)\Delta y$$
$$+\frac{Q_2}{5.615}=\frac{V_b}{5.615}\frac{\partial}{\partial t}\left[\phi\left(S_o\frac{\rho_{osc}}{MW_o\,B_o}\;+S_g\frac{\rho_{osc}\,R_v}{MW_o B_g}\right)\right] \qquad (4.7a)$$

Multiplying equation (4.7a) by the constant terms $\left[\frac{MW_o}{\rho_{osc}}\right]$ will yield to an expression representing the molar differential equation of component-2.

$$\frac{\partial}{\partial x}\left(A_x\frac{k_x k_{ro}}{\mu_o B_o}\frac{\partial p_o}{\partial x}+R_v A_x\frac{k_x k_{rg}}{\mu_g B_g}\frac{\partial p_g}{\partial x}\right)\Delta x+\frac{\partial}{\partial y}\left(A_y\frac{k_y k_{ro}}{\mu_o B_o}\frac{\partial p_o}{\partial y}+R_v A_y\frac{k_y k_{rg}}{\mu_g B_g}\frac{\partial p_g}{\partial y}\right)\Delta y$$
$$+\frac{Q_2 MW_o}{5.615\,\rho_{osc}}=\frac{V_b}{5.615}\frac{\partial}{\partial t}\left[\phi\left(\frac{S_o}{B_o}\;+R_v\frac{S_g}{B_g}\right)\right] \qquad (4.7b)$$

Equation (4.7b) is now similar to the oil-phase flow equation in the black-oil approaches since the term $\left[\frac{Q_2 MW_o}{5.615\rho_{osc}}\right]$ is demonstrating the oil surface rate (*stb/day*). The final representation of the oil-phase flow equation is seen by equation (4.7c).

$$\frac{\partial}{\partial x}\left( A_x \frac{k_x k_{ro}}{\mu_o B_o}\frac{\partial p_o}{\partial x} + R_v A_x \frac{k_x k_{rg}}{\mu_g B_g}\frac{\partial p_g}{\partial x}\right)\Delta x + \frac{\partial}{\partial y}\left( A_y \frac{k_y k_{ro}}{\mu_o B_o}\frac{\partial p_o}{\partial y} + R_v A_y \frac{k_y k_{rg}}{\mu_g B_g}\frac{\partial p_g}{\partial y}\right)\Delta y$$

$$+ q_{sc,o} = \frac{V_b}{5.615}\frac{\partial}{\partial t}\left[\phi\left(\frac{S_o}{B_o} + R_v \frac{S_g}{B_g}\right)\right] \qquad (4.7c)$$

The above development makes it undoubtable that the molar flow equations for compositional simulators can be related to black-oil formulations through proper definition of composition variables. This relationship is believed to hold stand even with compositions being expressed in mass fractions. In order to prove this claim, mass-fraction compositions will be defined as functions of fluid properties and substituted into equation (4.2b).

$$\omega_{1o} = \frac{Mass\ of\ P_1 in\ 1\ STB\ of\ oil\left(\frac{lbm}{stb}\right)}{Mass\ of\ liquid\ phase\ in\ 1\ STB\ of\ oil\left(\frac{lbm}{stb}\right)} = \frac{\rho_{gsc}\, R_{so}}{5.615\left(\frac{ft^3}{rb}\right)\rho_o B_o} \qquad (4.8a)$$

$$\omega_{2o} = \frac{Mass\ of\ P_2\ in\ 1\ STB\ of\ oil\left(\frac{lbm}{stb}\right)}{Mass\ of\ liquid\ phase\ in\ 1\ STB\ of\ oil\left(\frac{lbm}{stb}\right)} = \frac{5.615\left(\frac{scf}{stb}\right)\rho_{osc}}{5.615\left(\frac{ft^3}{rb}\right)\rho_o B_o}$$

$$= \frac{\rho_{osc}}{\rho_o B_o} \qquad (4.8b)$$

$$\omega_{1g} = \frac{Mass\ of\ P_1\ in\ 1\ SCF\ of\ gas\left(\frac{lbm}{scf}\right)}{Mass\ of\ vapor\ phase\ in\ 1\ SCF\ of\ gas\left(\frac{lbm}{scf}\right)} = \frac{\rho_{gsc}}{5.615\left(\frac{ft^3}{rb}\right)\rho_g B_g} \qquad (4.8c)$$

$$\omega_{2g} = \frac{Mass\ of\ P_2\ in\ 1\ SCF\ of\ gas\left(\frac{lbm}{scf}\right)}{Mass\ of\ vapor\ phase\ in\ 1\ SCF\ of\ gas\left(\frac{lbm}{scf}\right)} = \frac{5.615\left(\frac{scf}{stb}\right)\rho_{osc}\, R_v}{5.615\left(\frac{ft^3}{rb}\right)\rho_g B_g}$$

$$= \frac{\rho_{osc}\, R_v}{\rho_g B_g} \qquad (4.8d)$$

Restating the mass-flow equation (4.2b) and defining the compositional variables according to the number of components in the system. The mass-flow equation for each component is represented by equation (4.9) and (4.10) respectively.

$$\frac{\partial}{\partial x}\left(\omega_{1o}\rho_o A_x \frac{k_x k_{ro}}{\mu_o}\frac{\partial p_o}{\partial x} + \omega_{1g}\rho_g A_x \frac{k_x k_{rg}}{\mu_g}\frac{\partial p_g}{\partial x}\right)\Delta x + \frac{\partial}{\partial y}\left(\omega_{1o}\rho_o A_y \frac{k_y k_{ro}}{\mu_o}\frac{\partial p_o}{\partial y} + \omega_{1g}\rho_g A_y \frac{k_y k_{rg}}{\mu_g}\frac{\partial p_g}{\partial y}\right)\Delta y + \frac{Q_1^{\omega}}{5.615} = \frac{V_b}{5.615}\frac{\partial}{\partial t}\left[\phi\left(S_o\omega_{1o}\rho_o + S_g\omega_{1g}\rho_g\right)\right] \quad ; \quad m = 1 \tag{4.9}$$

The following is the representation of component 2 in mass form:

$$\frac{\partial}{\partial x}\left(\omega_{2o}\rho_o A_x \frac{k_x k_{ro}}{\mu_o}\frac{\partial p_o}{\partial x} + \omega_{2g}\rho_g A_x \frac{k_x k_{rg}}{\mu_g}\frac{\partial p_g}{\partial x}\right)\Delta x + \frac{\partial}{\partial y}\left(\omega_{2o}\rho_o A_y \frac{k_y k_{ro}}{\mu_o}\frac{\partial p_o}{\partial y} + \omega_{2g}\rho_g A_y \frac{k_y k_{rg}}{\mu_g}\frac{\partial p_g}{\partial y}\right)\Delta y + \frac{Q_2^{\omega}}{5.615} = \frac{V_b}{5.615}\frac{\partial}{\partial t}\left[\phi\left(S_o\omega_{2o}\rho_o + S_g\omega_{2g}\rho_g\right)\right] \quad ; \quad m = 2 \tag{4.10}$$

Substituting mass fraction definitions for component-1 into equation (4.9) yields:

$$\frac{\partial}{\partial x}\left(\frac{\rho_{gsc}\,R_{so}}{5.615\,B_o}A_x\frac{k_x k_{ro}}{\mu_o}\frac{\partial p_o}{\partial x} + \frac{\rho_{gsc}}{5.615\,B_g}A_x\frac{k_x k_{rg}}{\mu_g}\frac{\partial p_g}{\partial x}\right)\Delta x + \frac{\partial}{\partial y}\left(\frac{\rho_{gsc}\,R_{so}}{5.615\,B_o}A_y\frac{k_y k_{ro}}{\mu_o}\frac{\partial p_o}{\partial y} + \frac{\rho_{gsc}}{5.615\,B_g}A_y\frac{k_y k_{rg}}{\mu_g}\frac{\partial p_g}{\partial y}\right)\Delta y + \frac{Q_1^{\omega}}{5.615} = \frac{V_b}{5.615}\frac{\partial}{\partial t}\left[\phi\left(S_o\frac{\rho_{gsc}\,R_{so}}{5.615\;B_o} + S_g\frac{\rho_{gsc}}{5.615\,B_g}\right)\right] \tag{4.11a}$$

Multiply equation (4.11a) by the constant $\left[\frac{5.615}{\rho_{gsc}}\right]$ to illustrate the equation of component-1 in a compact form.

$$\frac{\partial}{\partial x}\left(R_{so}\,A_x\frac{k_x k_{ro}}{\mu_o B_o}\frac{\partial p_o}{\partial x} + A_x\frac{k_x k_{rg}}{\mu_g B_g}\frac{\partial p_g}{\partial x}\right)\Delta x + \frac{\partial}{\partial y}\left(R_{so}A_y\frac{k_y k_{ro}}{\mu_o B_o}\frac{\partial p_o}{\partial y} + A_y\frac{k_y k_{rg}}{\mu_g B_g}\frac{\partial p_g}{\partial y}\right)\Delta y + \frac{Q_1^{\omega}}{\rho_{gsc}} = \frac{V_b}{5.615}\frac{\partial}{\partial t}\left[\phi\left(\frac{S_o}{B_o}R_{so} + \frac{S_g}{B_g}\right)\right] \tag{4.11b}$$

Since equation (4.11b) is written in mass form, $Q_1^{\omega}$ is the rate of mass per day (*lbm/day*). Equation (4.11b) represents the gas-phase flow equation, where the term $\left[\frac{Q_1^{\omega}}{\rho_{gsc}}\right]$ is presented in the units of gas surface rate (*scf/day*). The final form as presented in equation (4.11c) matches the gas-phase equation in molar form depicted by equation (4.9c).

$$\frac{\partial}{\partial x}\left(R_{so}\,A_x\frac{k_x k_{ro}}{\mu_o B_o}\frac{\partial p_o}{\partial x}+A_x\frac{k_x k_{rg}}{\mu_g B_g}\frac{\partial p_g}{\partial x}\right)\Delta x+\frac{\partial}{\partial y}\left(R_{so}A_y\frac{k_y k_{ro}}{\mu_o B_o}\frac{\partial p_o}{\partial y}+A_y\frac{k_y k_{rg}}{\mu_g B_g}\frac{\partial p_g}{\partial y}\right)\Delta y$$
$$+q_{sc,g}=\frac{V_b}{5.615}\frac{\partial}{\partial t}\left[\phi\left(\frac{S_o}{B_o}R_{so}+\frac{S_g}{B_g}\right)\right] \qquad (4.11c)$$

For component-2, substituting the mass fractions shown by the definitions in (4.8b) and (4.8d) into equation (4.10) will produce the following equation:

$$\frac{\partial}{\partial x}\left(\frac{\rho_{osc}}{B_o}\,A_x\frac{k_x k_{ro}}{\mu_o}\frac{\partial p_o}{\partial x}+\frac{\rho_{osc}\,R_v}{B_g}A_x\frac{k_x k_{rg}}{\mu_g}\frac{\partial p_g}{\partial x}\right)\Delta x$$
$$+\frac{\partial}{\partial y}\left(\frac{\rho_{osc}}{B_o}A_y\frac{k_y k_{ro}}{\mu_o}\frac{\partial p_o}{\partial y}+\frac{\rho_{osc}\,R_v}{B_g}A_y\frac{k_y k_{rg}}{\mu_g}\frac{\partial p_g}{\partial y}\right)\Delta y$$
$$+\frac{Q_2^{\omega}}{5.615}=\frac{V_b}{5.615}\frac{\partial}{\partial t}\left[\phi\left(S_o\frac{\rho_{osc}}{B_o}+S_g\frac{\rho_{osc}\,R_v}{B_g}\right)\right] \qquad (4.12a)$$

Multiplying equation (4.12a) by the constant term $\left[\frac{1}{\rho_{osc}}\right]$will yield the compact form of the mass differential equation of component-2.

$$\frac{\partial}{\partial x}\left(A_x\frac{k_x k_{ro}}{\mu_o B_o}\frac{\partial p_o}{\partial x}+R_v A_x\frac{k_x k_{rg}}{\mu_g B_g}\frac{\partial p_g}{\partial x}\right)\Delta x+\frac{\partial}{\partial y}\left(A_y\frac{k_y k_{ro}}{\mu_o B_o}\frac{\partial p_o}{\partial y}+R_v A_y\frac{k_y k_{rg}}{\mu_g B_g}\frac{\partial p_g}{\partial y}\right)\Delta y$$
$$+\frac{Q_2^{\omega}}{5.615\,\rho_{osc}}=\frac{V_b}{5.615}\frac{\partial}{\partial t}\left[\phi\left(\frac{S_o}{B_o}+R_v\frac{S_g}{B_g}\right)\right] \qquad (4.12b)$$

It is apparent that the equation of (4.12b) is similar to the oil-phase flow equation in the black-oil approaches with the term $\left[\frac{Q_2^{\omega}}{5.615\,\rho_{osc}}\right]$ being converted to oil surface rate (*stb/day*). Similarly, the final representation for the oil phase equation in mass format is as follows:

$$\frac{\partial}{\partial x}\left( A_x \frac{k_x k_{ro}}{\mu_o B_o}\frac{\partial p_o}{\partial x} + R_v A_x \frac{k_x k_{rg}}{\mu_g B_g}\frac{\partial p_g}{\partial x}\right)\Delta x + \frac{\partial}{\partial y}\left( A_y \frac{k_y k_{ro}}{\mu_o B_o}\frac{\partial p_o}{\partial y} + R_v A_y \frac{k_y k_{rg}}{\mu_g B_g}\frac{\partial p_g}{\partial y}\right)\Delta y$$
$$+ q_{sc,o} = \frac{V_b}{5.615}\frac{\partial}{\partial t}\left[\phi\left(\frac{S_o}{B_o} + R_v \frac{S_g}{B_g}\right)\right] \quad (4.12c)$$

Ultimately, the development of the governing differential equations through proper definition of fluids' compositions in molar and mass formulation had proven to be equivalent. An important indication of definiteness in expressing compositions in both formulations was that both methods have reformed to the same equations. Equation (4.11c) and equation (4.6c) were alike, and both are representing the gas-phase flow equation in the black-oil approaches. Similarly, equation (4.12c) was comparable to equation (4.7c), and both have converged to the oil-phase flow equation used in the black-oil methods.

**4.2 Compositional model formulations**

Formulating a compositional simulator requires the knowledge of fluid properties calculated at reservoir conditions. Compositional models capture these changes through the use of a built-in Equation-of-State (EOS) model, where fluid properties are calculated based on changes of pressure, temperature, and compositions. In this work, Peng-Robinson EOS (Peng and Robinson, 1976) is utilized as part of a Phase Behavior Model (PBM) to perform flash calculation that will produce fluid properties. Formulations of PBM can be found in Appendix B.

The equilibrium molar vapor fraction of the reservoir mixture ($\alpha_g$) and the vapor-liquid equilibrium ratio ($K_m$) of each component are estimated through flash calculations at any given pressure ($p_g$), overall composition ($z_m$), and reservoir temperature. These properties quantify percentage of fluids in each phase, and phase preference. The results of the flash calculations are then carried to calculate the condensate compositions ($x_i$) and the gas compositions ($y_i$) for each component, which also yield to the calculations of densities and viscosities for each phase. Throughout flash calculations, the constraints shown be equation (4.13) is fulfilled at all times.

$$\sum_{m=1}^{n_c} z_m = 1 \tag{4.13}$$

Using the fluid properties and the equilibrium molar vapor fraction, gas saturation can be calculated as a function of ($p_g$,$z_m$,T, $\alpha_g$) with equation (4.14a). The derivation that captures the relationship between saturation and the equilibrium molar vapor fraction is shown by equations (4.14a) to (4.16n). Since water saturation is considered constant, oil saturation is calculated using the general saturation constraint shown in equation (4.14a). Finally, with the utilization of the capillary pressure equation, condensate pressure is calculated using equation (4.16o).

The relationship obtained between the equilibrium molar fraction and saturation can be derived by applying molar volume to molar density conversion starting from fluid saturation equation.

$$S_o + S_g + S_w = 1 \tag{4.14a}$$

Re-arranging equation (4.14a) to have gas and oil saturation in the left-hand-side (LHS) of the equation yield:

$$S_o + S_g = 1 - S_w \tag{4.14b}$$

Water in this study is assumed to never react with hydrocarbons, and only gas and oil can be found in solution. Knowing that saturation is the relative volume of a fluid to the volume of the mixture, each saturation term of hydrocarbons can be expressed in volume relationships. Note that volumes can be expressed in molar volumes, which subsequently bring in the molar fraction as the fraction of moles of the fluid per total moles.

$$S_g = \frac{V_g}{V_T} = \frac{\bar{v}_g}{\bar{v}_T}\frac{n_g}{n_T} = \alpha_g \frac{\bar{v}_g}{\bar{v}_T} \tag{4.15a}$$

$$S_o = \frac{V_o}{V_T} = \frac{\bar{v}_o}{\bar{v}_T}\frac{n_o}{n_T} = \alpha_o \frac{\bar{v}_o}{\bar{v}_T} \tag{4.15b}$$

Manipulating equation (4.14b) is essential to simplify the conversion in terms of molar densities and avoid calculating the total molar volume term. First, equation (4.14b) is multiplied by ($S_o$) to produce the following representation:

$$S_o\left(S_o + S_g\right) = S_o(1 - S_w) \tag{4.16a}$$

Re-arranging equation (4.16a) gives:

$$S_o = \frac{S_o}{\left(S_o + S_g\right)}\ (1 - S_w) \tag{4.16b}$$

Substituting the definitions of oil and gas saturation into equation (4.16b):

$$S_o = \frac{\alpha_o \frac{\bar{v}_o}{\bar{v}_T}}{\left(\alpha_o \frac{\bar{v}_o}{\bar{v}_T} + \alpha_g \frac{\bar{v}_g}{\bar{v}_T}\right)}\ (1 - S_w) \tag{4.16c}$$

Equation (4.16c) is now in a form that will allow mathematical manipulation to eliminate the total molar volume. Multiplying and dividing the right-hand-side (RHS) of equation (4.16c) by the total molar volume yields:

$$S_o = \frac{\bar{v}_T}{\bar{v}_T}\frac{\alpha_o \frac{\bar{v}_o}{\bar{v}_T}}{\left(\alpha_o \frac{\bar{v}_o}{\bar{v}_T} + \alpha_g \frac{\bar{v}_g}{\bar{v}_T}\right)}\ (1 - S_w) = \frac{\alpha_o \bar{v}_o}{\left(\alpha_o \bar{v}_o + \alpha_g \bar{v}_g\right)}\ (1 - S_w) \tag{4.16d}$$

Molar volume is the reciprocal of molar density. Thus, converting molar volume to molar density shall provide an expression of oil saturation in terms of molar fraction.

$$S_o = \frac{\alpha_o \frac{1}{\bar{\rho}_o}}{\left(\alpha_o \frac{1}{\bar{\rho}_o} + \alpha_g \frac{1}{\bar{\rho}_g}\right)}\ (1 - S_w) \tag{4.16e}$$

Equation (4.16e) can be re-arranged by mathematical manipulation to the RHS of the expression as follows:

$$S_o = \frac{\bar{\rho}_g \bar{\rho}_o}{\bar{\rho}_g \bar{\rho}_o} \frac{\alpha_o \frac{1}{\bar{\rho}_o}}{\left(\alpha_o \frac{1}{\bar{\rho}_o} + \alpha_g \frac{1}{\bar{\rho}_g}\right)} \ (1 - S_w) = \frac{\alpha_o \bar{\rho}_g}{\left(\alpha_o \bar{\rho}_g + \alpha_g \bar{\rho}_o\right)} \ (1 - S_w) \tag{4.16f}$$

Knowing that molar fraction of gas and oil brings unity, gives the final form of the relationship between saturation and the equilibrium molar fraction:

$$S_o = \frac{\left(1 - \alpha_g\right)\bar{\rho}_g}{\left(\left(1 - \alpha_g\right)\bar{\rho}_g + \alpha_g \bar{\rho}_o\right)} \ (1 - S_w) \tag{4.16g}$$

Equation (4.16g) can be defined explicitly in terms of $\alpha_g$ and $S_g$ with proper re-arrangement of variables. Transforming the equation to solve for the equilibrium molar fraction will require multiplication of both sides by $\left[\left(1 - \alpha_g\right)\bar{\rho}_g + \alpha_g \bar{\rho}_o\right]$ to give:

$$S_o \bar{\rho}_g - S_o \alpha_g \bar{\rho}_g + S_o \alpha_g \bar{\rho}_o = \bar{\rho}_g - \alpha_g \bar{\rho}_g - \bar{\rho}_g S_w + \alpha_g \bar{\rho}_g S_w \tag{4.16h}$$

Re-arraigning (4.16h) to have the variables depending on $\alpha_g$ on one side of the expression:

$$\alpha_g\left(-S_o \bar{\rho}_g + S_o \bar{\rho}_o + \bar{\rho}_g - \bar{\rho}_g S_w\right) = \bar{\rho}_g - \bar{\rho}_g S_w - \bar{\rho}_g S_o \tag{4.16i}$$

Assembling both sides by the common product $\bar{\rho}_g$, which yields:

$$\alpha_g\left(\bar{\rho}_g(1 - S_o - S_w) + S_o \bar{\rho}_o\right) = \bar{\rho}_g(1 - S_o - S_w) \tag{4.16j}$$

Substituting the definition of $S_g$ from the saturation constraint equation (4.14a):

$$\alpha_g\left(\bar{\rho}_g S_g + S_o \bar{\rho}_o\right) = \bar{\rho}_g S_g \tag{4.16k}$$

Simply, equation (4.16k) can be expressed in terms of $\alpha_g$ and $S_g$ as shown in the following forms:

$$\alpha_g = \frac{\bar{\rho}_g S_g}{\bar{\rho}_o S_o + \bar{\rho}_g S_g} \tag{4.16l}$$

$$S_g = \frac{\alpha_g \bar{\rho}_o S_o}{\bar{\rho}_g (1 - \alpha_g)} \tag{4.16m}$$

Since $S_o$ is unknown and it depends on the knowledge of $S_g$, substituting equation (4.16g) into equation (4.16m) will show $S_o$ in terms of the primary unknown $S_g$ as a function of pressure:

$$S_g = \frac{\frac{\alpha_g \, \bar{\rho}_o}{\bar{\rho}_g - \alpha_g \, \bar{\rho}_g}(1 - S_w)}{\left(1 + \frac{\alpha_g \, \bar{\rho}_o}{\bar{\rho}_g - \alpha_g \, \bar{\rho}_g}\right)} \tag{4.16n}$$

As inidacated earlier, $p_o$ is calculated in terms of the primary unknown $p_g$ with the knowledge of capilary pressure.

$$p_o = p_g - P_{cgo}(S_g) \tag{4.16o}$$

where: $P_{cgo}(S_g) = p_g - p_o$ (4.16p)

Compositional simulators evaluate reservoir behavior by accounting for each component making-up the fluid mixture. Obviously, compositional simulators rely heavily on EOS to provide the fluid properties needed to perform calculations. As a result, formulating a compositional simulator on a molar or mass bases is not a concern at this stage. In contrast, modified black-oil simulators predicts the performance of the reservoir based on a PVT model, where reservoir conditions are reinstated based on the volumes of fluids retrieved at surface conditions. A valuable source of information to conduct modified black-oil calculations is a CVD experiment from PVT laboratory testing. This type of tests provides insight on gas and condensate such as; compositions, volumes, compressibility factors, maximum liquid dropout, instantaneous recoveries, and cumulative recoveries. Using the experimental PVT data, the modified black-oil

PVT functions are obtained through mathematical procedures. Walash and Towler (2003) algorithm is a straightforward method to determine PVT properties from CVD data, which is explained in details in Appendix C.

The complexity associated with capturing liquid-rich gas behaviors advocate expressing reservoir fluids as mixtures of components for both simulators. As indicated in the previous section of this chapter, compositions can be expressed in molar or mass form. The two approaches to represent the governing equation will yield the typical black-oil governing equation of a two-phase system. However, the formulation of modified black-oil model can only be expressed in mass form. Appendix D illustrate the formulation necessary to build a modified black-oil simulator.

### 4.3 Finite difference approximation

In general, the formulations of reservoir simulators are combined to form a system of partial differential equations (PDEs). These PDE's are non-linear equation, which require replacing the partial derivatives with finite difference approximation. The finite differential representation of the compositional differential equation (4.2a) is represented in the following form after the substitution of the unknowns with the primary unknowns:

$$\frac{A_x k_x}{\Delta x}\Big|_{i+\frac{1}{2},j} \frac{\rho_o}{\mu_o}\Big|_{i+\frac{1}{2},j}^{n+1} x_m k_{ro}|_{i+\frac{1}{2},j}^{n+1} \left(p_g{}_{i+1,j}^{n+1} - p_g{}_{i,j}^{n+1}\right)$$

$$-\frac{A_x k_x}{\Delta x}\Big|_{i-\frac{1}{2},j} \frac{\rho_o}{\mu_o}\Big|_{i-\frac{1}{2},j}^{n+1} x_m k_{ro}|_{i-\frac{1}{2},j}^{n+1} \left(p_g{}_{i,j}^{n+1} - p_g{}_{i-1,j}^{n+1}\right)$$

$$+\frac{A_x k_x}{\Delta x}\Big|_{i+\frac{1}{2},j} \frac{\rho_g}{\mu_g}\Big|_{i+\frac{1}{2},j}^{n+1} y_m k_{rg}|_{i+\frac{1}{2},j}^{n+1} \left(p_g{}_{i+1,j}^{n+1} - p_g{}_{i,j}^{n+1}\right)$$

$$-\frac{A_x k_x}{\Delta x}\Big|_{i-\frac{1}{2},j} \frac{\rho_g}{\mu_g}\Big|_{i-\frac{1}{2},j}^{n+1} y_m k_{rg}|_{i-\frac{1}{2},j}^{n+1} \left(p_g{}_{i,j}^{n+1} - p_g{}_{i-1,j}^{n+1}\right)$$

$$-\frac{A_x k_x}{\Delta x}\Big|_{i+\frac{1}{2},j} \frac{\rho_o}{\mu_o}\Big|_{i+\frac{1}{2},j}^{n+1} x_m k_{ro}|_{i+\frac{1}{2},j}^{n+1} \left(p_{cgo}{}_{i+1,j}^{n+1} - p_{cgo}{}_{i,j}^{n+1}\right)$$

$$+\frac{A_x k_x}{\Delta x}\Big|_{i-\frac{1}{2},j}\frac{\rho_o}{\mu_o}\Big|_{i-\frac{1}{2},j}^{n+1} x_m k_{ro}|_{i-\frac{1}{2},j}^{n+1}\left({p_{cgo}}_{i,j}^{n+1}-{p_{cgo}}_{i-1,j}^{n+1}\right)$$

$$+\frac{A_y k_y}{\Delta y}\Big|_{i,j+\frac{1}{2}}\frac{\rho_o}{\mu_o}\Big|_{i,j+\frac{1}{2}}^{n+1} x_m k_{ro}|_{i,j+\frac{1}{2}}^{n+1}\left({p_g}_{i,j+1}^{n+1}-{p_g}_{i,j}^{n+1}\right)$$

$$-\frac{A_y k_y}{\Delta y}\Big|_{i,j-\frac{1}{2}}\frac{\rho_o}{\mu_o}\Big|_{i,j-\frac{1}{2}}^{n+1} x_m k_{ro}|_{i,j-\frac{1}{2}}^{n+1}\left({p_g}_{i,j}^{n+1}-{p_g}_{i,j-1}^{n+1}\right)$$

$$+\frac{A_y k_y}{\Delta y}\Big|_{i,j+\frac{1}{2}}\frac{\rho_g}{\mu_g}\Big|_{i,j+\frac{1}{2}}^{n+1} y_m k_{rg}|_{i,j+\frac{1}{2}}^{n+1}\left({p_g}_{i,j+1}^{n+1}-{p_g}_{i,j}^{n+1}\right)$$

$$-\frac{A_y k_y}{\Delta y}\Big|_{i,j-\frac{1}{2}}\frac{\rho_g}{\mu_g}\Big|_{i,j-\frac{1}{2}}^{n+1} y_m k_{rg}|_{i,j-\frac{1}{2}}^{n+1}\left({p_g}_{i,j}^{n+1}-{p_g}_{i,j-1}^{n+1}\right)$$

$$-\frac{A_y k_y}{\Delta y}\Big|_{i,j+\frac{1}{2}}\frac{\rho_o}{\mu_o}\Big|_{i,j+\frac{1}{2}}^{n+1} x_m k_{ro}|_{i,j+\frac{1}{2}}^{n+1}\left({p_{cgo}}_{i,j+1}^{n+1}-{p_{cgo}}_{i,j}^{n+1}\right)$$

$$+\frac{A_y k_y}{\Delta y}\Big|_{i.j-\frac{1}{2}}\frac{\rho_o}{\mu_o}\Big|_{i,j-\frac{1}{2}}^{n+1} x_m k_{ro}|_{i,j-\frac{1}{2}}^{n+1}\left({p_{cgo}}_{i,j}^{n+1}-{p_{cgo}}_{i,j-1}^{n+1}\right)+M_m$$

$$=\frac{V_b}{5.615\Delta t}\left[\left(\phi\left(1-S_g-S_w\right)x_m\rho_o+\phi S_g y_m\rho_g\right)_{i,j,k}^{n+1}-\left(\phi\left(1-S_g-S_w\right)x_m\rho_o+\phi S_g y_m\rho_g\right)_{i,j,k}^{n}\right]$$

$$;\qquad m=1,2 \qquad (4.17)$$

Equation (4.17) can be reduced to a shorter form by defining the transmissibility terms and substituting in the previous finite differential equations.

$$T_{ox}|_{i\pm\frac{1}{2}}^{n+1}=\frac{A_x k_x}{\Delta x}\Big|_{i\pm\frac{1}{2},j}\frac{\rho_o}{\mu_o}\Big|_{i\pm\frac{1}{2},j}^{n+1} x_m k_{ro}|_{i\pm\frac{1}{2},j}^{n+1} \qquad (4.18a)$$

$$T_{gx}|_{i\pm\frac{1}{2}}^{n+1}=\frac{A_x k_x}{\Delta x}\Big|_{i\pm\frac{1}{2},j}\frac{\rho_g}{\mu_g}\Big|_{i\pm\frac{1}{2},j}^{n+1} y_m k_{rg}|_{i\pm\frac{1}{2},j}^{n+1} \qquad (4.18b)$$

$$T_{oy}|_{j\pm\frac{1}{2}}^{n+1}=\frac{A_y k_y}{\Delta y}\Big|_{i,j\pm\frac{1}{2}}\frac{\rho_o}{\mu_o}\Big|_{i,j\pm\frac{1}{2}}^{n+1} x_m k_{ro}|_{i,j\pm\frac{1}{2}}^{n+1} \qquad (4.18c)$$

$$T_{gy}|_{j\pm\frac{1}{2}}^{n+1}=\frac{A_y k_y}{\Delta y}\Big|_{i,j\pm\frac{1}{2}}\frac{\rho_g}{\mu_g}\Big|_{i,j\pm\frac{1}{2}}^{n+1} y_m k_{rg}|_{i,j\pm\frac{1}{2}}^{n+1} \qquad (4.18d)$$

The substitution of each of the transmissibility terms into the finite difference equation (4.17) for hydrocarbon would form the following expression:

$$
\begin{aligned}
&T_{ox}|_{i+\frac{1}{2}}^{n+1}\left(p_{g}{}_{i+1,j}^{n+1}-p_{g}{}_{i,j}^{n+1}\right)-T_{ox}|_{i-\frac{1}{2}}^{n+1}\left(p_{g}{}_{i,j}^{n+1}-p_{g}{}_{i-1,j}^{n+1}\right)\\
&+T_{gx}|_{i+\frac{1}{2}}^{n+1}\left(p_{g}{}_{i+1,j}^{n+1}-p_{g}{}_{i,j}^{n+1}\right)-T_{gx}|_{i-\frac{1}{2}}^{n+1}\left(p_{g}{}_{i,j}^{n+1}-p_{g}{}_{i-1,j}^{n+1}\right)\\
&-T_{ox}|_{i+\frac{1}{2}}^{n+1}\left(p_{cgo}{}_{i+1,j}^{n+1}-p_{cgo}{}_{i,j}^{n+1}\right)+T_{ox}|_{i-\frac{1}{2}}^{n+1}\left(p_{cgo}{}_{i,j}^{n+1}-p_{cgo}{}_{i-1,j}^{n+1}\right)\\
&+T_{oy}|_{j+\frac{1}{2}}^{n+1}\left(p_{g}{}_{i,j+1}^{n+1}-p_{g}{}_{i,j}^{n+1}\right)-T_{oy}|_{j-\frac{1}{2}}^{n+1}\left(p_{g}{}_{i,j}^{n+1}-p_{g}{}_{i,j-1}^{n+1}\right)\\
&+T_{gy}|_{j+\frac{1}{2}}^{n+1}\left(p_{g}{}_{i,j+1}^{n+1}-p_{g}{}_{i,j}^{n+1}\right)-T_{gy}|_{j-\frac{1}{2}}^{n+1}\left(p_{g}{}_{i,j}^{n+1}-p_{g}{}_{i,j-1}^{n+1}\right)\\
&-T_{oy}|_{j+\frac{1}{2}}^{n+1}\left(p_{cgo}{}_{i,j+1}^{n+1}-p_{cgo}{}_{i,j}^{n+1}\right)+T_{oy}|_{j-\frac{1}{2}}^{n+1}\left(p_{cgo}{}_{i,j}^{n+1}-p_{cgo}{}_{i,j-1}^{n+1}\right)+M_{m}\\
&=\frac{V_{b}}{5.615\Delta t}\left[\left(\phi\left(1-S_{g}-S_{w}\right)x_{m}\rho_{o}+\phi S_{g}y_{m}\rho_{g}\right)_{i,j,k}^{n+1}-\left(\phi\left(1-S_{g}-S_{w}\right)x_{m}\rho_{o}+\phi S_{g}y_{m}\rho_{g}\right)_{i,j,k}^{n}\right]\\
&\qquad\qquad ;\qquad m=1,2 \qquad\qquad (4.19)
\end{aligned}
$$

The flow of fluids expressed by equation (4.17) and (4.19) can be reduced to shorter notations. The new form will describe the flow equations in terms of interfacial molar flows ($N_m$) in two flow directions (x, and y) as illustrated by equations (4.20a) and (4.20b).

$$N_{m}{}_{i\pm\frac{1}{2}}^{n+1}=\left(T_{ox}|_{i\pm\frac{1}{2}}^{n+1}+T_{gx}|_{i\pm\frac{1}{2}}^{n+1}\right)\left(p_{g}{}_{i\pm1,j}^{n+1}-p_{g}{}_{i,j}^{n+1}\right)-T_{ox}|_{i\pm\frac{1}{2}}^{n+1}\left(p_{cgo}{}_{i\pm1,j}^{n+1}-p_{cgo}{}_{i,j}^{n+1}\right) \quad \ldots \ (4.20a)$$

$$N_{m}{}_{j\pm\frac{1}{2}}^{n+1}=\left(T_{oy}|_{j\pm\frac{1}{2}}^{n+1}+T_{gy}|_{j\pm\frac{1}{2}}^{n+1}\right)\left(p_{g}{}_{i,j\pm1}^{n+1}-p_{g}{}_{i,j}^{n+1}\right)-T_{oy}|_{j\pm\frac{1}{2}}^{n+1}\left(p_{cgo}{}_{i,j\pm1}^{n+1}-p_{cgo}{}_{i,j}^{n+1}\right) \quad \ldots \ (4.20b)$$

Substituting the interface molar flow terms into equation (4.19) yield the final form of the flow equation in short notation:

$$N_{m}{}_{i+\frac{1}{2}}^{n+1}+N_{m}{}_{i-\frac{1}{2}}^{n+1}+N_{m}{}_{j+\frac{1}{2}}^{n+1}+N_{m}{}_{j-\frac{1}{2}}^{n+1}+M_{m}=Accumulation_{m} \ ; \quad m=1,2 \qquad (4.21)$$

**4.4 Evaluating transmissibility terms**

The reduced representation of the finite difference equation defined as transmissibility terms have produced a set of constants and non-linear functions. The constants parts are the geometrical attributes of the grid perpendicular to the direction of flow. In this study, a uniform grid sizes are depicted for the entire reservoir. Harmonic averaging technique is used to calculate the constant parts at the interface between neighboring blocks, which requires knowledge of the area perpendicular to the flow, permeability in the flow direction, and the finite difference space. These properties are calculated only once at the beginning of the simulation session. A general form for calculating harmonic mean of an arbitrary property "*a*" is given by equation (4.22). Since the transmissibility is calculated at the interface of two adjacent blocks, the constant parts at each direction is calculated as illustrated by equation (4.23a) through equation (4.23d).

$$H = \frac{1}{n}\sum_{i=1}^{n}\frac{1}{a_i} \tag{4.22}$$

for $n = 2$ : $\quad H(a_1, a_2) = \frac{2a_1a_2}{a_1+a_2}$

$$\left.\frac{A_x k_x}{\Delta x}\right|_{i+\frac{1}{2}} = \frac{2\left(\left.\frac{A_x k_x}{\Delta x}\right|_i\right)\left(\left.\frac{A_x k_x}{\Delta x}\right|_{i+1}\right)}{\left(\left.\frac{A_x k_x}{\Delta x}\right|_i\right)+\left(\left.\frac{A_x k_x}{\Delta x}\right|_{i+1}\right)} \tag{4.23a}$$

$$\left.\frac{A_x k_x}{\Delta x}\right|_{i-\frac{1}{2}} = \frac{2\left(\left.\frac{A_x k_x}{\Delta x}\right|_{i-1}\right)\left(\left.\frac{A_x k_x}{\Delta x}\right|_i\right)}{\left(\left.\frac{A_x k_x}{\Delta x}\right|_{i-1}\right)+\left(\left.\frac{A_x k_x}{\Delta x}\right|_i\right)} \tag{4.23b}$$

$$\left.\frac{A_y k_y}{\Delta y}\right|_{j+\frac{1}{2}} = \frac{2\left(\left.\frac{A_y k_y}{\Delta y}\right|_j\right)\left(\left.\frac{A_y k_y}{\Delta y}\right|_{j+1}\right)}{\left(\left.\frac{A_y k_y}{\Delta y}\right|_j\right)+\left(\left.\frac{A_y k_y}{\Delta y}\right|_{j+1}\right)} \tag{4.23c}$$

$$\left.\frac{A_y k_y}{\Delta y}\right|_{j-\frac{1}{2}} = \frac{2\left(\left.\frac{A_y k_y}{\Delta y}\right|_{j-1}\right)\left(\left.\frac{A_y k_y}{\Delta y}\right|_{j}\right)}{\left(\left.\frac{A_y k_y}{\Delta y}\right|_{j-1}\right)+\left(\left.\frac{A_y k_y}{\Delta y}\right|_{j}\right)} \tag{4.23d}$$

The displacement of fluids in the transmissibility terms is controlled by fluids densities and viscosities. Because they are weak functions of pressure, they are characterized as weak non-linear functions. Using a compositional EOS model, density and viscosity for each phase will be provided from PBM calculations. Genuinely, once the fluid densities and viscosities are known and considering their weak non-linearity, an Arithmetic average is taken at the interface in each direction. More techniques are available to estimate properties at the interface, such as one-point upstream weighting. This technique is used to approximate a property in a grid-space based on the upstream flow direction. Evaluating a property "*a*" between blocks *i* and *i+1*, as illustrated by equation (4.24a), depends on the pressure of the upstream block. The magnitude of property "*a*" where block pressure is higher will overwrite the one with the least pressure. One-point upstream weighting is primarily used for the strong non-linearities such as capillary pressures and relative permeabilities, which are dependent on saturation. However, one-point upstream can also be used for weak-linearities since they are weak functions of pressure and the outcomes are similar (Ayala, 2004). In this work, one-point upstream is used to approximate all non-linearities as shown by equation (4.24a) and equation (4.24b).

$$a|_{i\pm\frac{1}{2}} = \begin{cases} a|_i & if\ p_g|_i > p_g|_{i\pm1} \\ a|_{i\pm1} & if\ p_g|_{i\pm1} > p_g|_i \end{cases} \tag{4.24a}$$

$$a|_{j\pm\frac{1}{2}} = \begin{cases} a|_j & if\ p_g|_j > p_g|_{j\pm1} \\ a|_{j\pm1} & if\ p_g|_{j\pm1} > p_g|_j \end{cases} \tag{4.24b}$$

where : $a = \{x_m, y_m, \bar{\rho}_f, \mu_f, k_{rf}\}$

Furthermore, transmissibility through interfaces requires knowledge of compositions and relative permeabilities of fluids to flow. The composition of the phases will be provided by PBM after conducting flash calculations. The relative permeability to gas ($k_{rg}$), and relative permeability to

water ($k_{rw}$), are functions of gas saturation and water saturation respectively. Since water saturation in this study is constant, relative permeability to water is constant as well. Gas saturation is calculated as a function of ($p_g$,$z_m$,T) with equation (4.21j). Using the saturation values in hand, the relative permeaiblities to water and gas are read form oil-water and gas-oil relative permeability tables. Yet, relative permeability to oil ($k_{ro}$) is a function of gas saturation and water saturation, which reflects the existence of the other phases during the presence of oil. For the calculation of $k_{ro}$, Stone's II model (Stone, 1973) is utilized in this work as described by equation (4.25).

$$k_{ro} = k_{rocw}\left\{\left(\frac{k_{row}}{k_{rocw}} + k_{rw}\right)\left(\frac{k_{rog}}{k_{rocw}} + k_{rg}\right) - \left(k_{rw} + k_{rg}\right)\right\} \qquad (4.25)$$

where: $k_{ro}$ : relative permeability to oil in the presence of gas and water

$k_{rg}$ : relative permeability to gas in the presence of oil and water

$k_{rw}$ : relative permeability to water in the presence of oil and gas

$k_{rocw}$ : relative permeability to oil at connate water saturation (irreducible water).

$k_{row}$ : relative permeability to oil in an oil-water system with no gas present.

$k_{rog}$ : relative permeability to oil in an oil-gas system with no water present.

**4.5 Source term**

The source term is an external source for extraction or injection in the control volume as part of the material balance of fluids flowing into and out of the system. In this formulation, the source term is denoted as $M_m$ for molar flow of the $m^{th}$ component in $\left(\frac{lbmol\ .RB}{RCF\ day}\right)$. The scope of this study will be limited to explore production cases, which means the source terms will always be negative to indicate extraction of fluids. Molar flow is represented by the concentration of the $m^{th}$ component multiplied by the production rate as illustrated in equation (4.26).

$$M_m|_{i,j} = \left[x_m\ \bar{\rho}_o q_{res,o} + y_m\ \bar{\rho}_g q_{res.g}\right]_{i,j} \quad ; \quad m = 1, 2 \qquad (4.26)$$

where: $x_m$ : molar fraction of $m^{th}$ component in the condensate phase

$y_m$ : molar fraction of $m^{th}$ component in the gas phase

$\bar{\rho}_f$ : molar density of the phase, *lbmol/RCF*

$q_{res,o}$ : reservoir condensate flow rate, *RB/day*

$q_{res.g}$ : reservoir gas flow rate, *RB/day*

Peaceman (1983) presented a well model shown by equations (4.27a) and (4.27b) to calculate production rate in (*Rb/day*) for each phase as a function of phase mobility, production index, and pressure gradient. In this formulation, one perforated layer is assumed at all times.

$$q_{res,o}|_{i,j} = -\Omega \left.\frac{k_{ro}}{\mu_o}\left(p_o - p_{wf}\right)\right|_{i,j} \tag{4.27a}$$

$$q_{res,g}|_{i,j} = -\Omega \left.\frac{k_{rg}}{\mu_g}\left(p_g - p_{wf}\right)\right|_{i,j} \tag{4.27b}$$

Production index found in Peaceman's wellbore model can be calculated as follows:

$$\Omega|_{i,j} = \left.\frac{2\pi k_h h}{ln\left(\frac{r_e}{r_w}\right) + s}\right|_{i,j} \tag{4.28}$$

where: $p_f$ : phase pressure, *psia*

$p_{wf}$ : flowing bottomhole pressure, *psia*

$\mu_f$ : phase viscosity, *cp*

$k_h$ : geometric mean of the permeability in the xy-directions, *perm*

$h$ : thickness of the gridblock hosting the well, *ft*

$r_e$ : equivalent radius of the well, *ft*

$r_w$ : wellbore radius of the well, *ft*

$s$ : skin

The geometrical mean of the permeabilities in x- and y- directions are calculated for each gridblock using equation (4.29) in (*perms*).

$$k_h|_{i,j} = \left(k_x . k_y\right)^{\frac{1}{2}}\Big|_{i,j} \tag{4.29}$$

For each gridblock hosting a well, the equivalent radius is calculated based on the system's homogeneity in terms of permeability and spacing. Systems consisting of variant permeability and spacing in x- and y- directions require the use of the following expression for the equivalent radius:

$$r_e|_{i,j} = 0.28\left[\frac{\left(\frac{k_y}{k_x}\right)(\Delta x)^2 + \left(\frac{k_x}{k_y}\right)(\Delta y)^2}{\left(\frac{k_y}{k_x}\right)^{\frac{1}{4}} + \left(\frac{k_x}{k_y}\right)^{\frac{1}{4}}}\right]_{i,j} \tag{4.30a}$$

For isotropic systems where $k_x = k_y$ and $\Delta x \neq \Delta y$, the following expression is used for equivalent radius:

$$r_e|_{i,j} = 0.14\sqrt{(\Delta x)^2 + (\Delta y)^2}\Big|_{i,j} \tag{4.30b}$$

For isotropic systems where $k_x = k_y$ and $\Delta x = \Delta y$, equivalent radius is simply calculated as follows:

$$r_e|_{i,j} = 0.14\sqrt{2}\,\Delta x\Big|_{i,j} \tag{4.30c}$$

Evaluating the source term for each time-step is accounted for based on production specification. Production can be constraint by flowing bottomhole pressure or production at reservoir conditions. For the purpose of this study, only two form of production specification has been adopted; flowing bottomhole pressure and reservoir gas flow rate. During production under both specifications, the wells are designed to shut-off once pressure becomes very close to the flowing

bottomhole pressure, in order to prevent backflow into formation. The following constraint has to be met all times for the wells to stay in operative mode.

$$p_{wf}\big|_{i,j} < \min\left(p_g\right) \tag{4.31}$$

Production rates for condensate and gas can be directly calculated using equations (4.27a) and (4.27b) once production is constraint by flowing bottomhole pressure. However, if gas flow rate is specified at reservoir conditions, then the flowing bottomhole pressure needs to be calculated by re-arranging equation (4.27b) to form the expression in equation (4.32). Then, the condensate flow rate at reservoir conditions is calculated with direct plug-in of the outcome of equation (4.32) into equation (4.27a).

$$p_{wf}\big|_{i,j} = \frac{q_{res,g} + \Omega \frac{k_{rg}}{\mu_g} p_g}{\Omega \frac{k_{rg}}{\mu_g}} \tag{4.32}$$

**4.6 Solution technique**

Solution techniques for non-linear equations are available in different forms, but these techniques depend on many factors; such as computational overhead, speed of convergence, level of accuracy, and stability. In this model, the equations were discretized in a fully-implicit finite difference form, where the principle unknowns ($z_m$ and $p_g$) can be solved simultaneously at the same time. Despite the large computational expense of a fully-implicit computational solver, the numerical solution can be achieved in less iterative steps using Newton-Raphson procedure. The Newton-Raphson algorithm linearize the discretized set of equations allowing all the primary unknowns to be calculated at the same time step, and updating the solution using iterative procedure until convergence is achieved. Once the specified tolerance is met, all the values are updated and can be carried to the next time step. In order to apply Newton-Raphson procedures, the material balance equation derived in equation (4.21) need to be written in its residual form as shown by equation (4.33).

$$R_m{}^{n+1} = N_{m_{i+\frac{1}{2}}}{}^{n+1} + N_{m_{i-\frac{1}{2}}}{}^{n+1} + N_{m_{j+\frac{1}{2}}}{}^{n+1} + N_{m_{j-\frac{1}{2}}}{}^{n+1} + M_m - Accum_m \quad ; \quad m = 1,2 \qquad (4.33)$$

It is necessary to present the residual form as a function of the primary unknowns ($z_m$ and $p_g$) as follows:

$$R_{m_{i,j}}{}^{n+1}\left(z_1{}^{n+1}, p_g{}^{n+1}\right) = f\left(z_{1_{i,j-1}}{}^{n+1}, z_{1_{i-1,j}}{}^{n+1}, z_{1_{i,j}}{}^{n+1}, z_{1_{i+1,j}}{}^{n+1}, z_{1_{i,j+1}}{}^{n+1},\right.$$
$$\left. p_{g_{i,j-1}}{}^{n+1}, p_{g_{i-1,j}}{}^{n+1}, p_{g_{i,j}}{}^{n+1}, p_{g_{i,j+1}}{}^{n+1}, p_{g_{i+1,j}}{}^{n+1}\right) \quad ; \quad m = 1, 2 \qquad (4.34)$$

Applying Newton-Raphson linearization on equation (4.34) leads to the following representation:

$$-R_{m_{i,j}}{}^{n+1} = \left(\frac{\partial R_{m_{i,j}}}{\partial z_{1_{i,j-1}}}\right)^{n+1} \Delta z_{1_{i,j-1}}{}^{n+1} + \left(\frac{\partial R_{m_{i,j}}}{\partial z_{1_{i-1,j}}}\right)^{n+1} \Delta z_{1_{i-1,j}}{}^{n+1} + \left(\frac{\partial R_{m_{i,j}}}{\partial z_{1_{i,j}}}\right)^{n+1} \Delta z_{1_{i,j}}{}^{n+1}$$
$$+ \left(\frac{\partial R_{m_{i,j}}}{\partial z_{1_{i+1,j}}}\right)^{n+1} \Delta z_{1_{i+1,j}}{}^{n+1} + \left(\frac{\partial R_{m_{i,j}}}{\partial z_{1_{i,j+1}}}\right)^{n+1} \Delta z_{1_{i,j+1}}{}^{n+1} + \left(\frac{\partial R_{m_{i,j}}}{\partial p_{g_{i,j-1}}}\right)^{n+1} \Delta p_{g_{i,j-1}}{}^{n+1}$$
$$+ \left(\frac{\partial R_{m_{i,j}}}{\partial p_{g_{i-1,j}}}\right)^{n+1} \Delta p_{g_{i-1,j}}{}^{n+1} + \left(\frac{\partial R_{m_{i,j}}}{\partial p_{g_{i,j}}}\right)^{n+1} \Delta p_{g_{i,j}}{}^{n+1} + \left(\frac{\partial R_{m_{i,j}}}{\partial p_{g_{i+1,j}}}\right)^{n+1} \Delta p_{g_{i+1,j}}{}^{n+1}$$
$$+ \left(\frac{\partial R_{m_{i,j}}}{\partial p_{g_{i,j+1}}}\right)^{n+1} \Delta p_{g_{i,j+1}}{}^{n+1} \quad ; \quad m = 1,2$$

… (4.35)

The linearization presented in equation (4.35) is written for each gridblock to obtain an expression in the form of equation (4.36).

$$[J^{n+1}]^k . [\Delta\delta^{n+1}]^{k+1} = [-R^{n+1}]^k \qquad (4.36)$$

where: $J$ : Jacobian matrix

$\Delta\delta$ : change in primary unknown for every iteration

$R$ : residual of the equation

A Jacobian matrix with a dimension of $(n_b\ x\ n_c) \cdot (n_b\ x\ n_c)$ is generated to stack the linearized equations, where $n_b$ is the number of blocks and $n_c$ is the number of components. Each gridblock can be illustrated using the Jacobian representation below:

$$\begin{bmatrix} \left(\frac{\partial R_1}{\partial z_1}\right)^{n+1} & \left(\frac{\partial R_1}{\partial p_g}\right)^{n+1} \\ \left(\frac{\partial R_2}{\partial z_1}\right)^{n+1} & \left(\frac{\partial R_2^{\omega}}{\partial p_g}\right)^{n+1} \end{bmatrix}^{k}_{n_b n_c\ x\ n_b n_c} \begin{bmatrix} {\Delta z_1}^{n+1} \\ {\Delta p_g}^{n+1} \end{bmatrix}^{k+1}_{n_b n_c\ x1} = \begin{bmatrix} -{R_1}^{n+1} \\ -{R_2}^{n+1} \end{bmatrix}^{k}_{n_b n_c\ x1}$$

For a system of (*2x1*) gridblocks, the Jacobian matrix dimension will be (*4x4*) according to the dimension constraint $(n_b\ x\ n_c) \cdot (n_b\ x\ n_c)$:

$$\begin{bmatrix} \left(\frac{\partial R_1|_1}{\partial z_1|_1}\right)^{n+1} & \left(\frac{\partial R_1|_1}{\partial p_g|_1}\right)^{n+1} & \left(\frac{\partial R_1|_1}{\partial z_1|_2}\right)^{n+1} & \left(\frac{\partial R_1|_1}{\partial p_g|_2}\right)^{n+1} \\ \left(\frac{\partial R_2|_1}{\partial z_1|_1}\right)^{n+1} & \left(\frac{\partial R_2|_1}{\partial p_g|_1}\right)^{n+1} & \left(\frac{\partial R_2|_1}{\partial z_1|_2}\right)^{n+1} & \left(\frac{\partial R_2|_1}{\partial p_g|_2}\right)^{n+1} \\ \left(\frac{\partial R_1|_2}{\partial z_1|_1}\right)^{n+1} & \left(\frac{\partial R_1|_2}{\partial p_g|_1}\right)^{n+1} & \left(\frac{\partial R_1|_2}{\partial z_1|_2}\right)^{n+1} & \left(\frac{\partial R_1|_2}{\partial p_g|_2}\right)^{n+1} \\ \left(\frac{\partial R_2|_2}{\partial z_1|_1}\right)^{n+1} & \left(\frac{\partial R_2|_2}{\partial p_g|_1}\right)^{n+1} & \left(\frac{\partial R_2|_2}{\partial z_1|_2}\right)^{n+1} & \left(\frac{\partial R_2|_2}{\partial p_g|_2}\right)^{n+1} \end{bmatrix}^{k}_{4\ x\ 4} \begin{bmatrix} {\Delta z_1|_1}^{n+1} \\ {\Delta p_g|_1}^{n+1} \\ {\Delta z_1|_2}^{n+1} \\ {\Delta p_g|_2}^{n+1} \end{bmatrix}^{k+1}_{4\ x1} = \begin{bmatrix} -{R_1|_1}^{n+1} \\ -{R_2|_1}^{n+1} \\ -{R_1|_2}^{n+1} \\ -{R_2|_2}^{n+1} \end{bmatrix}^{k}_{4\ x1}$$

A solution is obtained by evaluating the entries of the Jacobian matrix using numerical differentiation:

$$\left(\frac{\partial R_{m_{i,j}}}{\partial z_1}\right)^{n+1} = \frac{R_{m_{i,j}}\left({z_1}^{n+1} + \epsilon_z,\ {z_{n_c-1}}^{n+1} - \epsilon_z,\ p_g^{n+1}\right) - R_{m_{i,j}}\left({z_1}^{n+1},\ {z_{n_c-1}}^{n+1},\ p_g^{n+1}\right)}{\epsilon_z}$$

$$;\quad m = 1,2 \quad and\ \epsilon_z = 10^{-6} \quad \ldots\ (4.37a)$$

$$\left(\frac{\partial R_{m_{i,j}}}{\partial p_g}\right)^{n+1} = \frac{R_{m_{i,j}}\left({z_1}^{n+1},\ {z_{n_c-1}}^{n+1},\ p_g^{n+1} + \epsilon_p\right) - R_{m_{i,j}}\left({z_1}^{n+1},\ {z_{n_c-1}}^{n+1},\ p_g^{n+1}\right)}{\epsilon_p}$$

$$;\quad m = 1,2 \quad and\ \epsilon_p = 10^{-4} \quad \ldots\ (4.37b)$$

**4.7 Internal checks**

The solution of the governing differential equation, where hydrocarbon fluid are flowing through a control volume, are conserved by material balance. The material entering and leaving the system over time ($\Delta t$) must be equivalent to the amount of material accumulated in the reservoir at all times. Thus, measuring the ratio of the material leaving the system to the production rate over time, should be equivalent. This material-balance check is used to measure accuracy of the numerical solution. There are two material balance checks; incremental material balance (*IMB*), and cumulative material balance (*CMB*). The incremental material balance is performed every time step after convergence is achieved, and is illustrated by equation (4.38a).

While, the cumulative material balance is performed at the end of the last time step and covers the entire time of simulation. Equation (4.38b) present the CMB material check. According to Ertekin *et al.* (2001), CMB has less accuracy than IMB because it tends to smooth errors captured at each time step.

$$IMB_m = \left| \frac{(SIP_m)_{t_f} - (SIP_m)_{t_f - \Delta t}}{5.615\ N_m^*\ \Delta t} \right| \quad ; \quad m = 1, 2 \tag{4.38a}$$

$$CMB_m = \left| \frac{(SIP_m)_{t_f} - (SIP_m)_{t_i}}{5.615\ M_{Pm}} \right| \quad ; \quad m = 1, 2 \tag{4.38b}$$

where:

$$SIP_m = \sum_{i=1}^{n_x} \sum_{j=1}^{n_y} ( x_m^{i,j} \bar{\rho}_o^{i,j} S_o^{i,j} + y_m^{i,j} \bar{\rho}_g^{i,j} S_g^{i,j} ) V_p^{i,j} \tag{4.38c}$$

$$N_m^* = \sum_{i=1}^{n_x} \sum_{j=1}^{n_y} M_m^{i,j} \tag{4.38d}$$

$$M_{Pm} = \int_t N_m^*\, dt \quad ; \quad m = 1, 2 \tag{4.38e}$$

$SIP_m$ : species-in-place, *lbmol*

$N_m^*$ : molar rate of m[th] component leaving the system, $\frac{lbmol\ .RB}{RCF\ day}$

$M_{Pm}$ : cumulative molar production of m[th] component, $\frac{lbmol\ .RB}{RCF\ day}$

$\Delta t$ : time step, *days*

$t_i$ : initial time before simulation starts, *days*

$t_f$ : time at the end of the time step, *days*

**4.8 Production and recoveries at surface conditions**

Productivity is measured by the volume of fluids retrieved on surface. The fluid mixture that makes it to surface has the same characteristics as the fluids found in the near wellbore region. According to Kumar (1987), as the wellstream travels from reservoir conditions to surface conditions it will undergo phase transitions owed to the thermodynamic changes. The transfer in phases is a result of weak attraction unveiling with the change of temperature and pressure as a function of depth. Molecules with higher tendency to be in the liquid phase will drop out, and those with tendency to be as gas will stay in the gas. Ultimately, the market is bias toward hydrocarbons in the liquid phase for its high price and rich thermal energy. Thus, fluids sent through sale lines must be thermodynamically stable to avoid changes in volumes. In order to reach stability in the wellstream, volumes are accounted for after separating the wellstream fluid into saleable products. The separated volumes are estimated through a separation facility in the field or experimentally in laboratories by replicating conditions of actual separation facility.

Capturing surface production through reservoir simulation is achieved differently depending on the type of simulator used. For the compositional simulator built, surface facilities are designed on the bases of PBM described in Appendix B, which is used to flash the wellstream as a function of pressure and temperature. However, for the MBO simulator, experimental data in the form of (CCE, CVD, and Recovery) as presented in Appendix C, are used to capture fluids separated at surface facility. Furthermore, evaluating the productivity of reservoirs is relatively measured by taking the ratio of the volumes retrieved at surface conditions to the volumes of fluids found in the reservoir. In this section, an overview on capturing productivity and recovery at surface

conditions are illustrated as incorporated in the building of the compositional simulator used in this study. For comparison, surface production for a modified black-oil simulator is presented in Appendix D.

### 4.8.1 Surface facilities for compositional simulator

Designing the surface facility is intended to maximize liquid extraction from the wellstream to maximize profit. The design consists of several separation facilities as depicted by Figure **4.1**, with pressure and temperature decreasing toward the stock tank. The reduction in the Pressure and temperature, allows the light components to escape in the form of gas, and the intermediates with the heavies joins into a liquid phase. The number of separation stages allows further refinement of the wellstream fluids, and extend the condensate extraction. Every separation facility is concluded with a stock tank vessel under standard conditions of pressure and temperature. Fluids recovered from stank tank are considered saleable and can be transferred directly to customers.

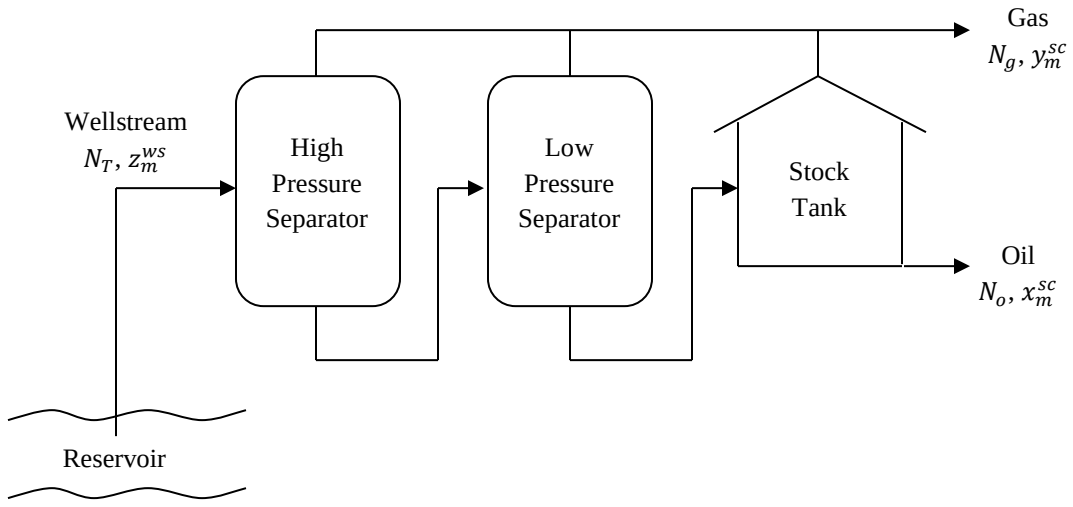


**Figure 4.1: Surface separation facility**

The simulation tools in hand have been built with a surface facility consisting of three separation vessels; a high pressure separator, a low pressure separator, and a stock tank. The code for the

separation facility allows the user to identify up to 5 stages with their pressures and temperatures. Regardless of the number of stages ($n_s$), the material balance in equation (4.39a) is maintained at all times.

$$N_T = N_g + N_o \tag{4.39a}$$

where:

$$N_T = \sum_{m=1}^{n_c} N_m^* \tag{4.39b}$$

$N_T$: total molar rate feeding into surface facility, $\frac{lbmol\ .RB}{RCF\ day}$

$N_m^*$ : molar rate of m[th] component leaving the reservoir, $\frac{lbmol\ .RB}{RCF\ day}$

$N_g$ : gas molar rate leaving the stock tank, $\frac{lbmol\ .RB}{RCF\ day}$

$N_o$ : oil molar rate leaving the stock tank, $\frac{lbmol\ .RB}{RCF\ day}$

The molar rates of gas and oil leaving stock tank are estimated through several flash calculations conducted using PBM. Each separator has a specified pressure and temperature and require knowledge of the overall molar composition of the wellstream feeding into it. The overall molar composition of each component is attained using equation (4.40) by dividing molar rate of the $m^{th}$ component leaving the reservoir by the total molar rate.

$$z_m^{ws} = \frac{N_m^*}{N_T} \quad ; \ m = 1,2 \tag{4.40}$$

Equation (4.40) is only used to estimate the wellstream composition feeding into the first separator. The wellstream feeding the rest of the separators are defined as the oil phase concentration resulting from the flash conducted in the preceded separation vessel. An illustration of the wellstream composition of the stages following the primary separator is given by equation (4.41).

$$z_m^{ws}|_{n_s} = x_m|_{n_s-1} \quad ; \ m = 1,2 \quad ; \ n_s = 2,3 \tag{4.41}$$

where: $n_s$ : number of stage

$z_m^{ws}$: wellstream molar composition of the $m^{th}$ component

Flash calculation conducted at each stage will provide properties similar to the output expected from PBM; which include (equilibrium molar fractions, molar compositions of the phases, compressibility factors). The oil composition of each stage define the wellstream composition of the next stage until leaving the final stage, were the output of oil composition is referred to as the stock tank oil composition ($x_m^{sc}$). Gas leaving each separator require no further processing, and is collected and forwarded to gas sale line directly. The composition of the gas leaving the surface facility ($y_m^{sc}$) is calculated as a function of $x_m^{sc}$ using equation (4.42a).

$$y_m^{sc} = \frac{z_m^{ws} - x_m^{sc} fs_o}{1 - fs_o} \tag{4.42a}$$

where:

$$fs_o = \prod_{s=1}^{n_s} \alpha_{os} \qquad ; \quad s = 1, 2, 3 \tag{4.42b}$$

$fs_o$: overall liquid molar fraction

$\alpha_{os}$: equilibrium molar liquid fraction at each stage

$y_m^{sc}$: molar composition of the gas phase at stock tank of the m$^{th}$ component

$x_m^{sc}$: molar composition of the oil phase at stock tank of the m$^{th}$ component

With the knowledge of the overall liquid molar fraction, gas and oil molar rate leaving stock tank are calculated using equations (4.43a) and (4.43b).

$$N_o = fs_o \, N_T \tag{4.43a}$$

$$N_g = \left(1 - fs_o\right) N_T \tag{4.43b}$$

The separation facility calculations are concluded with the estimation of surface flow rates of oil and gas, which are achieved in terms of the volumes retrieved on surface as follows:

$$q_{sc,o} = \frac{N_o}{\bar{\rho}_{osc}} \tag{4.44a}$$

$$q_{sc,g} = 5.615 \left(\frac{ft^3}{bbl}\right) \frac{N_g}{\bar{\rho}_{gsc}} \tag{4.44b}$$

where:

$$\bar{\rho}_{osc} = \frac{p_{sc}}{Z_{osc} R T_{sc}} \tag{4.44c}$$

$$\bar{\rho}_{gsc} = \frac{p_{sc}}{Z_{gsc} R T_{sc}} \tag{4.44d}$$

$q_{sc,o}$: surface oil flow rate at standard conditions, $stb/day$

$q_{sc,g}$: surface gas flow rate at standard conditions, $scf/day$

$\bar{\rho}_{osc}$: specific density of oil at standard conditions , $lbmol/ft^3$

$\bar{\rho}_{gsc}$: specific density of gas at standard conditions , $lbmol/ft^3$

$Z_{sc}$: compressibility factor of each fluid at standard conditions, where $Z_{gsc} = 1$

### 4.8.2 Fluid-in-place

During the depletion of liquid-rich gas reservoirs and as the pressure reduces below dew point pressure, productivity experiences a reduction in recovery due to the appearance of condensate. Assessing recovery scheme of liquid-rich gas reservoirs requires knowing the amount of fluids occupying the pore volumes of the reservoir at initial conditions. Thus, it is necessary to estimate original hydrocarbons (OHIP), original species in place (OSIP), and original gas and condensate in place (OGIP) and (OCIP) respectively. Formulating fluids-in-place calculations for compositional and modified black oil simulators are the same except for the evaluation of original gas and condensate in place.

Original hydrocarbons in place include all species presented initially in a gaseous phase. It is calculated in (*lbmol*) as a function of molar density and pore volume as indicated by equation (4.45a).

$$OHIP = \int_V \bar{\rho}_g (1 - S_{wi}) \phi \, dV \tag{4.45a}$$

The system under study is made up of several gridblocks in the x- and y- direction, integrating equation (4.45a) for each gridblock and summing the results will yield the OHIP of the entire field as follows:

$$OHIP\ (lbmol) = \sum_{i=1}^{n_x} \sum_{j=1}^{n_y} \bar{\rho}_g^{i,j} (1 - S_{wi}^{i,j}) V_p^{i,j} \tag{4.45b}$$

Moreover, the estimation of original species in place enables tracking of the amount of each component present in the reservoir. The OSIP is estimated in (*lbmol*) and is calculated using equation (4.46a).

$$OSIP_m(lbmol) = \sum_{i=1}^{n_x} \sum_{j=1}^{n_y} ( x_m^{i,j} \bar{\rho}_o^{i,j} S_o^{i,j} + y_m^{i,j} \bar{\rho}_g^{i,j} S_g^{i,j}) V_p^{i,j} \quad ; \quad m = 1, 2 \tag{4.46a}$$

Since OSIP is evaluated at initial conditions where hydrocarbons are found in gaseous form, OSIP can be calculated by multiplying the initial overall composition $z_m^i$ of each species by OHIP as follows:

$$OSIP_m(lbmol) = z_m^i OHIP \quad ; \quad m = 1, 2 \tag{4.46b}$$

For a compositional simulator, PBM is an advantageous tool which can be used to depict surface separation facility and provide estimates of initial volumes to the surface. After sending an initial wellstream feed to the surface facilities, an estimate of the initial overall liquid molar fraction is attained. The original gas in place (*scf*) and original condensate in place (*stb*) are calculated as functions of initial overall liquid molar fraction and OHIP. Equations (4.47a) and (4.47b) represent the calculation of OGIP and OCIP respectively.

$$OGIP\ (scf) = \frac{10.73\ T_{sc}\ (1 - fs_o^i\ )\ OHIP}{p_{sc}} \tag{4.47a}$$

$$OCIP(stb) = \frac{1}{5.615\ \bar{\rho}_{o,ST}^i} fs_o^i\ OHIP \tag{4.47b}$$

At initial conditions, the molar rate of the $m^{th}$ component anticipated to leave the system is assumed to have similar compositions as the initial overall compositions. Thus, the molar composition of each component feeding into the first separator is defined as the initial overall molar composition of each component according to the expression in (4.48).

$$z_m^{wsi} = z_m^i \quad ;\ m = 1,2 \tag{4.48}$$

At surface conditions, liquid-rich gas reservoirs yield production at a gas and condensate ratio up to 313 STB/MMSCF (McCain, 1993). The initial liquid-rich gas ratio (GOR), also referred to as the initial amount of volatilized condensate in the gas phase ($R_{vi}$), is a primary indicator of the reservoir type and the potential condensate production. As a function of OGIP and OCIP, $R_{vi}$ can be calculated as displayed by equation (4.49).

$$R_{vi}\left(\frac{stb}{MMscf}\right) = 1.10^3 \frac{OCIP}{OGIP} \tag{4.49}$$

During depletion, condensate content is expected to deplete as well due to the loss of heavy components to the reservoir. Tracking the condensate content throughout the production history is made possible by continuing to estimate the amount of fluids in place. Similarly, the amount of volatilized condensate in the gas phase ($R_v$) is measured by dividing condensate-in-place (CIP) by gas-in-place (GIP) as shown below:

$$R_v\left(\frac{stb}{MMscf}\right) = 1.10^3 \frac{CIP}{GIP} \tag{4.50}$$

Evaluating CIP and GIP is achieved by measuring the total amount of free gas in place (GHIP) and estimating the average free gas composition feeding into surface facilities. With respect to the reservoir's pore volume, GHIP is calculated in (*lbmol*) by applying equation (4.51a).

$$GHIP(lbmol) = \sum_{m=1}^{n_c} g_m \tag{4.51a}$$

where:

$$g_m = \sum_{i=1}^{n_x}\sum_{j=1}^{n_y} y_m^{i,j}\,\bar{\rho}_g^{i,j} S_g^{i,j} V_p^{i,j} \qquad ; \quad m = 1,2 \tag{4.51b}$$

$g_m$: moles of each component in the free gas, $lbmol$

$y_m$: gas molar composition of the $m^{th}$ component

$V_p$: pore volume, $ft^3$

$S_g$: gas saturation

$\bar{\rho}_g$: gas molar density, $lbmol/ft^3$

The overall molar composition of each component feeding into the first separator is defined as the average molar composition of free gas calculated as a function of GHIP according to the expression in (4.52). This will allow obtaining the current stock tank molar density and overall liquid molar fraction needed for the calculations of GIP and CIP.

$$z_m^{ws} = y_m^{av} = \frac{g_m}{GHIP} \qquad ; \; m = 1,2 \tag{4.52}$$

Plugging the outcomes of the separation facility calculations into equations (4.53a) and (4.53b) yield the current CIP and GIP respectively.

$$CIP(stb) = \frac{fs_o\, GHIP}{5.615\ \bar{\rho}_{o,ST}} \tag{4.53a}$$

$$GIP\ (scf) = \frac{10.73\, T_{sc}\,(1 - fs_o) GHIP}{p_{sc}} \tag{4.53b}$$

### 4.8.3 Recovery calculations

Overall performance of liquid-rich gas reservoirs are addressed through recovery calculations, which reflects the efficiency of the production scheme. Recovery factors estimate the ratio of the amount of volumes retrieved to the original amount of fluids in place. Knowing the initial amount of fluids in the reservoir, recovery factors calculations are attained using equations (4.54a) through (4.54d) which include; recovery factor of hydrocarbon, species, gas, and condensate ($R_{HC}, R_m, R_g, and\ R_o$).

$$R_{HC}(\%) = \frac{5.615 M_P}{OHIP} x100 \tag{4.54a}$$

$$R_m(\%) = \frac{5.615 M_{Pm}}{OSIP_m} x100 \quad ; \quad m = 1,2 \tag{4.54b}$$

$$R_g(\%) = \frac{G_P}{OGIP} x100 \tag{4.54c}$$

$$R_o(\%) = \frac{N_P}{OCIP} x100 \tag{4.54d}$$

In order to estimate cumulative production to satisfy recovery factor calculations, surface production for hydrocarbons, species, gas and condensate ( $N_t,\ N_m^*, q_{sc,g}, and\ q_{sc,o}$ ) are integrated with respect to time as follows:

$$M_P = \int_t N_t\, dt \tag{4.55a}$$

$$M_{Pm} = \int_t N_m^*\, dt \quad ; \quad m = 1,2 \tag{4.55b}$$

$$G_P = \int_t q_{sc,g}\, dt \tag{4.55c}$$

$$N_P = \int_t q_{sc,o}\, dt \tag{4.55d}$$

where: $M_P$ : cumulative molar production of hydrocarbons, $\frac{lbmol\ .RB}{RCF\ day}$

$M_{Pm}$ : cumulative molar production of each m$^{th}$ component, $\frac{lbmol\ .RB}{RCF\ day}$

$G_P$ : cumulative production of surface gas, *scf*

$N_P$ : cumulative production of surface oil, *stb*

$q_{sc,g}$ : gas production at stock tank conditions, *scf/day*

$q_{sc,o}$ : oil production at stock tank conditions, *stb/day*

# Chapter 5

# VALIDATION OF THE MODEL

## 5.1 In-house simulator versus commercial software

Numerical reservoir simulation is a modeling technique greatly used in the development, forecasting, and prediction of productivity of reservoirs to obtain higher recoveries. At this time, a fully-implicit compositional simulator was developed on MATLAB according to the formulations presented in Chapter 4. MATLAB is a technical programming language providing high performance computations for complex mathematical expressions. The reason MATLAB was selected over other computational methods, such as FORTRAN and C++, was for its built-in tools of editing, debugging, visualization, and functions of specific mathematical operations.

The in-house model was developed on molar units to allow validation against commercial software, which commonly accommodates flow of fluids in molar bases. This research utilizes a commercial numerical simulator developed by the Computer Modeling Group (CMG), which has many features including compositional simulation called GEM, and a phase behavior toolbox called WinProp. This tool has been proven to provide accurate estimation of phase behavior and properties of reservoir fluids especially for systems with complex compositional variation. For this study, CMG-GEM is used to generate a compositional model for the purpose of calibrating the in-house simulator's accuracy.

It was essential to have the in-house simulator built using the same units as the commercial software to provide grounds of comparison. Consistency in results is aimed for to suggest confidence in the approach and mathematical formulations used for the in-house simulator. In addition, it produces the starting point for future development of more complex models. This chapter aims to present a case study to be computed by both simulators to illustrate consistency in the produced results. The testing include matches of reservoir pressure, compositional evolution, saturations, reservoir productivity, and surface cumulative recoveries.

**5.2 System under study**

The setup of the validation model and data sets are introduced in this section. An elemental volume of a two-dimensional structure is built to host a liquid-rich gas system with equal dimensions in the x and y directions. All the sides of the inner blocks are open for flow upon the establishment of boundary conditions. However, the system is considered to have no flow at outer boundaries, placing the well as the primary source of fluid movement in the system. One production well is located in the center of the matrix as illustrated by Figure **5.1**. The purpose of placing the well in the center was to allow visual monitoring of a symmetrical wellbore region evolution. Placing the well near the border will create echo waves that will affect the pressure and saturation distribution and subsequently the condensate accumulation.

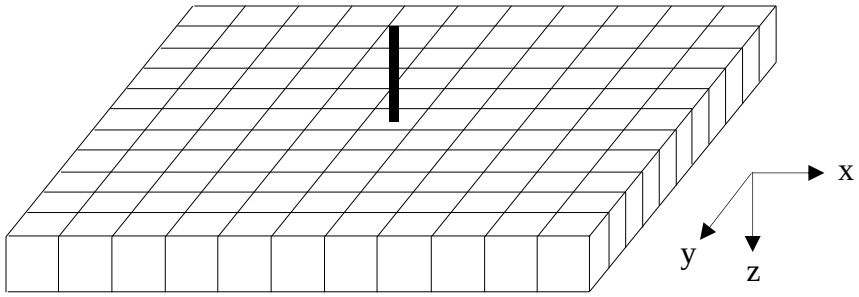


**Figure 5.1: Two-dimensional grid system (11x11) with one producer at (6x6)**

Tables **5.1** to Table **5.7**, document the data used as parameters for the validation of the in-house simulator. Table **5.1** represents the variables that were kept constant throughout the testing, which include the rock properties of the matrix along with the initial pressures and temperatures of the reservoir. Notably, time step is set at its default value of *1 day*, but at times where condensate suddenly appears and instability in calculation is encountered, a lower time step is used. In run-cases where instability becomes a concern at the start of the simulation, smaller time steps are used to initiate calculations. The time step is programmed to gain back its default value once stability is maintained for a reasonable period of time.

**Table 5.1: Constant variables throughout the study**

| Matrix | | |
|---|---|---|
| Matrix | $n_x$=11, $n_y$=11, $n_z$=1 | |
| Block dimension | Δx=Δy= 264 | ft |
| Height | 50 | ft |
| Top depth | 4000 | ft |
| Permeability | 1 | mD |
| Porosity | 0.13 | |
| Rock compressibility | 0 | $cp^{-1}$ |
| Initial pressure | 2200 | psia |
| Temperature | 100 | $^{o}F$ |
| Time step* | 1 | day |

(*) Time step default is 1 day, but is assigned in the range $0.01<\Delta t\leq 1$ day based on stability and when needed

Table **5.2** shows the properties of the phases present in the system, which includes the properties of hydrocarbon and water. Hydrocarbon properties are referenced in Table **5.3**, where the concentration of the mixture's components and physical properties are characterized in detail. The hydrocarbon properties were retrieved from physical property tables of pure components found in most petroleum engineering handbooks.

More information on the well properties and production constraints are displayed in Table **5.4**, where the flow is constrained by flowing bottom-hole pressure. Surface separation facility design is shown by Table **5.5**, which includes two separators and a stock tank. Table **5.6** displays the oil/gas relative permeability and capillary pressure data, where the capillary pressure data is initiated with zero values at this stage. Moreover, table **5.7** displays the oil/water relative permeability data with fixed capillary pressure data. Since the interaction between water and hydrocarbon is absent, the effect of oil/water capillary is neglected. Lastly, it is important to indicate that all the scenarios considered in this study have been set to run for a simulation period of 1,000 days.

**Table 5.2: Fluid properties**

| Hydrocarbon | | |
|---|---|---|
| Hydrocarbon properties | Table 5.3 | |
| **Water** | | |
| Water saturation (Swirr) | 0.16 | |
| Water compressibility | 0 | $cp^{-1}$ |
| Initial water FVF | 1 | rb/stb |
| Water viscosity | 0.89 | cp |
| Water density at SC | 62.4 | $lb/ft^3$ |

**Table 5.3: Hydrocarbon fluid properties**

Fluid Characterization

| Comp | $MW_m$ (lbm/lbmol) | $T_{cm}$ (R) | $P_{cm}$ (psia) | $Z_{cm}$ | $\omega_m$ | $\Omega_{am}$ | $\Omega_{bm}$ |
|---|---|---|---|---|---|---|---|
| P1 | 16.043 | 343.33 | 666.4 | 0.2874 | 0.0104 | 0.457235529 | 0.077796074 |
| P2 | 58.123 | 765.62 | 550.6 | 0.2728 | 0.1995 | 0.457235529 | 0.077796074 |

Note: Volume shifts are set to zero

Concentrations

| Comp | $z_i$ |
|---|---|
| P1 | 0.75 |
| P2 | 0.25 |

Binary Interaction Coefficients

| Comp | P1 | P2 |
|---|---|---|
| P1 | 0 | 0.01474853 |
| P2 | 0.01474853 | 0 |

**Table 5.4: Well information**

| Well-1 | | |
|---|---|---|
| Location | $n_x$=6, $n_y$=6, $n_z$=1 | |
| Well specification | Bottom-hole pressure ($p_{wf}$) | |
| | 1500 | psia |
| Wellbore radius | 0.25 | ft |
| Skin | 0 | |

**Table 5.5: Surface separation facility information**

| Separator | Pressure (psia) | Temperature (F) |
|---|---|---|
| Primary | 815 | 80 |
| Second Stage | 315 | 80 |
| Stock Tank | 14.7 | 60 |

**Table 5.6: Oil/gas relative permeability and capillary pressure data**

| $S_g$ | $K_{rg}$ | $K_{rog}$ | $P_{cgo}$ |
|---|---|---|---|
| 0.00 | 0.000 | 0.800 | 0.0 |
| 0.04 | 0.005 | 0.650 | 0.0 |
| 0.08 | 0.013 | 0.513 | 0.0 |
| 0.12 | 0.026 | 0.400 | 0.0 |
| 0.16 | 0.040 | 0.315 | 0.0 |
| 0.20 | 0.058 | 0.250 | 0.0 |
| 0.24 | 0.078 | 0.196 | 0.0 |
| 0.28 | 0.100 | 0.150 | 0.0 |
| 0.32 | 0.126 | 0.112 | 0.0 |
| 0.36 | 0.156 | 0.082 | 0.0 |
| 0.40 | 0.187 | 0.060 | 0.0 |
| 0.44 | 0.222 | 0.040 | 0.0 |
| 0.48 | 0.260 | 0.024 | 0.0 |
| 0.52 | 0.300 | 0.012 | 0.0 |
| 0.56 | 0.348 | 0.005 | 0.0 |
| 0.60 | 0.400 | 0.000 | 0.0 |
| 0.64 | 0.450 | 0.000 | 0.0 |
| 0.68 | 0.505 | 0.000 | 0.0 |
| 0.72 | 0.562 | 0.000 | 0.0 |
| 0.76 | 0.620 | 0.000 | 0.0 |
| 0.80 | 0.680 | 0.000 | 0.0 |
| 0.84 | 0.740 | 0.000 | 0.0 |

**Table 5.7: Oil/water relative permeability and capillary pressure data**

| $S_w$ | $K_{rw}$ | $K_{row}$ | $P_{cow}$ |
|---|---|---|---|
| 0.16 | 0.000 | 0.800 | 50.0 |
| 0.20 | 0.002 | 0.650 | 32.0 |
| 0.24 | 0.010 | 0.513 | 21.0 |
| 0.28 | 0.020 | 0.400 | 15.5 |
| 0.32 | 0.033 | 0.315 | 12.0 |
| 0.36 | 0.049 | 0.250 | 9.2 |
| 0.40 | 0.066 | 0.196 | 7.0 |
| 0.44 | 0.090 | 0.150 | 5.3 |
| 0.48 | 0.119 | 0.112 | 4.2 |
| 0.52 | 0.150 | 0.082 | 3.4 |
| 0.56 | 0.186 | 0.060 | 2.7 |
| 0.6 | 0.227 | 0.040 | 2.1 |
| 0.64 | 0.277 | 0.024 | 1.7 |
| 0.68 | 0.330 | 0.0124 | 1.3 |
| 0.72 | 0.390 | 0.005 | 1.0 |
| 0.76 | 0.462 | 0.000 | 0.7 |
| 0.80 | 0.540 | 0.000 | 0.5 |
| 0.84 | 0.620 | 0.000 | 0.4 |
| 0.88 | 0.710 | 0.000 | 0.3 |
| 0.92 | 0.800 | 0.000 | 0.2 |
| 0.96 | 0.900 | 0.000 | 0.1 |
| 1.00 | 1.000 | 0.000 | 0.0 |

Generally, tuning the tolerances of the numerical performance to have tight convergence criteria contributes to the accuracy of the results. In this work, the defined numerical tolerances, illustrated by Table **5.8**, were significantly important to attain comparable results between the in-house simulator and CMG-GEM. Moreover, the allowable changes of pressure and composition between iterations were controlled and were not allowed to reach negative values. In initiating the simulation runs, a smaller time step than *1 day* was used until completing one day of simulation, then the time step was returned to its default value.

**Table 5.8: Numerical tolerance for calculations**

| Numerical Constraint | Value |
|---|---|
| Maximum Change in pressure per time step | 1000 psia |
| Maximum Change in overall composition per time step | 0.35 |
| Maximum tolerance for any equation | Tighter |
| Linear Solver Precision | 1e-6 |
| Convergence criterion for pressure | 1e-4 |
| Convergence criterion for overall composition | 1e-6 |
| Relative Tolerance for water molar density | 0.001 |
| Maximum allowable NR iterations per time step | 20 |
| Stability tolerance for NR iterations | 10 |
| Maximum allowable NR iteration for bicgstab | 5000 |

## 5.3 Preliminary results

This section presents the performance of the developed in-house simulator in comparison to the results of a commercial software program using the given data. In this work, CMG-GEM was utilized to simulate the same scenario given in order to establish a reference point for the comparison. The well is put under production at the start of the simulation according to a specified bottom-hole pressure of 1,500 psia for 1,000 days. During the production period, performance data were retrieved, such as reservoir pressure, compositional evolution, saturations, reservoir productivity, and surface cumulative productions. In order to prove the accuracy of the in-house simulator, the results are presented in two ways in comparison to CMG. First, an aerial overview of some of the properties are created to assure consistency in the evolution from the wellbore region toward the borders of the reservoir. Second, proving the capability of the in-house simulator to capture well performance through x-y plots with comparison to the commercial simulator's results. With both simulators, the reservoir is found in its gaseous form at the initial time of simulation. The results are aimed to capture the complexity as condensate starts accumulating until reaching the critical saturation of 28% at which condensate starts flowing.

Aerial views of pressure, global molar composition of P1, and oil saturation are illustrated by Figures **5.2** to **5.4,** respectively. For consistency on plot configurations, the results from both simulators were plotted using the plotting toolbox of MATLAB. Figure **5.2** presents the gas pressure of the 2-D system captured by the in-house and CMG simulators after 1,000 days. The results show the match between the two simulators, where the pressure is about 1,970 psia at the well location and higher than 2,050 psia at the corners of the 2-D system.

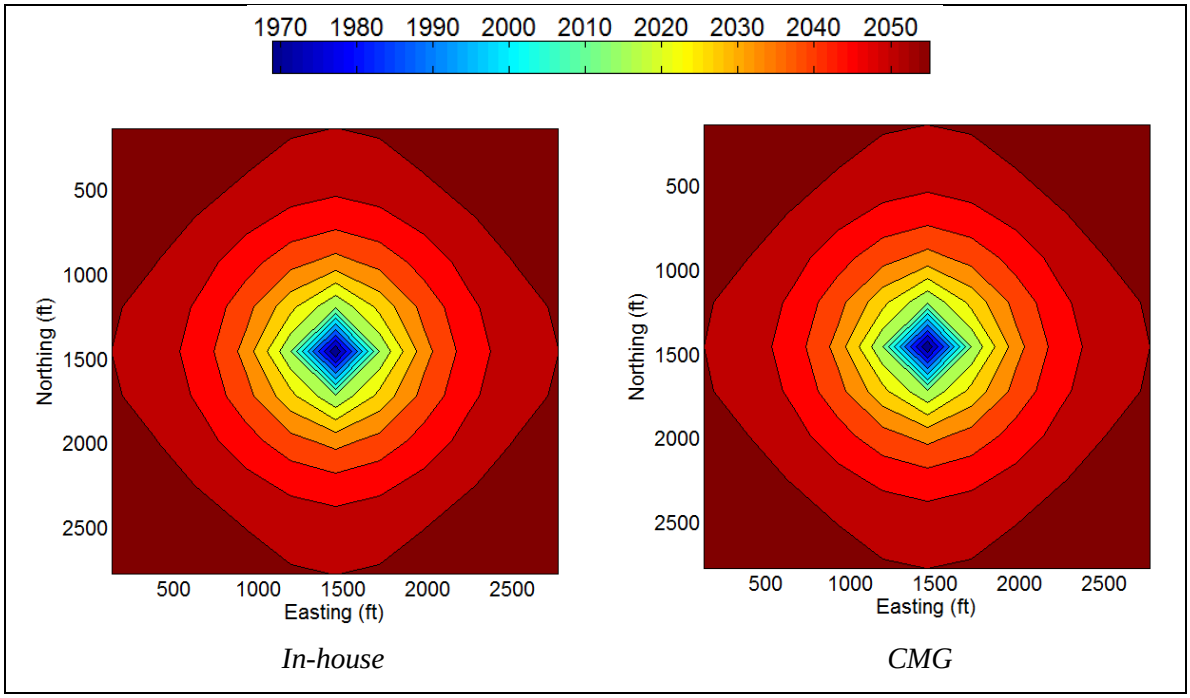


**Figure 5.2: Gas pressure after 1000 days (in-house simulator vs. CMG)**

Figures **5.3** and **5.4** present an overlook on the evolution of condensate saturation and overall composition in the reservoir with pressure depletion. Since the permeability of the reservoir is low, the well drawdown effect is limited to the near wellbore region. Areas that are far from the wellbore are still above dew point pressure (1991.6 psia), which will require time before the well effect transmits to the boundaries of the reservoir. For this reason, the changes in global composition and condensate evolution are limited to the wellbore region at 1,000 days. Figures **5.3** and **5.4** present the aerial changes in composition as being captured by the two simulators.

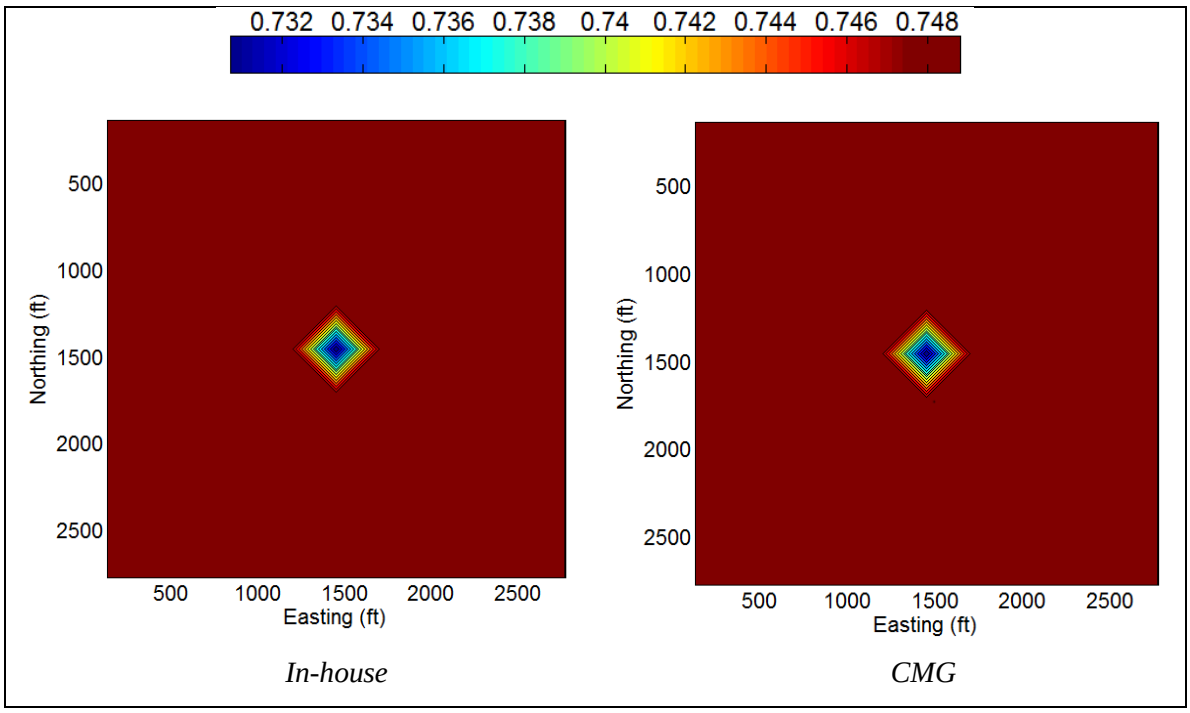


**Figure 5.3: Global composition of P1 after 1000 days (in-house simulator vs. CMG)**

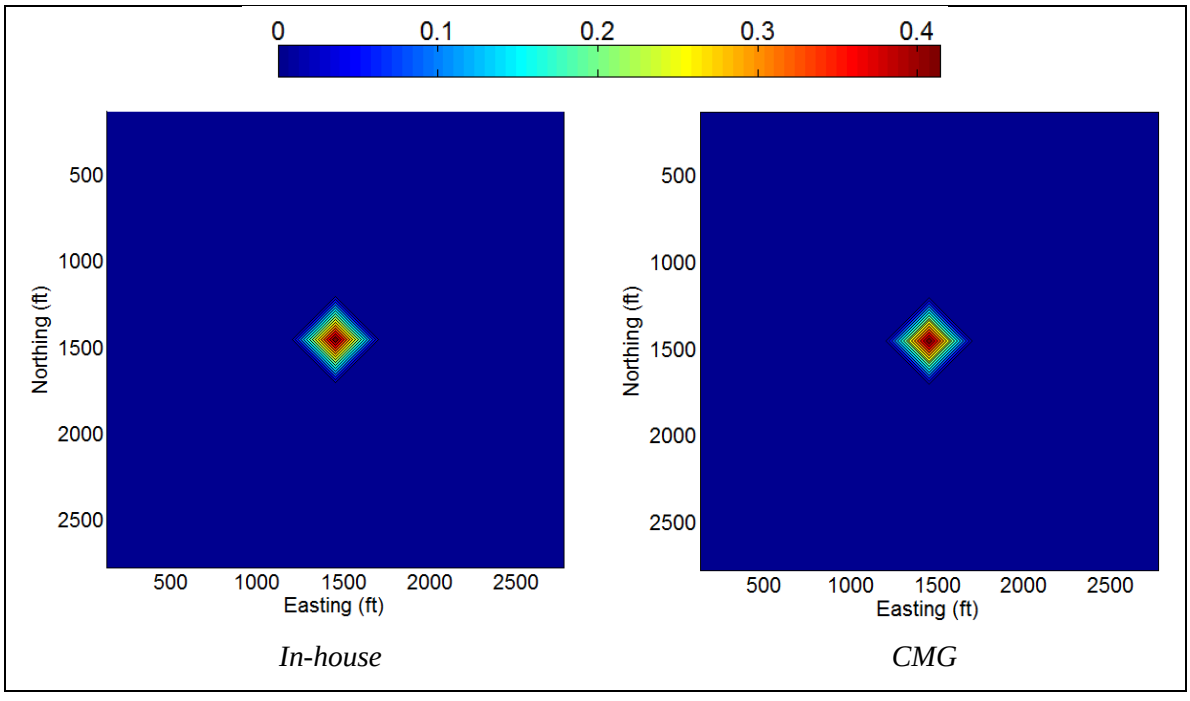


**Figure 5.4: Oil saturation after 1000 days (in-house simulator vs. CMG)**

Figures **5.5** to Figure **5.12** illustrate x-y plots to validate well performance of the in-house simulator in comparison to CMG. Pressure depletion is captured with Figure **5.5** showing saturation pressure being reached after 30 days of production, where the dew point pressure is captured at 1,991.6 psia. After 600 days, pressure declines notably because condensate starts mobilizing after a period of accumulation. Since the content of heavies in the mixture is not significant, the accumulation of condensate has no apparent influence to cause an increase in pressure.

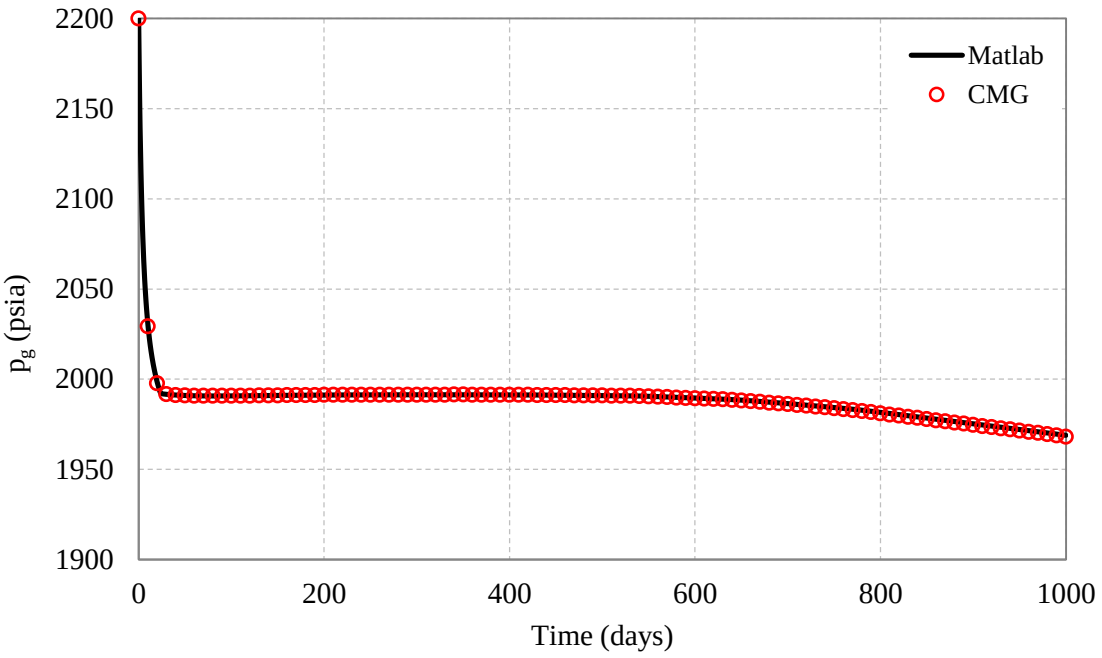


**Figure 5.5: Gas pressure at the well (in-house simulator vs. CMG)**

The compositional changes in the reservoir are captured using Figure **5.6**, where the molar fraction of P1 and P2 are plotted versus time. Since the system only consists of two components, the changes in P1 are reflected on P2 with the relationship that both add up to unity. For about a month, the molar fraction of P1 and P2 are maintained at their initial compositions because the reservoir is still in its gaseous form. As saturation pressure is reached, gas keeps flowing and condensate starts accumulating, allowing the non-volatile components to pick up in concentrations. The in-house simulator proves its validity against CMG with the matches shown in Figure **5.6**.

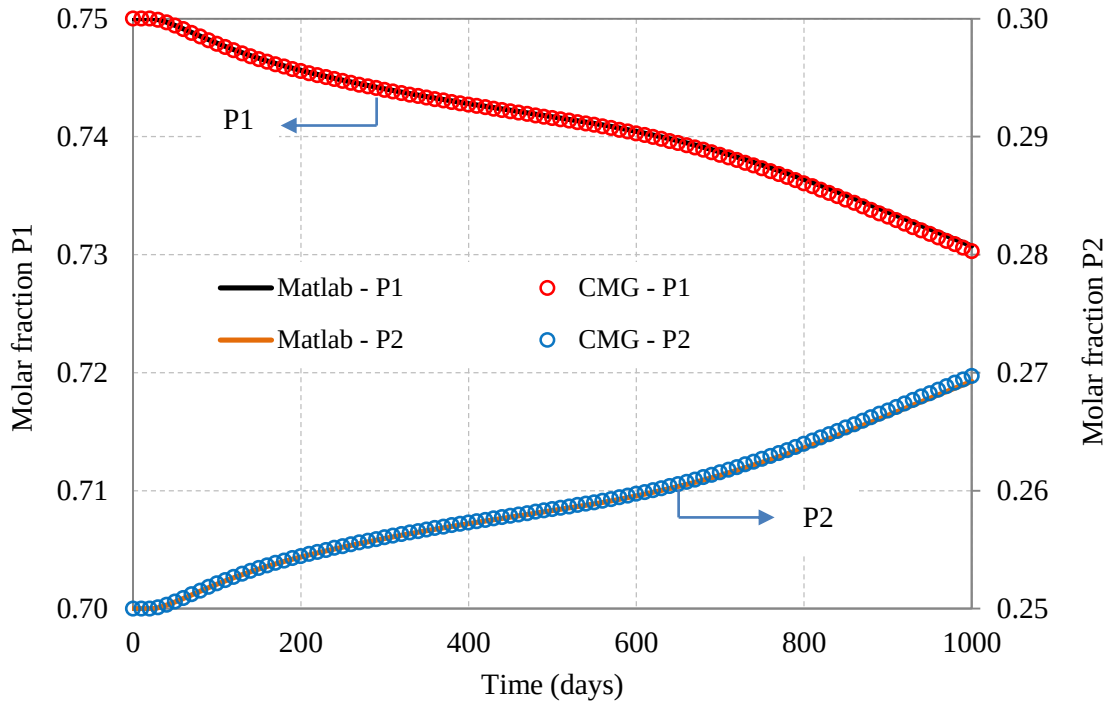


**Figure 5.6: Overall composition at the well (in-house simulator vs. CMG)**

Gas saturation and condensate saturation are demonstrated by Figures **5.7** and **5.8,** respectively. The results demonstrate the capability of the in-house simulator to handle the transition from single-phase to two-phase. The evolution of both phases is controlled by pressure since saturation was defined as a function of pressure earlier in the formulations. During the period where only one phase exists in the reservoir, gas saturation is maintained at its initial value. Once the pressure depletes below the dew point pressure and condensate starts appearing, the gas saturation is reduced while the condensate saturation is initiated. Condensate saturation continues to increase until reaching its maximum at 44% during the 1,000 days. This percentage marks the maximum liquid drop-out during this period. According to relative permeability tables, condensate reaches critical saturation at 28%, where condensate is expected to start flowing. Notably, during the period of 1,000 days, there is no vaporization of condensate taking place, because saturation is on the rise until reaching its maximum for the window of time investigated.

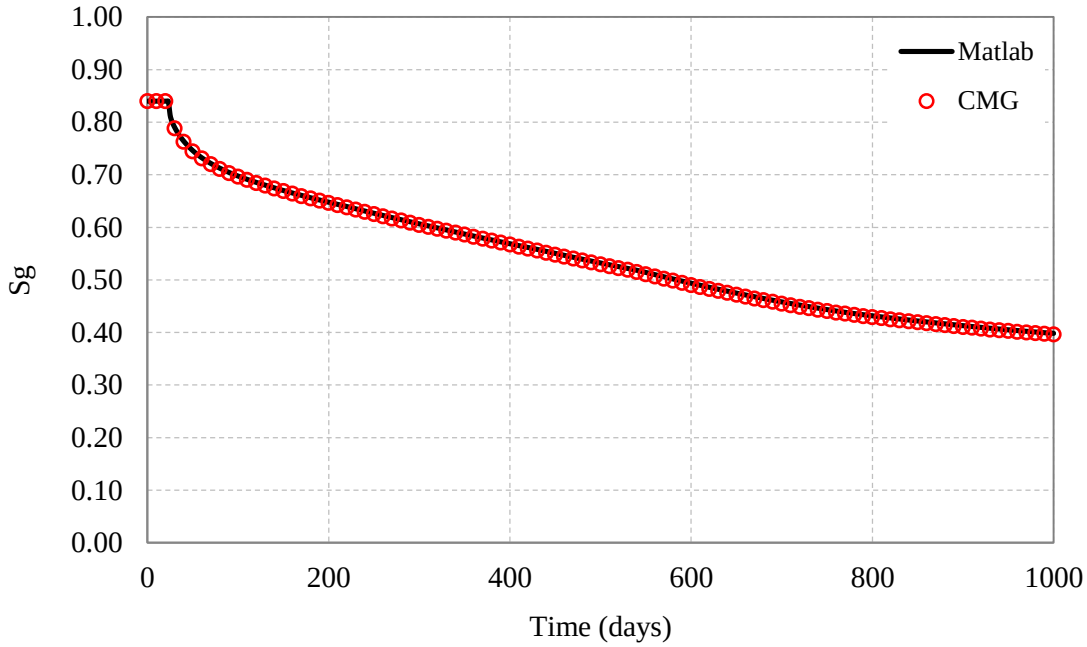


**Figure 5.7: Gas saturation at the well (in-house simulator vs. CMG)**

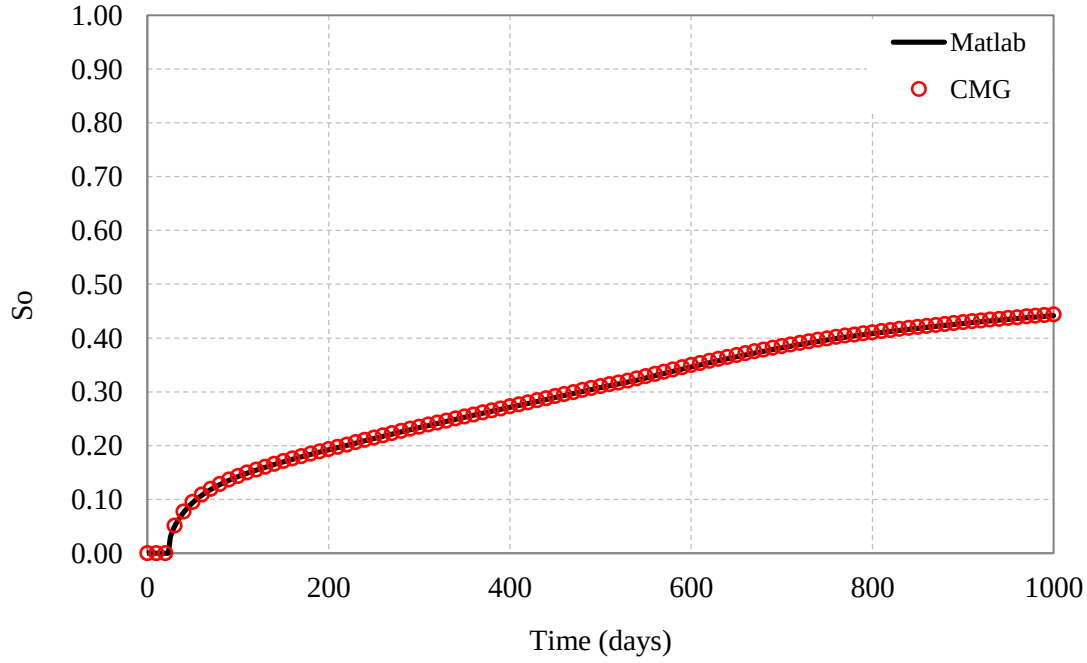


**Figure 5.8: Condensate saturation at the well (in-house simulator vs. CMG)**

Furthermore, Figures **5.9** and **5.10** provide a window to see production at reservoir conditions. Gas production as shown by Figure **5.9** is initiated at 6,000 (rcf/day) then declines significantly until reaching a flow rate constrained by minimum flowing bottom-hole pressure. The kink in production found at 30 days is caused by the appearance of condensate in the reservoir as indicated earlier by the saturation plots. The sudden appearance of condensate influences the significant decline in gas production as indicated by the trend of the curve beyond 30 days. On the other hand, Figure **5.10** illustrates the condensate production at reservoir conditions starting at 350 days, where critical saturation is reached allowing condensate to mobilize. Before this time, condensate is found as droplets inside the pores in quantities that are below the threshold of forming a flow stream. In this case, the threshold is the critical saturation of 28%. Overall, an acceptable match is found in the capturing of fluid productivity at reservoir conditions between the in-house simulator and CMG.

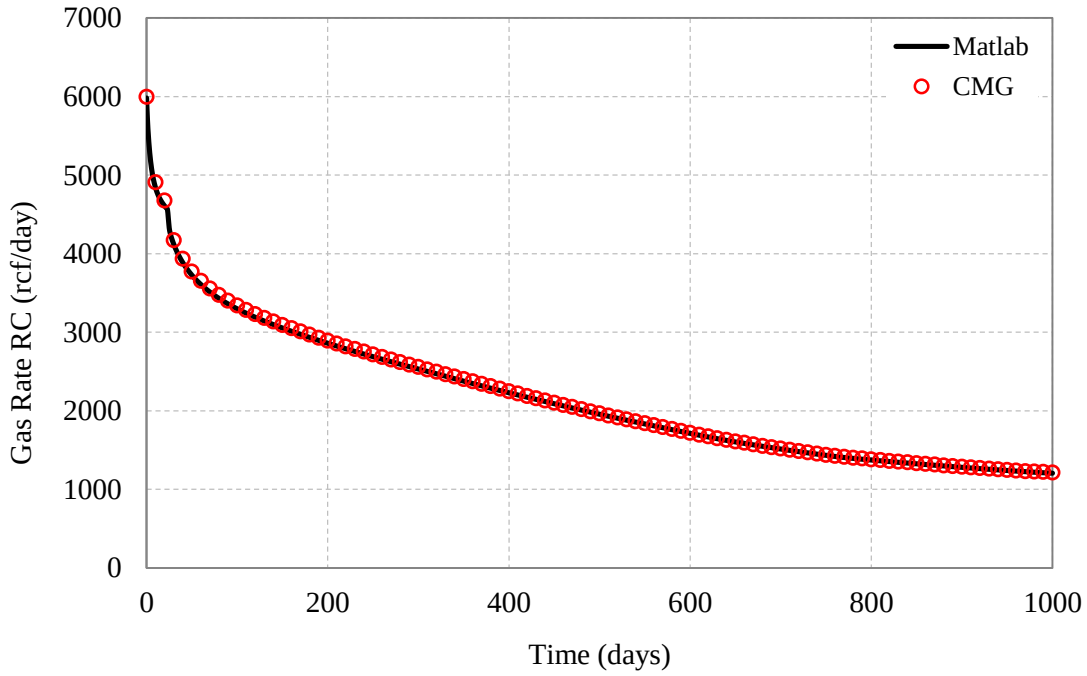


**Figure 5.9: Gas rate at reservoir conditions (in-house simulator vs. CMG)**

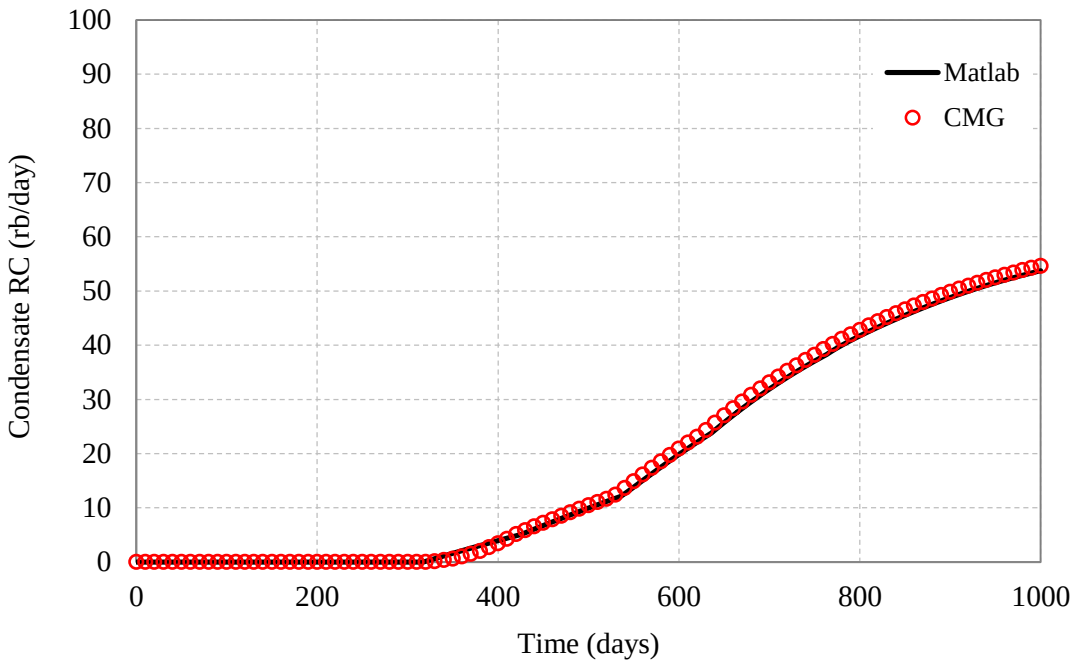


**Figure 5.10: Condensate rate at reservoir conditions (in-house simulator vs. CMG)**

The capability of the in-house simulator is once more tested to capture productivity at surface conditions, which is achieved through the separation battery formulations coupled with the in-house simulator. Figures **5.11** and **5.12** represent gas production and cumulative gas production at surface for the production period of 1,000 days. Gas production at surface conditions has a trend similar to the behavior achieved at reservoir conditions as expected. Since the condensate content is significantly lower in the reservoir mixture, condensate production was scarce at surface conditions. Utilizing various compositional combinations is the focus of analyzing condensate evolution in the reservoir with little emphasis on surface productivity. The current compositional combination used yielded no surface production of condensate, but future test cases with severe condensate content are expected to deliver surface condensate production. Figure **5.12** provides an illustration of the match between the surface cumulative productions of gas captured using the in-house simulator and CMG. Clearly, the validation process contained in this section has provided confidence on the basic framework of the in-house simulator, which shows its competency of capturing performance both at reservoir and surface conditions.

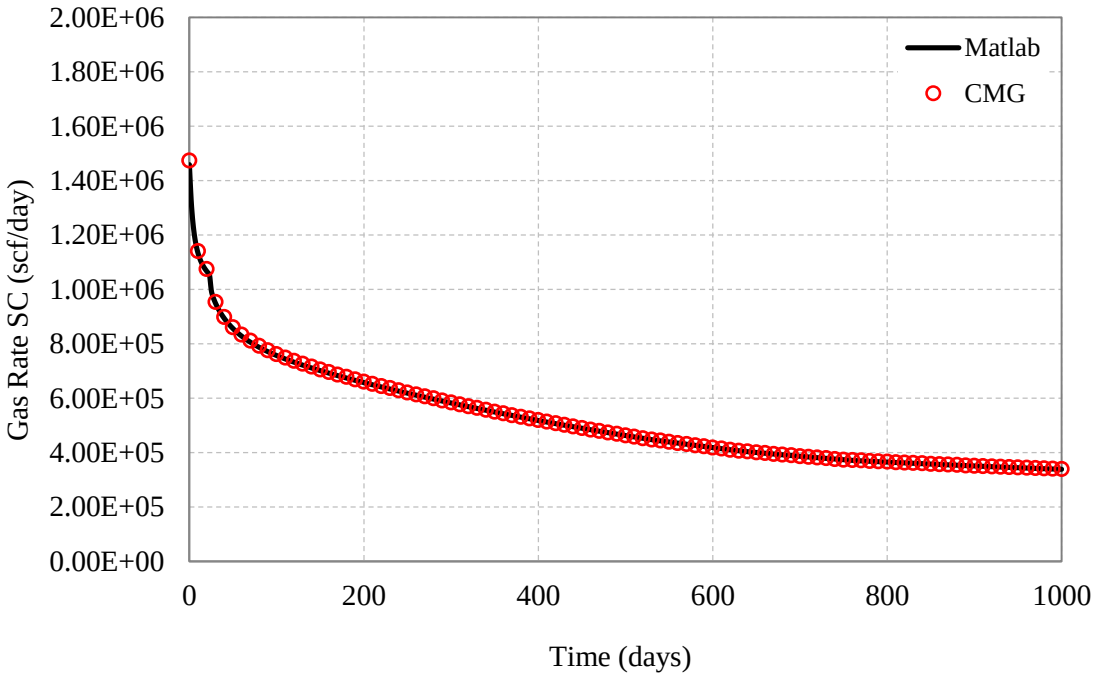


**Figure 5.11: Gas rate at surface conditions (in-house simulator vs. CMG)**

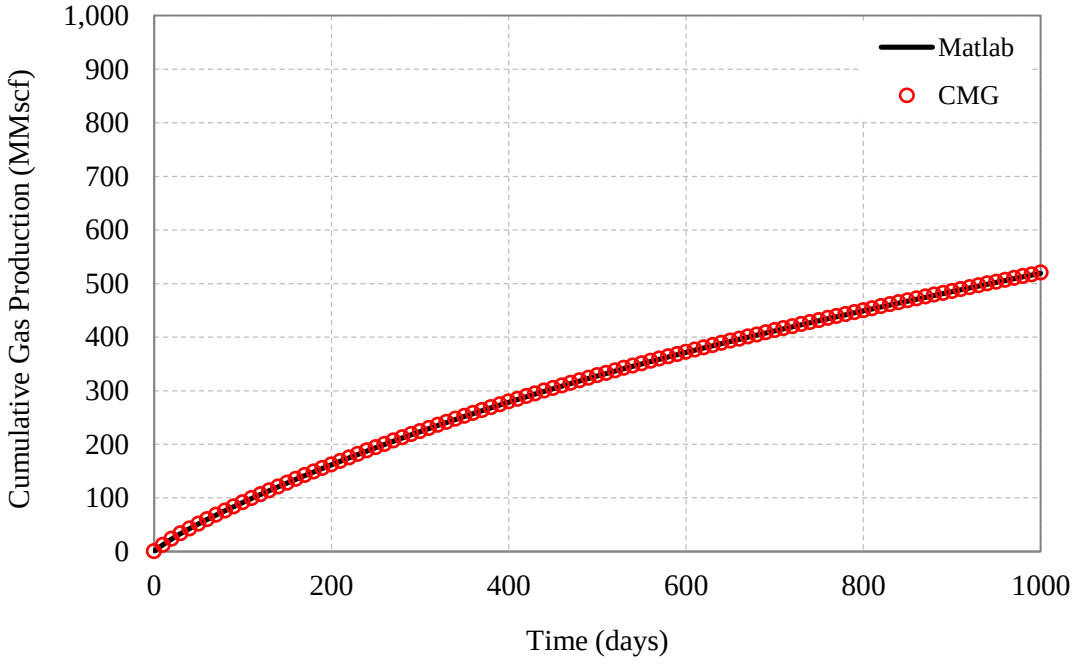


**Figure 5.12: Cumulative gas production (in-house simulator vs. CMG)**

The accuracy of the solutions attained by the in-house simulator is measured by two material balance checks: incremental material balance (IMB), and cumulative material balance (CMB). The IMB is performed every time step after convergence is achieved, and is illustrated by Figure **5.13**. Meanwhile the CMB as presented by Figure **5.14** is performed at the end of the last time step and covers the entire time of simulation. The IMB plot of each component is following the same distribution throughout the simulation period. At the beginning, the fluids-in-place are found in single phase and the accuracy of results is stable. Once condensate presents itself in the reservoir and sudden changes in condensate saturation per time steps are sensed, as shown by Figure **5.15**, the accuracy of results deteriorates. The in-house simulator is equipped with formulations to correct for sudden changes in properties to limit errors in the calculation within the loops of a time step. As soon as the results improve and the changes per time step become smaller, the accuracy of the results increases notably. The CMB experiences instability initially once condensate appears then it picks up in accuracy afterward. According to Ertekin *et al.* (2001), CMB has less accuracy than IMB because it tends to smooth errors captured within time steps. Thus, the accuracy of CMB is acceptable considering that the introduction of a new phase at the beginning of simulation degraded the accuracy of the results.

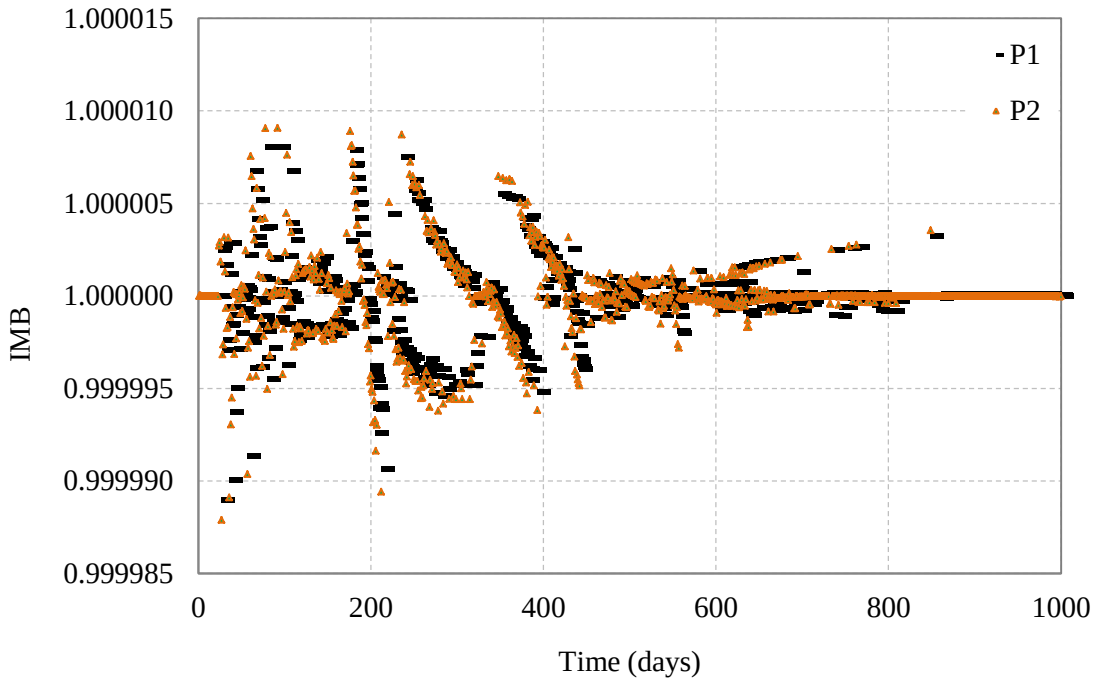


**Figure 5.13: Incremental material balances per component (in-house simulator)**

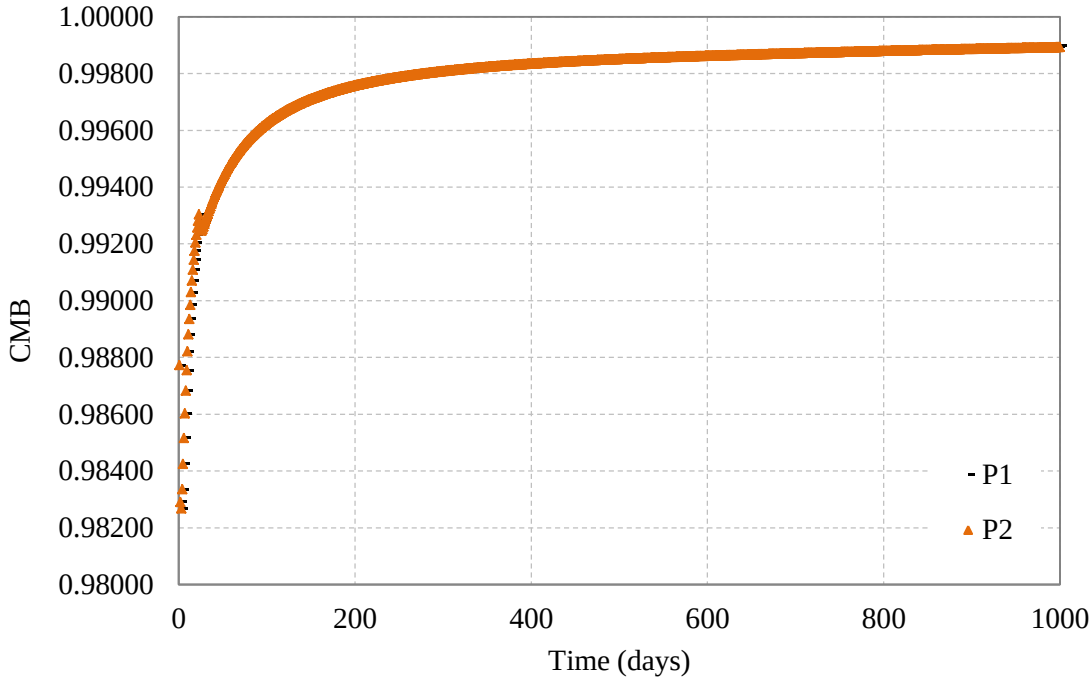


**Figure 5.14: Cumulative material balances per component (in-house simulator)**

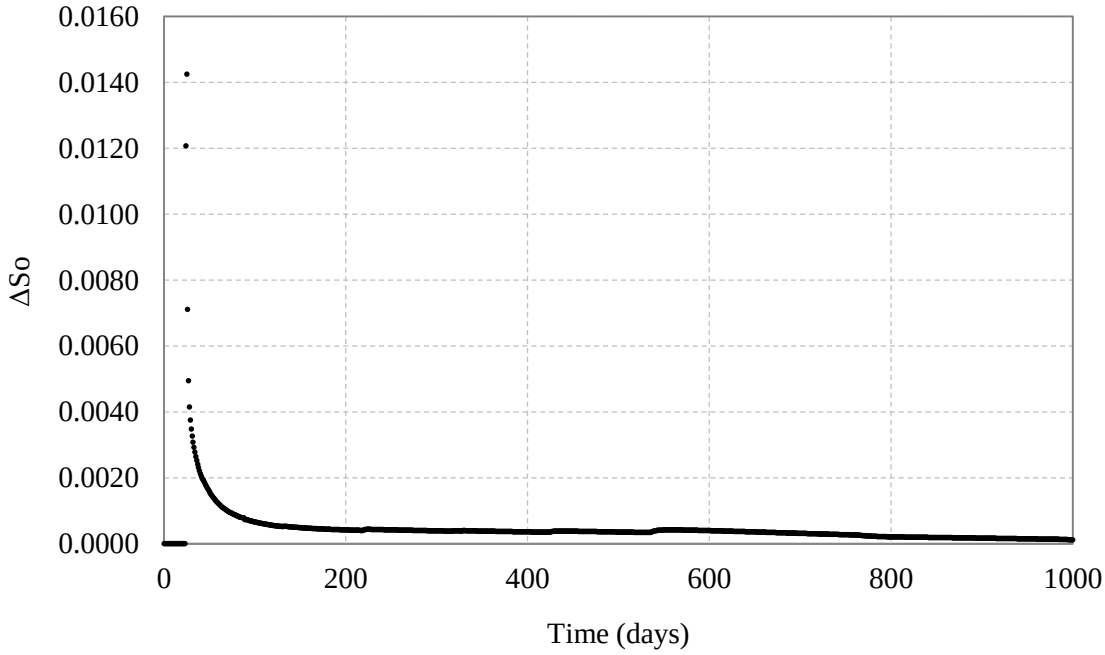


**Figure 5.15: Maximum change in condensate saturation (in-house simulator)**

# Chapter 6

## EFFECT OF CAPILLARY PRESSURE ON DEW POINT IN NANOPORES

Capillary pressure exists with the presence of two immiscible fluids in contact with each other through an interface. The curvature of the interface represents the difference in pressure between the two fluids, where the non-wetting phase is trying to pass through a resisting wetting phase attached to the surfaces of the pores. In a system where gas and condensate exist after pressure depletes below the dew point, condensate will invade the pore spaces previously available for the gas and will resist the passage of gas toward production channels. Through the interface between the two fluids, condensate will form a convex shape curve, while the gas will be acting with higher pressure toward the concave side of the curve. A replica of such behavior is seen in laboratories through capillary tube experiments to measure capillary pressure of various fluids in different tube radiuses. The main purpose of the capillary tube tests is to understand capillary pressure effects between fluids by mimicking different pore size settings. Thus, in thinner tubes, the level of fluids is elevated and capillary pressure increases due to the increase in surface tension.

Nojabaei *et al.* (2013) provided a numerical proof of this conclusion, where the outcomes showed an increasing capillary pressure with smaller pore sizes. In addition, the research was extended to investigate the effect of capillary pressure on bubble point of an oil reservoir, which appeared to be decreasing with increasing capillary pressure. These outcomes were applied to the work of Nojabaei *et al.* (2014) to investigate their influence on the productivity of the Bakken oil reservoir. With oil-wet reservoir settings, the results showed an increase in oil recovery by 7-9%, and 10% in gas recovery. However, the findings of the research are questionable, especially with systems consisting of heavy oil and oil-wet settings, which imply higher retention and intensive holding of oil in place. Furthermore, the work of Nojabaei *et al.* (2013) demonstrated the capillary pressure effect on phase envelopes of mixtures consisting of different sets of composition as shown by Figure **6.1**. The phase envelopes showing the capillary pressure effect were generated at 10 nm pores radius where capillary pressure was pronounced. The lightest mixture shows no effect on phase behavior, while the moderate mixtures have notable effect on bubble point curve and some effect on dew point curve. However, the mixture that includes $C_{10}$

shows only the slightest influence on phase behavior, which was expected to return a higher effect on saturation pressure than in the moderate cases since the mixture contains more heavies.

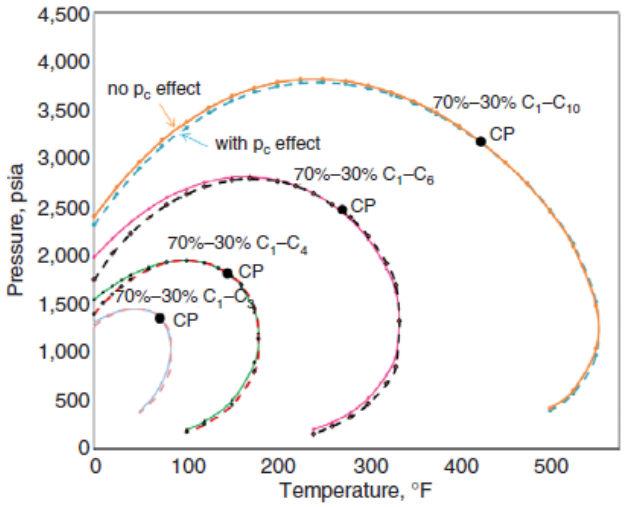


**Figure 6.1: Capillary pressure effect on phase envelopes (Nojabaei *et al.*, 2013)**

The hypothesis is that capillary pressure would increase the residence time of condensate and impose higher resistance impacting productivity. In this work, the effect of capillary pressure with the inclusion of different composition combinations will be examined to capture the influence on dew point pressure of liquid-rich gas systems.

## 6.1 Coupling a phase behavior model with a capillary pressure equation

Generally, a phase behavior model is used to predict behavior of a fluid system as a function of phase pressure, composition and temperature using an Equation-of-State. In the absence of capillary pressure, the pressure is the same for both phases, and the fluid properties are calculated as a function of the same pressure. With the inclusion of capillary pressure, the vapor-liquid equilibrium flash needs to be adjusted to accommodate for calculating the fluid properties of each phase according to the phase pressure. All commercial software that provides compositional computations performs phase behavior calculations without the inclusion of capillary pressure. Thus, this section will demonstrate the modification to the current phase behavior model described in Appendix B, to include phase pressures ($p_o$ *and* $p_g$).

First, in order to examine the stability of the fluid-in-place under two-phase pressures, the Michelsen (1982) method is modified while creating the second-phase inside the mixture. All of the steps in the fugacity calculations consider the selection of the Z-factor root that minimizes Gibbs free energy. Vapor-like second mixture calculations are initiated by calculating the mixture fugacity ($f_{ci}$) as a function of the liquid phase pressure and overall composition ($c_i$), as shown by equation (6.1a).

$$f_{ci} = \phi_{ci} \,.\, c_i \,.\, p_o \quad ; \quad i = 1,2 \tag{6.1a}$$

where:

$$\phi_{ci} = f(c_i \,.\, p_o) \tag{6.1b}$$

$\phi_{ci}$: fugacity coefficient of the $i^{th}$ component in the mixture

Then, the vapor second-phase fugacity ($f_{gi}$) is measured using vapor phase pressure and the normalized second-phase vapor mole fractions ($y_i$), which can be calculated using equation (6.2a).

$$f_{gi} = \phi_{gi} \,.\, y_i . p_g \quad ; \quad i = 1,2 \tag{6.2a}$$

where:

$$y_i = \frac{Y_i}{S_V} \tag{6.2b}$$

$$Y_i = c_i . K_i \tag{6.2c}$$

$$S_V = \sum_{i}^{n_c} Y_i \tag{6.2d}$$

$y_i$: normalized second-phase vapor mole fractions of the $i^{th}$ component

$Y_i$: second-phase mole number of the $i^{th}$ component

$K_i$: vapor-liquid equilibrium ratio of the $i^{th}$ component

Liquid-like second mixture calculations are initiated by calculating the mixture fugacity ($f_{ci}$) as a function of the vapor phase pressure and overall composition ($c_i$) as shown by equation (6.3a).

$$f_{ci} = \phi_{ci} \,.\, c_i \,.\, p_g \quad ; \quad i = 1,2 \tag{6.3a}$$

where:

$$\phi_{ci} = f(c_i \,.\, p_g) \tag{6.3b}$$

$\phi_{ci}$: fugacity coefficient of the $i^{th}$ component in the mixture

Then, the liquid second-phase fugacity ($f_{li}$) is measured using liquid phase pressure and the normalized second-phase liquid mole fractions ($x_i$), as illustrated below.

$$f_{li} = \phi_{li} \,.\, y_i . p_o \quad ; \quad i = 1,2 \tag{6.4a}$$

where:

$$x_i = \frac{Y_i}{S_L} \tag{6.4b}$$

$$Y_i = c_i / K_i \tag{6.4c}$$

$$S_L = \sum_i^{n_c} Y_i \tag{6.4d}$$

Once fugacities of the mixture and second-phase are measured, the K-values are updated until convergence or trivial solution is achieved. The updating of K-values is conducted on each second-phase separately by checking for the conditions described by equations (6.5a) and (6.5b).

$$Convergence\ criterion: \sum_i^{n_c} (R_i - 1)^2 < 10^{-10} \quad ; \quad i = 1,2 \tag{6.5a}$$

$$Trivial\ solution\ criterion: \sum_i^{n_c} (In\ K_i)^2 < 10^{-4}; \quad i = 1,2 \tag{6.5b}$$

where:

$$R_i = \frac{f_{ci}}{f_{gi}} . \frac{1}{S_V} \quad ; \quad for\ vapor\ second - phase \tag{6.5c}$$

$$R_i = \frac{f_{li}}{f_{ci}} . S_L \quad ; \quad for\ liquid\ second - phase \tag{6.5d}$$

$$K_i^{(n+1)} = K_i^{(n)} . \ R_i \tag{6.5e}$$

Once a solution has been achieved for both cases, the mixture is determined to be in two-phase if either of the tests revealed $S > 1$. In contrast, the mixture is in a single-phase if both tests arrive at a trivial solution, both tests produce $S \leq 1$, or one of the tests yields a trivial solution and the other one gives $S \leq 1$.

Second, the phase behavior model is modified to predict the compositional behavior of a fluid system as a function of two-phase pressure, composition and temperature. In conditions where single-phase prevails, the phase behavior model will act as previously documented in Appendix B using one of the given pressures. However, under two-phase conditions, the fugacity of a component in liquid phase ($f_{li}$) is calculated as a function of liquid phase pressure and compared to the fugacity in gaseous phase ($f_{gi}$) calculated as a function of vapor phase pressure. Equations (6.6a) and (6.6b) are used to attain fugacities and update K-values through the Successive Substitution Method (SSM) until a net transfer of zero is achieved.

$$f_{gi} = \phi_{gi} \,.\, y_i . p_g \quad ; \quad i = 1,2 \tag{6.6a}$$

$$f_{li} = \phi_{li} \,.\, y_i . p_o \quad ; \quad i = 1,2 \tag{6.6b}$$

where:

$$\phi_{gi} = f(y_i \,.\, p_g) \tag{6.6c}$$

$$\phi_{li} = f(x_i \,.\, p_o) \tag{6.6d}$$

$$K_i^{(n+1)} = K_i^{(n)} . \left(\frac{f_{li}}{f_{gi}}\right)^{(n)} \tag{6.6e}$$

$$Convergence\ criterion: \sum_i^{n_c} \left(\frac{f_{li}}{f_{gi}} - 1\right)^2 < 10^{-13} \tag{6.6f}$$

After a thermodynamic equilibrium is reached and the constraint in (6.6f) is accomplished, the composition of all the phases can be reliably estimated using the recent K-values. Furthermore, the properties of vapor and liquid can be predicted easily using the phase pressures accordingly, and that includes the estimation of molecular weights, densities, and viscosities.

## 6.2 Estimating capillary pressure and dew-point pressure in nanopores

Macleod (1923) and Sugden (1924) introduced the empirical equation (2.3) to estimate interfacial tension (IFT) for pure substances, which was developed in accordance with the assumptions of van der Waals (1910) on the fundamental relationship between cohesion forces and density. For mixtures, Weinaug and Katz (1943) developed an expression as illustrated by equation (2.4), which is implemented in this study to estimate IFT and capillary pressure. The determination of capillary pressure is implicit; it depends on the changes in IFT, radius of the pores, and thermodynamic changes. Thus, to estimate capillary pressure given radius of the pores, the flow chart in Figure **6.2** is considered with the utilization of the bisection method to reach a solution.

In order to start the calculation, maximum and minimum values for $p_{cgo}$ are specified to initiate the calculations. The minimum value is assumed to be close to zero; a default value was set to 0.0001 psia, while the maximum $p_{cgo}$ can be set to any value greater than 0.0001. A good estimate of $p_{cgo}$ can help in achieving faster conversion; however, it is not an easy predication because the phase behavior model is sensitive to $p_{cgo}$ values. Capillary pressure, as it will be shown later in this chapter, is a function of composition, temperature, and radius of the pores. Using different composition concentration of different mixtures at various temperatures showed that the maximum $p_{cgo}$ can reach up to 50 psia, and as low as 0.003 psia. In order to start the calculation, it is best to set the $p_{cgo}$ maximum at a default value of 0.003 and increase it while monitoring the computation stance of the PBM.

Furthermore, a $p_{gi}^{(n)}$ inside the phase envelope needs to be chosen to initiate the search for the dew-point pressure using the estimated $p_{cgo}^{(n)}$. Selecting the right $p_{gi}^{(n)}$ is associated with difficulty, since PBM is very sensitive to the value of capillary pressure. Three things may take place with a bad estimate of $p_{gi}^{(n)}$: the code will overpass the actual dew-point pressure, the fugacities of the phases will never get closer to each other and convergence will be eliminated, or the vapor molar fraction will decline to values below zero. The ability of PBM to handle capillary pressure depends on the composition of the mixture and temperature. At certain locations inside the phase envelope, the value of capillary pressure becomes very low and exerts no influence on the fluid behavior. Any point selected beyond the location of “no influence” will stall the PBM calculations.

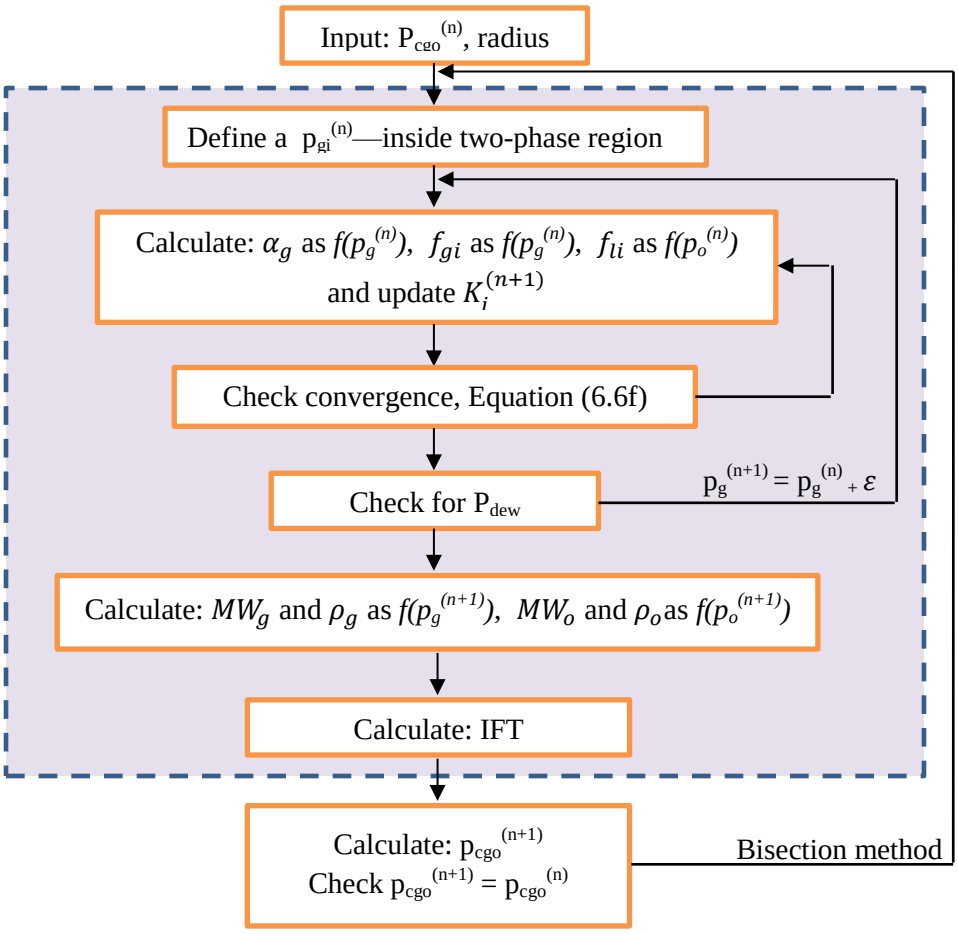


**Figure 6.2: Flow chart to estimate capillary pressure given radius of the pores**

Now, the oil and gas pressures are known to initiate the phase-behavior modeling, where fugacities are calculated according to the phase pressures. After each thermodynamic equilibrium convergence, the developed model will check for single phase conditions. This is aimed at finding the capillary pressure while pursuing dew-point pressure. It is worth mentioning that the dew-point under investigation is the original dew-point pressure without the incorporation of capillary pressure. The goal is to find the maximum capillary pressure as a function of the IFT properties found at the original dew-point pressure. It is known that the highest capillary pressure is found at the lowest oil saturation, and it decreases as oil saturation increases. Once the original dew-point is found, IFT can be calculated as a function of molecular weights and densities of the phases. The final step would be to calculate capillary pressure as a function of IFT and radius of the pores, then to conduct an equality check to $p_{cgo}^{(n)}$ and update if necessary.

The influence on the phase envelope's dew-point curve is estimated once capillary pressure is known. Capillary pressure is considered a fixed value and is sent to the highlighted loop in Figure **6.2** with dashed-line borders. This loop will conduct a search for the upper dew-point pressure while incorporating capillary pressure. Once the new dew-point pressure is found, the interfacial tension at the new dew-point is calculated. In order to find the impact of capillary pressure on the lower dew-point curve, the same procedure needs to be started by finding the capillary pressure at the lower dew-point pressure, then calculating the new lower dew-point pressure.

### 6.3 Validating the coupled phase behavior – capillary pressure model

The validity of the developed modified Michelsen (1982) method and the phase behavior model was examined by reproducing similar results to those generated by Nojabaei *et al.* (2013). Although their work was concentrated on bubble point and oil reservoirs, there was little emphasis on the liquid retrograde region. The goal of this section is to regenerate results attained in the liquid retrograde region, which were conducted using a binary mixture of methane-decane at a temperature of 550 $^{o}$F. Results have been generated across a variety of pore size radiuses, including capillary pressure, dew-point pressure differences, and interfacial tensions. Table **6.1** illustrates the input data used for the binary system methane-decane used for the validation. Pore sizes in the range of 2.86 – 20 nm were considered in the development of Figure **6.3**, Figure **6.5**, and Figure **6.8**. Supporting tables and results can be found in Appendix E.

Figure **6.3** shows capillary pressure at a temperature of 550 $^{o}$F for methane 70% - decane 30%. In order to maintain consistency in the calculations, the same initial $p_{gi}^{(n)}$ was used while evaluating the influence of the various pore sizes. A $p_{gi}^{(n)}$ of 1,225.4 psia was used for the upper dew-point pressure, and 1,108 psia was used for the lower dew-point pressure. Due to the absence of assumptions, description of initial conditions, and limitations in the work of Nojabaei *et al.* (2013), $p_{gi}^{(n)}$ had to be evaluated using trial and error. The results shown by Figure **6.3** are simulating the trends presented in Figure **6.4** by Nojabaei *et al.* (2013) for the same temperature and dew-point curve. Capillary pressure increases as the pore sizes reduce at the upper and lower dew-point curve, but significantly for the lower dew-point curve. Toward the lower dew-

point curve, the pressure of the system is very low, which is allowing the wetting phase to imply higher capillary pressure against the non-wetting phase.

**Table 6.1: Hydrocarbon fluid properties for methane 70% - decane 30%**

Fluid Characterization

| Comp | $MW_m$ (lbm/lbmol) | $T_{cm}$ (R) | $P_{cm}$ (psia) | $Z_{cm}$ | $\omega_m$ | $\Omega_{am}$ | $\Omega_{bm}$ |
|---|---|---|---|---|---|---|---|
| C1 | 16.043 | 343.33 | 666.4 | 0.2874 | 0.0104 | 0.457235529 | 0.077796074 |
| n-C10 | 142.28 | 1112.0 | 305.2 | 0.2503 | 0.4898 | 0.457235529 | 0.077796074 |

Note: Volume shifts are set to zero

Concentrations

| Comp | $c_i$ |
|---|---|
| C1 | 0.70 |
| n-C10 | 0.30 |

Binary Interaction Coefficients

| Comp | C1 | n-C10 |
|---|---|---|
| C1 | 0 | 0.00234 |
| n-C10 | 0.00234 | 0 |

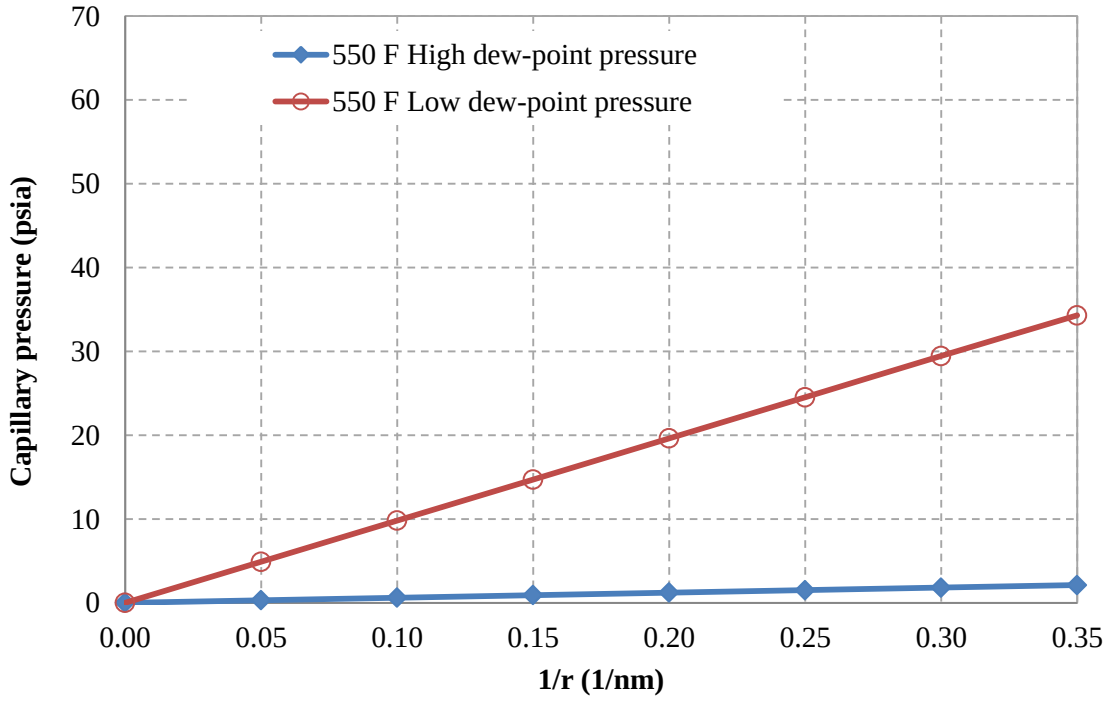


**Figure 6.3: Capillary pressure for methane 70% - decane 30%**

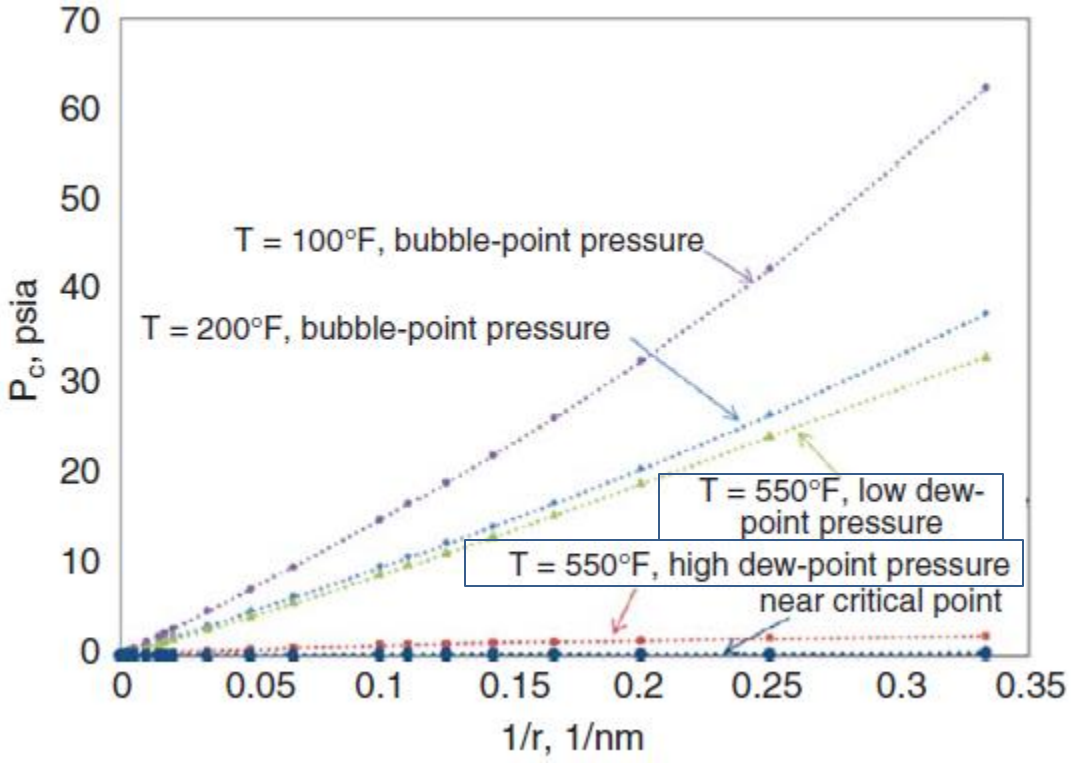


**Figure 6.4: Capillary pressure for methane 70% - decane 30% (Nojabaei *et al.*, 2013)**

The relationship between surface tension and pore sizes is presented in Figure **6.5**. Interfacial tensions were calculated by equation (2.4) using parachor coefficients of 77.33 and 392.25 for methane and decane. Liquid density controls surface tension, with higher liquid density leading to higher surface tension. The interfacial tension for the higher dew-point is mimicking the results in Figure **6.6**. However, there are some differences for the lower dew-point curve and that could be attributed to dissimilarity in the conditioning of the phase behavior model between the two studies. Interfacial tension for the lower dew-point curve increases as pore sizes reduce. This is due to the increased differences between the densities as pressure reduces. Figure **6.7** demonstrates the relationship between density and pressure. In contrast, moving toward the upper dew-point reduces the difference in densities, which subsequently reduces the interfacial tension. The decrease in IFT at lower pore sizes suggests that the higher dew-point curve must be shifting upward, while, the increase in IFT for the lower dew-point curve suggests that the dew-point curve section at the bottom is shifting downward.

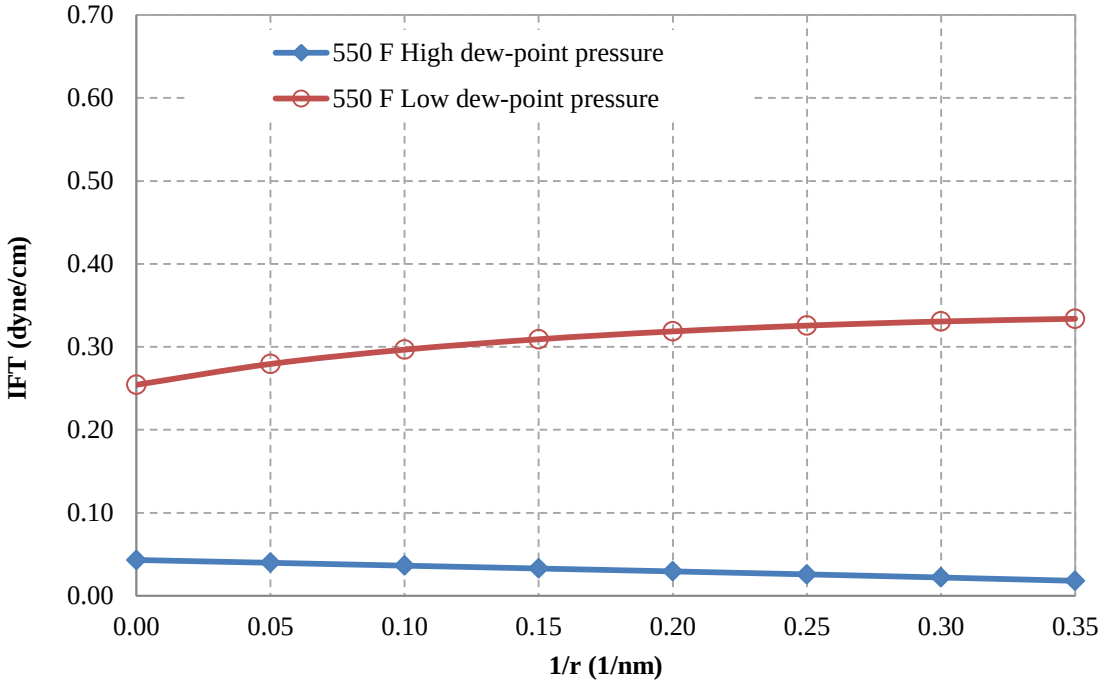


**Figure 6.5: Interfacial tension for methane 70% - decane 30%**

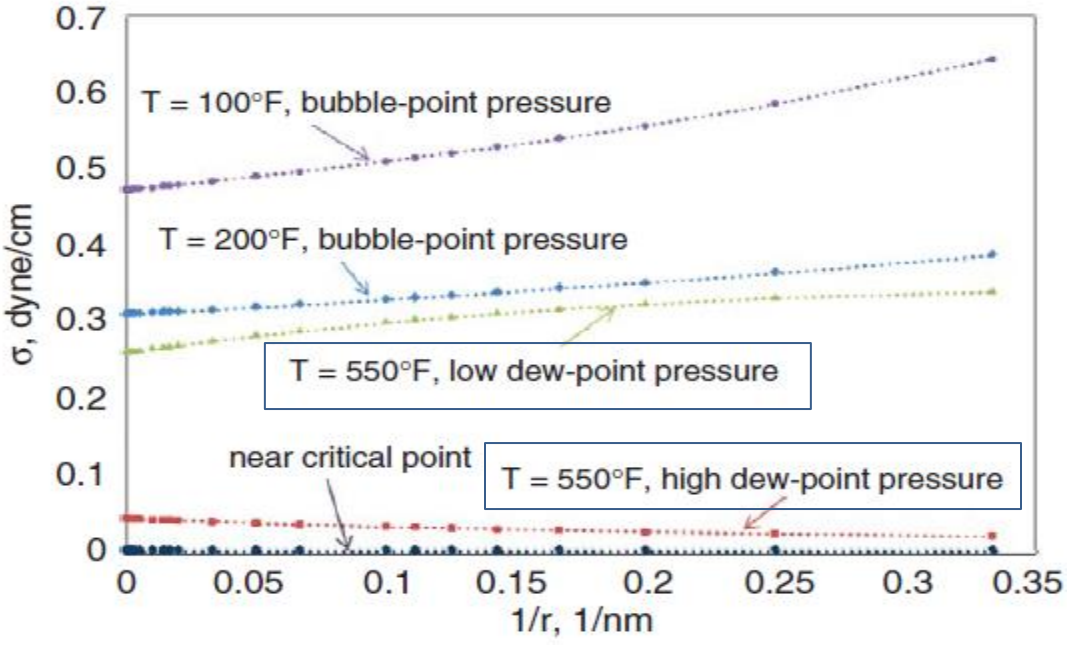


**Figure 6.6: Interfacial tension for methane 70% - decane 30% (Nojabaei *et al.*, 2013)**

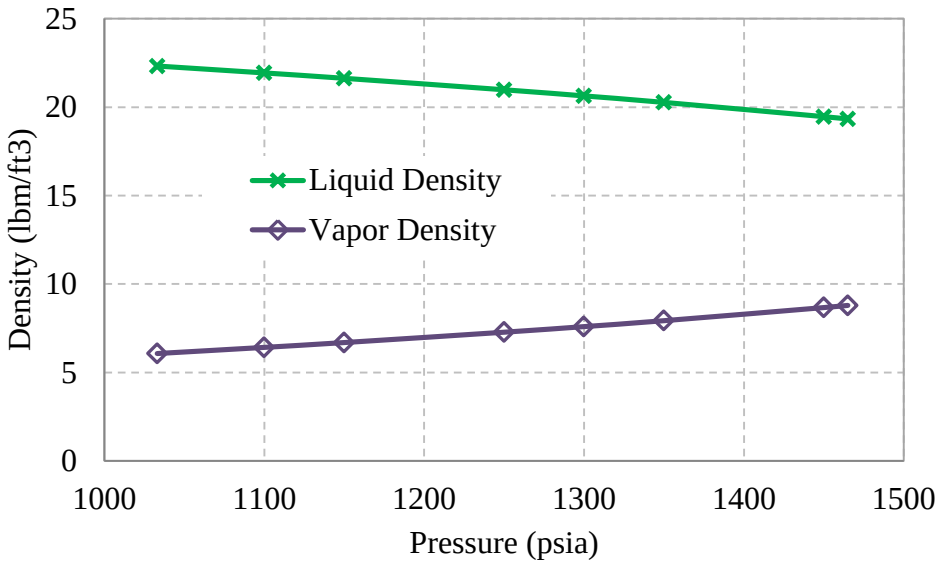


**Figure 6.7: Density versus pressure for 70% - decane 30% at 550 $^{o}$F without $P_{cgo}$**

An extension to the validation of the model, the work flow shown by Figure **6.2** was used to capture the influence of various pore sizes on dew-point pressure. Only the shaded part with dash-line borders was implemented because $p_{cgo}^{(n+1)}$ is already known. The changes in dew-point pressure are captured in Figure **6.8**, which continues to prove validity against the work of Nojabaei *et al.* (2013) shown in Figure **6.9**. Capillary pressure influenced the upper dew-point pressure to increase and the lower dew-point pressure to decrease with smaller pore sizes. The outcome from this figure follows the same findings discussed with IFT and densities, where the results suggested an increasing upper dew-point and decreasing lower dew-point curves.

The relationship of capillary pressure, IFT, pore sizes, and dew-point pressure shows an increasing capillary pressure with smaller pore sizes for the upper and lower dew-point curves. Interfacial tension has a strong relationship with the differences in densities. Yet, higher changes in capillary pressure are associated with higher changes in interfacial tensions. Thus, instead of relating capillary pressure directly to dew-point pressure, it is best to use interfacial tensions. Capillary pressure increases as pore sizes reduce for the upper and lower dew-point pressures, but the phase envelope reacts differently for both curves. The upper dew-point curve increases as the interfacial tension decreases, whereas the lower dew-point curve decreases as IFT increases. Thus, dew-point pressure is inversely proportional to interfacial tensions.

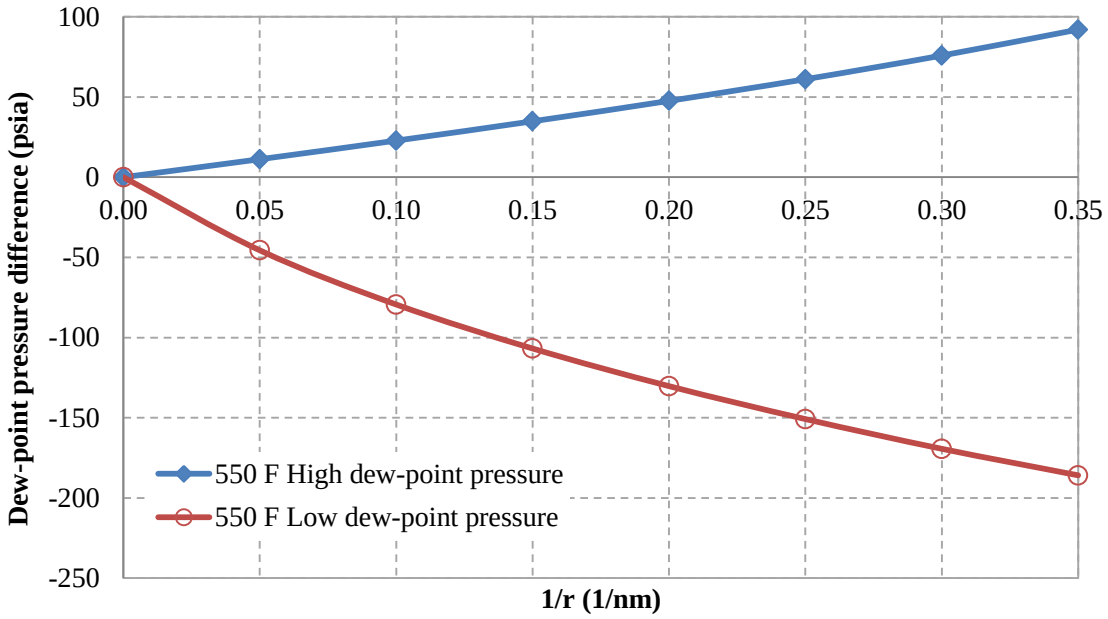


**Figure 6.8: Dew-point pressure difference for methane 70% - decane 30%**

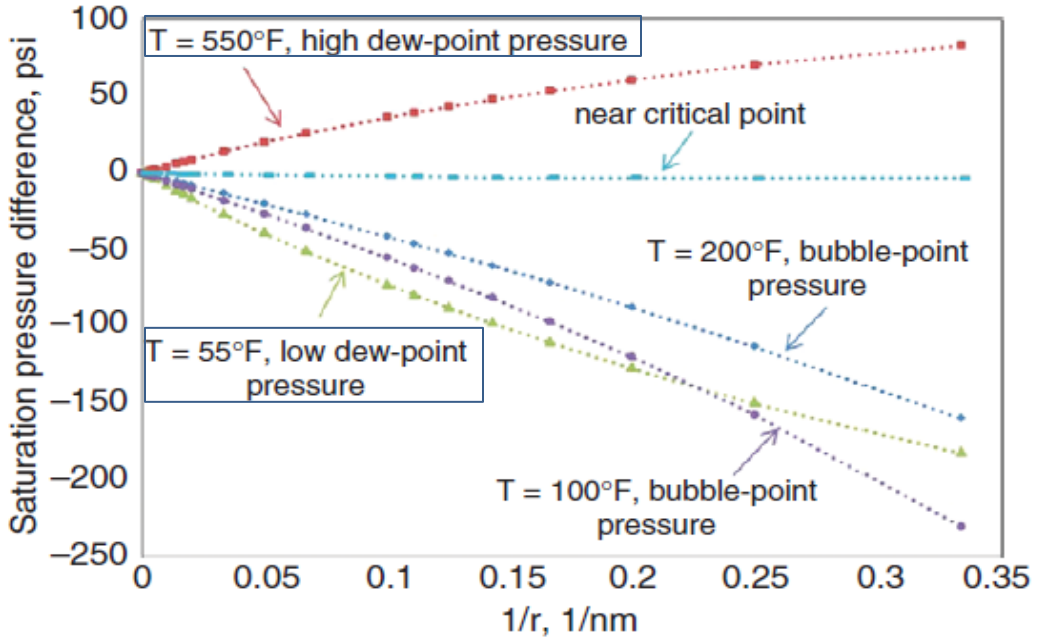


**Figure 6.9: Sat. pressure difference for methane 70% - decane 30% (Nojabaei *et al.*, 2013)**

In closing to the validation of the developed modified Michelsen (1982) method and the phase behavior model, their performance was examined against each other to capture dew-point pressure at different pore sizes. The testing was run on methane-decane using 70%-30% concentration and at a temperature of 550$^{o}$ F. Table **6.2** demonstrates the capability of both methods in converging to the same upper dew-point pressure. Furthermore, the lower dew-point pressure was mimicked successfully by both methods as shown in Table **6.3**. Thus, both methods can be used with confidence once incorporated as subroutines in the in-house simulator.

**Table 6.2: Stability versus PBM in predicting upper dew-point pressure**

| | | | *Stability* | *PBM* |
|---|---|---|---|---|
| 1/r (1/nm) | r (nm) | Pcgo (psia) | Pdew (psia) | Pdew (psia) |
| 0 | ∞ | 0.0000 | 1467.34 | 1467.35 |
| 0.05 | 20.00 | 0.3035 | 1478.42 | 1478.43 |
| 0.1 | 10.00 | 0.6069 | 1490.25 | 1490.26 |
| 0.15 | 6.67 | 0.9100 | 1502.17 | 1502.18 |
| 0.2 | 5.00 | 1.2139 | 1514.7 | 1514.70 |
| 0.25 | 4.00 | 1.5174 | 1528.48 | 1528.49 |
| 0.3 | 3.33 | 1.8227 | 1542.96 | 1542.96 |
| 0.35 | 2.86 | 2.1222 | 1559.14 | 1559.14 |

**Table 6.3: Stability versus PBM in predicting lower dew-point pressure**

| | | | *Stability* | *PBM* |
|---|---|---|---|---|
| 1/r (1/nm) | r (nm) | Pcgo (psia) | Pdew (psia) | Pdew (psia) |
| 0 | ∞ | 0.0000 | 1031.69 | 1031.69 |
| 0.05 | 20.00 | 4.9056 | 986.09 | 986.09 |
| 0.1 | 10.00 | 9.8112 | 952.30 | 952.30 |
| 0.15 | 6.67 | 14.7160 | 924.84 | 924.84 |
| 0.2 | 5.00 | 19.6223 | 901.42 | 901.42 |
| 0.25 | 4.00 | 24.5279 | 880.86 | 880.86 |
| 0.3 | 3.33 | 29.4629 | 862.33 | 862.33 |
| 0.35 | 2.86 | 34.3047 | 845.79 | 845.79 |

This section had demonstrated the capability of the developed methods to capture various properties in nanopores. However, it is worth illustrating the importance of predicting $p_{gi}^{(n)}$ to the calculations of capillary pressure, IFT, and dew-point pressure. Different $p_{gi}^{(n)}$ with a magnitude of $\pm$100 psia have been used in the calculations toward the upper and lower dew-point curves. Figure **6.10** reflects greater influence on capillary pressure for the lower dew-point pressure as the pore sizes reduce. An increase of 100 psia in $p_{gi}^{(n)}$ increases capillary pressure by 41%, while insignificant changes in capillary pressure were captured at the upper dew-point pressure.

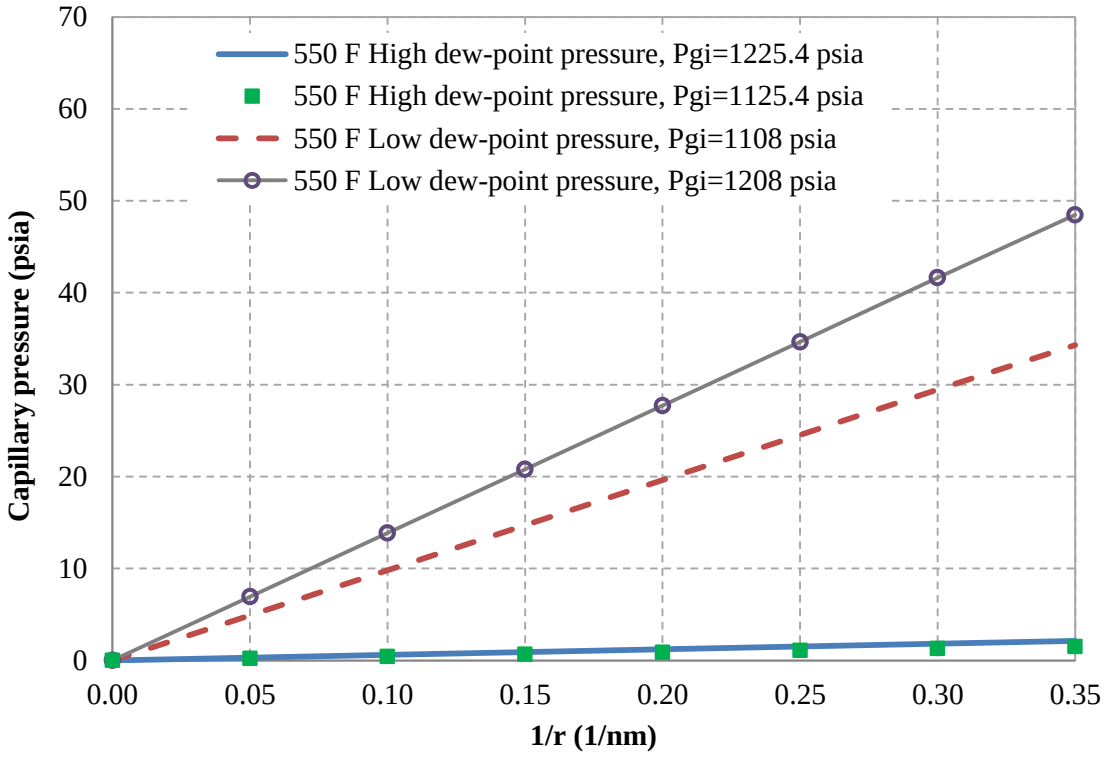


**Figure 6.10: $P_{gi}^{(n)}$ effect on capillary pressure for methane 70% - decane 30%**

Similar signature with the interfacial tension had been observed as shown by Figure **6.11**, where inconsequential changes occurred at the upper dew-point. The interfacial tension at the lower dew-point shows an increase between 4% and 11% with changing $p_{gi}^{(n)}$. Figure **6.12** reveals the impact of changing $p_{gi}^{(n)}$ on the calculation of dew-point pressure with the inclusion of capillary pressure. A 100 psia difference may cause the upper dew-point to be shifted by up to 2% at the lowest pore size, whereas the proposed difference in $p_{gi}^{(n)}$ could land the lower dew-point pressure off by 1.5% to 4.9%. All supporting results can be found in Table **D.2** of Appendix E.

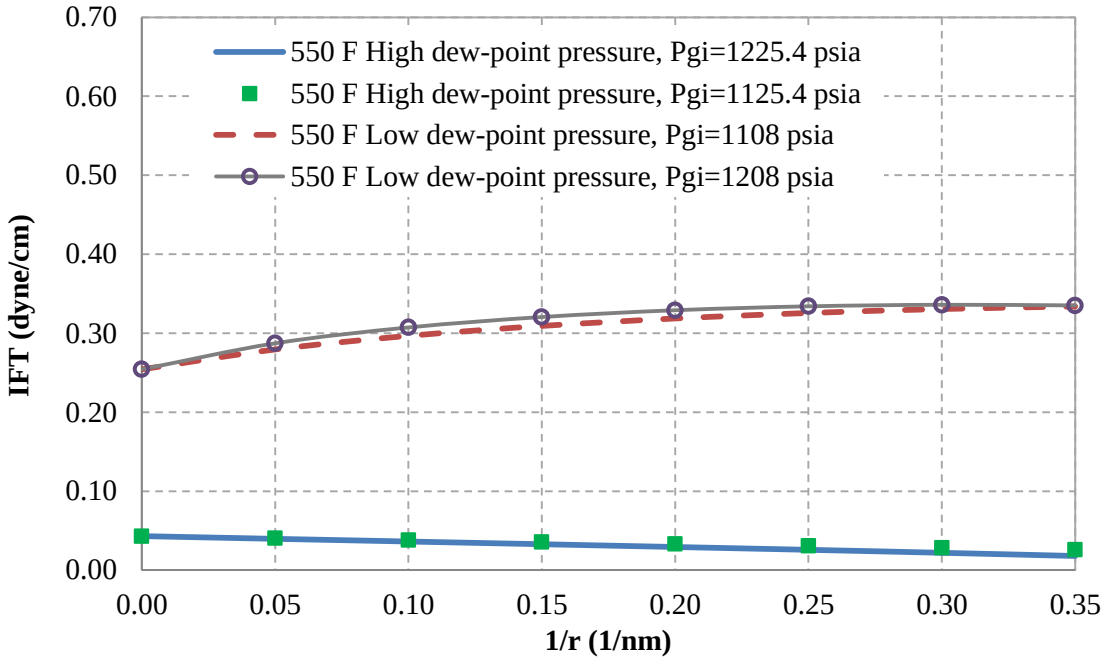


**Figure 6.11: $P_{gi}^{(n)}$ effect on interfacial tension for methane 70% - decane 30%**

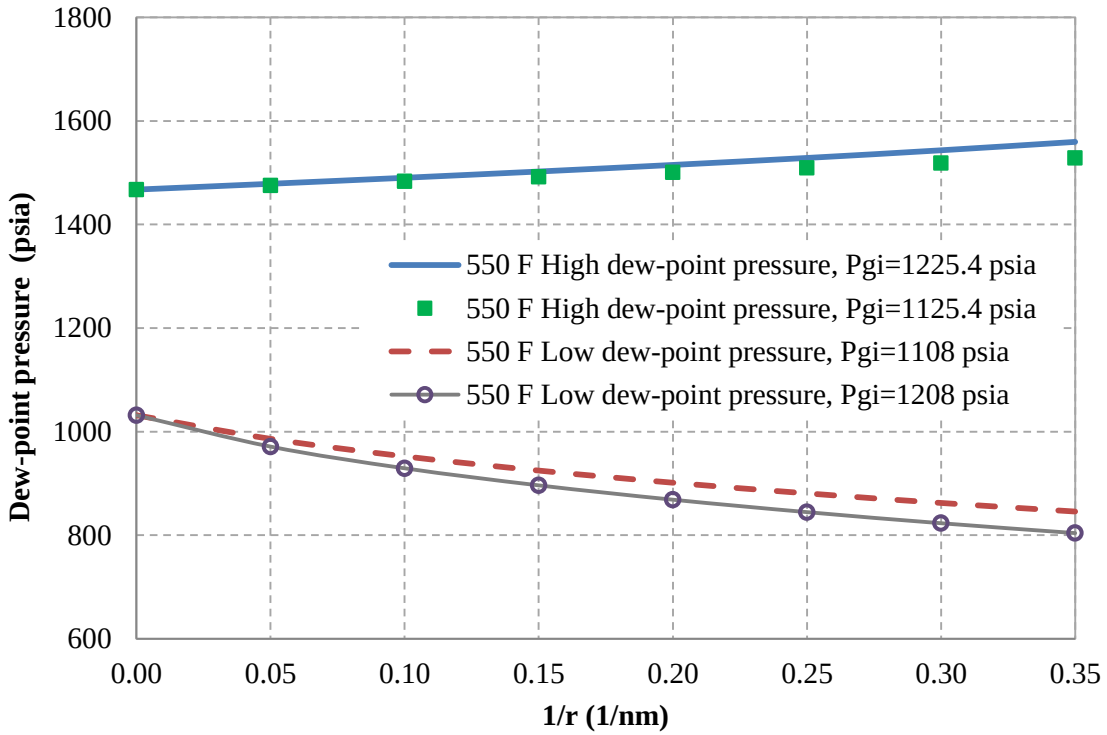


**Figure 6.12: $P_{gi}^{(n)}$ effect on dew-point pressure for methane 70% - decane 30%**

The best way that was most helpful in picking the initial two-phase pressure was to try to select the highest $p_{gi}^{(n)}$ using the smallest pore size of 2.86 nm, where PBM will return the highest capillary pressure and lowest IFT for the upper dew-point. A similar approach is used with the lower dew-point curve. In case PBM is unable to simulate the thermodynamic behavior using the input conditions, then $p_{gi}^{(n)}$ is not a reasonable value. The focus of this study is concentrated toward the upper dew-point curve, where the first droplet of condensate appears. Incorporating capillary pressure effects to simulate flow behavior of liquid-rich gas reservoirs will target pores in the range of 10-20 nanopores. Thus, the influence of miscalculating $p_{gi}^{(n)}$ by 100 psia at the upper dew-point demonstrates diminutive effect as seen in Figure **6.10** through Figure **6.12**.

### 6.4 Examining the influence of capillary pressure under different conditions

Capillary pressure causes different effects on saturation pressure based on the compositions of the fluids-in-place. In addition to the binary mixture of methane-decane used earlier, more combinations including methane-butane and methane-hexane were examined at different concentrations and temperatures. This exercise is intended to map the influence of including capillary pressure on phase behavior. Tables **6.4** and **6.5** present the input fluid properties with the proposed concentrations.

**Table 6.4: Fluid properties for methane-butane with different concentrations**

Fluid Characterization

| Comp | $MW_m$ (lbm/lbmol) | $T_{cm}$ (R) | $P_{cm}$ (psia) | $Z_{cm}$ | $\omega_m$ | $\Omega_{am}$ | $\Omega_{bm}$ |
|---|---|---|---|---|---|---|---|
| C1 | 16.043 | 343.33 | 666.4 | 0.2874 | 0.0104 | 0.457235529 | 0.077796074 |
| n-C4 | 58.123 | 765.62 | 550.6 | 0.2728 | 0.1995 | 0.457235529 | 0.077796074 |

Note: Volume shifts are set to zero
Parachor coefficient: 77.0 and 189.9, respectively

Concentrations

| Comp | $c_{i\_1}$ | $c_{i\_2}$ | $c_{i\_3}$ |
|---|---|---|---|
| C1 | 0.85 | 0.70 | 0.6 |
| n-C4 | 0.15 | 0.30 | 0.4 |

Binary Interaction Coefficients

| Comp | C1 | n-C4 |
|---|---|---|
| C1 | 0 | 0.00147 |
| n-C4 | 0.00147 | 0 |

**Table 6.5: Fluid properties for methane-hexane with different concentrations**

Fluid Characterization

| Comp | $MW_m$ (lbm/lbmol) | $T_{cm}$ (R) | $P_{cm}$ (psia) | $Z_{cm}$ | $\omega_m$ | $\Omega_{am}$ | $\Omega_{bm}$ |
|---|---|---|---|---|---|---|---|
| C1 | 16.043 | 343.33 | 666.4 | 0.2874 | 0.0104 | 0.457235529 | 0.077796074 |
| n-C6 | 86.177 | 913.60 | 436.9 | 0.2635 | 0.2994 | 0.457235529 | 0.077796074 |

Note: Volume shifts are set to zero
Parachor coefficient: 77.0 and 271.0, respectively

Concentrations

| Comp | $c_{i\_1}$ | $c_{i\_2}$ | $c_{i\_3}$ |
|---|---|---|---|
| C1 | 0.85 | 0.70 | 0.6 |
| n-C6 | 0.15 | 0.30 | 0.4 |

Binary Interaction Coefficients

| Comp | C1 | n-C6 |
|---|---|---|
| C1 | 0 | 0.00218 |
| n-C6 | 0.00218 | 0 |

The three binary mixtures selected are meant to represent light, moderate, and heavy mixtures. The same concentration combinations were used for the three binary mixtures, where the non-volatile component increases from 15% to 40%. As the non-volatile concentration increases, the mixture becomes richer in heavies and the phase envelope shifts to the right toward higher temperatures. For each binary mixture, a high temperature was chosen for the testing where the highest capillary pressure is believed to be found. As it will be seen later in this section, capillary pressure is found to be increasing with higher temperatures. Similar testing was conducted on various pore sizes to capture changes in capillary pressure, interfacial tension, and dew-point pressure. Hereafter, the study is focused toward the upper dew-point curve where the condensate dropout takes place.

Figure **6.13** shows capillary pressure for the different combinations versus pore sizes. Despite expecting methane-decane to exert the highest capillary pressure, methane-hexane and methane-butane showed the highest with concentrations of 85% and 15%, respectively. The rest of the combinations were compiled between capillary pressures of 0 psia and 5 psia. Among all concentrations used, the 60% volatile and 40% non-volatile recorded the least capillary pressures. Mixtures with higher non-volatile concentrations deliver more condensate than those with the least heavies. As the condensate phase becomes dominant inside the pores, the capillary pressure moves toward zero. Thus, the light and moderate mixtures reflected the highest capillary pressures.

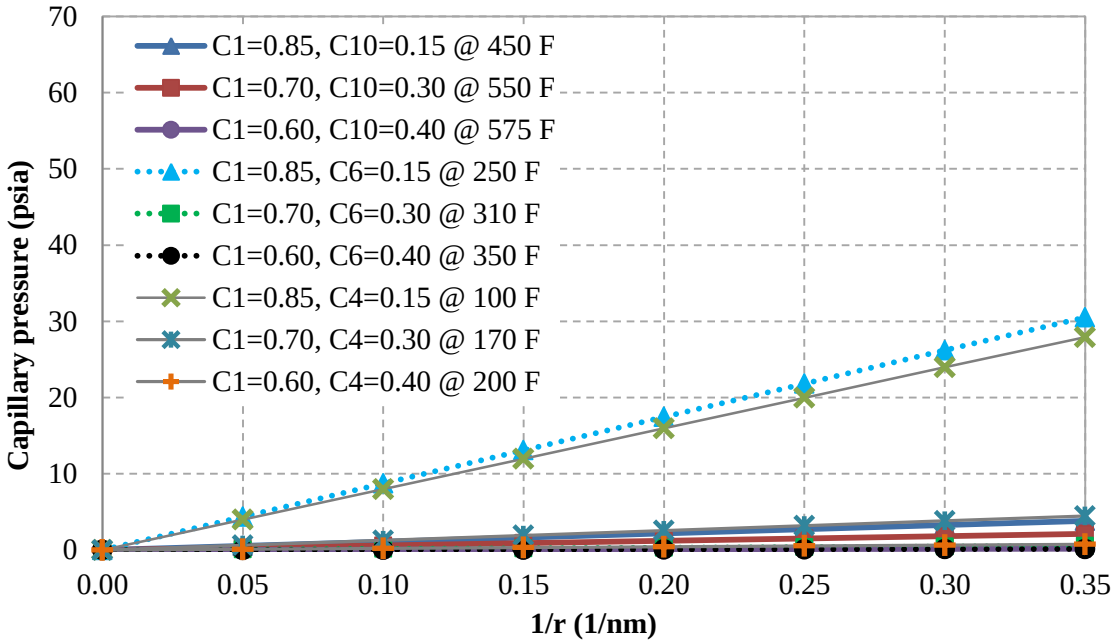


**Figure 6.13: Capillary pressure for binary mixtures with different concentrations**

The relationship between capillary pressure, IFT, pore sizes, and dew-point pressure remains as explored earlier. Figure **6.14** reflects the interfacial tension against various nanopores. Higher changes in capillary pressure are associated with higher changes in interfacial tensions. The moderate and lightest mixtures continue to show the highest interfacial tension as seen with the capillary pressure due to the richness in leaner components. Interfacial tension for the upper dew-point decreases as the pore sizes reduces, but with noticeable differences between the mixtures recording the highest IFT and the rest of the binary mixtures.

The inverse relationship of dew-point pressure with interfacial tension causes the dew-point pressure for methane-hexane and methane-butane to be increasing as shown in Figure **6.15**. Methane-hexane reflects higher capillary pressure, IFT, and influence on dew-point pressure as long as the mixture is rich in volatile concentration. The same applies to methane-butane with 85% and 15% composition. Although the mixture of methane-butane with 70% and 30% shows higher capillary and IFT than the rest of the mixtures, it does not return higher influence on dew-point pressure. In comparison, methane-decane with ≥70% methane reflects higher influence on dew-point pressure than methane-butane with 70% methane concentration. This contrast is owed to one mixture being lean and the other being richer in heavies.

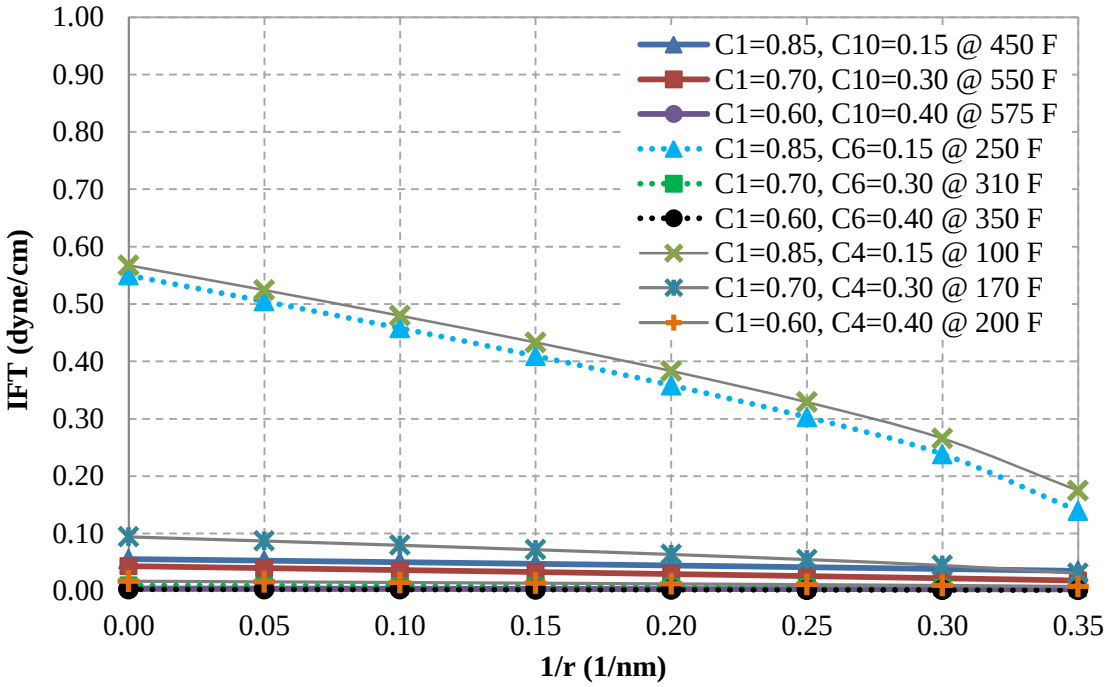


**Figure 6.14: Interfacial tension for binary mixtures with different concentrations**

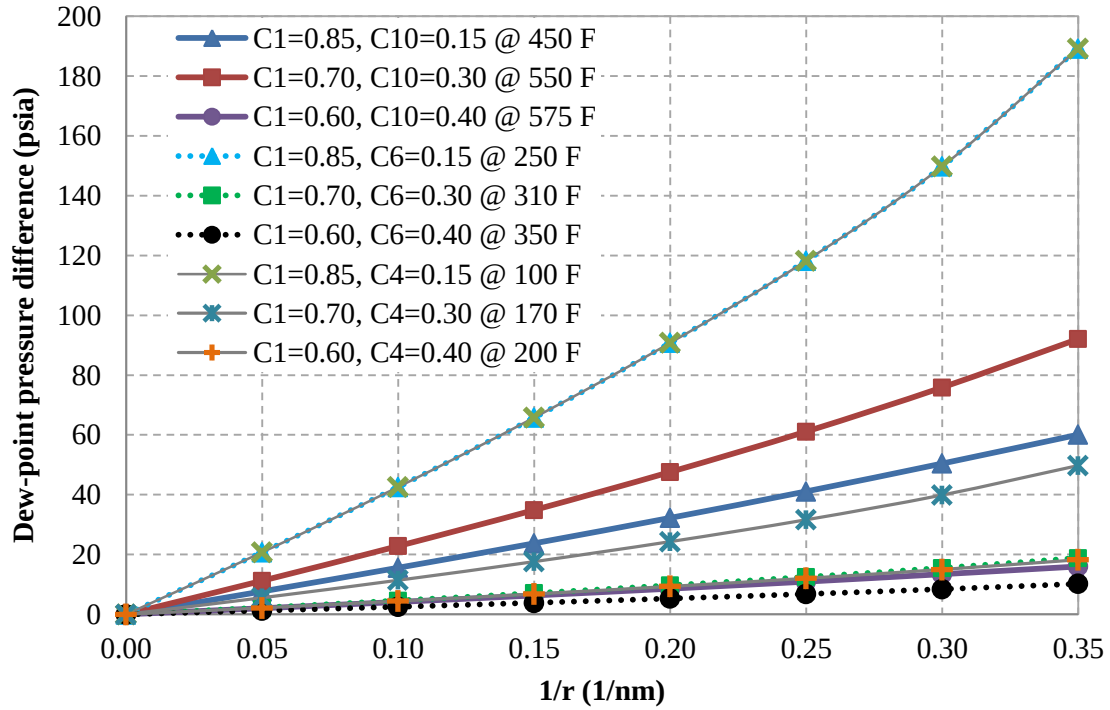


**Figure 6.15: Dew-point pressure difference for mixtures with different concentrations**

Several temperatures were used to test changes in capillary pressure, which ranges between the critical point and cricondentherm. Fluid properties at the critical point are known to have undistinguishable differences. Since the density and molecular weight of the phases share similarities, the interfacial tension becomes zero. Thus, capillary pressure in the proximity of the critical point reaches a value of zero. As temperature increases along the upper dew-point curve where the first droplet of condensate appears, capillary pressure is increasing. Figure **6.16**, Figure **6.17**, and Figure **6.18** illustrate the increase in capillary pressure based on temperature. Temperatures that are close to the cricondentherm reflect the highest capillary pressure, whereas temperatures that are closest to the critical point produce the least capillary pressures. Among the three binary mixtures used, methane-hexane generates higher capillary pressure across its phase envelope. In accordance with previous observations, the moderate case returned the highest capillaries, and the heaviest returned the least. More illustrations and results on capturing capillary pressure at different temperatures for the same mixture can be seen in Appendix E.

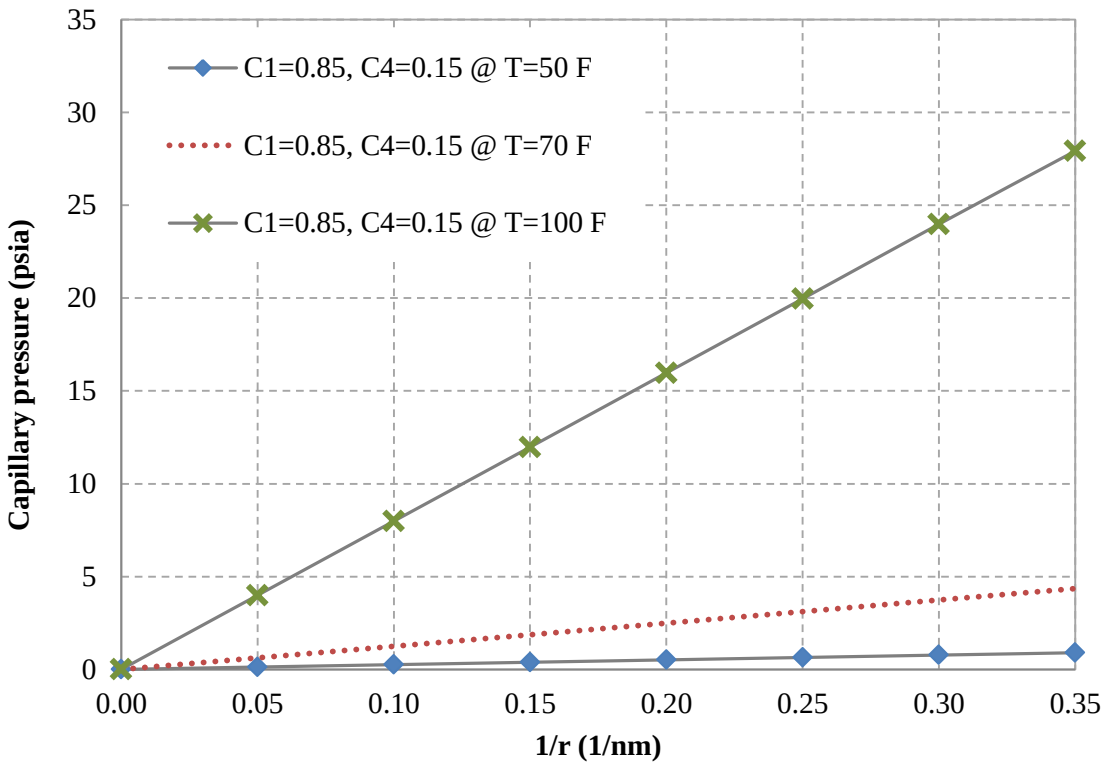


**Figure 6.16: Capillary pressure for methane-butane: different temperatures**

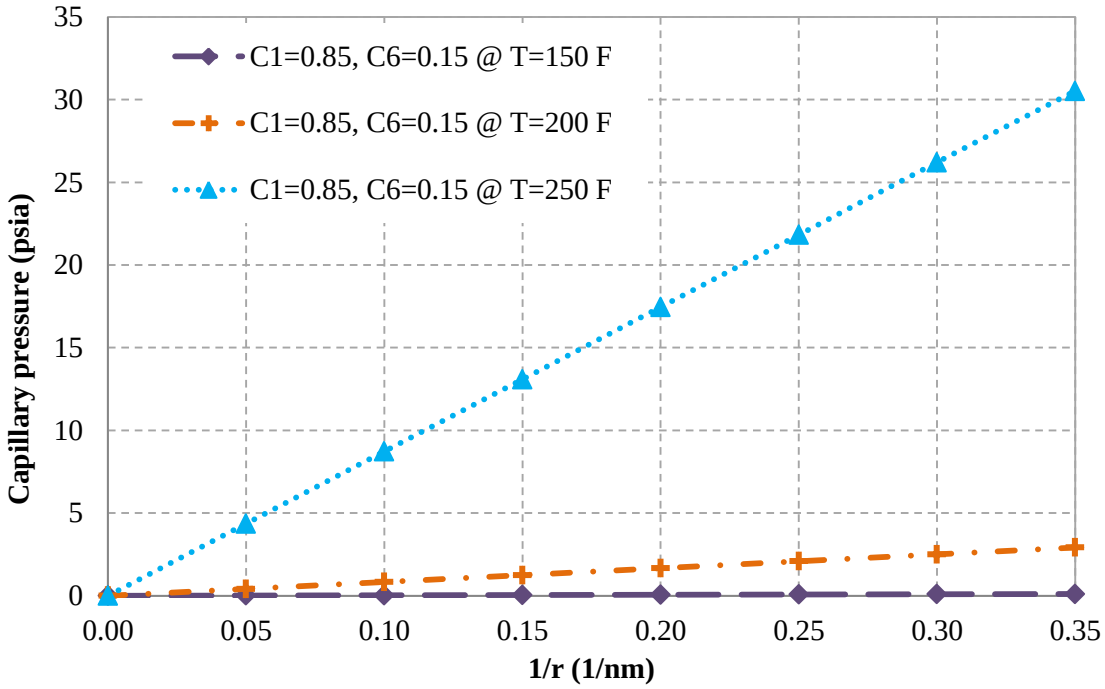


**Figure 6.17: Capillary pressure for methane-hexane: different temperatures**

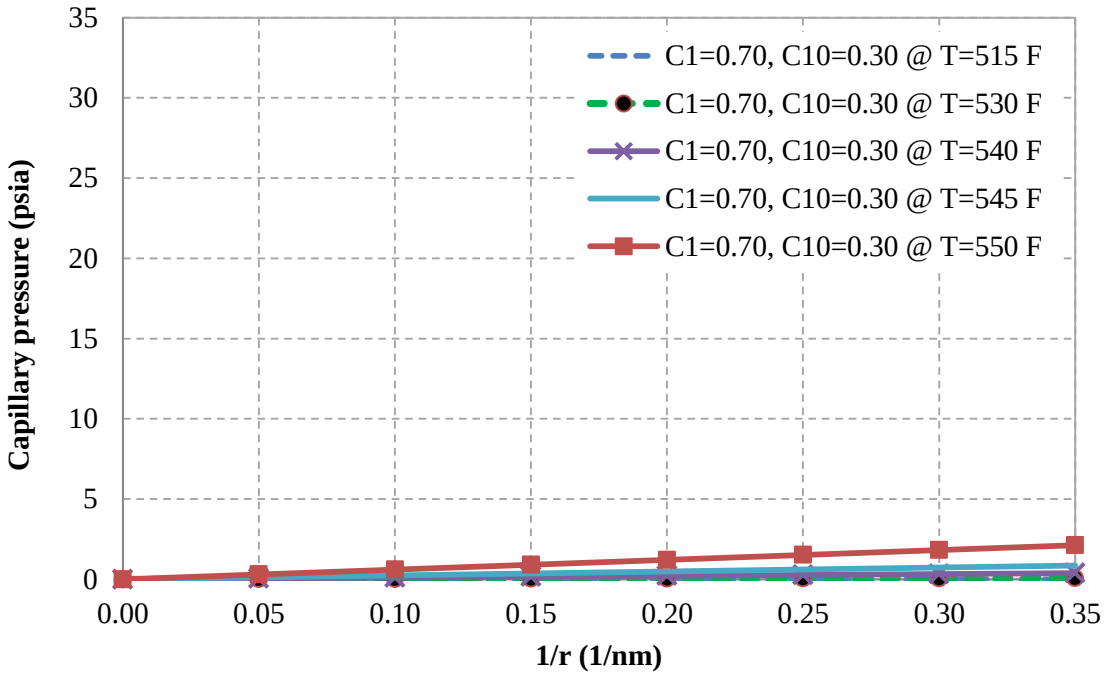


**Figure 6.18: Capillary pressure for methane-decane: different temperatures**

Furthermore, the temperature-capillary pressure relationship was examined using the three binary mixtures at 10 nm. Figure **6.19** demonstrates the increase in capillary pressure as temperature increases. In support of the increase in capillary pressure and the interfacial tension, Figure **6.20** provides an explanation of the increase. Interfacial tension is a function of vapor and liquid densities, where higher differences produce higher values of IFT. Figure **6.20** illustrates the divergence between vapor and liquid densities as a function of temperature, which is captured at the upper dew-point curve. The departure between the two curves shown for all of the cases is small at lower temperatures, which is reflected on low IFT, and subsequently low capillary pressure. Meanwhile, the highest departure is captured at higher temperatures leading to higher capillary pressures. In brief, capillary pressure is a function of IFT that is a function of density divergence, and density is a function of temperature. Thus, in addition to the influence applied by composition combination on capillary pressure calculations, temperature also adds a noticeable impact.

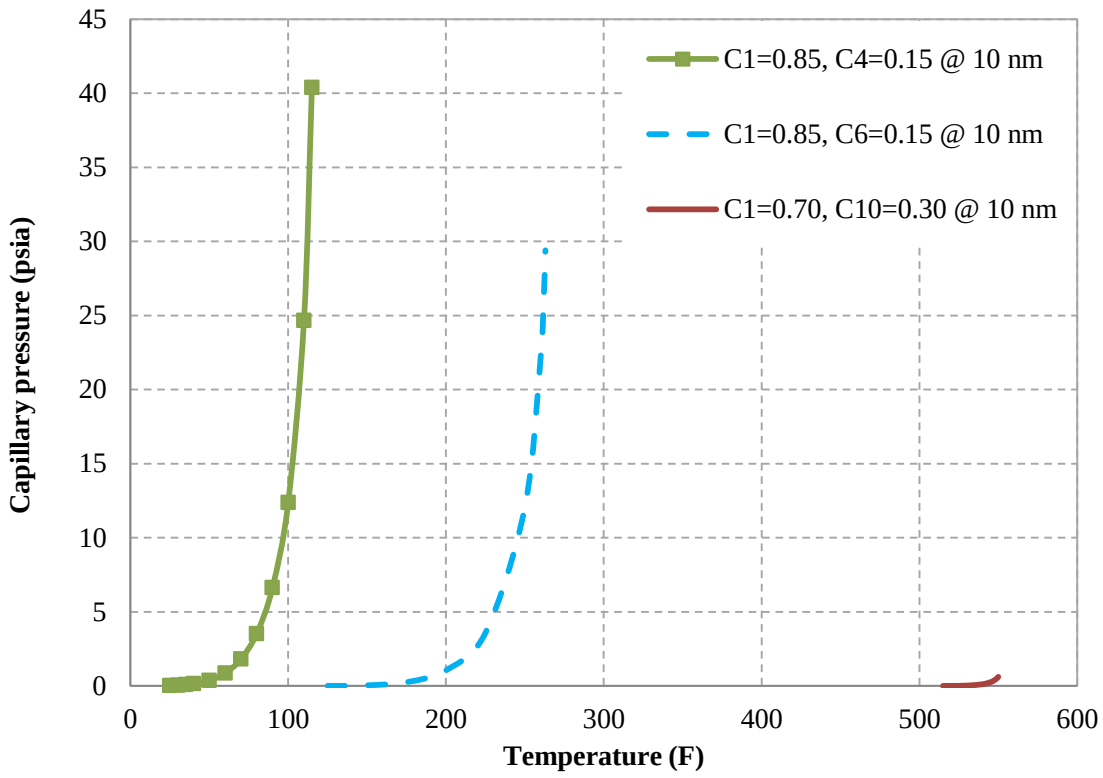


**Figure 6.19: Capillary pressure versus temperature at 10 nm**

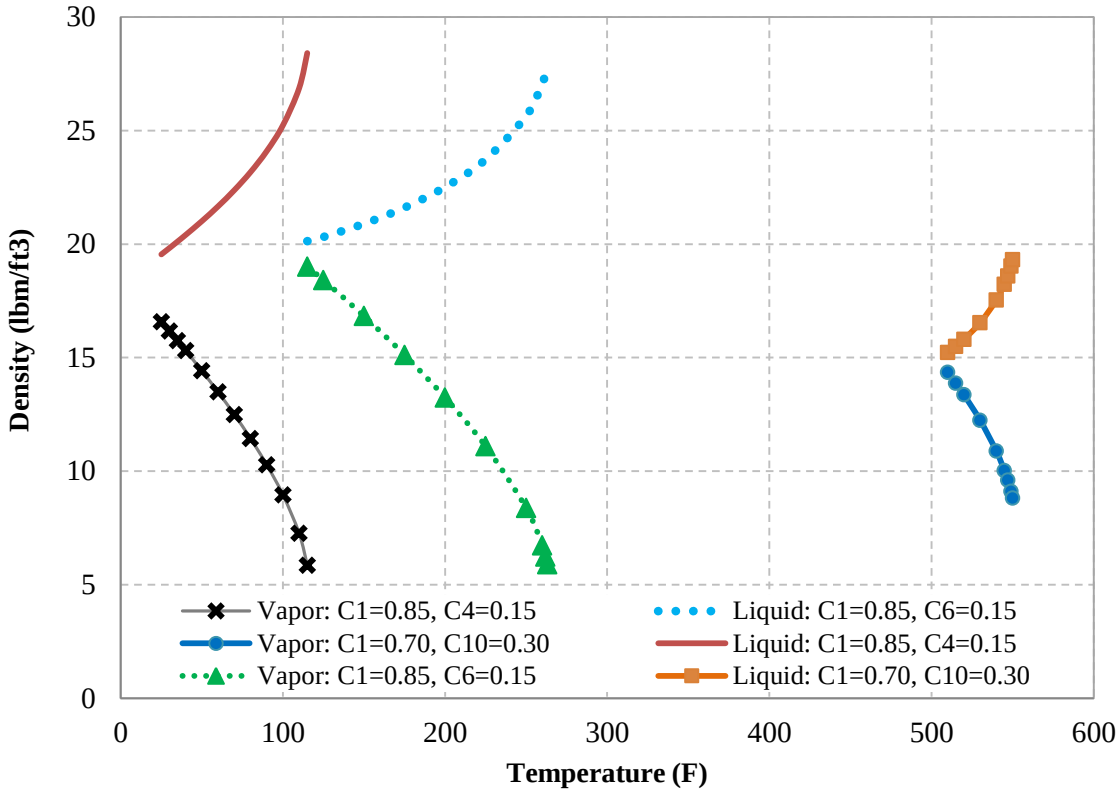


**Figure 6.20: Vapor and liquid densities versus temperature for different mixtures**

In order to summarize the influence of capillary pressure on phase behavior, phase envelopes were developed for the three mixtures under study at 10 nm. The aim is to capture changes imposed on the dew-point upper and lower curves. Figure **6.21** compares the phase envelopes with the addition of capillary pressure to the original phase envelopes. In the generation of the phase envelopes considering capillary effects, points near the critical point were not achievable because IFT and capillary pressure returned zero values. Thus, those points were extended from the last results showing zero capillary pressure to the critical point with values mimicking the original curve. This was encountered for a few points for methane-decane at temperatures between 425-500$^{o}$ F, and for methane-hexane at temperatures between 87-115$^{o}$ F.

In this exercise, the effect on temperature was also captured using the same workflow introduced in Figure **6.2**, by solving for $T^{(n)}$ instead of $p_g^{(n)}$. In contrast to the results of Nojabaei *et al.* (2013) showing no change at the cricondentherm temperature for the mixtures tested, the current

model had captured shifts in the positive direction. The search for the change in temperature was only used when it was impossible to give a $p_g^{(n)}$ and where the dew-point line was almost vertical. Table **6.6** summarizes the results for the three mixtures by showing the minimum and maximum changes captured for the upper and lower dew-point, and temperature. Currently, the coupling of PBM with capillary pressure enabled the prediction of fluid behavior as a function of reservoir pressure, capillary pressure, composition, and temperature. Next, the modified PBM model will be incorporated with the in-house simulator for further testing on flow behavior in nanopores.

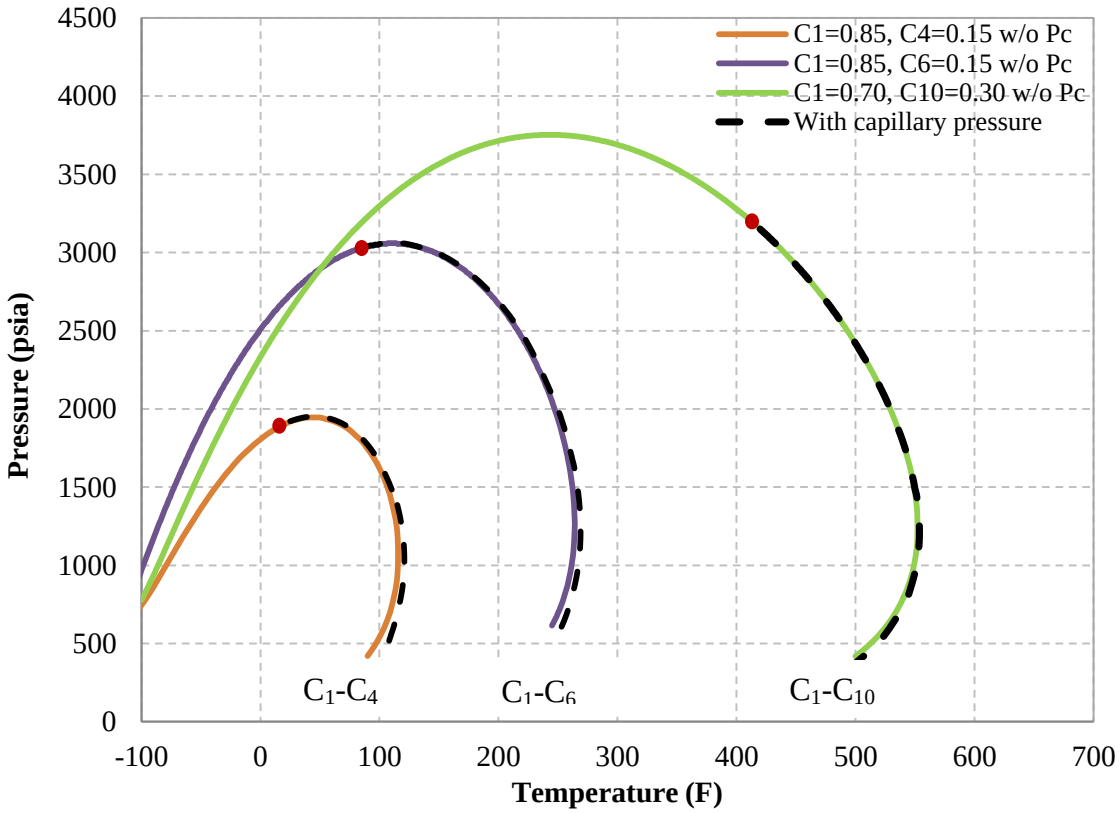


**Figure 6.21: Influence of capillary pressure on phase envelopes**

**Table 6.6: Fluid properties for methane-butane with difference concentrations**

| | Upper dew-point (psia) | | Lower Dew-Point (psia) | | Temperature (F) | |
|---|---|---|---|---|---|---|
| | Min | Max | Min | Max | Min | Max |
| methane 85% - butane 15% | +0.79 | +166.19 | -167.02 | -222.9 | +3.85 | +6.10 |
| methane 85% - hexane 15% | +0.40 | +210.76 | -131.47 | -210.86 | +3.85 | +6.26 |
| methane 70% - decane 30% | +0.24 | +22.82 | -42.31 | -79.39 | +0.88 | +2.43 |

# Chapter 7

## IMPLEMENTING SINGLE-BLOCK SIMULATION WITH FRACTURES

In fractured liquid-rich gas reservoirs, the representation of a single continuum system with dual permeability suggests that most of the gas is stored in the inner potion of the matrix blocks, and flow takes place through the fracture network. During depletion, the fractured reservoir will experience a higher pressure drop compared to the inner matrix blocks. As pressure drops below dew-point pressure, condensate will form and accumulate on the edges of the matrix blocks. Eventually, the accumulation of condensate will hinder the flow of the gas from the inner part of the matrix to the flow channels.

The concept of a single-matrix block is utilized in this research as an elemental volume where fluids are accumulating and flowing into and out of the system. The best method to magnify the imbibition process in the pores created by the dropped-out condensate, which is displacing the gas from the pores, would be through a single-block model. An important advantage of this approach is that a single-block surrounded by fractures is a representative sample of stacked matrix blocks in a fractured reservoir (Van Golf-Racht, 1982). One single-matrix block is sufficient because it shares no interface with its neighboring blocks. The optimum way to represent a single-block matrix with fractures is as presented in Figure **7.1**.

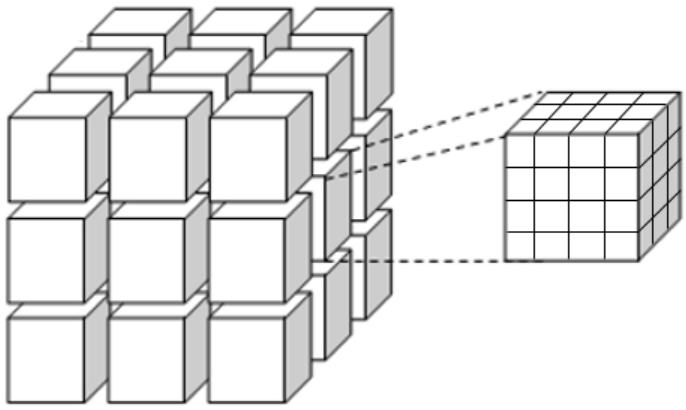

**Figure 7.1: Single-block representation**

Ayala *et al.* (2004) studied the impact of multi-mechanistic flow in a naturally fractured retrograde gas reservoir using a single-block model. A dual permeability system was considered with the activation of gravitational forces and assuming constant diffusion coefficients throughout the simulation period. Several observations can be attained from the body of work of Ayala *et al.* (2004). The inclusion of diffusion contributed to capturing higher recovery than if the flow was only flowing according to the pressure gradient. The activation of gravitational forces in tight formation appeared to have a negligible effect on the vertical evolution of condensate with time. Furthermore, capillary pressure was kept null throughout the study between gas and condensate, which is believed to have had imposed an additional constraint to the movement of gas in tight formations and impacted recovery.

In this work, a 2D representation of the single block with equal dimensions is used to depict the reservoir since gravitational forces effects are negligible in tight formations. Fractures were placed surrounding the system from the sides as shown in Figure **7.2**, and all the sides of the block are open for flow upon the establishment of boundary conditions. The fractures impose the flow path with higher permeability, while the matrix is presented with the least permeability and stores most of the fluids-in-place. The single-block is discretized with refined blocks near the fractures to capture the behavior of fluids near the edges of the matrix where condensate impairment is prone to occur. The most important addition of this work is the activation of capillary pressure with the inclusion of flow under Fick's law.

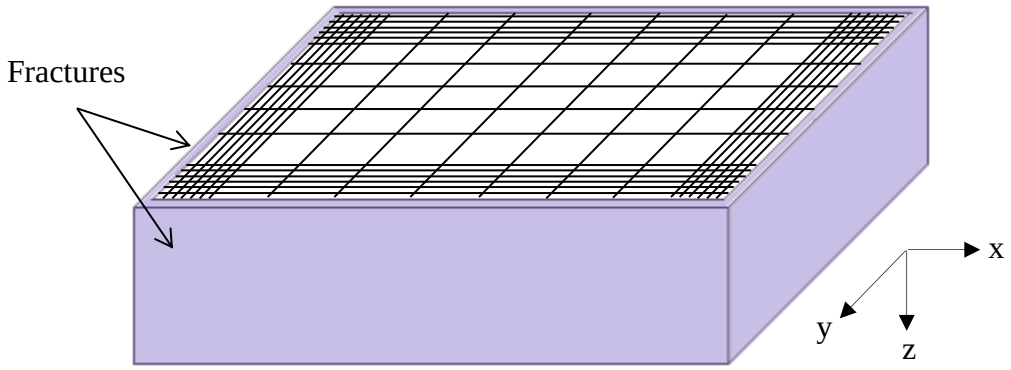


**Figure 7.2: Fractures surrounding the matrix from the sides**

The activation of capillary pressure is believed to increase the thickness of condensate and subsequently impose higher resistance for gas to flow. With more condensate attached to the grains, the likelihood of losing more heavies to the formation is present. In relationship to Figure **7.2**, condensate would trap more gas inside the matrix for a longer period of time. Thus, it is important to monitor the thickness and spread of condensate toward the inner part of the single-block with the inclusion of capillary pressure. It is also essential to evaluate the impact on recovery and understand the contribution of the matrix to production in nanopores, knowing that diffusion will dominate recovery in such conditions.

### 7.1 Quarter-block representation

Flow is symmetrical with respect to the x and y directions which allows one quarter of the single-block matrix to be capable of representing the behavior of the whole block. Due to the absence of gravitational forces, symmetry is possible in the z direction. Figure **7.4** illustrates the new representation of the single-block matrix considering symmetrical flow. However, with the new representation, it is considered that there are no flow boundaries in the symmetry planes due to the absence of conductive channels. The quarter-block matrix is surrounded by fractures at the two sides that are opposite from the symmetry planes. Figure **7.5** illustrates the quarter-block with the implementation of refined gridblocks toward the edges, where the fractures are located.

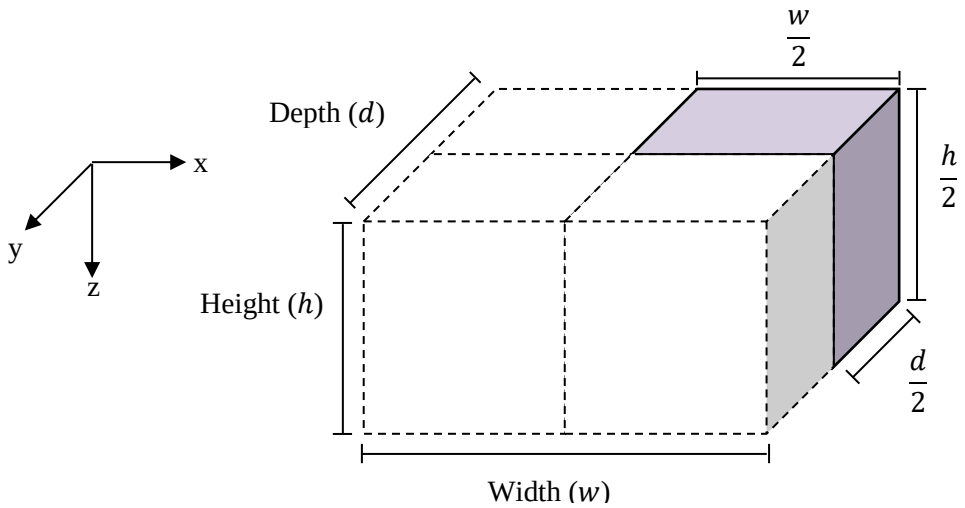


**Figure 7.3: Representation of the quarter single-block matrix (*after Ayala, 2004*)**

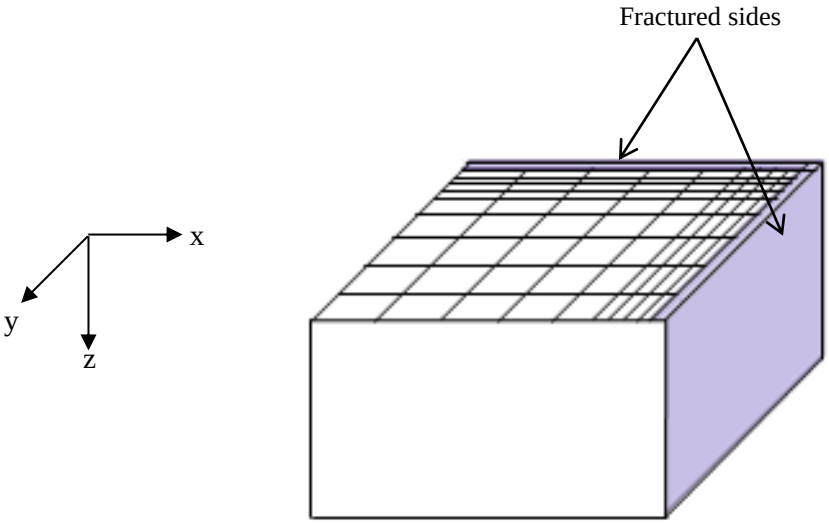


**Figure 7.4: Grid refinement toward fractures**

The matrix is discretized with the fractures, but since fractures are defined with a fixed depletion pressure, they are not included in the construction of the Jacobian. The adjacent blocks to the edges will have an additional transmissibility equation toward the fracture blocks. Since pressure in the neighboring blocks to the fractures is higher than the pressure in the fracture block, the physical properties are assumed to be equal. Equation (7.1a) and equation (7.1b) demonstrate the transmissibility term toward fractures, where $\omega$ represents the composition for either the vapor phase or the liquid phase. As a result, the source term is modified to account for all the fluids that reach the fractures. Equation (7.2) is the new source term equation for the fractured system in this study.

$$T_{fx\_fract}\Big|_{i\pm\frac{1}{2}}^{n+1} = \frac{A_x k_x}{\Delta x}\Big|_{i\pm\frac{1}{2},j} \frac{\rho_f}{\mu_f}\Big|_{i,j}^{n+1} \omega_m k_{rf}\Big|_{i,j}^{n+1} \quad ; \quad f = oil\ or\ gas \tag{7.1a}$$

$$T_{fy\_fract}\Big|_{j\pm\frac{1}{2}}^{n+1} = \frac{A_y k_y}{\Delta y}\Big|_{j\pm\frac{1}{2},j} \frac{\rho_f}{\mu_f}\Big|_{i,j}^{n+1} \omega_m k_{rf}\Big|_{i,j}^{n+1} \quad ; \quad f = oil\ or\ gas \tag{7.1b}$$

$$M_m|_{i,j} = T_{ox\_fract}\Big|_{i\pm\frac{1}{2}}^{n+1} + T_{gx\_fract}\Big|_{i\pm\frac{1}{2}}^{n+1} + T_{ox\_fract}\Big|_{j\pm\frac{1}{2}}^{n+1} + T_{gx\_fract}\Big|_{j\pm\frac{1}{2}}^{n+1} \tag{7.2}$$

## 7.2 Space discretization

A 2D representation of the single block with equal dimensions was presented earlier to depict the reservoir. Because of the symmetry of flow, a quarter-block was sufficient to simulate the same results. The quarter-block was discretized with refined blocks near the edges to capture the behavior of fluids near the fractures where condensate accumulation was expected the most. This section aims to assess the space discretization of the quarter-block with fractures.

The space discretization is applied on a 1D representation of a quarter-block system with a length of 186 ft. as shown by Figure **7.5**. Various uniform gridblock sizes were included in the testing, presented by a number of blocks ranging from 3 to 35. Ultimately, improved results would be attained with a 2D representation. Due to the computational limitation of the in-house simulator, that was built on MATLAB, to handle a 35x35 grid system; a 1D model with one fractured block was used. The system employed various sizes in the x-direction ($\Delta x$) as presented in Table **7.1** while maintaining constant total length ($\Delta L$). In this representation, the gridblock sizes in the y-direction ($\Delta y$) and height (h) were kept equal ($\Delta y = h$) for all the different cases. The reason the size in the y-direction and height must be maintained alongside the total length was to sustain consistency in the testing. This is only applicable with the selected 1D model for the discretization testing. With a 2D model, a system consisting of ($\Delta x = \Delta y$) and constant h can be utilized as long as the ($\Delta L$) is the same in the x- and y-direction.

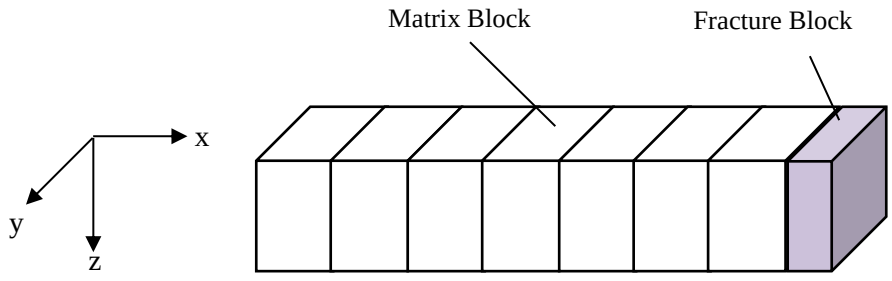


**Figure 7.5: 1D grid discretization toward a fracture**

**Table 7.1: Grid discretization testing cases**

| | $\Delta x$ (ft) | $\Delta y = h$ (ft) | # of matrix blocks (x-direction) |
|---|---|---|---|
| Case 1 | 62 | 15 | 3 |
| Case 2 | 37.2 | 15 | 5 |
| Case 3 | 18.6 | 15 | 10 |
| Case 4 | 12.4 | 15 | 15 |
| Case 5 | 9.3 | 15 | 20 |
| Case 6 | 7.44 | 15 | 25 |
| Case 7 | 6.2 | 15 | 30 |
| Case 8 | 5.31 | 15 | 35 |

Throughout the examination, time step is set by default to *1 day*, but once instability in calculation was experienced, a lower time step was used. The cases with the number of blocks less than 15 simulated from 7 to 40 CPU minutes. Simulation time was increasing concurrently as the number of blocks increased, where the 20, 25, and 30 blocks completed calculations in 140 min., 187 min., and 432 minutes respectively. Case 8 represented with 35 blocks completed simulation in 9 hours, which is 540 minutes. Ultimately, this exercise provided useful insight on the capabilities of the in-house simulator in terms of handling a number of grids.

Figure **7.6** illustrates the performance of various cases demonstrating condensate content in the reservoir. The presence of condensate appears to accumulate earlier with smaller grid sizes, while it is delayed in larger blocks. Actually, condensate content is highly dependent on gridblock volume, which was also seen in the work of Ayala (2004). In his work, condensate saturation was not predicted during 1,500 days of simulation using a grid size of 500 ft. With larger gridblock sizes, condensate saturation is averaged over a large volume which results in reducing condensate content and delaying its appearance. In contrast, smaller blocks recover higher condensate saturation and the accumulation starts within a smaller time window as shown for the gridblock sizes from 5.31 ft. to 18.6 ft. Thus, depletion is enhanced in smaller blocks. As a result, condensate will reach its maximum accumulation volume quicker and start the vaporization process earlier. This is clearly shown by the short condensate content cycle with the gridblock sizes ranging between 5.31 ft. to 9.3 ft. Therefore, in the selection of the gridblock

sizes, refined blocks with the size of 5 ft. are assigned to the neighboring blocks of the fractures to capture detailed performance of condensate evolution. The blocks which are in the center of the single-block configuration will have the largest size, not exceeding 50 ft., while the blocks in between will range in sizes from 7.5 ft. to 37.5 ft., in increasing order toward the inner portion of the matrix system.

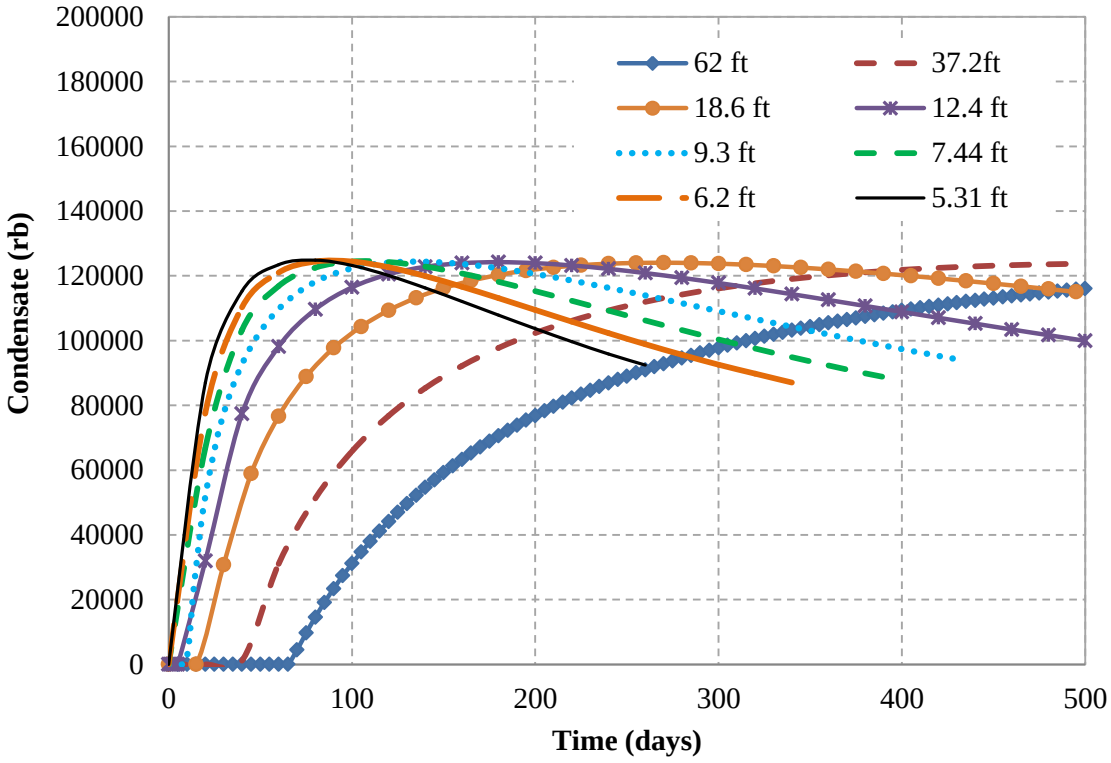


**Figure 7.6: Reservoir condensate content using different discretization scenarios**

# Chapter 8

# INVESTIGATING THE INFLUENCE OF CAPILLARY PRESSURE ON NEAR CRITICAL FLUIDS

The productivity of liquid-rich gas reservoirs experiences a reduction in recovery due to the appearance of condensate near the flow channels, which in turn reduces the overall flow of hydrocarbons to the surface. The variation of reservoir fluid properties is controlled by many factors, such as: reservoir pressure, composition combination, concentrations, temperature, capillary forces, and pore radius. Meanwhile, the severity of condensate accumulation depended on composition combinations and concentrations of the non-volatile components. Using the knowledge from the previous investigation on capillary pressure and phase behavior of various mixtures, the deliverability performance of those mixtures is explored in detail. Several cases will examine reservoir performance in different rock environments under the influence of capillary pressure and diffusion. Investigating capillary pressure of various magnitudes will provide valuable knowledge on possible impairment in terms of fluid distribution and recoveries for different composition combinations. In addition, the study is expected to provide more insight on productivity characteristics in fractured reservoirs with the inclusion of diffusion through evaluating condensate movement, residence time, and retention effects on productivity.

## 8.1 Numerical study input

A summary of the inputs to the simulation runs considered in this study are introduced here, which is in correspondence with the data set presented in Chapter 6. The aim is to study a reservoir grid system consisting of (22x22x1) with a length of 372 ft. Selecting the length and number of blocks was achieved with care after taking into consideration the discretization analysis and computational capabilities. With a quarter-block representation, a grid system of 11x11x1 can reproduce the same results of a single-block after multiplying the output by 4. Tables **8.1** to **8.4** show the data used as parameters for the simulation study. Table **8.1** represents the variables that were kept constant throughout all simulations scenarios, which include the rock properties of the matrix and the fracture attributes.

**Table 8.1: Grid properties of the matrix and fractures**

| Matrix | | |
|---|---|---|
| Matrix block length (Single-Block Model) | 372 | ft |
| Matrix block length (Quarter-Block Model) | 186 | ft |
| # of Blocks (SBM) | 22x22x1 | |
| # of Blocks (QBM) | 11x11x1 | |
| Rock compressibility | 0 | $cp^{-1}$ |
| Porosity | 0.13 | |
| Pore radius | $1x10^{12}$, 10, 20 | nm |
| Permeability | 0.10 | mD |
| Time step* | 1 | day |
| **Fracture** | | |
| Fracture pressure | 500 | psia |
| Fracture width | 0.01 | ft |
| Fracture porosity | 0.13 | |
| Fracture permeability | 2000 | mD |

(*) Time step default is 1 day, but is assigned in the range $0.01<\Delta t\leq 1$ day based on stability and when needed

Table **8.2** shows the hydrocarbon properties of the mixtures, and the transport properties considered for the flow of fluids in the system. For each mixture, the table below refers the hydrocarbon properties in tables presented earlier in Chapter 6, which were used to investigate the effect of capillary pressure on dew-point curve. Table **6.4**, Table **6.5**, and Table **6.1** contain the physical properties and binary coefficients for methane-butane, methane-hexane, and methane-decane mixtures, respectively. Included in Table **8.2** are references to the oil/gas and oil/water relative permeability tables found in Chapter 5. Table **5.6** presents the oil/gas relative permeability without capillary pressure data, because capillary pressure effects are imbedded in the phase behavior model. Since the interaction between hydrocarbon and water is neglected, the capillary pressure data included in Table **5.7** for the oil/water relative permeability data has a restricted effect.

**Table 8.2: Fluid properties of the mixtures under study**

| Hydrocarbon Properties | | |
|---|---|---|
| Light mixture | Table 6.4 | |
| Moderate mixture | Table 6.5 | |
| Rich mixture | Table 6.1 | |
| Effective Diffusion | 0, and 10 | $ft^2/day$ |
| **Relative Permeability** | | |
| Water saturation (Swirr) | 0.16 | |
| Critical oil saturation | 0.28 | |
| Oil/Gas | Table 5.6 | |
| Oil/Water | Table 5.7 | |

Different sets of compositions are considered in this study, which are presented in Table **8.3**. As seen in Chapter 6, capillary pressure causes different effects based on the compositions of the fluids-in-place, reservoir pressure and temperature. Table **8.3** presents the reservoir conditions with each set, including $p_{gi}^{(n)}$, which is needed to estimate capillary pressure at the given pore radius. The models have been constructed to run for different simulation periods based on the individual cases. The sets that are aimed to study the influence of capillary pressure, without the inclusion of diffusion, run for a simulation period of 1,000 days. Since diffusion is known to enhance depletion as seen in the work of Ayala (2004), simulation time is reduced depending on the performance of the set under study. The need to reduce simulation time becomes necessary when at least one block in the matrix reaches a block pressure close to the flowing pressure at the fractures. This will cause no outflow toward the flow channels and will pressurize the system at the edges of the matrix. Lastly, Table **8.4** presents the surface separation facility consisting of a high pressure separator and a stock tank.

**Table 8.3: Composition combinations, and reservoir conditions of the mixtures**

| Combination | Concentrations | Reservoir Pressure (psia) | Reservoir Temperature (F) | Dew-point Pressure (psia) | $Pgi^{(n)}$ (psia) |
|---|---|---|---|---|---|
| C1-C4 (Light) | 0.85 - 0.15 | 1960 | 67.5 | 1903.21 | 1616.71 |
| | 0.70 - 0.30 | 1840 | 151 | 1788.03 | 1501.53 |
| | 0.60 - 0.40 | 1600 | 192.5 | 1558.05 | 1446.35 |
| C1-C6 (Moderate) | 0.85 - 0.15 | 2935 | 175 | 2867.62 | 2596.62 |
| | 0.70 - 0.30 | 2170 | 300 | 2115.8 | 1844.8 |
| | 0.60 - 0.40 | 1745 | 345 | 1698.96 | 1568.36 |
| C1-C10 (Heavy) | 0.85 - 0.15 | 3530 | 400 | 3453.82 | 3211.82 |
| | 0.70 - 0.30 | 2280 | 515 | 2224.55 | 1982.55 |
| | 0.60 - 0.40 | 1385 | 575 | 1336.94 | 1094.94 |

**Table 8.4: Surface separation conditions**

| Separator | Pressure (psia) | Temperature (F) |
|---|---|---|
| Primary | 400 | 60 |
| Stock Tank | 14.7 | 60 |

## 8.2 Reservoir performance without the inclusion of capillary pressure

Several mixtures with various compositional combinations have been used to apply different severities of condensate coating. Table **8.3** displayed the different sets which were denoted by light, moderate and heavy. Each case was simulated for a period of 1,000 days, without the activation of capillary pressure, to be used as a reference for future comparison. These runs were associated with various condensate content, which presumably would imply different blockage once capillary forces are activated. The three binary mixtures were tested against three concentration combinations, where the composition of the volatile component reduces from 85% to 60%. The decrease in volatility shifts the phase envelope to the right and downward, indicating heavier mixtures as shown by Figure **8.1** with the mixture of methane-butane. For

each binary mixture, a temperature was chosen for the testing which is located halfway between the critical point and the cricondentherm temperature. The selection of the temperature at the specified location was aimed to promote the condensate recovery at separator conditions.

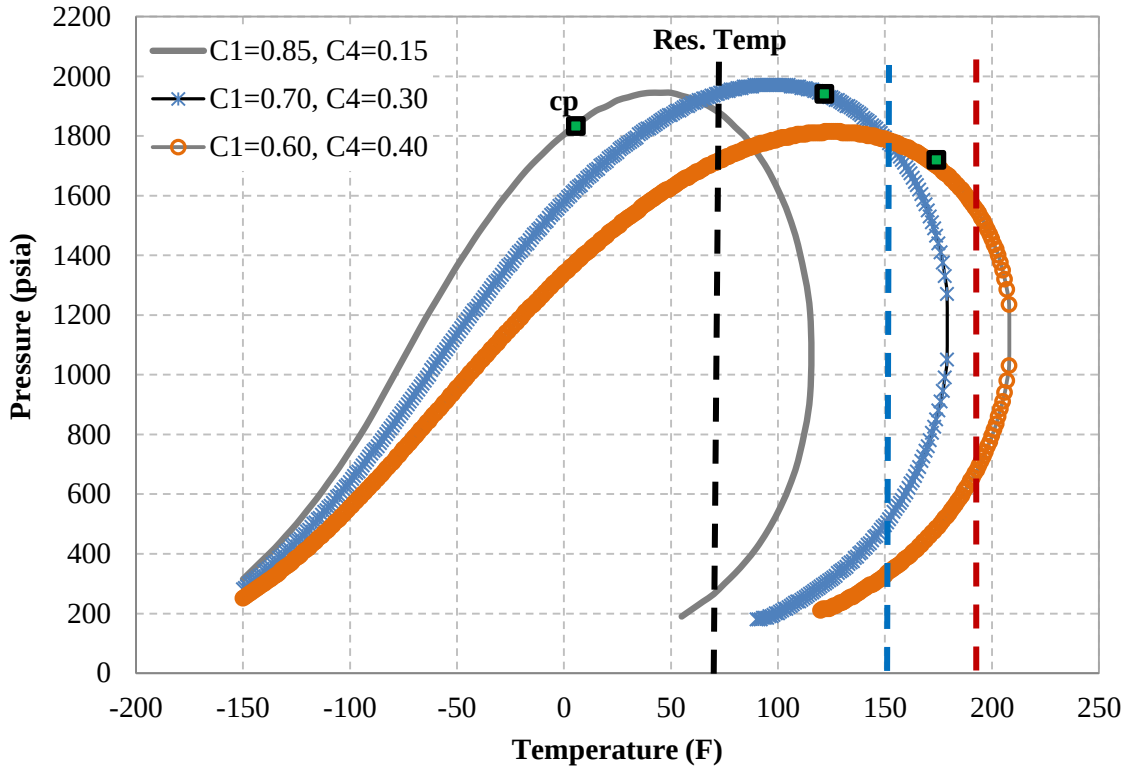


**Figure 8.1: Methane-butane phase envelope using different concentrations**

Figure **8.2**, Figure **8.4**, and Figure **8.5** demonstrate condensate at reservoir conditions for the three mixtures at different concentrations. For the light mixture represented by Figure **8.2**, condensate at reservoir conditions shows different behavior for the studied concentration combinations. It has the least content with the 85%-15% combination because this is the leanest mixture among the set. However, the 70%-30% concentration reflects higher condensate at reservoir conditions than the 60%-%40 case. This can be demonstrated by presenting the relationship between oil saturation and pressure at reservoir temperature for each of the combinations. Figure **8.3** presents the oil saturation profile for the three mixtures. This indicates that the amount of retrograde region decreases according to the area under the curve, in the following descending order: 70%-30%, 60%-%40, then 85%-15%. Larger area under the curve is associated with more condensate at reservoir conditions.

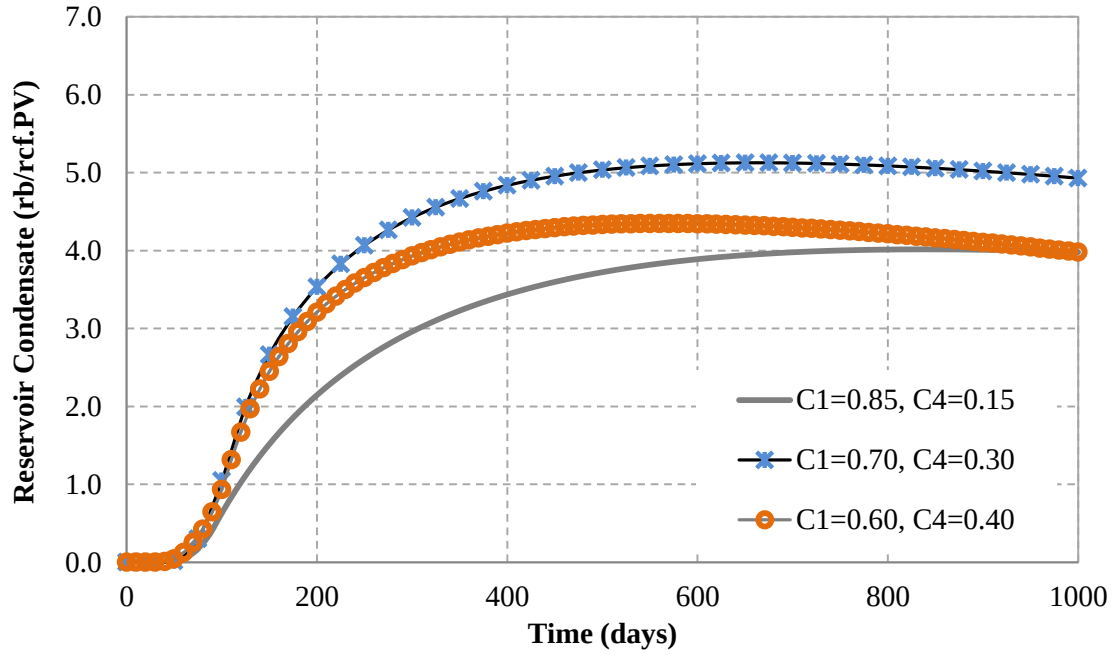


**Figure 8.2: Condensate at reservoir condition for methane-butane**

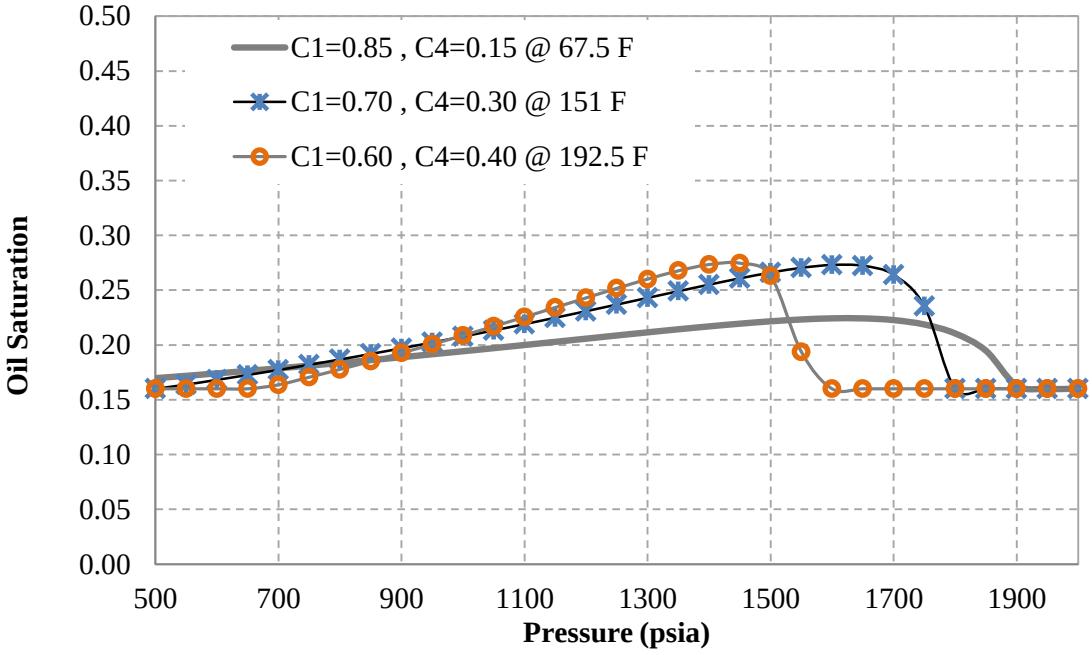


**Figure 8.3: Methane-butane oil saturation profile for different concentrations**

As the molecular weight of a component increases, its volatility decreases. Including methane and hexane in a binary mixture increased the mixture's content of condensate at reservoir conditions as shown by Figure **8.4**. This mixture, identified as the moderate fluid, reflected the maximum reservoir condensation in comparison to the light fluid and heavy fluid illustrated by Figure **8.2** and Figure **8.5**, respectively. Figure **8.5** demonstrates the condensate content of the heavy mixture containing methane-decane. Importantly, decane is considered a heavy component which can be found at low concentrations in liquid-rich gas reservoirs, and at higher concentrations in non-volatile and black-oil reservoirs. Its presence furthers the phase envelope to the right and toward higher temperatures as seen in Figure **6.21**. It also reduces the area of the retrograde region between the critical point and the cricondentherm.

The fluid methane-hexane, containing the highest condensate at reservoir conditions, is considered the base case in all of the simulation runs for comparison purposes of severity of condensate blockage. It is expected to provide more insight once capillary pressure and diffusion are activated, because condensate is dominating the pore spaces.

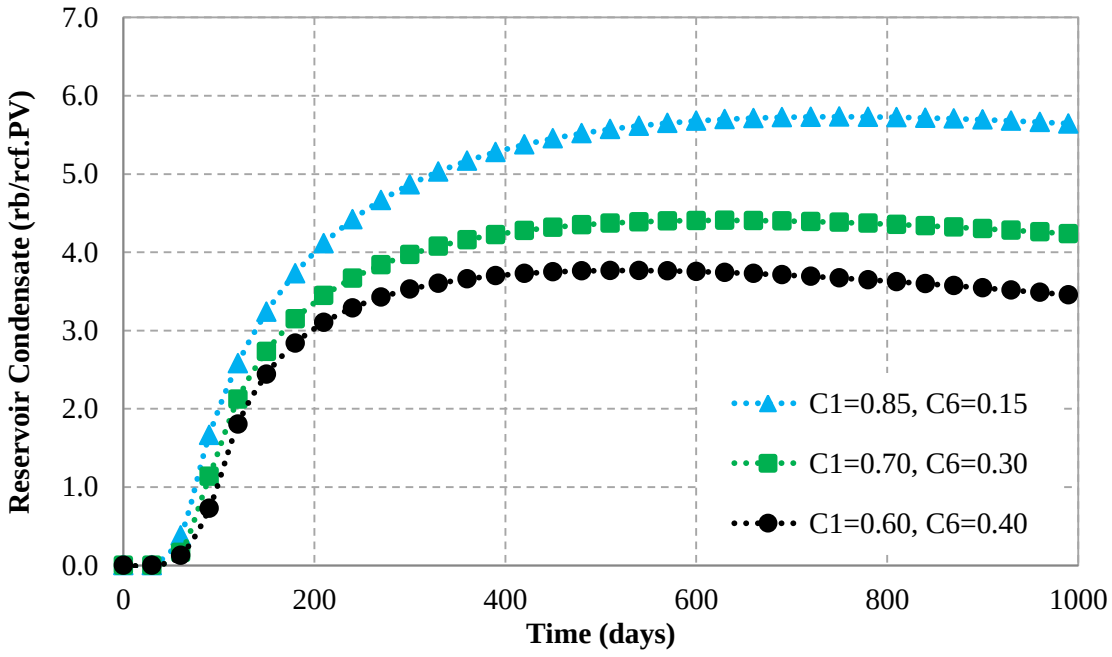


**Figure 8.4: Condensate at reservoir condition for methane-hexane**

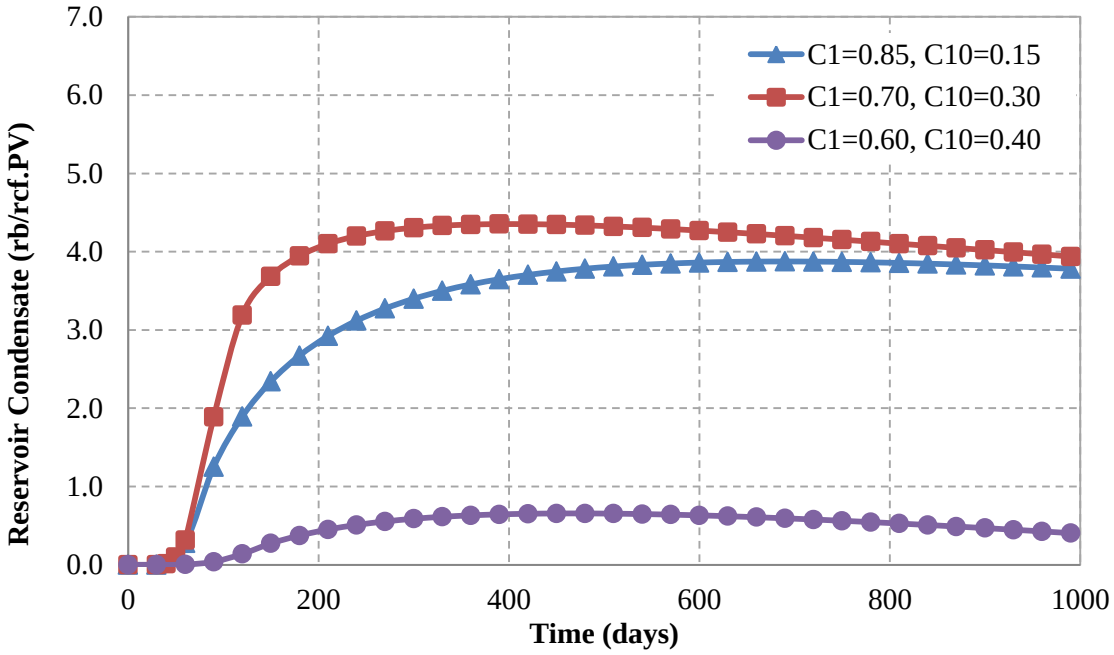


**Figure 8.5: Condensate at reservoir condition for methane-decane**

Figure **8.6** displays the molar recovery obtained from the numerical study using the compositional combinations that presented the highest condensate at reservoir conditions. The molar recovery of the lightest fluid came to be the highest, but was close to the results of the moderate fluid. Since butane is leaner than hexane, the condensate of the lightest mixture applies slight blockage to the flow of fluids. The molar recoveries for the light, moderate, and heavy mixtures were determined to be 27.38%, 24.51%, and 17.66%, respectively. Furthermore, recovery behavior in liquid-rich gas systems reflects similar recovery of molar, gas and condensate until the pressure drops below dew-point and condensate appears in the reservoir. Once condensate starts to appear in the system and becomes mobile, the recovery profile of the molar recovery and condensate recovery depart from the recovery of the gas. Figure **8.7** displays the condensate recovery for the same cases that presented more condensate-in-place. The moderate and heavy mixtures returned recoveries of 17.30% and 14.61%, respectively, while the leanest mixture had zero condensate dropout at surface conditions due to its volatility.

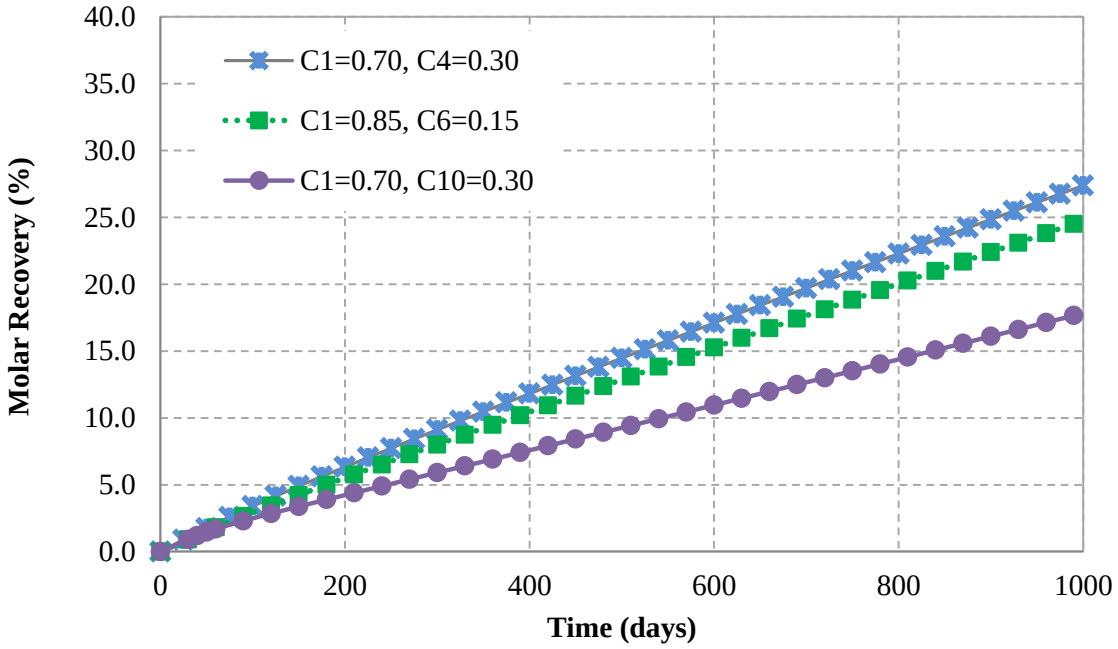


**Figure 8.6: Molar recovery for mixtures with the highest condensate**

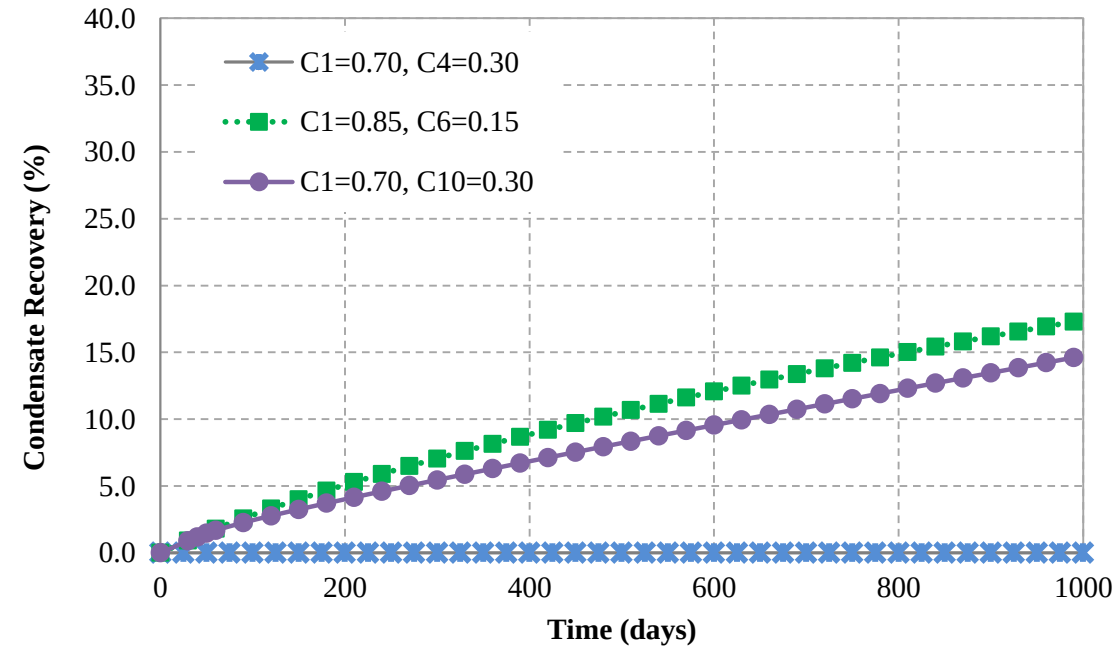


**Figure 8.7: Condensate recovery for mixtures with the highest condensate**

The condensate saturation profile was captured for methane-hexane at different locations across the single-block system, as shown by Figure **8.8**. The saturation profile at the corners experienced slightly more evolution than the center and sides of the block. However, re-vaporization was not witnessed within the studied timeframe of 1,000 days. The behavior captured for methane-hexane mimicked the same saturation behavior of the light and heavy mixtures, in terms of the appearance of condensate at different locations and the saturation trend toward the end of the simulated period. Figure **8.9** illustrates the accumulation and propagation of condensate from the edges of the matrix toward the inner portion of the single-block. The corners of the block were prone to higher depletion than in any other location because of the fractures. Pressure dropped below dew-point pressure at the corners first, and condensate started accumulating on the edges of the matrix as shown at 31 days. The accumulation continued coating the edges until the side of the matrix depleted below dew-point pressure. As time progressed, condensate tended to move toward the inner portion of the matrix to invade more pore spaces. As condensation continued to accumulate, the gas in the inner portion of the matrix started to experience the impairment against flowing to the production channels. Similar behavior was witnessed with the rest of the cases.

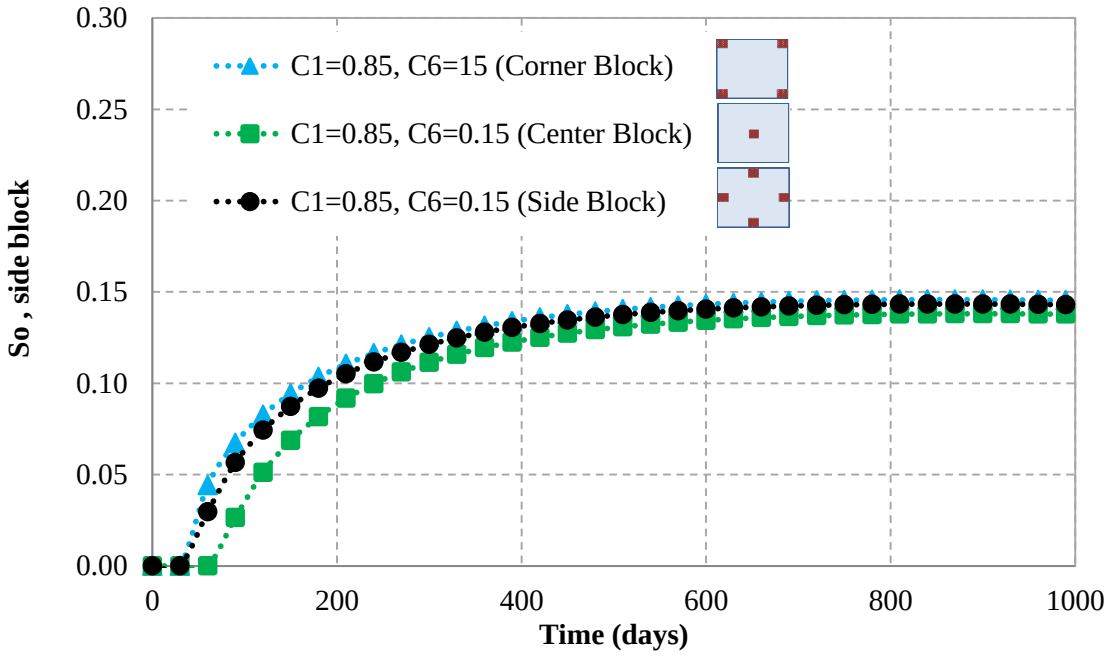


**Figure 8.8: Oil saturation profile across the single-block for methane-hexane**

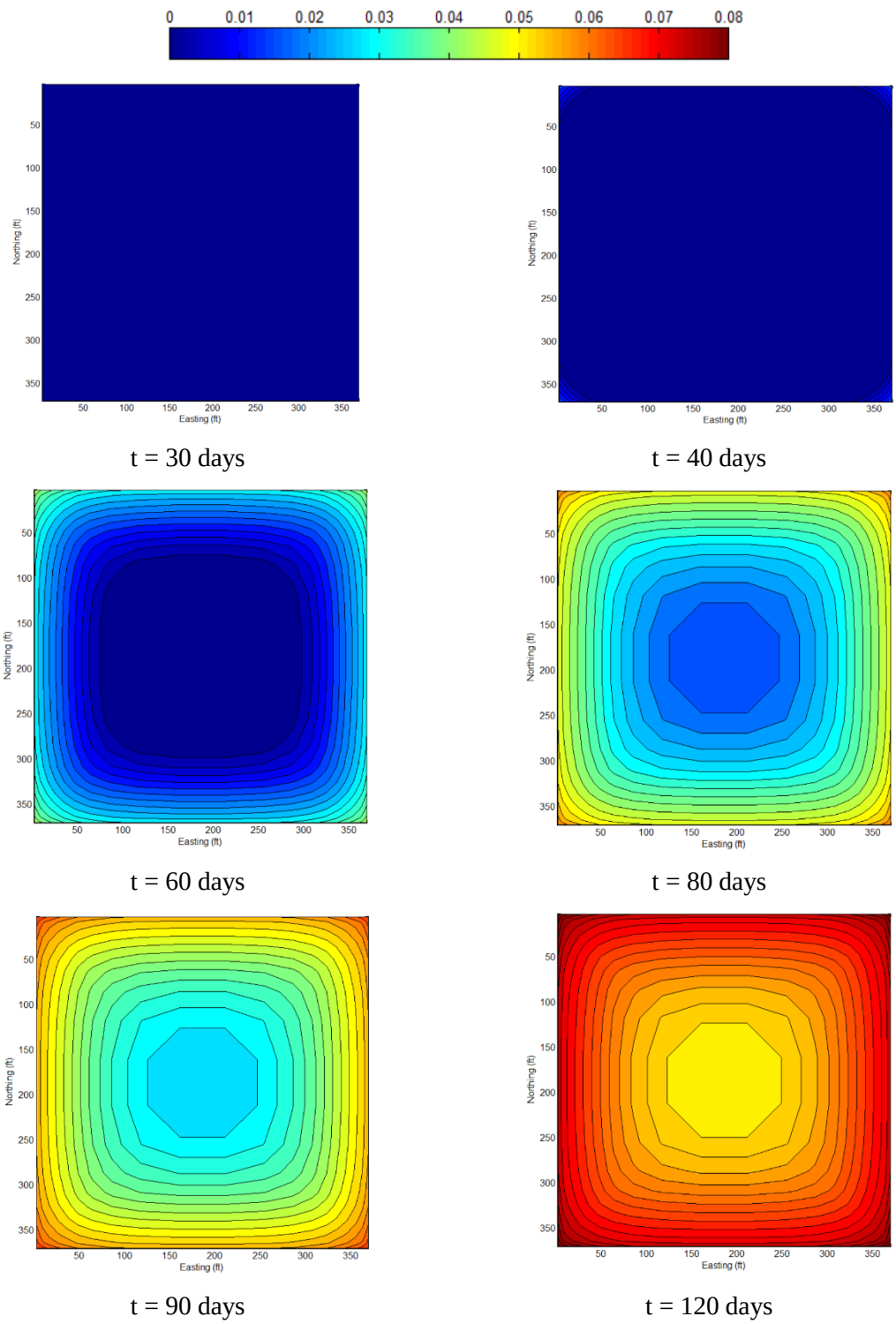


**Figure 8.9: Oil saturation evolution for methane-hexane without capillary pressure**

### 8.3 Flow behavior with the activation of capillary forces

The influence of activating capillary forces on the flow behavior of liquid-rich gas reservoirs is explored here in detail. Using the same conditions applied in Chapter 6, which mapped the magnitude of capillary forces against different composition concentrations, the recovery, appearance of condensate in different regions of the matrix block, and the condensate saturation profile has been studied. The analysis included compares the behavior of the fractured liquid-rich gas reservoir after the activation of capillary pressure resulting from using 10 nm and 20 nm pore radiuses. This section aims to display the effect of capillary pressure on residence time of condensate, resistance against gas flow, and impact on productivity. Table **8.5**, Table **8.6**, and Table **8.7** present the various cases that were simulated for the three mixtures (light – moderate – heavy). The performance data of each run were retrieved which included reservoir pressure profiles at different locations of the matrix, saturation profiles, condensate at reservoir conditions, surface flow rates, and recoveries. All of the cases were analyzed to capture the severity of condensate blockage in nanopores. More emphasis on the results of the mixture methane-hexane (85% - 15%) is considered since it showed the highest capillary forces and largest condensate at reservoir conditions.

**Table 8.5: Simulation cases for methane-butane with the inclusion of capillary forces**

| Case ID | Composition | Capillary Activated | Pore Radius (nm) | Diffusion (ft2/day) | CPU time (hrs) |
|---|---|---|---|---|---|
| C185C4NOPC | C1 = 0.85 , C4 = 0.15 | No | ∞ | 0 | 19 |
| C185C4R10 | C1 = 0.85 , C4 = 0.15 | Yes | 10 | 0 | 21 |
| C185C4R20 | C1 = 0.85 , C4 = 0.15 | Yes | 20 | 0 | 21 |
| C170C4NOPC | C1 = 0.70 , C4 = 0.30 | No | ∞ | 0 | 68 |
| C170C4R10 | C1 = 0.70 , C4 = 0.30 | Yes | 10 | 0 | 87 |
| C170C4R20 | C1 = 0.70 , C4 = 0.30 | Yes | 20 | 0 | 89 |
| C160C4NOPC | C1 = 0.60 , C4 = 0.40 | Yes | ∞ | 0 | 62 |
| C160C4R10 | C1 = 0.60 , C4 = 0.40 | No | 10 | 0 | 78 |
| C160C4R20 | C1 = 0.60 , C4 = 0.40 | Yes | 20 | 0 | 80 |

**Table 8.6: Simulation cases for methane-hexane with the inclusion of capillary forces**

| Case ID | Composition | Capillary Activated | Pore Radius (nm) | Diffusion (ft2/day) | CPU time (hrs) |
|---|---|---|---|---|---|
| C185C6NOPC | C1 = 0.85 , C6 = 0.15 | No | ∞ | 0 | 31 |
| C185C6R10 | C1 = 0.85 , C6 = 0.15 | Yes | 10 | 0 | 21 |
| C185C6R20 | C1 = 0.85 , C6 = 0.15 | Yes | 20 | 0 | 35 |
| C170C6NOPC | C1 = 0.70 , C6 = 0.30 | No | ∞ | 0 | 32 |
| C170C6R10 | C1 = 0.70 , C6 = 0.30 | Yes | 10 | 0 | 41 |
| C170C6R20 | C1 = 0.70 , C6 = 0.30 | Yes | 20 | 0 | 42 |
| C160C6NOPC | C1 = 0.60 , C6 = 0.40 | Yes | ∞ | 0 | 28 |
| C160C6R10 | C1 = 0.60 , C6 = 0.40 | No | 10 | 0 | 32 |
| C160C6R20 | C1 = 0.60 , C6 = 0.40 | Yes | 20 | 0 | 39 |

**Table 8.7: Simulation cases for methane-decane with the inclusion of capillary forces**

| Case ID | Composition | Capillary Activated | Pore Radius (nm) | Diffusion (ft2/day) | CPU time (hrs) |
|---|---|---|---|---|---|
| C185C10NOPC | C1 = 0.85 , C10 = 0.15 | No | ∞ | 0 | 27 |
| C185C10R10 | C1 = 0.85 , C10 = 0.15 | Yes | 10 | 0 | 34 |
| C185C10R20 | C1 = 0.85 , C10 = 0.15 | Yes | 20 | 0 | 36 |
| C170C10NOPC | C1 = 0.70 , C10 = 0.30 | No | ∞ | 0 | 33 |
| C170C10R10 | C1 = 0.70 , C10 = 0.30 | Yes | 10 | 0 | 47 |
| C170C10R20 | C1 = 0.70 , C10 = 0.30 | Yes | 20 | 0 | 47 |
| C160C10NOPC | C1 = 0.60 , C10 = 0.40 | Yes | ∞ | 0 | 19 |
| C160C10R10 | C1 = 0.60 , C10 = 0.40 | No | 10 | 0 | 22 |
| C160C10R20 | C1 = 0.60 , C10 = 0.40 | Yes | 20 | 0 | 21 |

Figures **8.10** to **8.18** illustrate the results for the mixture methane-hexane with concentration of 85% and 15%. Figure **8.10** shows the reservoir pressure profile captured at the corners of the matrix system. It compares the pressure profile while activating capillary forces using pore radius of 20 nm and 10 nm to the case that neglected capillary effects. As shown from the plot, the depletion behavior of the reservoir was mirrored under the conditions specified. The outcome indicated minuscule effects of capillary forces on reservoir pressure. However, further analysis of the results needs to be considered before drawing a final conclusion.

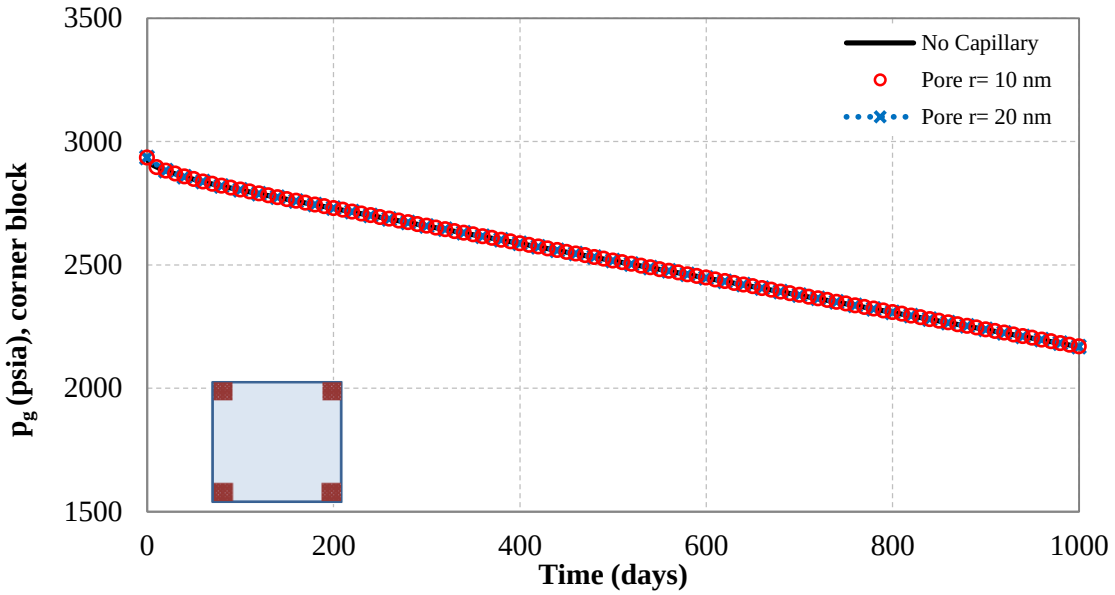


**Figure 8.10: Reservoir pressure profile for methane-hexane with capillary forces**

Condensate evolution for methane-hexane with the activation of capillary forces at 10 nm is presented by Figure **8.11**. The saturation profile with pore radius of 10 nm shows more rapid evolution than the case presented in Figure **8.9** without capillary forces. Higher capillary pressure is anticipated with a 10 nm pore radius than with 20 nm as seen in Chapter 6. Thus, with higher capillary pressure, dew-point increases. Since the dew-point is higher, condensate is expected to appear earlier. For this mixture with 85% and 15% concentration, the liquid dropped out 3 days earlier than before, which covered 3% of the number of blocks by the end of 30 days. By 40 days, condensate had invaded 44% of the blocks in comparison to 23% without activating capillary pressure. This indicates that capillary pressure had increased the spread of condensate by 91.3% at the specified time. As time progresses and condensate reaches the inner part of the block, the increase in spread becomes smaller. After 60 days of simulation, 99% of the blocks have accumulated some condensate, which is only a 5% increase from the case without capillary pressure. Although the spread was enhanced, the values of saturation were still low, which makes the aerial evolution presented in Figure **8.11** very close to the profile in Figure **8.9**. In addition, it is very difficult to pin down the differences using x-y plots as shown in Figure **8.12** and Figure **8.13**. These plots illustrate oil saturation using different pore radiuses against the base case of no capillary pressure at the corners and center of the single block.

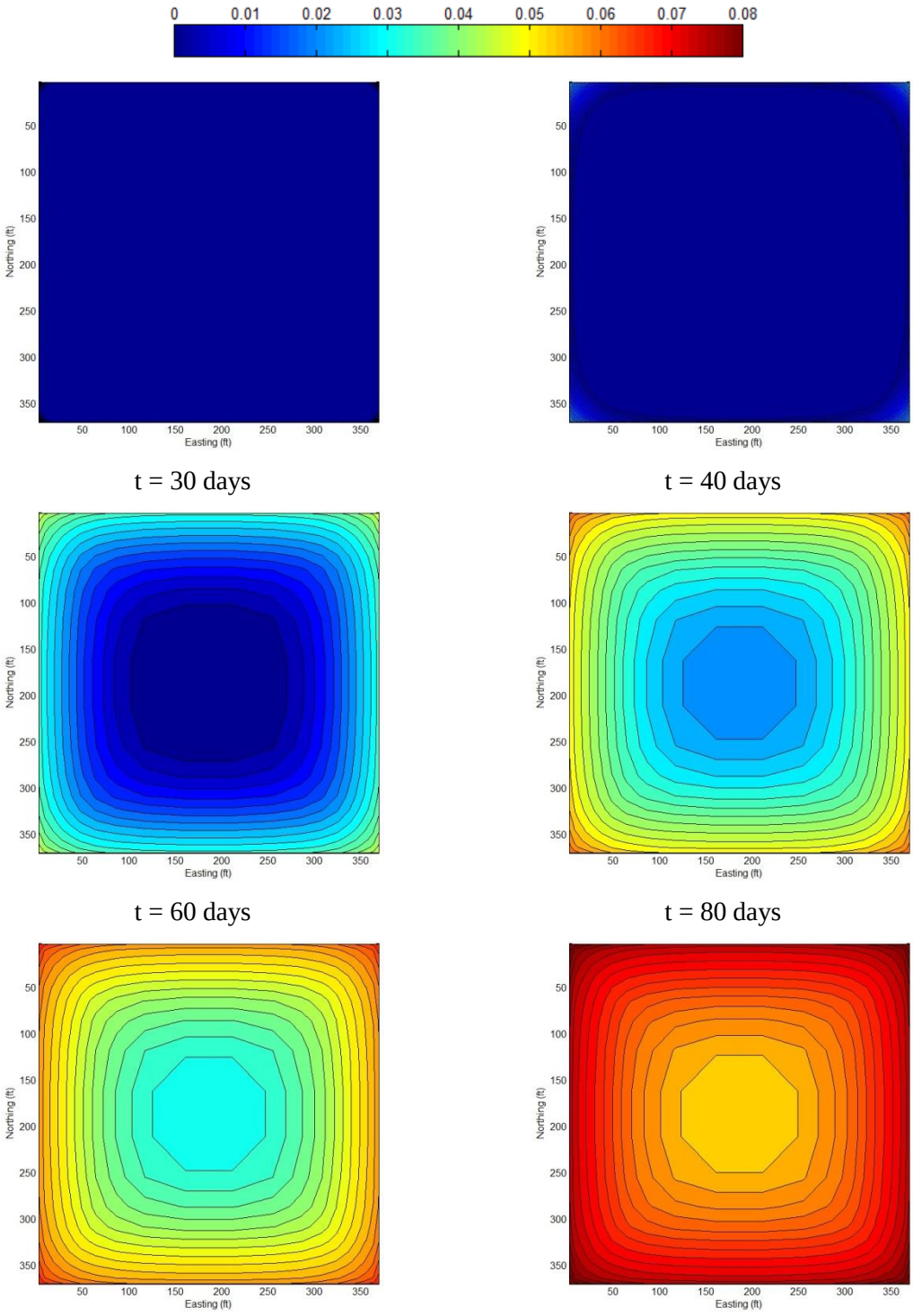


t = 30 days

t = 40 days

t = 60 days

t = 80 days

t = 90 days

t = 120 days

**Figure 8.11: Oil saturation for methane-hexane with capillary forces in a radius of 10 nm**

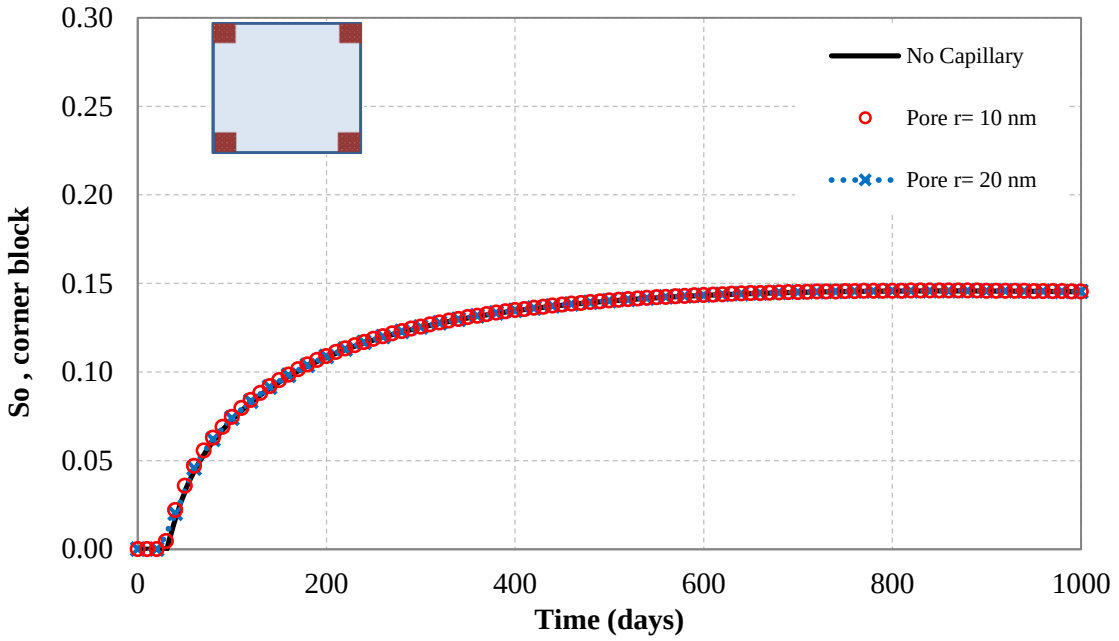


**Figure 8.12: Oil saturation at the corners for methane-hexane with capillary forces**

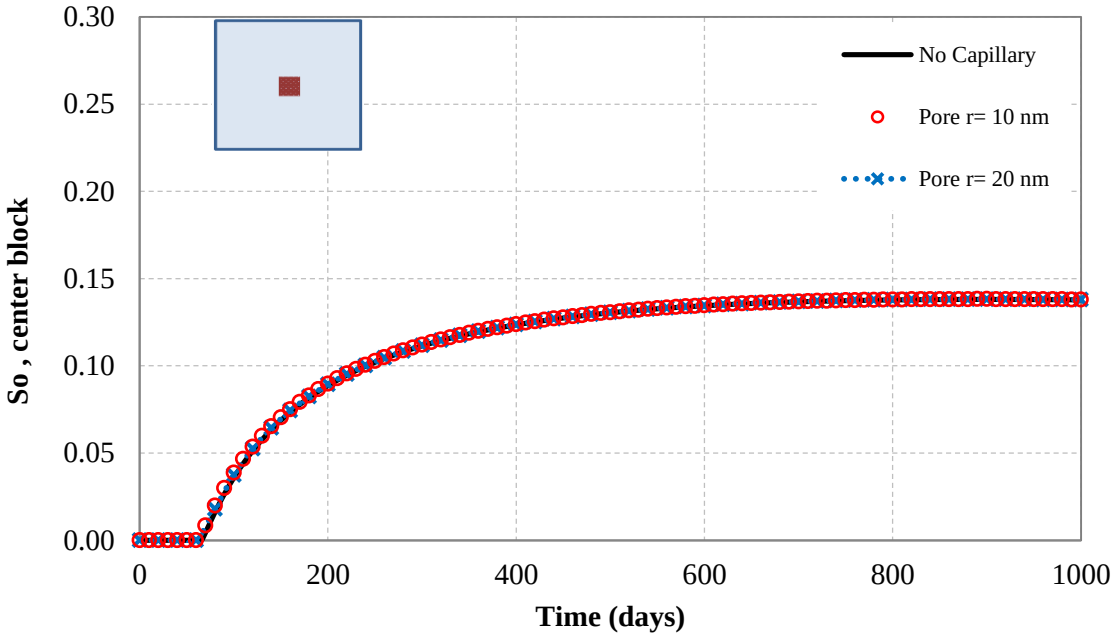


**Figure 8.13: Oil saturation at the center for methane-hexane with capillary forces**

The activation of capillary pressure had increased the propagation of condensate and subsequently is expected to impose higher resistance for gas to flow. With more condensate attached to the grains, the likelihood of losing more heavies to the formation is also present. Therefore, it is important to examine the amount of condensate at reservoir conditions and recoveries in relationship to the cases that discount capillary forces. Figure **8.14**, Figure **8.15**, and Figure **8.16** capture condensate at reservoir conditions for the three binary mixtures referenced in the previous section. The differences are not visible due to the diminutive variances between the results in each plot. However, looking closely at the result data retrieved, the differences occur at the early times when the spread of condensate is enhanced. The mixture methane-butane with 70%-30% showed slightly more differences during the first 120 days, and then it collapsed with the methane-hexane mixture. Meanwhile, methane-decane recorded the least changes in comparison to the other two cases. Once condensate reaches the inner part of the matrix, those differences in results become nonexistent. Overall, the residence time for condensate with the three binary mixtures was extended diminutively with the inclusion of capillary pressure.

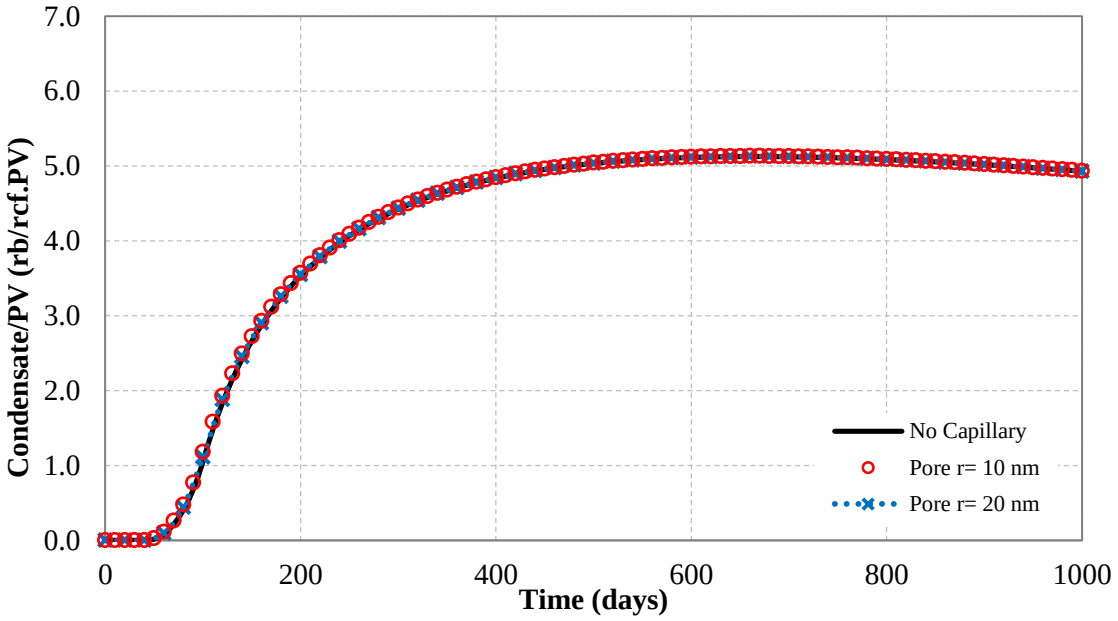


**Figure 8.14: Condensate at reservoir condition for methane-butane (70%-30%) with capillary forces**

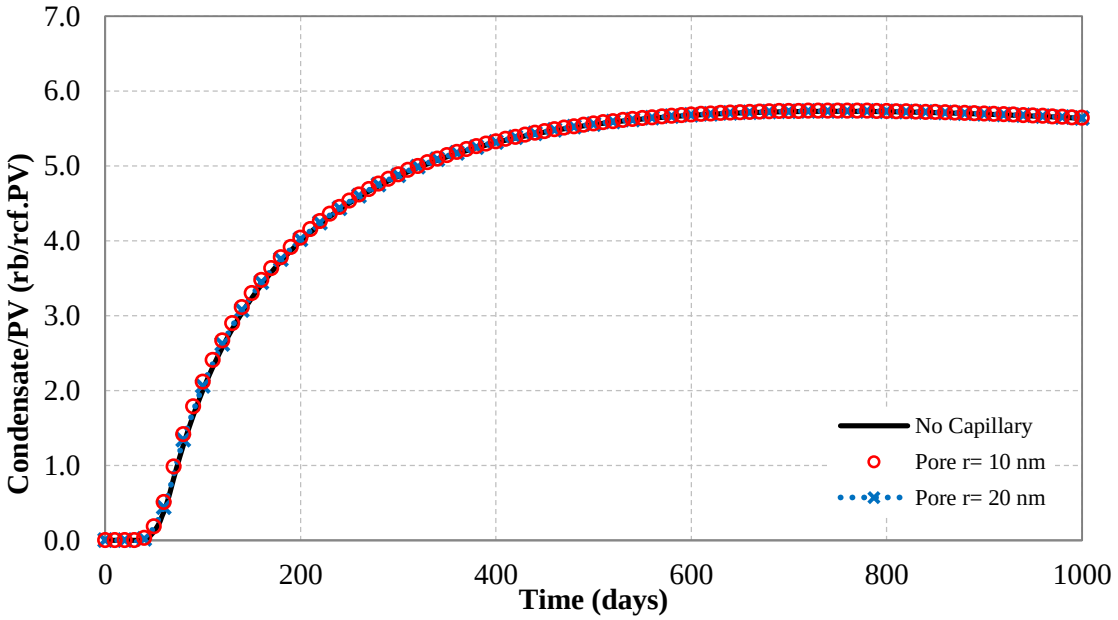


**Figure 8.15: Condensate at reservoir condition for methane-hexane (85%-15%) with capillary forces**

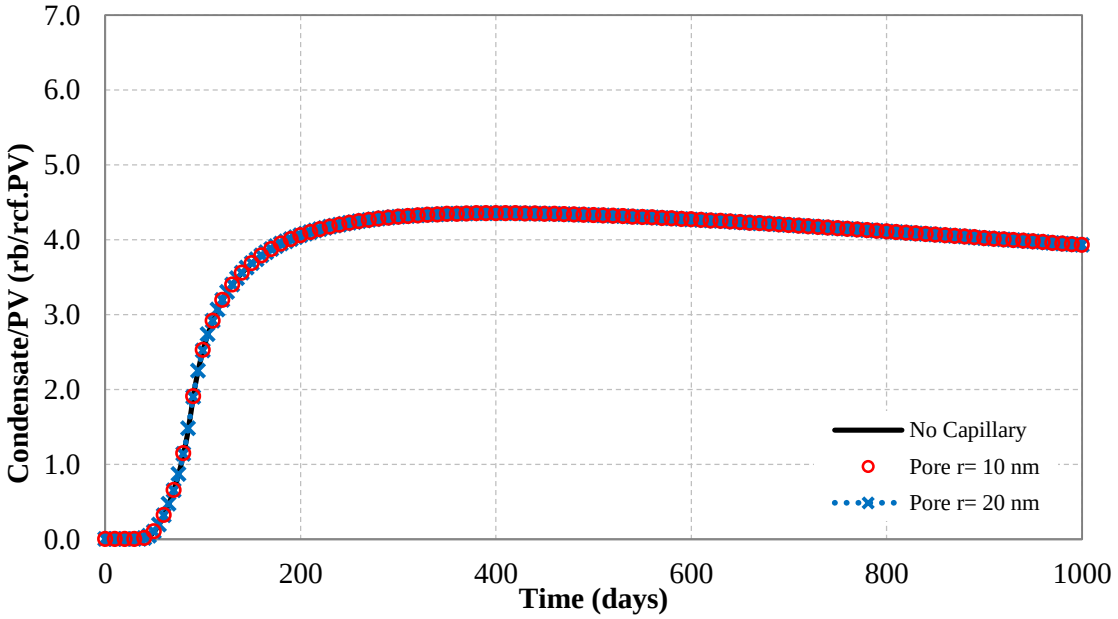


**Figure 8.16: Condensate at reservoir condition for methane-decane (70%-30%) with capillary forces**

During the production period of each case, performance data were collected and analyzed, which included gas and condensate surface production, cumulative productivities, and recovery factors. In order to assess the influence of capillary forces on the performance of the mixture methane-hexane (85%-15%), gas and condensate recoveries were examined closely. It is essential to evaluate the impact on recovery in order to understand the contribution of the matrix to production in nanopores, knowing that capillary forces will employ retention on the movement of fluids. As seen earlier, capillary pressure applied diminutive influences to increase the residence time of condensate, which is expected to impose resistance of the same power to impact productivity. For a better demonstration, instead of illustrating overlapping curves that have little difference to display, percent change was calculated in reference to the results that rendered the capillary forces null. Figure **8.17** and Figure **8.18** display percent change in gas and condensate recoveries using the positive-negative scale to indicate the influence of capillary pressure in nanopores. Eventually, both plots show decreases in recoveries, and the most significant loss is seen with the smallest pore radius. Although the reduction in recoveries does not exceed 1%, it is seen as an impact within the limited scale of influence that has been witnessed. Eventually, gas recovery was reduced due to the increase in flow resistance. The reduction in condensate recovery is owed to losing condensate to the formation, resulting from the elongated residence time of condensate.

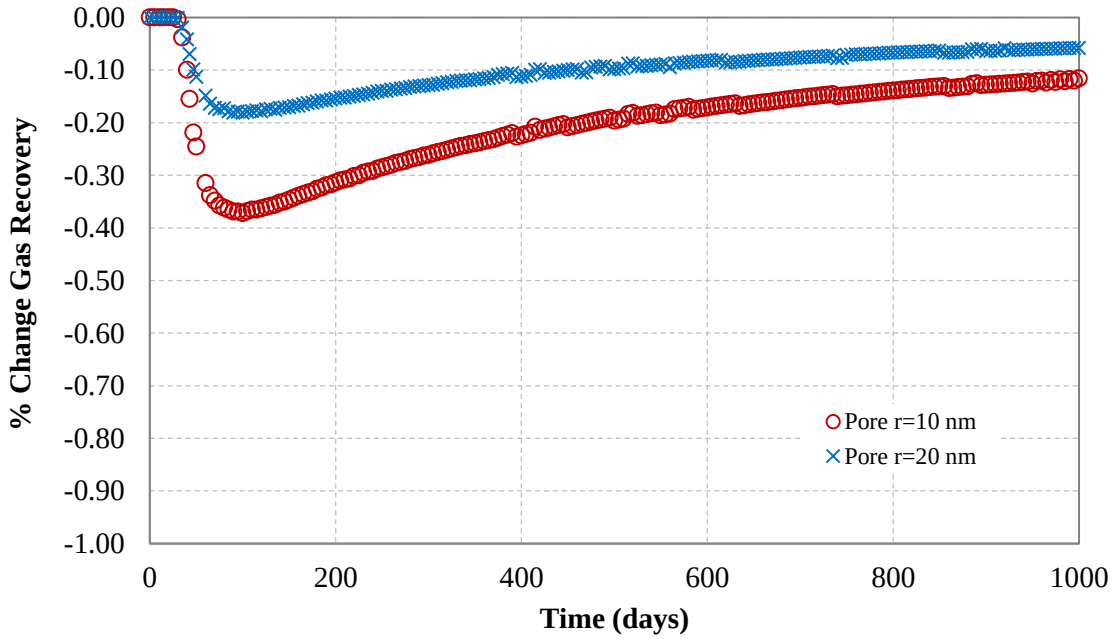


**Figure 8.17: Percent change in gas recovery for methane-hexane (85%-15%)**

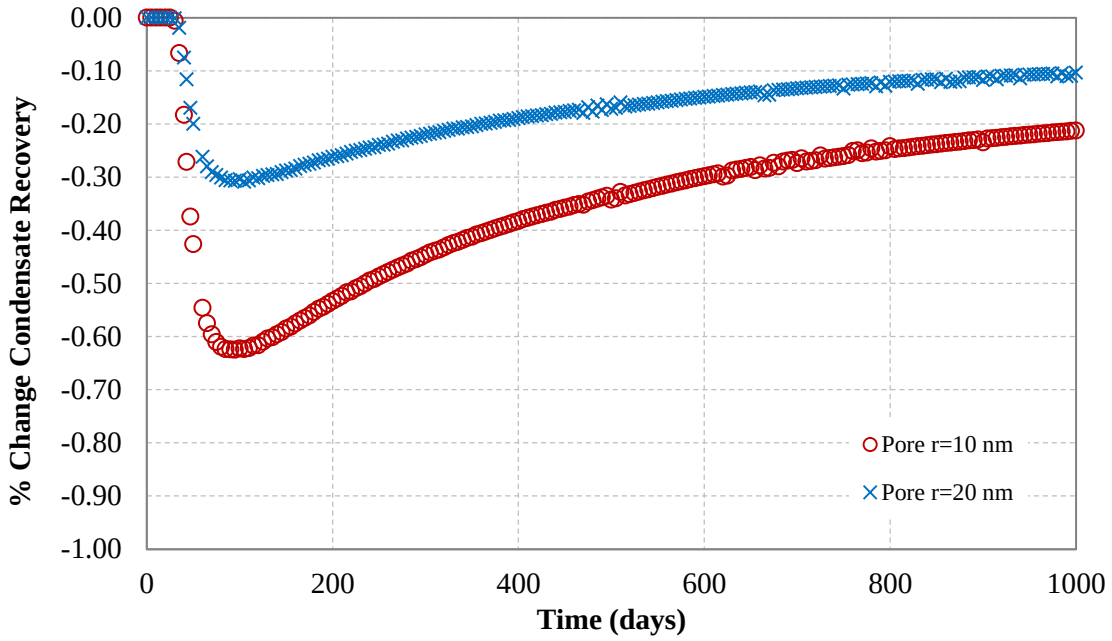


**Figure 8.18: Percent change in condensate recovery for methane-hexane (85%-15%)**

In reference to previous research work on studying the effect of capillary pressure on productivity, the results showed ineffective influence on recoveries (Al Ghamdi, 2009). Brooks and Corey's model was used to construct several capillary pressure curves that were inserted in the oil-gas relative permeability tables. The curves were generated using different distribution index values, which were employed to reflect interfacial tensions between rocks and fluids, grain sizes and distribution, and geometry of pore spaces. The results indicated that the accumulation of condensate appeared to progress on the sides of the block similarly with and without the inclusion of capillary pressure tables. Further analysis indicated insignificant influences on fluid distribution, movement, and recoveries.

However, this work indicates the existence of significant limitations in using fixed distribution index values, because it ignores the relationship between surface tension and the physical properties of fluids-in-place. This disadvantage makes the coupled phase behavior model with the capillary pressure equations (2.4) and (2.5) consistent with the fundamental relationship between cohesion forces and density. The question that remains to be answered: why were there opposing results on the performance of the oil-wet reservoir seen in the work of Nojabaei *et al.* (2014)?

### 8.3.1 Interfacial tension based on a fluid-dominant system

The changes in IFT are controlled by the changes in densities. Higher differences between liquid and gas densities lead to an increase in IFT. Near the critical point, where the bubble-point curve and dew-point curve interconnect, the physical properties of the liquid and gas are indistinguishable. Due to the similarity in the properties, the differences in densities are minimal which produce zero IFT values. Subsequently leading to no capillary pressure effect owing to the absence of the interface between the wetting and non-wetting phases. Away from the critical point, where the physical properties of the two phases are apart from each other, IFT values vary in magnitude. In addition, IFT values are highly dependent on the reservoir temperature, which classifies the system as gas-dominant or oil-dominant. The classification disassociates its dependency on the mixture's chromatography, but instead associated with reservoir temperatures that fall within the phase envelope spectrum. This classification is determined at the initial transition into the two-phase region during reservoir depletion. Capillary pressure and IFT have the highest values at the initial contact between the two immiscible fluids in contact with each other through an interface. This interface takes place on the upper and lower dew-point curve, and the bubble-point curves. The magnitude of IFT depends on the saturation point curve under study.

In gas-dominant systems, where the reservoir temperature falls between the critical point and the cricondentherm, condensate drops out at the upper dew-point curve, and the last droplet evaporates at the lower dew-point curve. It was learned from this research that the IFT values were the highest at the lower dew-point curve and lowest at the upper curve. This is a result of having higher density difference as the pressure reduces at a fixed temperature. Examining the influence of IFT on the dew-point curve indicated an increase in the upper dew-point pressure, and a decrease in the lower dew-point pressure. In contrast, the work of Nojabaei *et al.* (2013) was focused on oil-dominant systems, where the reservoir temperature is found to the left of the critical point. Their work agreed that IFT values become zero around the critical point, but suggested they increase toward lower temperatures. The increase in IFT values lead to decreasing the bubble-point pressure indicating more domination of the oil phase, and delay to the gas phase appearance. Investigating the magnitude of IFTs in oil and gas dominated systems

for a mixture containing methane-hexane (70%-30%), showed notable variances as shown by Figure **8.19.**

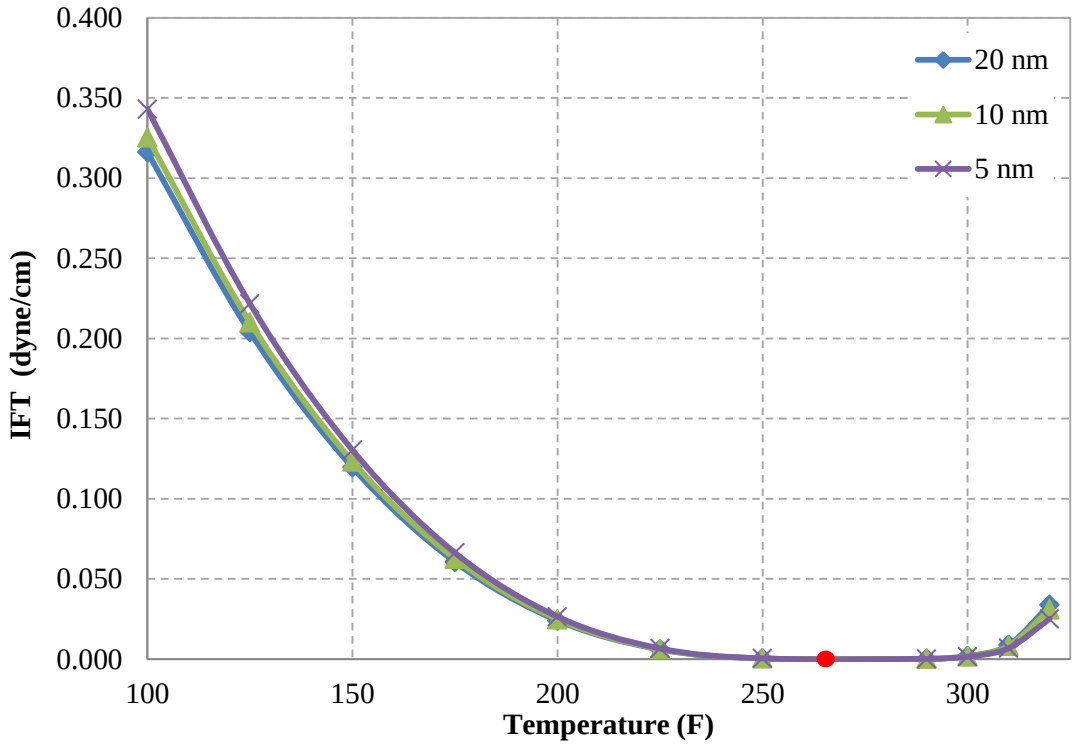


**Figure 8.19: IFT values at different temperatures for methane-hexane (70%-30%)**

Interfacial tension values were retrieved at temperatures to the right and left of the critical point. The values of IFT as the temperature extends toward the oil-dominant system at lower temperatures expand largely due to the increase in liquid density. In contrast, the changes in IFT toward higher temperatures in the gas-dominant system shows limited effect compared to those found in the oil side. The outcome of this exercise advocates lower impact of capillary pressure on the performance of gas reservoirs in comparison to oil reservoirs. Furthermore, an investigation on the sensitivity of nanopore sizes to the behavior of IFTs according to temperature was carried. Three nanopore sizes were used, 20, 10, and 5 nm. The overall behavior of IFTs at temperatures ranging between $100^{o}$ F to $320^{o}$ F showed little influence on the values of IFTs. Most of these values as illustrated by Figure **8.19** were in a close approximate of each other.

In order to justify the lower significance of the inclusion of capillary pressure on the performance of liquid-rich gas reservoirs in contrast to oil reservoirs, IFT values were examined closely. Two mixtures with moderate compositional combinations were selected for this study, methane-decane (70%-30%) and methane-hexane (70%-30%). More testing was done on the two mixtures with heavier concentration (60%-40%), but similar behavior was attained. A single reference temperature was placed at 150° F in the oil-dominant region for both mixtures, and several temperatures were tested in the gas-dominant side. Those temperatures in the gas-dominant system were selected with consideration of previous knowledge about the areas where IFT values were significant. Figure **8.20** shows the phase envelope and selected temperature for methane-decane (70%-30%). The temperatures selected in the gas-dominant region were 520° F, 530° F, 540° F, and 550° F. Similarly, Figure **8.21** illustrates the temperatures considered for methane-hexane which were 290° F, 300° F, 310° F, and 320° F. At the specified temperatures, IFT values were calculated at the saturation point, and the ratios of IFT's in the form of oil-to-gas were obtained for analysis.

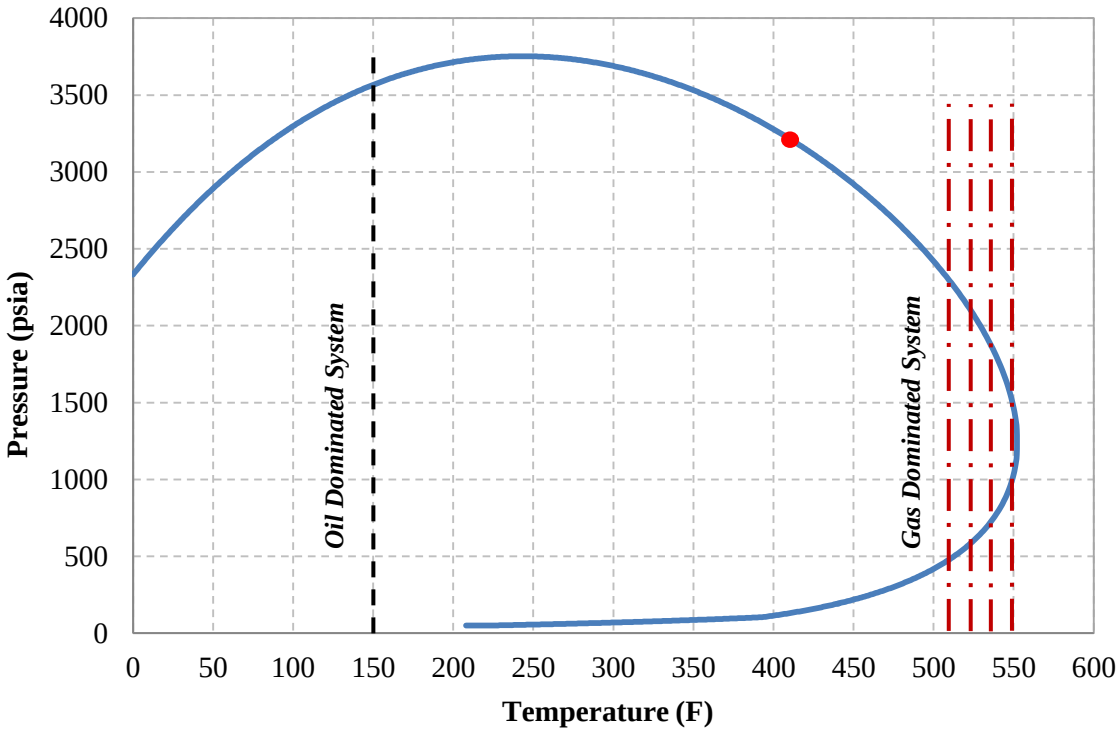


**Figure 8.20: Phase behavior for methane-decane (70%-30%)**

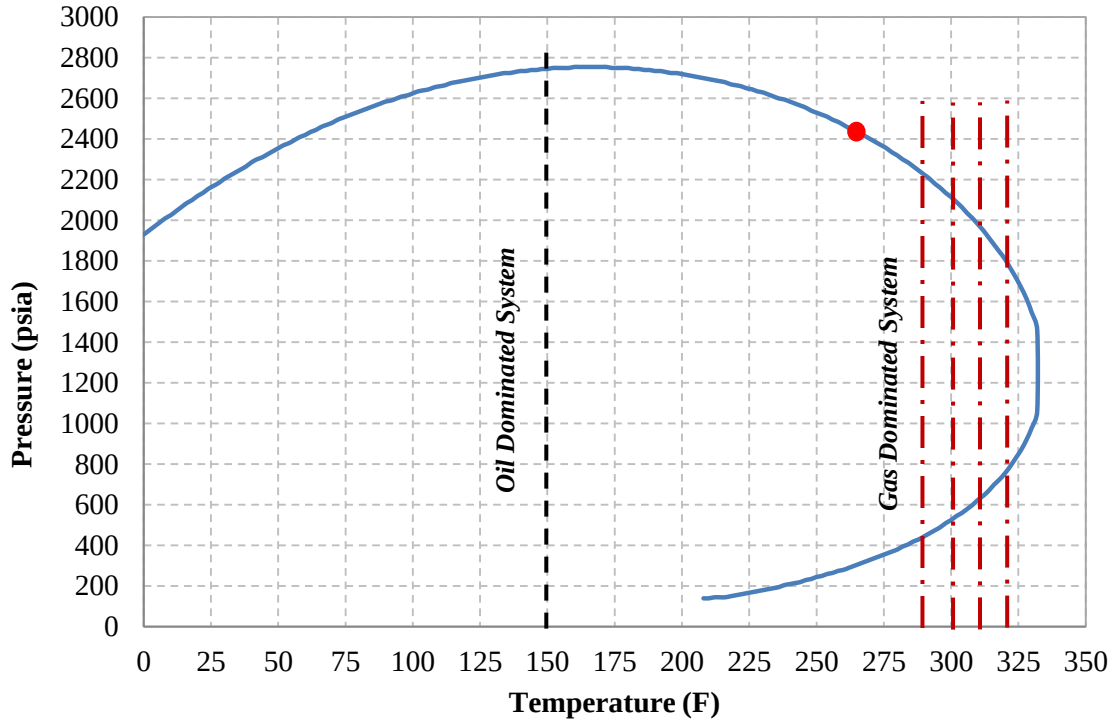


**Figure 8.21: Phase behavior for methane-hexane (70%-30%)**

Figure **8.22** presents an IFT ratio of oil-to-gas dominated systems for methane-decane (70%-30%) obtained at different pore sizes. In all of the cases, the IFT values for the oil dominated system are fixed. As the pore sizes become smaller, the IFT values in the gas system lessen, causing the IFT ratio to increase. The decrease in IFT values in the gas dominated system becomes vivid at lower temperatures, which approaches zero as the temperature descends toward the critical point. Furthermore, Figure **8.23** demonstrates the IFT ratio for methane-hexane (70%-30%) which mimics the same behavior seen with methane-decane. It can be seen that IFT ratios become very low at higher temperatures indicating higher IFT values in the gas region. However, reservoirs with temperatures closer to the cricondentherm contain less condensate, and fall under the classification of wet-gas reservoirs. Figure **8.24** shows the reduction in oil saturation at temperatures extending from the critical point toward the cricondentherm. Consequently, the temperatures selected for the simulated cases in this research were placed where adequate condensation is expected. In summary, Figure **8.22** and Figure **8.23** suggest that IFT values are more significant in oil dominated reservoirs than in gas reservoirs. As a result, the influence of IFT on the performance of liquid-rich gas reservoirs was less evident.

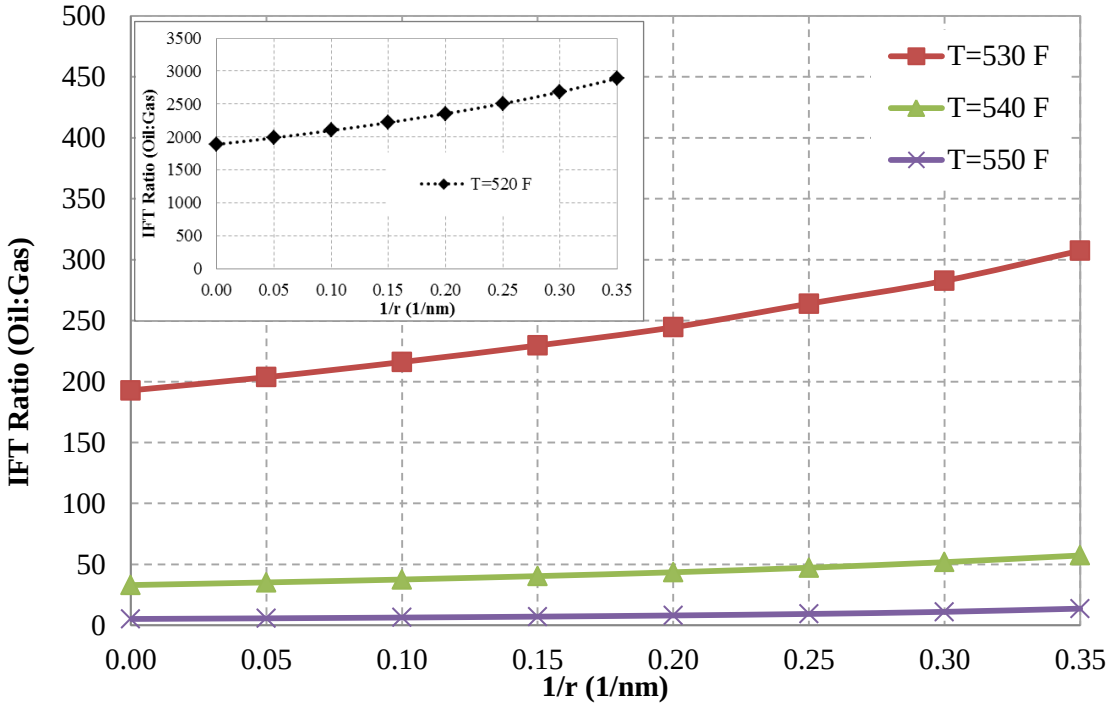


**Figure 8.22: IFT ratio of oil-gas dominated systems for methane-decane (70%-30%)**

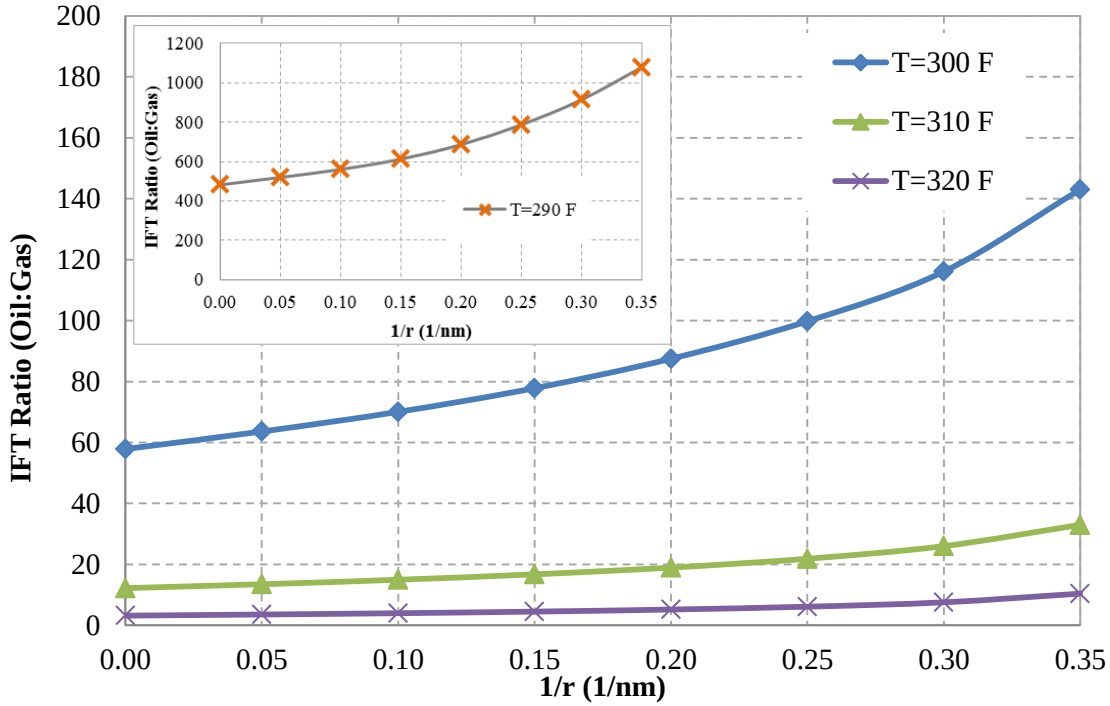


**Figure 8.23: IFT ratio of oil-gas dominated systems for methane-hexane (70%-30%)**

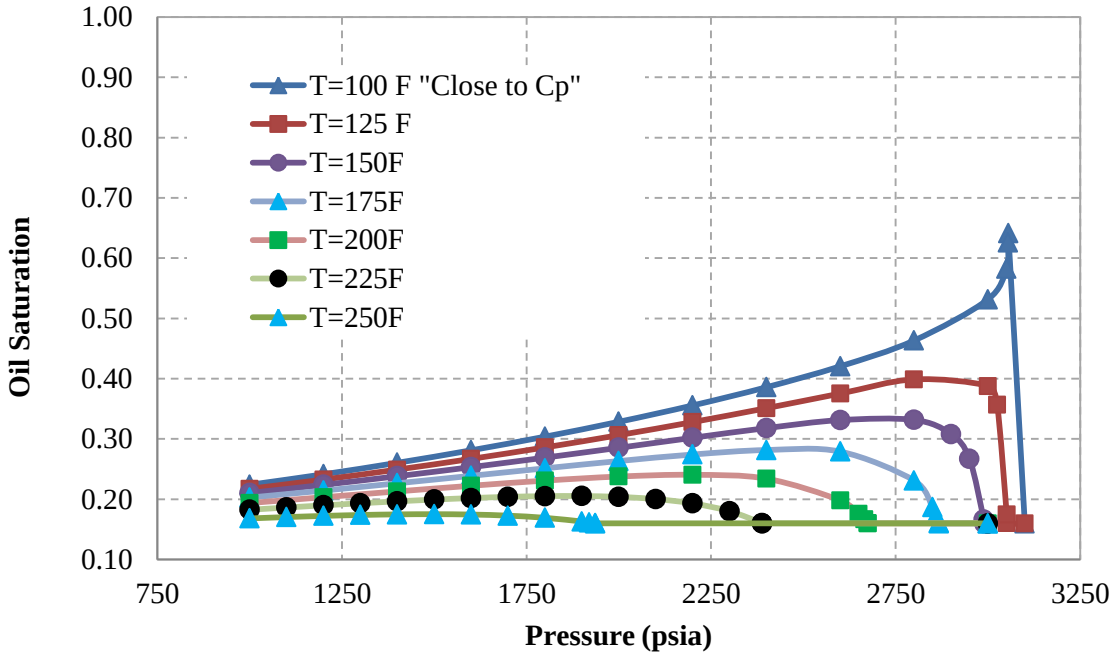


**Figure 8.24: Oil saturation versus pressure at different temperatures for methane-hexane (85%-15%)**

### 8.4 Influence of diffusion while activating capillary pressure inside nanopores

Diffusion was first introduced by Fick in 1855 to capture flow resulting from the exchange of matters through porous media. In 1986, Ertekin *et al.* introduced the concept of multi-mechanistic domains, where the fluids flow as a function of pressure and concentration gradients. Thus, allowing the gas to flow as per Darcy's law in pressure domains, and flows by diffusion under Fick's law when conductivity becomes an issue. This work continues to evaluate flow performance of unconventional phenomena in liquid-rich gas reservoirs such as the inclusion of diffusion while activating capillary forces. The study utilized the same grid system consisting of (22x22x1) with a quarter block representation of 11x11x1. Also, it examined the same combination of fluids used to explore the capillary forces' influence on flow behavior. Table **8.8**, Table **8.9**, and Table **8.10** show the different combinations of the three mixtures (light – moderate – heavy) that were simulated with the inclusion of capillary forces and diffusion. The simulation

time for each of the cases did not exceed 150 days, because the blocks near the fractures reached the specified flow pressure at the fractures due to the enhanced depletion behavior. The results of each run were collected and analyzed, which included reservoir pressure, saturation profile, condensate evolution, and flow performance.

**Table 8.8: Simulation cases for methane-butane with the inclusion of capillary forces and diffusion (t ≤ 150 days)**

| Case ID | Composition | Capillary Activated | Pore Radius (nm) | Diffusion (ft2/day) | CPU time (hrs) |
|---|---|---|---|---|---|
| C185C4NOPCDF10 | C1 = 0.85 , C4 = 0.15 | No | ∞ | 10 | 26 |
| C185C4R10DF10 | C1 = 0.85 , C4 = 0.15 | Yes | 10 | 10 | 29 |
| C185C4R20DF10 | C1 = 0.85 , C4 = 0.15 | Yes | 20 | 10 | 28 |
| C170C4NOPCDF10 | C1 = 0.70 , C4 = 0.30 | No | ∞ | 10 | 34 |
| C170C4R10DF10 | C1 = 0.70 , C4 = 0.30 | Yes | 10 | 10 | 42 |
| C170C4R20DF10 | C1 = 0.70 , C4 = 0.30 | Yes | 20 | 10 | 42 |
| C160C4NOPCDF10 | C1 = 0.60 , C4 = 0.40 | Yes | ∞ | 10 | 20 |
| C160C4R10DF10 | C1 = 0.60 , C4 = 0.40 | No | 10 | 10 | 34 |
| C160C4R20DF10 | C1 = 0.60 , C4 = 0.40 | Yes | 20 | 10 | 89 |

**Table 8.9: Simulation cases for methane-hexane with the inclusion of capillary forces and diffusion (t ≤ 150 days)**

| Case ID | Composition | Capillary Activated | Pore Radius (nm) | Diffusion (ft2/day) |
|---|---|---|---|---|
| C185C6NOPCDF10 | C1 = 0.85 , C6 = 0.15 | No | ∞ | 10 |
| C185C6R10DF10 | C1 = 0.85 , C6 = 0.15 | Yes | 10 | 10 |
| C185C6R20DF10 | C1 = 0.85 , C6 = 0.15 | Yes | 20 | 10 |
| C170C6NOPCDF10 | C1 = 0.70 , C6 = 0.30 | No | ∞ | 10 |
| C170C6R10DF10 | C1 = 0.70 , C6 = 0.30 | Yes | 10 | 10 |
| C170C6R20DF10 | C1 = 0.70 , C6 = 0.30 | Yes | 20 | 10 |
| C160C6NOPCDF10 | C1 = 0.60 , C6 = 0.40 | Yes | ∞ | 10 |
| C160C6R10DF10 | C1 = 0.60 , C6 = 0.40 | No | 10 | 10 |
| C160C6R20DF10 | C1 = 0.60 , C6 = 0.40 | Yes | 20 | 10 |

**Table 8.10: Simulation cases for methane-decane with the inclusion of capillary forces and diffusion (t ≤ 150 days)**

| Case ID | Composition | Capillary Activated | Pore Radius (nm) | Diffusion (ft2/day) |
|---|---|---|---|---|
| C185C10NOPCDF10 | C1 = 0.85 , C10 = 0.15 | No | ∞ | 10 |
| C185C10R10DF10 | C1 = 0.85 , C10 = 0.15 | Yes | 10 | 10 |
| C185C10R20DF10 | C1 = 0.85 , C10 = 0.15 | Yes | 20 | 10 |
| C170C10NOPCDF10 | C1 = 0.70 , C10 = 0.30 | No | ∞ | 10 |
| C170C10R10DF10 | C1 = 0.70 , C10 = 0.30 | Yes | 10 | 10 |
| C170C10R20DF10 | C1 = 0.70 , C10 = 0.30 | Yes | 20 | 10 |
| C160C10NOPCDF10 | C1 = 0.60 , C10 = 0.40 | Yes | ∞ | 10 |
| C160C10R10DF10 | C1 = 0.60 , C10 = 0.40 | No | 10 | 10 |
| C160C10R20DF10 | C1 = 0.60 , C10 = 0.40 | Yes | 20 | 10 |

In order to accommodate the continuity equation (A.9) with the diffusion velocity model, the total molar velocity needs to be redefined for oil and gas. Thus, the total molar velocity is expressed as the flow driven by the bulk Darcian effect ($v_{fs}^{D}$) added to the flow caused by the Flickian component ($v_{mfs}^{F}$). Since diffusion effect in the liquid phase has no significance on the flow of oil, the diffusion forces in the liquid phase are neglected (Ayala, 2004). Equations (8.1a) and (8.1b) demonstrate the velocity models for each phase.

$$v_{mos} = v_{os}^{D} \quad ; \quad s = x, y, \text{ and } z \qquad (8.1a)$$

$$v_{mgs} = v_{gs}^{D} + v_{mgs}^{F} \quad ; \quad s = x, y, \text{ and } z \qquad (8.1b)$$

where: $v_{fs}^{D} = -5.615 \frac{k_s k_{rf}}{\mu_f} \frac{\partial \Phi_f}{\partial s}$ ; $f = o$, or $g$ , $s = x, y$, and $z$ (8.1c)

and, $v_{gs}^{F} = -\phi S_g \frac{D_{eff}}{\bar{\rho}_g} \frac{\partial \bar{\rho}_g}{\partial s}$ ; $s = x, y$, and $z$ (8.1d)

By substituting the velocity terms into the continuity equation (A.9) and applying the same assumptions considered in the derivation presented in Appendix A, the following molar differential equation is achieved:

$$\frac{\partial}{\partial x}\left(x_m\bar{\rho}_o A_x \frac{k_x k_{ro}}{\mu_o}\frac{\partial \mathrm{p}_o}{\partial x} + y_m\bar{\rho}_g A_x \frac{k_x k_{rg}}{\mu_g}\frac{\partial \mathrm{p}_g}{\partial x} + y_m\phi S_g A_x \frac{D_{eff}}{5.615}\frac{\partial \bar{\rho}_g}{\partial x}\right)\Delta x$$
$$+\frac{\partial}{\partial y}\left(x_m\bar{\rho}_o A_y \frac{k_y k_{ro}}{\mu_o}\frac{\partial \mathrm{p}_o}{\partial y} + y_m\bar{\rho}_g A_y \frac{k_y k_{rg}}{\mu_g}\frac{\partial \mathrm{p}_g}{\partial y} + y_m\phi S_g A_y \frac{D_{eff}}{5.615}\frac{\partial \bar{\rho}_g}{\partial y}\right)\Delta y$$
$$+N_m = \frac{V_b}{5.615}\frac{\partial}{\partial t}\left[\phi\left(S_o x_m\bar{\rho}_o + S_g y_m\bar{\rho}_g\right)\right] \quad ; \quad m = 1, 2, \ldots, n_c \qquad (8.2)$$

In this work, the activation of capillary pressure showed relative increase in the thickness of condensate during the first 40 days of production prior to invading the majoring of the blocks. Subsequently, this imposed resistance for gas to flow and increased residence time of condensate. Thus, it is important to appraise flow behavior and contribution of the matrix to production knowing that diffusion will enhance recovery. Generally, diffusion is expected to improve the depletion behavior in nanopores, as it will be seen through the pressure and saturation profiles. Figure **8.25** suggests that the system containing the mixture methane-hexane with concentration of 85% and 15% is subjected to higher depletion with the inclusion of diffusion. It provides a comparison with the pressure profile while activating capillary forces using pore radius of 10 nm.

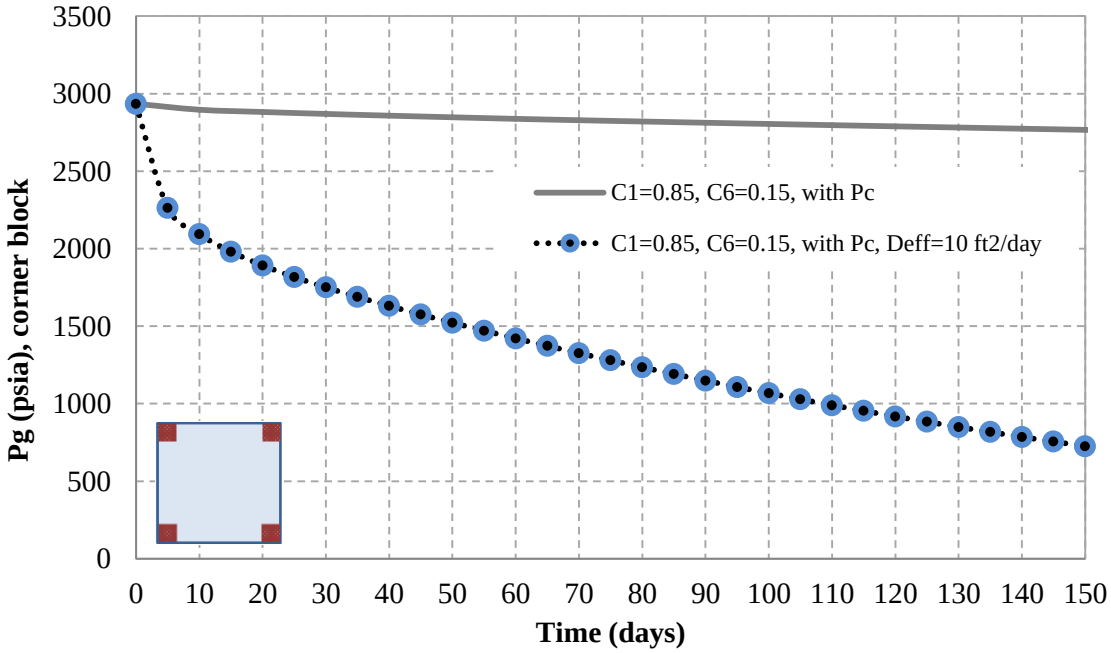


**Figure 8.25: Pressure at the corners for methane-hexane (85%-15%) with diffusion**

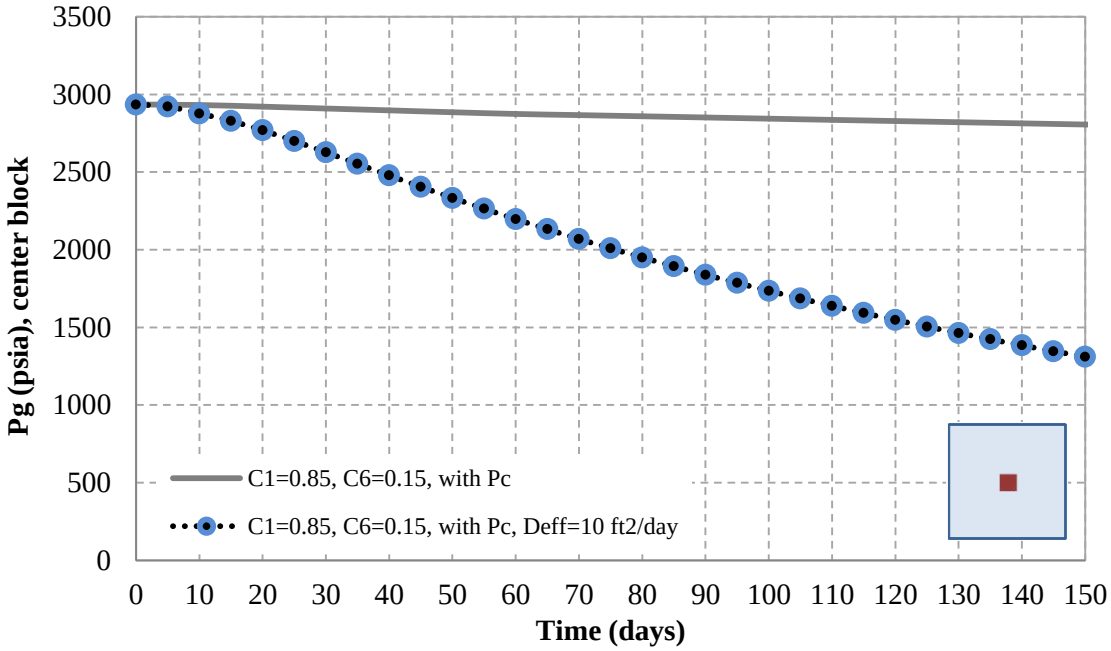


**Figure 8.26: Pressure at the center for methane-hexane (85%-15%) with diffusion**

The reservoir pressure profile captured at the corners of the matrix system shows a drop in pressure from the start of simulation indicating rapid fluid movement toward the fractures. Figure **8.26** indicates a delay in depletion enhancement toward the center of the block until condensate starts accumulating at 10 days. Capillary forces applied greater force at lower oil saturation, as studied earlier. Thus, the outcome indicates excessive influence of diffusion with the inclusion of capillary forces once condensate drops out in the system.

Condensate saturation profile is displayed by Figure **8.27** at different times, across the single-block system. The saturation profile at the corners and sides of the matrix experience higher evolution than the center of the block due to the enhancement in condensate evolution. Similar to the rest of the studied cases, diffusion advances the evolution of condensate at the neighboring blocks to the fractures. This capability had reduced the resistance applied on the stored gas at the inner part of the matrix from flowing toward the flow channels. Figure **8.28** presents an aerial view of condensate evolution and propagation from the edges of the block toward the center. Due to the rapid depletion behavior, the dew-point pressure was reached earlier in the life of the reservoir, which led to having a flush of condensate around 5 days. The thickness of the

condensation coating extended quicker to the sides and toward the center of the block in comparison to the profiles prior to the activation of diffusion. Condensate invasion is a function of the pressure of the individual blocks in the system. Once pressure declines toward the inner portion of the matrix, condensate invasion will immigrate to fully cover the inner portion of the matrix as shown at 30 days. Because of the enhanced evolution in condensate accumulation, condensation declined after reaching the maximum oil saturation. The continued depletion caused some of the condensate to re-vaporize, as shown at the edges of the matrix starting at 60 days.

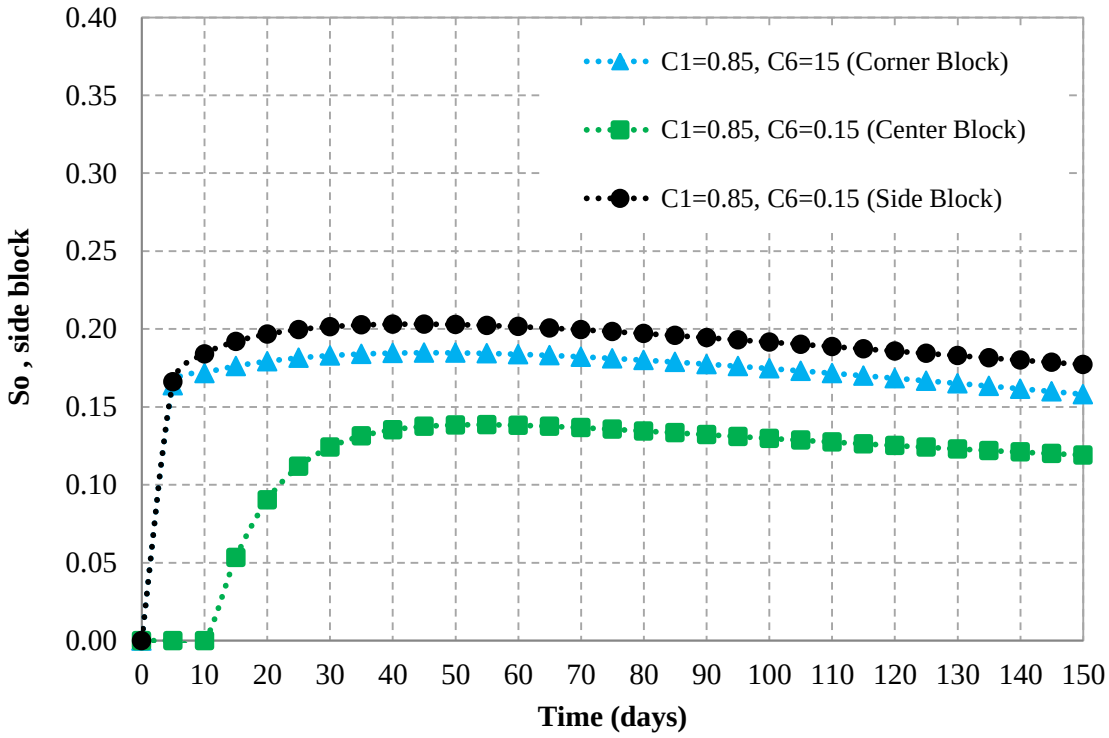


**Figure 8.27: Oil saturation profile for methane-hexane (85%-15%) with diffusion**

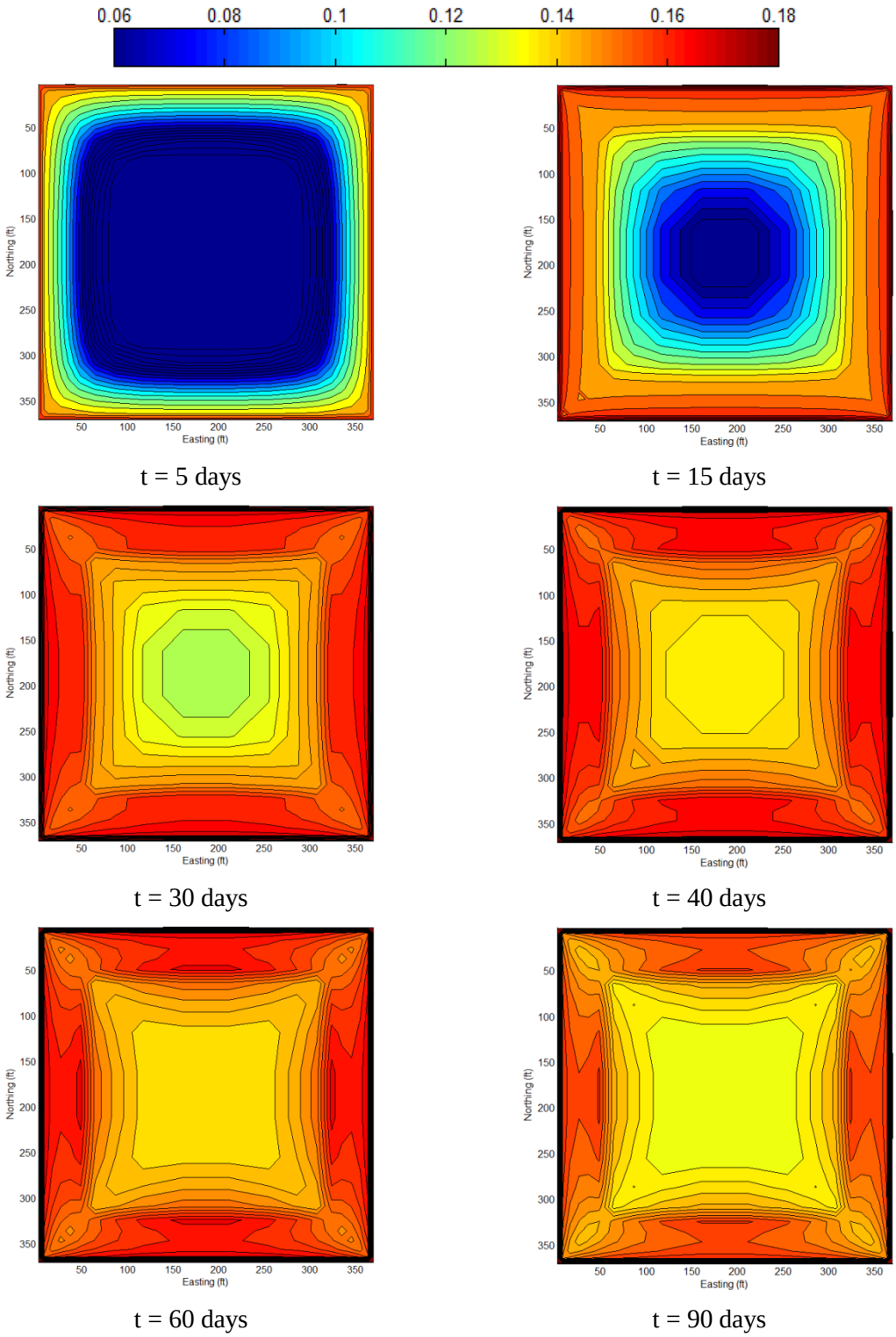


**Figure 8.28: Condensate evolution for methane-hexane (85%-15%) with diffusion**

Figure **8.29**, Figure **8.30**, and Figure **8.31** demonstrate condensate at reservoir conditions for the three mixtures at different concentrations. Each plot demonstrates the influence of diffusion with capillary forces. Certainly, diffusion shows great domination on reservoir performance over the Darcian flow mechanism. Diffusion enhanced the withdrawal of fluids, which subsequently expedited condensate evolution over time. In this study, a diffusion coefficient of 10 $ft^2$/day was used. Although it is considered high, the aim was to demonstrate the influence of diffusion on the flow of fluids that are subjected to capillary forces. Ayala (2004) demonstrated similar influence of condensate evolution with various diffusion coefficients. The degree of freedom for the trapped gas in the inner portion of the matrix to flow increased with the increase in diffusion coefficient. In the identified plots, Figure **8.29**, Figure **8.30**, and Figure **8.31**, it can be seen that the appearance of condensate came at the start of simulation, indicating enough drop-out in reservoir pressure. It is worth mentioning that the initial reservoir pressure was given an arbitrary value for each of the cases to shorten the reservoir life cycle. The goal was to zoom in to the region closest to saturation pressure, where capillary forces are expected to be the highest. The condensate content at reservoir conditions depends on the binary mixture and concentration as seen in Section 8.3. Due to the larger withdrawal carried by diffusion, the condensate content reached the maximum before condensate dropout for the cases using Darcy's law only. Eventually, expedited evolution of condensate led to earlier re-vaporization, as witnessed in all three cases.

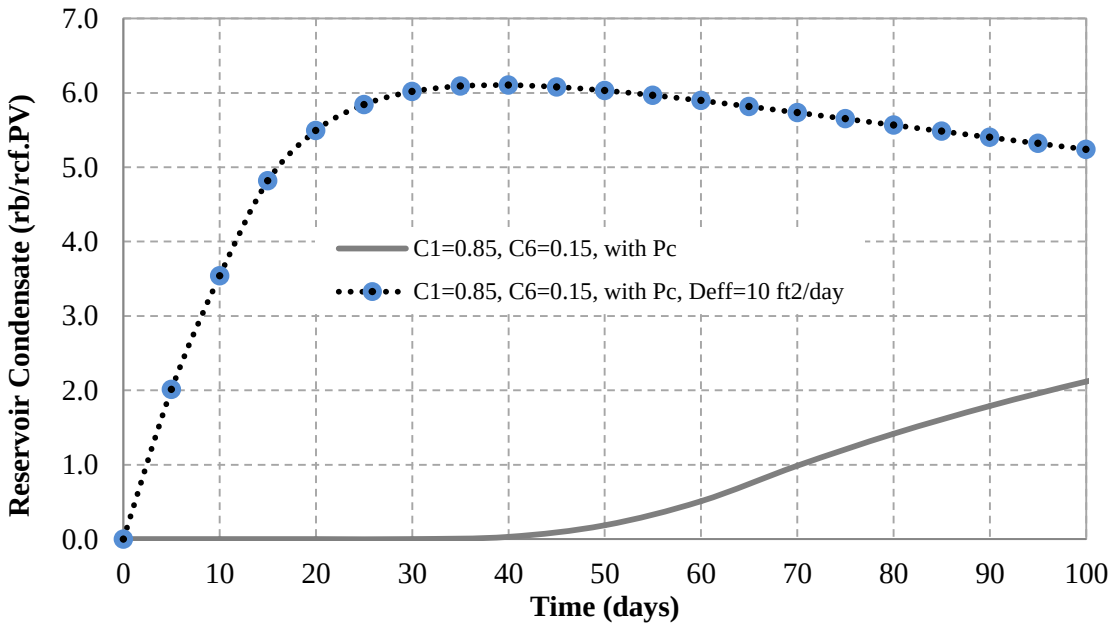


**Figure 8.29: Condensate at reservoir for methane-hexane (85%-15%) with diffusion**

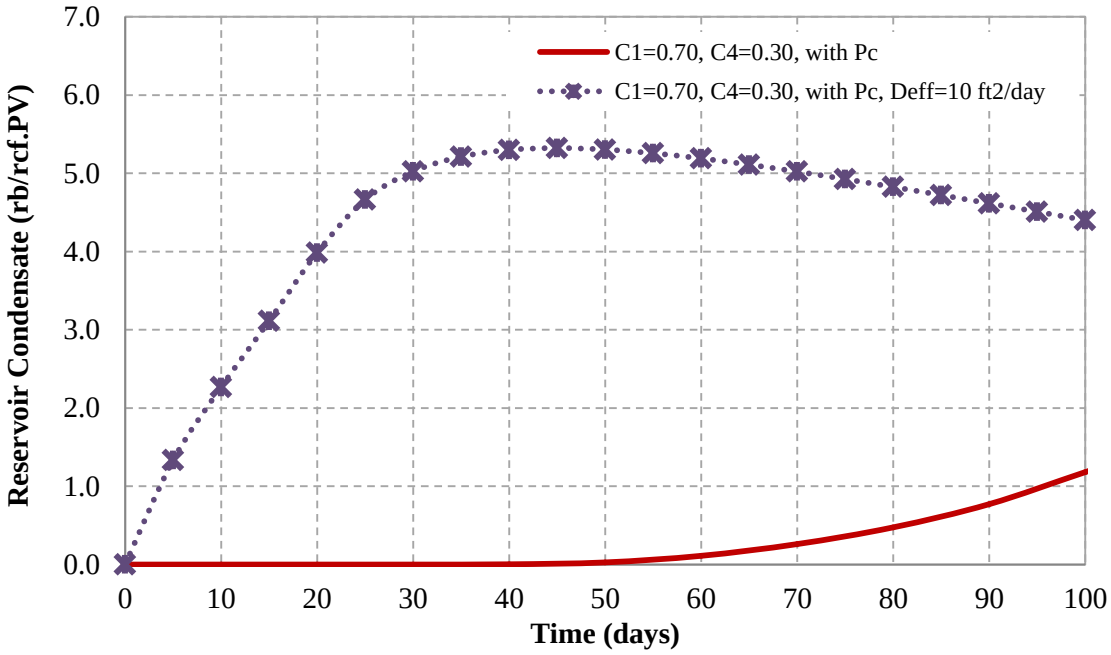


**Figure 8.30: Condensate at reservoir for methane-butane (70%-30%) with diffusion**

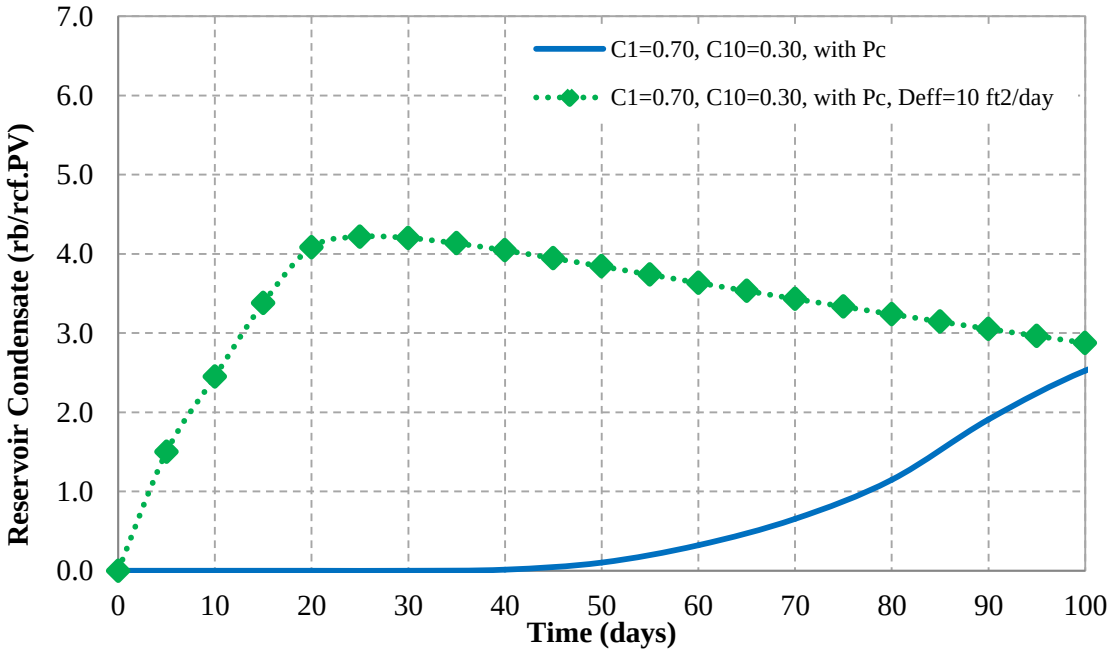


**Figure 8.31: Condensate at reservoir for methane-decane (70%-30%) with diffusion**

The predicted depletion behavior associated with activating diffusion enhanced recoveries for all the mixtures studied. Figure **8.32** and Figure **8.33** display the gas and condensate recovery obtained from the numerical study using the compositional combinations that presented the highest condensate at reservoir conditions. The gas recovery of the moderate fluid came to be the highest because of diffusion domination. Since the mixture methane-hexane (85%-15%) reflected higher reservoir condensation, it indicates severe impairment to the gas flow under pressure gradient. Once diffusion was activated, flowing under concentration gradient became a prominent factor leading to additional gas extractions. Gas recovery for the moderate, light and heavy mixtures with diffusion were determined to be 49.48%, 45.98%, and 43.17%, respectively. Figure **8.33** displays the condensate recovery for the same mixtures above. Methane-decane produced higher condensate recovery than the moderate mixture because it is the least volatile mixture. The heavy and moderate mixtures turned in condensate recovery of 29.76% and 20.15%, while, methane-butane continued to show the least amount of condensate at surface conditions. The recovery of liquid-rich gas in tight formations was improved with the activation of the multi-mechanistic flow to account for additional extractions that are able to flow in the concentration gradient domain.

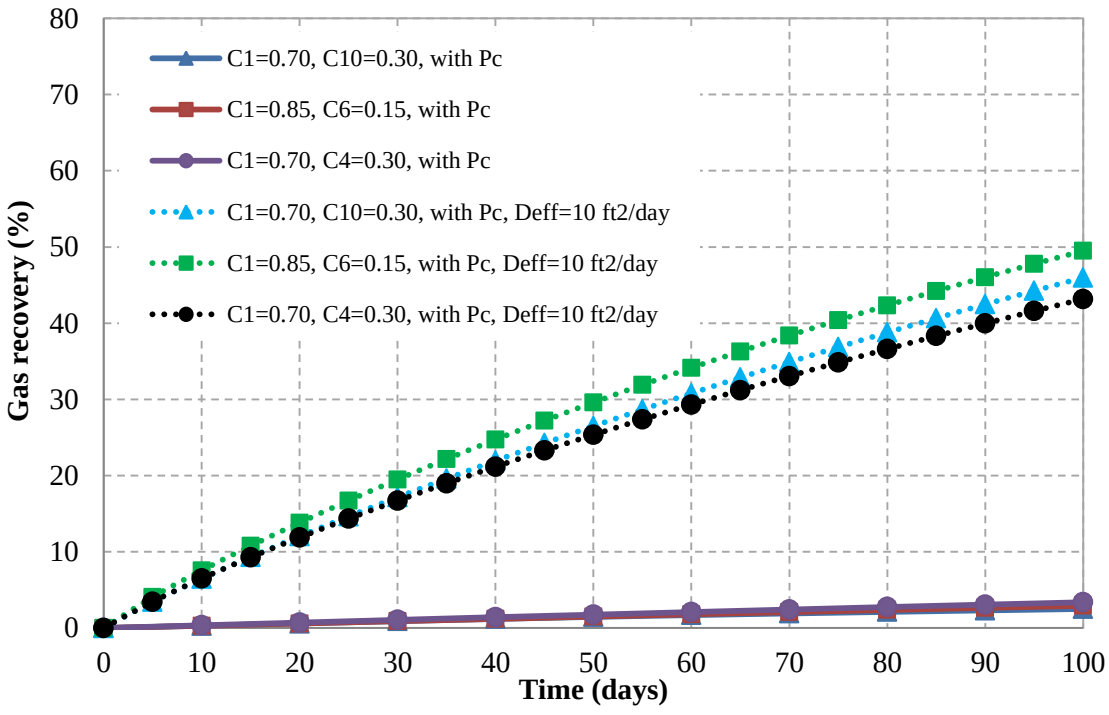


**Figure 8.32: Gas recovery improvement with diffusion**

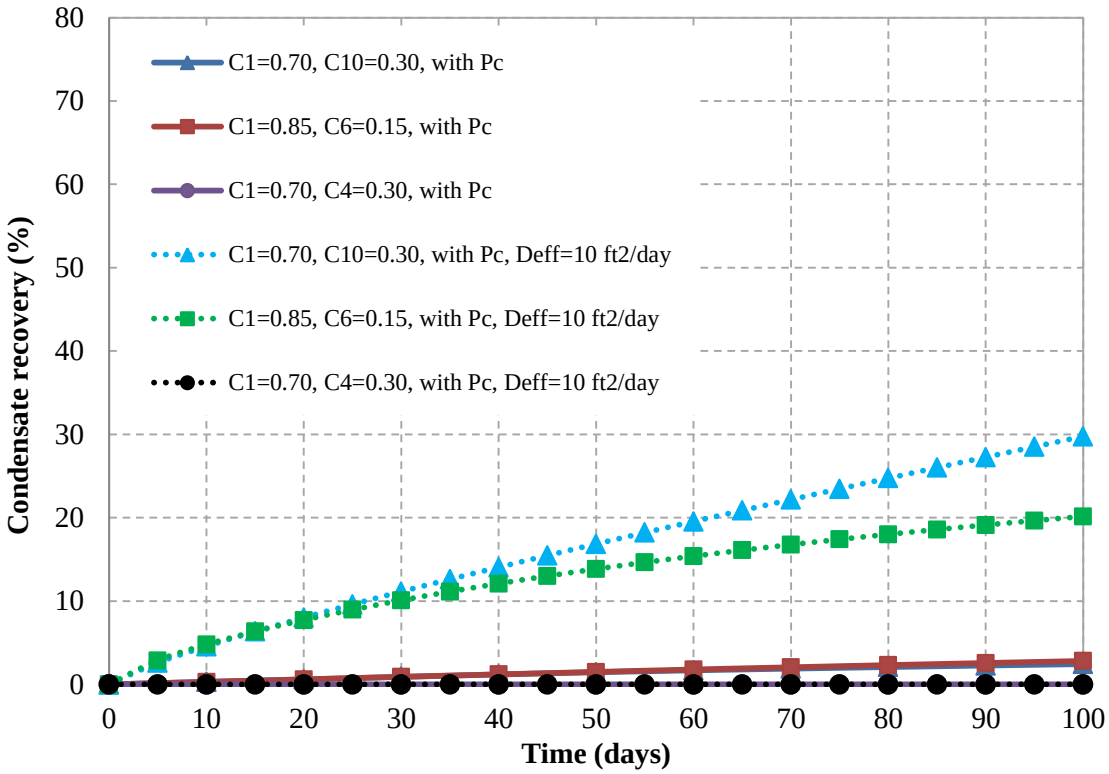


**Figure 8.33: Condensate recovery improvement with diffusion**

# Chapter 9

# CONCLUSION AND RECOMMENDATION

## 9.1 Concluding remarks

The hosting environment of the fluid-in-place carried an additional complexity to the overall performance of the reservoir. Fractured tight systems presented the reservoir as two continuums, a storage for the fluids-in-place, and a network of fractures representing the flow channels. For liquid-rich gas systems, higher permeability channels provided a sink of low pressure allowing the flow to move from the inner part of the matrix toward the fractures. As depletion progressed, condensate formed on the edges of the matrix blocks and propagated toward the inner portion of the matrix, which hindered the flow of the gas. In this study, the behavior of naturally fractured liquid-rich gas reservoirs was addressed using a developed in-house compositional simulator to examine unconventional phenomena such as capillary forces and multi-mechanistic flow. The model was equipped with a developed phase behavior model coupled with a capillary pressure equation. The inclusion of capillary pressure in the phase behavior model allows for vapor-liquid equilibrium flash according to the phase pressure.

An in-house model was developed and validated against commercial software developed by the Computer Modeling Group (CMG). The accuracy of the in-house simulator was proven by presenting the results using aerial overview of properties, and capturing well performance through x-y plots. All the results showed acceptable matches which assured the consistency of the in-house simulator. Furthermore, the validity of the coupled phase behavior model with a capillary equation was examined by reproducing the results generated by Nojabaei *et al.* (2013). Results have been generated across a variety of pore size radiuses, including capillary pressure, dew-point pressure differences, and interfacial tensions. The initial guess of $p_{gi}^{(n)}$ to the calculations of capillary pressure, IFT, and dew-point pressure reflected noticeable differences for the lower dew-point pressure as the pore sizes reduced. An increase of 100 psia in the initial guess of the two-phase pressure increased capillary pressure by 41%. More importantly, trivial changes in capillary pressure were captured at the upper dew-point pressure.

Several sets of composition combinations had been used for the analysis of the capillary pressure effect on dew-point in nanopores. The relationships developed showed an increase in capillary pressure with smaller pore sizes. Capillary pressure increased with smaller pore sizes for the upper and lower dew-point pressures. Evidently, higher changes in interfacial tensions were associated with higher capillary forces. However, the trend of interfacial tensions was decreasing with decreasing pore sizes for the upper dew-point, and increasing for the lower dew-point curve. As a result, the upper dew-point pressure increased as the interfacial tension decreased, and decreased as IFT increased for the lower dew-point pressures. Optimally, it is better to relate dew-point behavior to IFT instead of capillary pressure behavior. Thus, dew-point pressure was found to have an inverse proportionality to interfacial tensions. Capillary forces' magnitudes depended on composition combinations and concentrations. Among the three combinations for light, moderate and heavy mixtures, methane-hexane and methane-butane delivered the highest capillary pressures with concentration of 85% and 15%. Whereas, the mixtures with concentrations of 60% volatile and 40% non-volatile recorded the least capillary pressures.

The influence of capillary forces on the flow behavior of liquid-rich gas reservoirs was explored to assess flow resistance, condensate evolution, and performance. The analysis focused on the behavior of a fractured liquid-rich gas reservoir with capillary pressure resulting from using 10 nm and 20 nm pore radiuses. Overall, the outcome indicated minuscule effects of capillary forces on reservoir pressure, oil saturation, and productivity. Magnifying the influence of capillary forces using methane-hexane (85%-15%) with 10 nm pore radius showed enhanced condensate spread. Condensate had invaded 44% of the blocks in comparison to 23% without activating capillary pressure by 40 days. Once condensate reached the inner portion of the block, the spread evolution becomes negligible. Furthermore, the capillary forces employed limited retention on productivity. The least pore radius recorded a decrease in recoveries by a magnitude of less than 1%. Thus, diminutive influences were witnessed to increase the residence time of condensate and impose resistance to impact productivity.

The insignificance of the inclusion of capillary pressure on the performance of liquid-rich gas reservoirs in contrast to oil reservoirs was found to be highly dependent on IFT values. Investigating IFT values from an oil dominated system against IFT values from a gas dominated system showed significant variances. Interfacial tensions recorded the lowest values in a gas dominated system, and the highest in an oil dominated system. This was due to having lower

density differences in the gas side than in the oil side of the phase envelope. The decrease in IFT values in the gas dominated system becomes apparent at lower temperatures toward the critical point, and higher closer to the cricondentherm. In all the cases, IFTs in the oil side recorded the highest values, suggesting that IFT values are more significant in the oil dominated reservoirs than in gas reservoirs.

Depletion behavior associated with activating diffusion enhanced condensation evolution and recoveries for all the mixtures. Diffusion reduced the resistance applied against the flow of gas toward the flow channels, which excessively enhanced the depletion behavior. In addition, larger withdrawal was witnessed for both phases due to the domination of the diffusion mechanism over Darcy's law. Gas recoveries for all the mixtures reflected notable increases because of diffusion domination. Mixture with the least volatile concentrations recorded higher condensate recoveries. The improved performance is owed to the activation of the multi-mechanistic flow to account for additional recoveries that are unable to be extracted under the Darcy's law pressure gradient.

### 9.2 Recommendation

The variation of reservoir fluid distribution can be caused by many factors: production scheme, diffusion gradient, permeability, wettability conditions, and relative permeabilities. It is highly recommended for future work to apply the same testing conditions using different matrix permeabilities, as used in this study. Applying different matrix permeabilities might magnify the effect of capillary forces on the distribution of fluids, which is believed to have a great relevance in the form of residence time and resistance to flow. Altering wettability conditions is believed to increase the thickness of condensate, and subsequently impose higher resistance for gas to flow. With more condensate attached to the grains, the likelihood of losing more heavies to the formation is present. Condensate would trap more gas inside the matrix for longer periods of time. Thus, it is important to monitor the thickness and spread of condensate toward the inner part of the single-block.

Most importantly is to enhance the capability of the in-house compositional simulator to account for 3D representation of the single-block. This will enhance the accuracy in capturing the same performance with a reduced number of blocks. Numerical difficulties were witnessed in the discretization study because of using a 2D representation with non-uniform gridding. This is due to having a fixed thickness that can become larger than the length of the block, which sometimes disturbs the movement of flow, causing some of the properties to become negative. In addition, increasing the refinement of the blocks with a 3D representation will make the study become independent of the sizes of the blocks.

In order to support the validity of the coupled phase behavior model, additional insight is needed to initiate capillary pressure calculations. Selecting the right $p_{gi}^{(n)}$ was associated with difficulty due to the sensitivity of PBM to the values of capillary pressure. Certain locations inside the phase envelope stalled the performance of PBM, while other locations returned negative values for the vapor molar fraction. Solving these issues was done manually in this study depending on the mixture used. However, it is important to eliminate this deficiency for future use with complex mixtures. In addition, laboratory investigation is suggested using methane-butane (85%-15%) at $100^{o}$F to prove the accuracy and sensitivity of the generated coupled phase behavior model. Further examination on rescaling capillary pressures and interfacial tensions to match laboratory data are necessary to enhance the coupling of the model.

# BIBLIOGRAPHY

Abaa, K., Wang, J. Y., Ityokumbul, M. T.: *Parametric Study of Fracture Treatment Parameters for UltraTight Gas Reservoirs*. Paper SPE 152877 Presented at the Americas Unconventional Resources Conference held in Pittsburgh, Pennsylvania, USA, 5-7 June 2012.

Ahmed, Tarek H.: *Reservoir Engineering Handbook*, second edition, Gulf Professional Publishing Co, ISBN 0-88415-770-9, 2000.

Ayala, Luis F.: *Compositional Modeling of Naturally-Fractured Gas-Condensate Reservoirs in Multi-mechanistic Flow Domains*. PhD Dissertation, The Pennsylvania State University, 2004.

Ayala, L.F., Ertekin, T., and Adewumi, M.: *Analysis of Recovery Mechanisms for Naturally Fractured Gas-Condensate Reservoirs*, paper SPE 90010 presented at the SPE Annual Technical Conference and Exhibition held in Houston, TX, 26-29 September 2004.

Ayala, L.F., Ertekin, T., and Adewumi, M.: *Compositional Modeling of Naturally-Fractured Gas-Condensate Reservoirs in Multi-mechanistic Flow Domains*, *SPEJ* **11** (4): 480-487, 2006

Ayala, L.F., Ertekin, T., and Adewumi, M.: *Numerical analysis of multi-mechanistic flow effects in naturally fractured gas-condensate systems*. *J. Pet. Sci. Eng.* **58** (1-2): 13-29, 2007.

Ayyalasomayajula, P., Silpngarmlers, L., Berroteran, J., Sheffield, J., and Kamath, J.: *Measurement of Relevant Gas Condensate relative Permeability Data for Well Deliverability Predictions for a Deep Marine Sandstone Reservoir*, paper SCA2003-33 presented at the 2003 SCA International Symposium, Pau, France, 22-25 September 2003.

Al Ghamdi, B. N.: *Analysis of Capillary Pressure and Relative Permeability Effects on the Productivity of Naturally Fractured Gas-Condensate Reservoirs*. M.Sc. Thesis. The Pennsylvania State U., University Park, Pennsylvania, 2009.

Boom, W., Wit, K., Zeelenberg, J.W., Weeda, H.C., and Maas, J.G.: *On the Use of Model Experiments for Assessing Improved Gas-Condensate Mobility Under Near-Wellbore Flow Conditions*, paper SPE 36714 presented at the SPE ATCE, Denver, Colorado, 6-9 October 1996.

Coats, K. H.: *An Equation of State Compositional Model*, paper SPE 8284, SPE Journal, p. 533-554, December 1980.

Coats, K. H.: *Reservoir Simulation: State of the Art*, paper SPE 10020, 11927, and 12290, Journal of Petroleum Technology, p. 1633-1642, August 1982.

Coats, K. H.: *Simulation of Gas Condensate Reservoir Performance*, SPE Journal *JPT*, p. 1870-1886, October 1985.

Chopra, A. K., and Carter, Robert D.: *Proof of the Two-Phase Steady-State Theory for Flow Through Porous Media*, paper SPE 14472, SPE Journal, p. 603-608, December 1986.

Corey, A. T.: *The Interrelation between Gas and Oil Relative Permeabilities*, Prod. Monthly, 19, 38, November 1954.

Craft, B.C., and Hawkins, M.: *Applied Petroleum Reservoir Engineering*, second edition, Prentice Hall, Inc., 1991.

Danesh, A.: *PVT and Phase Behavior of Petroleum Reservoir Fluids*, Elsevier Publishing Co., 1998.

Danesh, A*: PVT and Phase Behavior of Petroleum Reservoir Fluids*, Elsevier, 2001.

Ellis, C. P.: *Ethyl Palmitate. Its Density, Surface Tension, Parachor, and Eötvös–Ramsay–Shields Coefficient*, J. Chem. Soc. p.1697-1699, 1932

Ertekin, T., King, G., and Schwerer, F.: *Dynamic Gas Slippage: A Unique Dual Mechanism Approach to the Flow of Gas in Tight Formations*, SPE Paper 12045, SPE Formation Evaluation, p. 43-52, February 1986.

Ertekin, T., Abou-Kassem, J. H., King, G. R.: *Basic Applied Reservoir Simulation*, SPE Textbook Series volume 7, Henry L. Doherty Memorial Fund of AIME, Richardson, TX, ISBN 1-55563-089-8, 2001.

Fan, Li, Harris, Billy W., Jamaluddin, A., Mott, Robert, Pope, Gary A., Shandrygin, Alexander, Whitson, Curtis H.: *Understanding Gas-Condensate Reservoirs*, Schlumberger Oil Field Review, p. 14-27, Winter 2005/2006.

Fevang, O., and Whitson, C. H.: *Modeling Gas-Condensate Well Deliverability*, SPE Paper 30714, SPE Journal, p. 221-230, November 1996.

Fevang, O., Singh, K., and Whitson, C. H.: *Guidelines for Choosing Compositional and Black-Oil Models for Volatile Oil and Gas-Condensate Reservoirs*, paper SPE 63087 presented at the 2000 SPE Annual Technical Conference and Exhibition held in Dallas, Texas, 1-4 October 2000.

Fick, A.: *Über Diffusion*. Annalen der Physik, 170 (1855) 59-86.

Gang, Tao, and Kelkar, Mohan: *A More General Capillary Pressure Curve and its Estimation from Production Data*, paper SPE 108180 presented at the SPE Rocky Mountain Oil & Gas Technology Symposium held in Denver, Colorado, April 2007.

Hepguler, G. , and Bard, W.: *Integration of a Field Surface and Production Network With a Reservoir Simulator*, paper SPE 38937, SPE Computer Application Journal, p. 80-92, June 1997.

Holditch SA: *Tight Gas Sands*, paper SPE 103356, Distinguished Author Series, 2006.

Hinchman, S.B. and Barree, R.D.: *Productivity loss in gas condensate reservoirs*, paper SPE 14203, doi:10.2118/14203-MS, January 1985.

Hilyard, Joseph: *The Oil & Gas Industry*. PennWell Publication Co., 2012.

Jossi, J. A., Stiel, L. I., and Thodos, G.: *The viscosity of pure substances in the dense gaseous and liquid phases*, AlChE Jour. **8**, 59. 1962.

Kazemi, H., Vestal, C. R., and Shank, G.D.: *An Efficient Multi-component Numerical Simulator*, paper SPE 6890, SPE Journal, p. 355-368, October 1978.

Kumar, S.: *Gas Production Engineering*. Houston: Gulf Pub. Co., Book Division, 1987.

Leverett, M. C.: *Capillary Behavior in Porous Solids*, Trans. AIME v. 142, p. 152-168, 1941.

Li, Kewen: *Generalized Capillary Pressure and Relative Permeability Model Inferred from Fractal Characterization of Porous Media*, paper SPE 89874 presented at the SPE Annual Technical Conference and Exhibition held in Houston, Texas, September 2004.

Li, Kewen: *Theoretical Development of the Brooks-Corey Capillary Pressure Model from Fractal Modeling of Porous Media*, paper SPE 89429 presented at the 2004 SPE/DOE Fourteenth Symposium on Improved Oil Recovery held in Tulsa, Oklahoma, April 2004.

Lohrenz, J., Bray, B.G., Clark, C.R.: *Calculating Viscosities of Reservoir Fluids from their compositions*, SPE Paper 915, Journal of Petroleum Technology, p. 1171-1176, 1964.

Macleod, D. B.: *On a Relation Between Surface Tension and Density*, Trans. Faraday Soc., v.**19**, p.38-41, 1923.

McCain, W. D. Jr.: *Chemical Composition Determines Behavior of Reservoir Fluids*, Petroleum Engineer International, p. 18-25, September 1993.

McCain, W. D. Jr.: *Revised Gas-Oil Ratio Criteria key Indicators of Reservoir Fluid Type*, Petroleum Engineering. Intl., p. 57-60, 1994.

Michelsen, M.: *The Isothermal Flash Problem. Part I. Stability. Fluid Phase Equilibria*, v. 9, p. 1-19, 1982.

Mott, Robert, Cable, Andrew, and Spearing, Mike: *Measurements and Simulation of Inertial and High Capillary Number Flow Phenomena in Gas-Condensate Relative Permeability*, paper SPE 62932 presented at the 2000 SPE ATCE held in Dallas, Texas, October 2000.

Nghiem, L. X., Fong, D. K. and Aziz, K.: *Compositional Modeling with and Equation of State*, paper SPE 9306, SPE Journal, p. 687-698, December 1981.

Nojabaei B., Johns, T. R., and Chu, L.: *Effect of Capillary Pressure on Phase Behavior in Tight Rocks and Shales*, SPEREE, v. **16**, p.281-289, 2013.

Nojabaei B., Siripatrachai, N., Johns, T. R., and Ertekin, T.: *Effect of Saturation Dependent Capillary Pressure on Production in Tight Rocks and Shales: A compositional-Extended Black Oil Formulation*, paper SPE 171028 presented at the SPE Eastern Regional Meeting, 21-23 October, Charleston, WV, USA

Peaceman, D.W.: *Convection in Fractured Reservoirs—The Effect of Matrix-Fissure Transfer on the Instability of a Density Inversion in a Vertical Fracture*, SPE Journal, p. 269-280, October 1976.

Peaceman, D.W.: *Interpretation of Wellblock Pressures in Numerical Reservoir Simulation with Nonsquare Gridblocks and Anisotropic Permeability*, paper SPE 10528, SPE Journal, p. 531, June 1983.

Phillip, C., Etherington, J. R., and Aguilera, R.: *A Process to Evaluate Unconventional Resources*, paper SPE 134602 presented at the SPE Annual Technical Conference and Exhibition held in Florence, Italy, 19-22 September 2010.

Peng, D.Y. and Robinson, D.B.: *A New Two-Constant Equation of State*, Ind. Eng. Chem. Fund., v. 15, p.59-64, 1976.

Rachford, H. H. and Rice, J. D.: *Procedure for Use of Electrical Digital Computers in Calculating Flash Vaporization Hydrocarbon Equilibrium*, Journal of Petroleum Technology, Technical Note 136, 19, October 1952.

Ramsay W., Shields J., Phys Z. Chem. Leipzig, **12**, p. 433, 1893.

Redlich, O., and Kwong, J. N.: On the Thermodynamics of Solutions. V. An Equation of State Fugacities of Gaseous Solutions, Chemical Reviews, **44,** p. 233-244, 1949.
Soave, G.: Chem. Eng. Sci. (1972), v. 27, p. 1197

Spivak, A., and Dixon, T. N., *Simulation of Gas Condensate Reservoirs*, paper SPE 4271 presented at the 3rd Numerical Simulation of Reservoir Performance Symposium, Houston, 10-12, January 1973.

Stiel, L. I., and Thodos, G.: *The viscosity of Nonpolar gases at normal pressures*, AlChE Jour. **7**, 611. 1961.

Stone, H.L.: *Estimation of Three-Phase Relative Permeability and Residual Oil Data,* Journal of Canadian Petroleum Technology, v. 12, n. 4, p. 53, April 1973.

Sugden. S.: The Variation of Surface Tension with Temperature and some Related Functions, J. Chem. Soc, **125**, p. 32-41, 1924.

Thomeer, J. H. M.: *Introduction of a Pore Geometrical Factor Defined by the Capillary Pressure Curve*, Paper number 1324-G, Society of Petroleum Engineers of AIME, Journal of Petroleum Technology, v. 12, number 3, p. 73-77, 1960.

Van der Waals, J.D.: The Equation of State for Gases and Liquids. Nobel lectures in Physics, pp. 254-265, December 1910.

Van Golf-Racht, T.D.: *Fundamentals of Fractured Reservoir Engineering*, Developments in Petroleum Science volume 12, Elsevier, New York, NY, ISBN 0-444-42046-0, 1982.

Walsh, M. P., and Towler, B. F.: *Method Computes PVT Properties for Gas Condensate*, Journal *OGJ*, p. 83-86, July 1994.

Walsh, M.P., and Lake, L.W.: *A Generalized Approach to Primary Hydrocarbon Recovery*. 1st edition. Handbook of Petroleum Exploration and Production, Volume 4. Elsevier Publishing Co., 2003.

Warren, J. E. and Root, P. J.: *The Behavior of Naturally Fractured Reservoirs*, SPE Journal, 3(03), 245-255, September 1963.

Weinaug, C.F. and Katz, D.L.: Surface Tension of Methane-Propane Mixtures, Ind. & Eng. Chem. **35**(2), p.239-246, Feb. 1943.

Whitson, C. H., and Torp, S. B.: *Evaluating Constant-Volume Depletion Data*, SPE Journal *JPT*, p. 610-620, March 1983.

Whitson, C. H., da Silva, F., and Soreide, I.: *Simplified Compositional Formulation for Modified Black-Oil Simulators*, SPE Paper 18315 presented at the 63rd SPE Annual Technical Conference and Exhibition held in Houston, Texas, 2-5 October 1988.

Whitson, C. H., Fevang, Oivind, and Saevareid, A.: *Gas Condensate Relative Permeability for Well Calculations*, Transport in Porous Media 52: p. 279–311, 2003.

# Appendix A

## DERIVATION OF FLUID FLOW EQUATION

The general form of the governing differential equations, where hydrocarbon fluid components are found both in the liquid and gas phases, were derived from the substitution of a velocity model responsible for the flow of fluids within the system into the continuity equation. The continuity equation can be derived by selecting control volume (CV) at which the fluids are flowing through each of its faces, and writing the material balance over the specified volume. Figure **A.1**, illustrates a rectangular coordinates hosting a rectangular flow system flowing through the six faces of the control volume (CV).

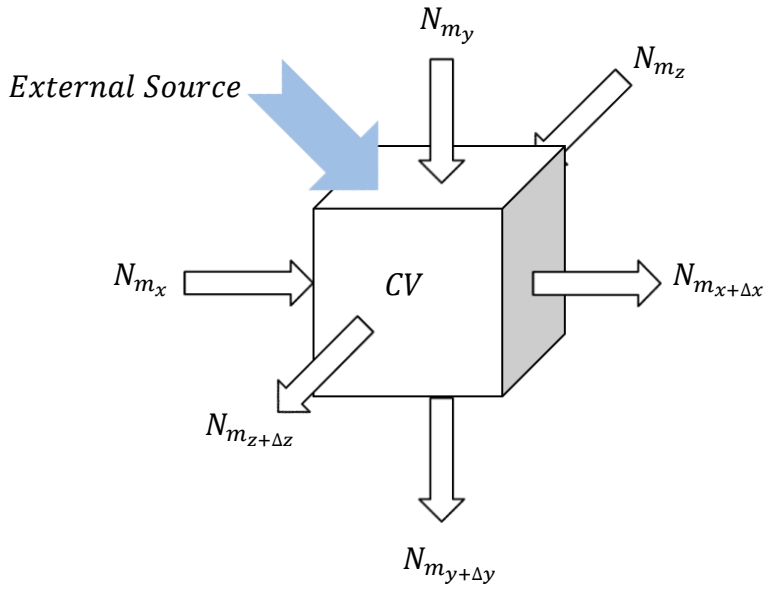


**Figure A.1: Rectangular control volume illustration**

Considering that the material balance can be written in molar formulation as indicated in Chapter 4, the continuity equation of each *m-th* component entering or leaving the system can be expressed over time ($\Delta t$) as follows:

(Molar flow In – Molar flow Out) + External source = Accumulation (A.1)

A mathematical representation of equation (A.1) is expressed as follows:

Molar flow of m-components IN = $(N_{m_x} + N_{m_y} + N_{m_z})\Delta t$

Molar flow of m-components OUT = $(N_{m_{x+\Delta x}} + N_{m_{y+\Delta y}} + N_{m_{z+\Delta z}})\Delta t$

Accumulation = $(\Delta x \Delta y \Delta z \phi(S_o x_m \bar{\rho}_o + S_g y_m \bar{\rho}_g))_{t+\Delta t} - (\Delta x \Delta y \Delta z \phi(S_o x_m \bar{\rho}_o + S_g y_m \bar{\rho}_g))_t$

Considering that the molar flow rate ($N_m$) in the previous illustration is a contribution of the flow rate of the components in the condensate and gas phase, equation (A.1) can be expressed as the following while dividing by ($\Delta t$) and assigning positive (+) sign to flow going into the system and negative (-) for flow leaving the system:

$$-\left[\left(N_{mo} + N_{mg}\right)_{x+\Delta x} - \left(N_{mo} + N_{mg}\right)_x\right] - \left[\left(N_{mo} + N_{mg}\right)_{y+\Delta y} - \left(N_{mo} + N_{mg}\right)_y\right] - \left[\left(N_{mo} + N_{mg}\right)_{z+\Delta z} - \left(N_{mo} + N_{mg}\right)_z\right] + Q_m = \Delta x \Delta y \Delta z \frac{\left[\phi(S_o x_m \bar{\rho}_o + S_g y_m \bar{\rho}_g)\right]_{t+\Delta t} - \left[\phi(S_o x_m \bar{\rho}_o + S_g y_m \bar{\rho}_g)\right]_t}{\Delta t} \quad \text{(A.3)}$$

The expression of (A.3) can be expanded by expressing the flow through each face of the control volume (x, y, and z) as a function of the phase movement velocity, the concentration of the phase, and the area perpendicular to the flow direction. The expression can be re-constructed to give the following form:

$$-\left[\left(C_{mo} v_{mox} A_x + C_{mg} v_{mgx} A_x\right)_{x+\Delta x} - \left(C_{mo} v_{mox} A_x + C_{mg} v_{mgx} A_x\right)_x\right] - \left[\left(C_{mo} v_{moy} A_y + C_{mg} v_{mgy} A_y\right)_{y+\Delta y} - \left(C_{mo} v_{moy} A_y + C_{mg} v_{mgy} A_y\right)_y\right] - \left[\left(C_{mo} v_{moz} A_z + C_{mg} v_{mgz} A_z\right)_{z+\Delta z} - \left(C_{mo} v_{moz} A_z + C_{mg} v_{mgz} A_z\right)_z\right] + Q_m = \Delta x \Delta y \Delta z \frac{\left[\phi(S_o C_{mo} + S_g C_{mg})\right]_{t+\Delta t} - \left[\phi(S_o C_{mo} + S_g C_{mg})\right]_t}{\Delta t} \quad \text{(A.4)}$$

where:

$$C_{mo} = x_m \frac{n\ moles}{Volume} = x_m \frac{m/MW}{m/\rho_o} = x_m \frac{\rho_o}{MW} = x_m \bar{\rho}_o \ \ (lbmol/ft^3) \quad \text{(A.5a)}$$

$$C_{mg} = y_m \frac{n\ moles}{Volume} = y_m \frac{m/MW}{m/\rho_g} = y_m \frac{\rho_g}{MW} = y_m \bar{\rho}_g \ \ (lbmol/ft^3) \quad \text{(A.5b)}$$

$\bar{\rho}_f$ : molar density of the fluid in ($lbmol/ft^3$) = $\frac{\rho_f}{MW_f}$

$\rho_f$ : mass density of the fluid in ($lbm/ft^3$),

Substituting (A.5a) and (A.5b) into equation (A.4) yields to the following form:

$$-\left[\left(x_m\bar{\rho}_o v_{mox}A_x + y_m\bar{\rho}_g v_{mgx}A_x\right)_{x+\Delta x} - \left(x_m\bar{\rho}_o v_{mox}A_x + y_m\bar{\rho}_g v_{mgx}A_x\right)_x\right]$$
$$-\left[\left(x_m\bar{\rho}_o v_{moy}A_y + y_m\bar{\rho}_g v_{mgy}A_y\right)_{y+\Delta y} - \left(x_m\bar{\rho}_o v_{moy}A_y + y_m\bar{\rho}_g v_{mgy}A_y\right)_y\right]$$
$$-\left[\left(x_m\bar{\rho}_o v_{moz}A_z + y_m\bar{\rho}_g v_{mgz}A_z\right)_{z+\Delta z} - \left(x_m\bar{\rho}_o v_{moz}A_z + y_m\bar{\rho}_g v_{mgz}A_z\right)_z\right]$$
$$+ Q_m = \Delta x\Delta y\Delta z\frac{\left[\phi(S_o x_m\bar{\rho}_o + S_g y_m\bar{\rho}_g)\right]_{t+\Delta t} - \left[\phi(S_o x_m\bar{\rho}_o + S_g y_m\bar{\rho}_g)\right]_t}{\Delta t} \quad \ldots (A.6)$$

By dividing equation (A.6) by the bulk volume ($V_b = \Delta x\Delta y\Delta z$), the following expression is obtained:

$$-\frac{\left[\left(x_m\bar{\rho}_o v_{mox} + y_m\bar{\rho}_g v_{mgx}\right)_{x+\Delta x} - \left(x_m\bar{\rho}_o v_{mox} + y_m\bar{\rho}_g v_{mgx}\right)_x\right]}{\Delta x}$$
$$-\frac{\left[\left(x_m\bar{\rho}_o v_{moy} + y_m\bar{\rho}_g v_{mgy}\right)_{y+\Delta y} - \left(x_m\bar{\rho}_o v_{moy} + y_m\bar{\rho}_g v_{mgy}\right)_y\right]}{\Delta y}$$
$$-\frac{\left[\left(x_m\bar{\rho}_o v_{moz} + y_m\bar{\rho}_g v_{mgz}\right)_{z+\Delta z} - \left(x_m\bar{\rho}_o v_{moz} + y_m\bar{\rho}_g v_{mgz}\right)_z\right]}{\Delta z} + \frac{Q_m}{V_b}$$
$$= \frac{\left[\phi(S_o x_m\bar{\rho}_o + S_g y_m\bar{\rho}_g)\right]_{t+\Delta t} - \left[\phi(S_o x_m\bar{\rho}_o + S_g y_m\bar{\rho}_g)\right]_t}{\Delta t} \quad \ldots (A.7)$$

In order to write equation (A.7) in the differential form, the limits of $\Delta x$, $\Delta y$, $\Delta z$, and $\Delta t$ need to be taken in for form of $\lim_{\Delta s\to 0}\{Left\ hand\ side\} = \lim_{\Delta s\to 0}\{Right\ hand\ side\}$. While recalling that $\lim_{\Delta s\to 0}\frac{f(s+\Delta s)-f(s)}{\Delta s} = \frac{\partial f}{\partial s}$, the previous expression can be re-written in the differential form as shown below:

$$-\frac{\partial}{\partial x}\left(x_m\bar{\rho}_o v_{mox} + y_m\bar{\rho}_g v_{mgx}\right) - \frac{\partial}{\partial y}\left(x_m\bar{\rho}_o v_{moy} + y_m\bar{\rho}_g v_{mgy}\right)$$
$$-\frac{\partial}{\partial z}\left(x_m\bar{\rho}_o v_{moz} + y_m\bar{\rho}_g v_{mgz}\right) + \frac{Q_m}{V_b} = \frac{\partial}{\partial t}\left[\phi(S_o x_m\bar{\rho}_o + S_g y_m\bar{\rho}_g)\right] \quad (A.8)$$

In order to express continuity equation for variable flow area, equation (A.8) need to be multiplied by the bulk volume which would give the following representation of the continuity equation used in this model:

$$-\frac{\partial}{\partial x}\left(x_m\bar{\rho}_o v_{mox}A_x + y_m\bar{\rho}_g v_{mgx}A_x\right) - \frac{\partial}{\partial y}\left(x_m\bar{\rho}_o v_{moy}A_y + y_m\bar{\rho}_g v_{mgy}A_y\right)$$
$$-\frac{\partial}{\partial z}\left(x_m\bar{\rho}_o v_{moz}A_z + y_m\bar{\rho}_g v_{mgz}A_z\right) + Q_m = V_b\frac{\partial}{\partial t}\left[\phi(S_o x_m\bar{\rho}_o + S_g y_m\bar{\rho}_g)\right] \quad \text{(A.9)}$$

To come up with the governing differential equation of hydrocarbon, a suitable velocity model needs to be substituted in the molar velocity terms of equation (A.9) to represent the flow of fluids within the system. According to Ayala (2006), the diffusion effect represented by Fick's law in the liquid phase is less significant than in the gas phase, which makes the diffusion forces in the condensate negligible. While, the total velocity of the gas is driven by Darcian and Fickian effect. However, the model used for this work was built to accommodate fluids flowing under Darcian law, which depend on permeability, viscosity, and the pressure gradient. Thus, the total molar/mass velocity of gas and condensate is a result of the flow driven by the bulk Darcian effect ($v_{mfs}^D$) as represented by equation (A.10).

$$v_{mfs} = v_{mfs}^D = -5.615\frac{k_s k_{rf}}{\mu_f}\frac{\partial \Phi_f}{\partial s} \qquad ; f = o, or\ g, \quad s = x, y, and\ z \qquad \text{(A.10)}$$

By substituting the velocity terms in the continuity equation (A.9) and dividing the whole term by 5.615 (*RCF/RB*) to adjust the units of each term to (*RB/day*)(*lbmole/RCF*), we get the following differential material balance equation:

$$\frac{\partial}{\partial x}\left(x_m\bar{\rho}_o A_x\frac{k_x k_{ro}}{\mu_o}\frac{\partial \Phi_o}{\partial x} + y_m\bar{\rho}_g A_x\frac{k_x k_{rg}}{\mu_g}\frac{\partial \Phi_g}{\partial x}\right)\Delta x$$
$$+\frac{\partial}{\partial y}\left(x_m\bar{\rho}_o A_y\frac{k_y k_{ro}}{\mu_o}\frac{\partial \Phi_o}{\partial y} + y_m\bar{\rho}_g A_y\frac{k_y k_{rg}}{\mu_g}\frac{\partial \Phi_g}{\partial y}\right)\Delta y$$
$$+\frac{\partial}{\partial z}\left(x_m\bar{\rho}_o A_z\frac{k_z k_{ro}}{\mu_o}\frac{\partial \Phi_o}{\partial z} + y_m\bar{\rho}_g A_z\frac{k_z k_{rg}}{\mu_g}\frac{\partial \Phi_g}{\partial z}\right)\Delta z$$
$$+M_m = \frac{V_b}{5.615}\frac{\partial}{\partial t}\left[\phi\left(S_o x_m\bar{\rho}_o + S_g y_m\bar{\rho}_g\right)\right] \qquad ; \quad m = 1, 2, \ldots, n_c \qquad \text{(A.9a)}$$

where:

$$M_m = \frac{Q_m}{5.615} \tag{A.9b}$$

$$\frac{\partial \Phi_f}{\partial s} = \frac{\partial p_f}{\partial s} - \frac{1}{144}\frac{g}{g_c}\rho_f \frac{\partial G}{\partial s} \qquad ; f = o, or\ g, \quad s = x, y, and\ z \tag{A.9c}$$

Re-arranging equation (A.9a), leads to the final representation of the governing differential equations.

$$\begin{aligned}
&\frac{\partial}{\partial x}\left(x_m\bar{\rho}_o A_x \frac{k_x k_{ro}}{\mu_o}\frac{\partial p_o}{\partial x} + y_m\bar{\rho}_g A_x \frac{k_x k_{rg}}{\mu_g}\frac{\partial p_g}{\partial x}\right)\Delta x \\
&\qquad - \frac{\partial}{\partial x}\left(\frac{1}{144}\frac{g}{g_c}\rho_o x_m\bar{\rho}_o A_x \frac{k_x k_{ro}}{\mu_o}\frac{\partial G}{\partial x} + \frac{1}{144}\frac{g}{g_c}\rho_g y_m\bar{\rho}_g A_x \frac{k_x k_{rg}}{\mu_g}\frac{\partial G}{\partial x}\right)\Delta x \\
&+ \frac{\partial}{\partial y}\left(x_m\bar{\rho}_o A_y \frac{k_y k_{ro}}{\mu_o}\frac{\partial p_o}{\partial y} + y_m\bar{\rho}_g A_y \frac{k_y k_{rg}}{\mu_g}\frac{\partial p_g}{\partial y}\right)\Delta y \\
&\qquad - \frac{\partial}{\partial y}\left(\frac{1}{144}\frac{g}{g_c}\rho_o x_m\bar{\rho}_o A_y \frac{k_y k_{ro}}{\mu_o}\frac{\partial G}{\partial y} + \frac{1}{144}\frac{g}{g_c}\rho_g y_m\bar{\rho}_g A_y \frac{k_y k_{rg}}{\mu_g}\frac{\partial G}{\partial y}\right)\Delta y \\
&+ \frac{\partial}{\partial z}\left(x_m\bar{\rho}_o A_z \frac{k_z k_{ro}}{\mu_o}\frac{\partial p_o}{\partial z} + y_m\bar{\rho}_g A_z \frac{k_z k_{rg}}{\mu_g}\frac{\partial p_g}{\partial z}\right)\Delta z \\
&\qquad - \frac{\partial}{\partial y}\left(\frac{1}{144}\frac{g}{g_c}\rho_o x_m\bar{\rho}_o A_z \frac{k_z k_{ro}}{\mu_o}\frac{\partial G}{\partial z} + \frac{1}{144}\frac{g}{g_c}\rho_g y_m\bar{\rho}_g A_z \frac{k_z k_{rg}}{\mu_g}\frac{\partial G}{\partial z}\right)\Delta z \\
&+ M_m = \frac{V_b}{5.615}\frac{\partial}{\partial t}\left[\phi\left(S_o x_m\bar{\rho}_o + S_g y_m\bar{\rho}_g\right)\right] \qquad ; \quad m = 1, 2, \ldots, n_c
\end{aligned} \tag{A.11}$$

Equation (4.1) in Chapter 4 has been re-arranged from its original form in equation (A.11) as a result of the assumptions considered. The assumptions were to account for two hydrocarbon phases; gas and condensate that flow according to Darcy's law through a 2-D system with uniform elevation. The 2-Dimentional Cartesian system expands in the x-direction and y-direction which eliminates the existence of the z-direction in equation (A.11). A uniform elevation (G) throughout the plane yields zero gradients $\frac{\partial G}{\partial x}$ and $\frac{\partial G}{\partial y}$. As a result, the flow potentials with respect to elevation are eliminated from Equation (A.11). Thus, applying these assumptions to the last equation yields to the final form of the molar differential equation.

$$\frac{\partial}{\partial x}\left(x_m\bar{\rho}_o A_x \frac{k_x k_{ro}}{\mu_o}\frac{\partial p_o}{\partial x} + y_m\bar{\rho}_g A_x \frac{k_x k_{rg}}{\mu_g}\frac{\partial p_g}{\partial x}\right)\Delta x + \frac{\partial}{\partial y}\left(x_m\bar{\rho}_o A_y \frac{k_y k_{ro}}{\mu_o}\frac{\partial p_o}{\partial y} + y_m\bar{\rho}_g A_y \frac{k_y k_{rg}}{\mu_g}\frac{\partial p_g}{\partial y}\right)\Delta y + M_m = \frac{V_b}{5.615}\frac{\partial}{\partial t}\left[\phi\left(S_o x_m\bar{\rho}_o + S_g y_m\bar{\rho}_g\right)\right] \quad ; \quad m = 1, 2, \dots, n_c \tag{A.12}$$

The representation of the mass differential equation require the substitution of the mass concentration shown by equation (A.13a) and equation (A.13b) into equation (A.4) and carrying the same derivation above until reaching the mass flow equation (A.14). It is also important to define flow rate of the source term in (*RB/day*)(*lbm/RCF*)— $M_m^{\omega}$ to maintain consistency of units for each term.

$$C_{mo} = \omega_{mo}\,\frac{mass}{Volume} = \omega_{mo}\,\frac{m}{m/\rho_o} = \omega_{mo}\;\rho_o \;\; (lbm/ft^3) \tag{A.13a}$$

$$C_{mg} = \omega_{mg}\,\frac{mass}{Volume} = \omega_{mg}\,\frac{m}{m/\rho_g} = \omega_{mg}\;\rho_g \;\; (lbm/ft^3) \tag{A.13b}$$

$$\frac{\partial}{\partial x}\left(\omega_{mo}\,\rho_o\; A_x \frac{k_x k_{ro}}{\mu_o}\frac{\partial p_o}{\partial x} + \omega_{mg}\;\rho_g A_x \frac{k_x k_{rg}}{\mu_g}\frac{\partial p_g}{\partial x}\right)\Delta x + \frac{\partial}{\partial y}\left(\omega_{mo}\,\rho_o\; A_y \frac{k_y k_{ro}}{\mu_o}\frac{\partial p_o}{\partial y} + \omega_{mg}\;\rho_g A_y \frac{k_y k_{rg}}{\mu_g}\frac{\partial p_g}{\partial y}\right)\Delta y + M_m^{\omega} = \frac{V_b}{5.615}\frac{\partial}{\partial t}\left[\phi\left(S_o\omega_{mo}\,\rho_o\; + S_g\omega_{mg}\,\rho_g\right)\right] \quad ; \quad m = 1, 2, \dots, n_c \tag{A.14}$$

Finally, a generalized form of the governing equation can be generated with correspondence to the nomenclatures defined in Table **4.1** as shown below:

$$\frac{\partial}{\partial x}\left(C_{mo}A_x \frac{k_x k_{ro}}{\mu_o}\frac{\partial p_o}{\partial x} + C_{mg}A_x \frac{k_x k_{rg}}{\mu_g}\frac{\partial p_g}{\partial x}\right)\Delta x + \frac{\partial}{\partial y}\left(C_{mo}A_y \frac{k_y k_{ro}}{\mu_o}\frac{\partial p_o}{\partial y} + C_{mg}A_y \frac{k_y k_{rg}}{\mu_g}\frac{\partial p_g}{\partial y}\right)\Delta y + F_m = \frac{V_b}{5.615}\frac{\partial}{\partial t}\left[\phi\left(S_o C_{mo}\; + S_g C_{mg}\right)\right] \quad ; \quad m = 1, 2, \dots, n_c \tag{A.15}$$

# Appendix B

# PHASE BEHAVOIR MODEL

The phase behavior model is an application that studies the compositional behavior of a fluid system as a function of pressure, composition and temperature using an Equations of State. The objective of the model is to provide a tool that uses the basic information of a compositional mixture and be able to generate a full report that includes compressibility factors, number of phases, compositions, equilibrium ratios, and physical properties of each phase.

## B.1 Equation of State

The phase behavior model has been built in a flexible format to allow the user to choose between the equations of state of Peng-Robinson (1976) or Soave RK (1972) for the prediction of fluids behavior. Equations (B.1) and (B.2) present the two equations of state respectively.

$$p = \frac{RT}{\tilde{v} - b_{mix}} - \frac{(a\alpha)_{mix}}{\tilde{v}^2 + 2b_{mix}\tilde{v} - b_{mix}^2} \tag{B.1}$$

$$p = \frac{RT}{\tilde{v} - b_{mix}} - \frac{(a\alpha)_{mix}}{\tilde{v}^2 + b_{mix}\tilde{v}} \tag{B.2}$$

where: $p$ : reservoir pressure, *psia*

$T$ : reservoir Temperature, $^oR$

$R$ : universal gas constant, *10.73* $\frac{psia\ ft^3}{lbmol\ R}$

$\tilde{v}$ : molar volume, *ft$^3$/lbmol*

$b_{mix}$ : co-volume of the mixture, *ft$^3$/lbmole*

$(a\alpha)_{mix}$ : attraction parameter of the mixture, $psia\ \left(\frac{ft^3}{lbmol}\right)^2$

Equations of States predict fluids properties at a known pressure and temperature. The attraction parameter and co-volume are determined based on the physical properties of the pure components making-up the mixture. Practical implementation suggests the implicit derivation of equation (B.1) and equation (B.2) in terms of the compressibility factor (Z), which is related to molar volume through Gas Law. The transformation will lead to the cubic representation shown by equation (B.3) and (B.4) for PR EOS and SRK EOS respectively.

$$Z^3 - (1 - B)Z^2 + (A - 3B^2 - 2B)Z - (AB - B^2 - B^3) = 0 \quad \text{(B.3)}$$

$$Z^3 - Z^2 + (A - B - B^2)Z - AB = 0 \quad \text{(B.4)}$$

where:

$$A = \frac{(a\alpha)_{mix}}{R^2T^2} \quad \text{(B.5a)}$$

$$B = \frac{b_{mix}p}{RT} \quad \text{(B.5b)}$$

According to Coats (1985) and Danesh (2001), all cubic EOS's can be utilized through one common formulation. One of these general equations that is applicable to PR EOS and SRK EOS is the one presented by Coats (1985) as shown be equation (B.6). The general equation of EOS has been fully utilized in the work to enable ease of selection between the two equations.

$$Z^3 + [(m_1 + m_2 - 1)B - 1]Z^2 + [A + m_1m_2B^2 - (m_1 + m_2)B(B + 1)]Z - [AB + m_1m_2B^2(B + 1)] = 0 \quad \text{… (B.6)}$$

where:

$$A = \sum_i^{n_c} \sum_j^{n_c} c_i\, c_j A_{ij} \quad \text{(B.7a)}$$

$$A_{ij} = \left(1 - \delta_{ij}\right)(A_iA_j)^{0.5} \quad \text{(B.7b)}$$

$$A_i = \Omega_{ai}^o[1 + m_i(1 - T_{ri}^{0.5})]^2 \frac{p_{ri}}{T_{ri}^2} \quad \text{(B.7c)}$$

$$B = \sum_{i=1}^{n_c} c_i\, B_i \quad \text{(B.7d)}$$

$$B_i = \Omega_{bi}^{o} \frac{p_{ri}}{T_{ri}} \tag{B.7e}$$

SRK: $m_i = 0.48 + 1.574\omega_i - 0.176\omega_i^2$ (B.7f)

PR: $\begin{cases} 0.374640 + 1.54226\omega_i - 0.26992\omega_i^2 & if\ \omega_i \leq 0.49 \\ 0.379642 + 1.48503\omega_i - 0.164423\omega_i^2 + 0.016666\omega_i^3\ if\ \omega_i > 0.49 \end{cases}$ (B.7g)

SRK: $m_1 = 0\,;\ \ m_2 = 1\,;\ \ \Omega_{ai}^{o} = 0.4274802\,;\ \ \Omega_{bi}^{o} = 0.08664035$

PR: $m_1 = 1 + \sqrt{2}\,;\ \ m_2 = 1 - \sqrt{2}\,;\ \ \Omega_{ai}^{o} = 0.457235529;\ \ \Omega_{bi}^{o} = 0.077796074$

$A$: dimensionless attraction parameter

$A_{ij}$: mixture attraction parameter

$A_i$: attraction parameter of the $i^{th}$ component

$B$: dimensionless co-volume parameter

$B_i$: co-volume parameter of the $i^{th}$ component

$\omega_i$: acentric factor of the $i^{th}$ component

$c_{ij}$: overall composition of the $i^{th}$ or $j^{th}$ component. To avoid confusion with Z-factor, $z_m$ are represented by $c_i$

$n_c$: number of components

$\delta_{ij}$: binary interaction coefficient in the mixture

$\Omega_{ai}^{o}$: attraction parameter constant for the $i^{th}$ component

$\Omega_{bi}^{o}$: co-volume parameter constant for the $i^{th}$ component

$p_{ri}$: dimensionless reduced pressure of the $i^{th}$ component

$T_{ri}$: dimensionless reduced temperature of the $i^{th}$ component

**B.2 Vapor-liquid equilibrium flash**

Foremost, it is essential to determine if the fluid in place under a given pressure and temperature has the potential to split into two phases or maintain a single phase. Michelsen (1982), presented a stability test to examine the system for a potential split in phases. In this study, Michelsen stability test is applied for the gridblocks that are in single phase only. While, gridblocks that

have already split into two phases, are exempt from stability testing to lower computational overhead.

Once a split in phases is detected using the stability testing, percentage of vapor and condensate in the system are calculated using the equation of Rachford and Rice (1952) shown below:

$$f(\alpha_g) = \sum_{i=1}^{n_c} \frac{c_i(K_i - 1)}{1 + \alpha_g(K_i - 1)} = 0 \qquad ; \quad i = 1,2 \ldots, n_c \tag{B.8}$$

where: $f(\alpha_g)$ : Rachford-Rice objective function

$\alpha_g$ : equilibrium molar fraction of vapor phase

$c_i$ : overall molar composition of the $i^{th}$ component

$K_i$ : vapor-liquid equilibrium ratio of the $i^{th}$ component

Rachford-Rice objective function is the bases to determine the compositions of the phases at equilibrium once attained. Yet, the vapor-liquid equilibrium ratio of each component ($K_i$) expressed by equation (B.9) are still not available. However, Wilson's correlation presented by equation (B.10) can be used to initiate the calculation of $K_i$, which will be updated afterward once fugacities are known.

$$K_i = \frac{y_i}{x_i} \qquad ; \quad i = 1,2 \ldots, n_c \tag{B.9}$$

$$K_i = \frac{1}{p_{ri}} EXP\left[5.37(1 + \omega_i)(1 - \frac{1}{T_{ri}})\right] \qquad ; \quad i = 1,2 \ldots, n_c \tag{B.10}$$

As the preliminary $K_i$ values are obtained for each component, equation (B.8) is solved using Newton-Raphson procedure to determine the equilibrium molar fraction of vapor phase.

$$\alpha_g^{new} = \alpha_g^{old} - \frac{f(\alpha_g^{old})}{f'(\alpha_g^{old})} \tag{B.11}$$

Where, $f'(\alpha_g^{old})$ is the derivative of the Rachford-Rice objective function determined as follows:

$$f'(\alpha_g) = -\sum_{i=1}^{n_c} \frac{c_i(K_i - 1)^2}{\left[1 + \alpha_g(K_i - 1)\right]^2} = 0 \qquad ; \quad i = 1,2 \ldots, n_c \tag{B.12}$$

Applying Newton-Raphson procedure in equation (B.11) requires number of iterations before converging. A criterion is set to allow arrival to an adequate estimation of the equilibrium vapor molar fraction in the system, which is described by the expression in (B.13).

$$\left|\alpha_g^{new} - \alpha_g^{old}\right| < 1.10^{-14} \tag{B.13}$$

Considering the relationship of equilibrium molar fractions of phases coming to unity, equation (B.14) is used to calculate the equilibrium molar liquid fraction.

$$\alpha_l = 1 - \alpha_g \tag{B.14}$$

Knowing the equilibrium molar fractions and equilibrium ratio of each component, the compositions of liquid and vapor are determined using equations (B15a) and (B15b).

$$x_i = \frac{c_i}{1 + \alpha_g(K_i - 1)} \qquad ; \quad i = 1,2 \ldots, n_c \tag{B.15a}$$

$$y_i = \frac{K_m c_i}{1 + \alpha_g(K_i - 1)} = K_i x_i \qquad ; \quad i = 1,2 \ldots, n_c \tag{B.15b}$$

Wilson's empirical correlation given by equation (B.10) is applicable only at low pressures because it over estimate the dependency of equilibrium ratios on composition (Ayala, 2004). Thus, improving the predictions of $K_i$ are achieved by Successive Substitution Method (SSM) which is formulated toward attaining a fugacity equilibrium constraint shown by equation (B.16).

$$f_{gi} = f_{li} \qquad ; \quad m = 1,2 \ldots, n_c \tag{B.16}$$

where: $f_{gi}$ : fugacity of the $i^{th}$ component in vapor phase

$f_{li}$ : fugacity of the $i^{th}$ component in liquid phase

Fugacity is a term used to represent the potential transfer of a component between two phases. Under any given conditions, the fugacity of a component in liquid phase ($f_{li}$) is compared to the fugacity in gaseous phase ($f_{gi}$) to determine the phase preference of the component. Once a net transfer of zero is achieved, where the transfer between the phases is halted, a thermodynamic equilibrium is reached and the constraint in (B.16) is accomplished. Attaining reliable values of $K_m$ require several successive substitution and a criterion of conversion. The steps of SSM are presented by equations (B.17) to (B.21).

Fugacity of phases are calculated using equations (B.17) and (B.18) as the product of fugacity coefficient and the partial pressure for each phase.

$$f_{gi} = \phi_{gi} \, . y_i \, p \quad ; \quad i = 1,2 \ldots, n_c \tag{B.17}$$

$$f_{li} = \phi_{li} \, . x_i \, p \quad ; \quad i = 1,2 \ldots, n_c \tag{B.18}$$

where: $\phi_{gi}$ : fugacity coefficient of the $i^{th}$ component in vapor phase

$\phi_{li}$ : fugacity coefficient of the $i^{th}$ component in liquid phase

$y_i$ : vapor composition of the $i^{th}$ component

$x_i$ : liquid composition of the $i^{th}$ component

Using the general equation of EOS presented by the expression in (B.6), the fugacity coefficient for each phase is calculated with equation (B.19). The Z-factor of liquid is attained by assuming the mixture of the system has overall compositions equal to the liquid phase compositions. Similarly, the Z-factor of the vapor phase is estimated using the vapor phase compositions as the overall compositions of the system.

$$ln\phi_{fi} = -\ln(Z - B) + \frac{A}{(m_1 - m_2)B}\left(\frac{2\sum_{j=1}^{n_c} A_{ij} c_j}{A} - \frac{B_i}{B}\right) ln\left[\frac{Z + m_2 B}{Z + m_1 B}\right] + \frac{B_i}{B}(Z - 1)$$

$$; \quad i = 1,2 \ldots, n_c \quad and \; f = g \; or \; l \qquad \ldots \; (B.19)$$

Once fugacities of the phases are known, successive substitutions into equation (B.20) are carried until the specified criterion in equation (B.21) is achieved. Satisfaction of the criterion suggests strong dependency of equilibrium ratios on the composition of the phases. As a result, the improved $K_i^{new}$ values are used to re-calculate the compositions of liquid and vapor with equations (B15a) and (B15b) presented earlier.

$$K_i^{new} = \frac{f_{gi}/y_i\, p}{f_{li}\,/\,x_i\, p} = \frac{f_{li}}{f_{gi}}.\frac{x_i}{y_i} = \left(\frac{f_{li}}{f_{gi}}\right)^{old} K_i^{old} \qquad \text{(B.20)}$$

$$\sum_i^{n_c}\left(\frac{f_{li}}{f_{gi}} - 1\right)^2 < 10^{-13} \quad ; \quad i = 1,2\ldots, n_c \qquad \text{(B.21)}$$

**B.3 Properties predictions**

The estimation of the equilibrium ratio is the key of achieving trustworthy description of mixtures at any given overall composition, pressure, and temperature. Since the composition of all the phases had been reliably estimated, the properties of vapor and liquid can be predicted easily. This section presents an overview on estimating the most important properties for vapor and liquid such as; molecular weight, density, and viscosity.

Molecular weight of the phases are calculated with respect to the phase molar compositions and the molecular weight of each component as shown by equations (B.22a) and (B.22b).

$$MW_g\left(\frac{lbm}{lbmol}\right) = \sum_{i=1}^{n_c} y_i MW_i \quad ; \quad i = 1,2\ldots, n_c \qquad \text{(B.22a)}$$

$$MW_l\left(\frac{lbm}{lbmol}\right) = \sum_{i=1}^{n_c} x_i MW_i \quad ; \quad i = 1,2\ldots, n_c \qquad \text{(B.22b)}$$

Real gas law is utilized to estimate densities as function of the compressibility factors of the phases attained from the EOS described earlier.

$$\rho_g \left(\frac{lbm}{ft^3}\right) = \frac{p\ MW_g}{Z_g RT} \quad \text{(B.23a)}$$

$$\rho_l \left(\frac{lbm}{ft^3}\right) = \frac{p\ MW_l}{Z_l RT} \quad \text{(B.23b)}$$

Molar densities are simply attained by dividing the mass densities specified in equations (B.23a) and (B.23b) by the molecular weight of each phase respectively.

$$\bar{\rho}_g \left(\frac{lbmol}{ft^3}\right) = \frac{p}{Z_g RT} \quad \text{(B.24a)}$$

$$\bar{\rho}_l \left(\frac{lbmol}{ft^3}\right) = \frac{p}{Z_l RT} \quad \text{(B.24b)}$$

While, viscosity of each phase is determined using Lohrenz *et al.* (1964) empirical correlation, which is an extension to the development of Jossi, Stiel and Thodos (1962). Lohrenz correlation presented by equation (B.25) is used to predict gas and liquid viscosities with minor differences in the prediction of the viscosity of each phase at atmospheric pressure.

$$\mu_f = \mu_f^* + \xi_f^{-1}\left[\left(0.1023 + 0.023364\rho_{r_f} + 0.058533\rho_{r_f}^2 - 0.040758\rho_{r_f}^3 + 0.0093724\rho_{r_f}^4\right)^4 - 1.10^{-4}\right] \quad ; \quad f = g\ or\ l \quad \text{… (B.25)}$$

where: $\mu_f$ : viscosity of the phase, *cp*

$\mu_f^*$: viscosity of the phase at atmospheric pressure, *cp*

$\xi_f$ : viscosity parameter of the phase, $cp^{-1}$

$\rho_{r_f}$ : reduced density of the phase

Lohrenze *et al.* (1964) recommends to calculate viscosities of the phases at atmospheric pressure using Herning & Zipperer equation illustrated below:

$$\mu_g^* = \frac{\sum_{i=1}^{n_c} y_i \mu_{i_f}^* \sqrt{MW_i}}{\sum_{i=1}^{n_c} y_i \sqrt{MW_i}} \quad ; \quad i = 1,2 \dots, n_c \tag{B.26a}$$

$$\mu_l^* = \frac{\sum_{i=1}^{n_c} x_i \mu_{i_f}^* \sqrt{MW_i}}{\sum_{i=1}^{n_c} x_i \sqrt{MW_i}} \quad ; \quad i = 1,2 \dots, n_c \tag{B.26b}$$

where: $\mu_{i_f}^*$ : viscosity of the *i*$^{th}$ component at low pressure in a phase of mixture, *cp*

It is also suggested in the work of Lohrenz *et al.* (1964) to use Stiel and Thodos (1961) correlation to calculate the viscosity of the *i*$^{th}$ component at low pressures. For vapor phase, the viscosity of the *i*$^{th}$ component is calculated using equations (B.27a) and (B.27b).

$$\mu_{i_g}^* = \frac{34.\,10^{-5} T_r^{0.94}}{\xi_i} \quad for\ T_r \leq 1.5 \quad ; \quad i = 1,2 \dots, n_c \tag{B.27a}$$

$$\mu_{i_g}^* = \frac{17.78.\,10^{-5} (4.58\,T_r - 1.67)^{0.625}}{\xi_i} \quad for\ T_r > 1.5 \quad ; \quad i = 1,2 \dots, n_c \tag{B.27b}$$

where:

$$\xi_i = \frac{5.4402\ T_{ci}^{1/6}}{\sqrt{MW_i}\ p_{ci}^{2/3}} \quad ; \quad i = 1,2 \dots, n_c \tag{B.27c}$$

$$T_r = \frac{T}{T_{pc_g}} \tag{B.27d}$$

$$T_{pc_g} = \sum_{i=1}^{n_c} y_i T_{ci} \quad ; \quad i = 1,2 \dots, n_c \tag{B.27e}$$

$\xi_i$ : viscosity parameter of the i$^{th}$ component, *cp*$^{-1}$

$p_{ci}$ : critical pressure of the i$^{th}$ component, *psia*

$T_{ci}$ : critical temperature of the i$^{th}$ component, $^{o}R$

$T_r$ : dimensionless reduced temperature of the mixture

$T_{pc_g}$ : critical temperature of a mixture in gaseous phase, $^{o}R$

$MW_i$ : molecular weight of the i$^{th}$ component, *lbm/lbmol*

Likewise, calculating the viscosity of the $i^{th}$ component for liquid phase is attained with equations (B.28a) and (B.28b). The difference in comparison with the vapor equation is in accommodating the reduced temperature of the $i^{th}$ component instead of the mixture's reduced temperature.

$$\mu_{i_l}^{*} = \frac{34.10^{-5} T_{ri}^{0.94}}{\xi_i} \quad for\ T_{ri} \leq 1.5 \quad ; \quad i = 1,2 \dots, n_c \tag{B.28a}$$

$$\mu_{i_l}^{*} = \frac{17.78.10^{-5} (4.58 T_{ri} - 1.67)^{0.625}}{\xi_i} \quad for\ T_{ri} > 1.5 \quad ; \quad i = 1,2 \dots, n_c \tag{B.28b}$$

Evaluating the viscosity parameter of a mixture is achieved as a function of the critical pressure and temperature of each phase respectively. The general form used for $\xi_f$ is presented as follows:

$$\xi_g = \frac{5.4402\ T_{pc_g}^{1/6}}{\sqrt{MW_g}\ p_{pc_g}^{2/3}} \quad ; \quad i = 1,2 \dots, n_c \tag{B.29a}$$

$$\xi_l = \frac{5.4402\ T_{pc_l}^{1/6}}{\sqrt{MW_l}\ p_{pc_l}^{2/3}} \quad ; \quad i = 1,2 \dots, n_c \tag{B.29a}$$

The pseudocritical properties of the mixture are determined using the following expressions for vapor and liquid:

$$\beta_{pc_g} = \sum_{i=1}^{n_c} y_i \beta_{ci} \quad ; \quad i = 1,2 \dots, n_c \quad and \quad \beta = p, T, or\ v \tag{B.30a}$$

$$\beta_{pc_l} = \sum_{i=1}^{n_c} x_i \beta_{ci} \quad ; \quad i = 1,2 \dots, n_c \quad and \quad \beta = p, T, or\ v \tag{B.30b}$$

where: $p_{pc}$ : critical pressure of the mixture, *psia*

$T_{pc}$ : critical temperature of the mixture, $^{o}R$

$v_{pc}$ : critical specific volume of the mixture, $ft^3/lbm$

Lastly, reduced density of the mixture as described by Lohrenz *et al.* (1964) is determined using equations (B.31a) and (B.31b) as function of the critical molar volume and molar density of each phase. The reason molar units are used for volume and density is to allow units to cancel each other to arrive at a dimensionless reduced density. This is applicable when critical specific volume are given for each component as input data.

$$\rho_{r_g} = \frac{\rho_g}{\rho_{pc_g}} = \frac{\rho_g}{MW_g} . \bar{v}_{pc_g} \tag{B.31a}$$

$$\rho_{r_l} = \frac{\rho_l}{\rho_{pc_l}} = \frac{\rho_l}{MW_l} . \bar{v}_{pc_l} \tag{B.31b}$$

where:

$$\bar{v}_{pc_g} = \sum_{i=1}^{n_c} y_i v_{ci} MW_i \qquad ; \qquad i = 1,2 \dots, n_c \tag{B.31c}$$

$$\bar{v}_{pc_l} = \sum_{i=1}^{n_c} x_i v_{ci} MW_i \qquad ; \qquad i = 1,2 \dots, n_c \tag{B.31d}$$

$\rho_{r_f}$ : dimensionless reduced density of the mixture

$\rho_f$ : specific density of the phase, *lbm/ft*$^3$

$\rho_{pc_f}$ : critical specific density of the mixture, *lbm/ft*$^3$

$\bar{v}_{pc_f}$ : critical molar volume of the mixture, *ft*$^3$*/lbmol*

$T_{pc_g}$ : critical temperature of a mixture in gaseous phase, $^oR$

$MW_i$ : molecular weight of the i$^{th}$ component, *lbm/lbmol*

All the variables of equation (B.25) are defined at this time, and once calculated, they can be directly plugged into Lohrenz *et al.* (1964) empirical correlation, to predict gas and liquid viscosities at any given pressure and temperature.

# Appendix C

# STANDARD PVT PROPERTY CALCULATIONS

The substation of Equation of States for reservoir simulators is achieved through the utilization and analysis of data provided by PVT experiments. Typical PVT laboratory experiments include wellstream chromatographic breakdown of compositions, Constant-Composition-Experiment (CCE), Constant-Volume-Depletion (CVD) experiments, and separation experiment (SEP). Essential information are retrieved from analyzing the various experimental data, which provide a mean for calculating; fluids-in-place, productivity, and recoveries.

## C.1 Fluids-in-place calculations

The total amount of fluids in place analysis is carried in this section to evaluate reservoir performance as pressure depletes isothermally in the reservoir. Separator experiment and recovery analysis from a typical PVT report, essentially support the estimation of fluids in place. The following calculations are considered to evaluate original gas in place (OGIP) and original condensate in place (OCIP).

First, the densities at stock tank conditions for condensate and gas are needed to predict mass compositions used in modified black oil simulators as presented in Chapter 4. Stock tank densities are also important for the prediction of gas-oil equivalency factor, initial mole fraction of the separator, and formation volume factors.

Using the value of API gravity provided by the separator test of the last separation stage, relative density ($\gamma_o$) of oil is calculated to assess the determination of density at stock tank conditions.

$$API = \frac{141.5}{\gamma_o} - 131.5 \tag{C.1}$$

Explicit re-arrangement of equation (C.1) with respect to relative density provide the following expression:

$$\gamma_o @\ 60^o F = \frac{141.5}{API + 131.5} \tag{C.2}$$

Relative density is the ratio of the density of a substance to a reference density. In the case of condensate at stock tank condition, the reference density is water. Equation (C.2) illustrates the relative density relationship, which can be re-arranged to represent the stock tank density of oil.

$$\gamma_o @\ 60^o F = \frac{\rho_{osc}}{\rho_{H_2O}} \tag{C.3a}$$

$$\rho_{osc} = \gamma_o\, \rho_{H_2O} \tag{C.3b}$$

where: $\gamma_o$ : relative density ratio of condensate at 60°F

$\rho_{osc}$ : oil density at stock tank condtions, *lbm/ft*$^3$

$\rho_{H_2O}$ : water density at 60°F, *62.4 lbm/ft*$^3$

For gas density at stock tank conditions, the process is straight-forward, since gas specific gravity is usually given in the PVT report. With the same analogue of relative density explained for condensate, the ratio is taken for gas density in relation to air density; air is the reference density in this case. Equation (C.4a) present the relative density of gas, while equation (C.4b) illustrate the stock tank density of gas.

$$\gamma_g @\ 60^o F = \frac{\rho_{gsc}}{\rho_{air}} \tag{C.4a}$$

$$\rho_{gsc} = \gamma_g\, \rho_{air} \tag{C.4b}$$

where: $\gamma_g$ : relative density ratio of gas at 60°F

$\rho_{gsc}$ : gas density at stock tank condtions, *lbm/ft*$^3$

$\rho_{air}$ : air density at 60°F, *0.0762 lbm/ft*$^3$

At this point, prediction of gas-oil equivalency factor, initial mole fraction of the separator, and formation volume factors for gas and condensate has come possible as shown by equations (C.5) to (C.8b). Note, determining the gas-oil equivalency factor ($R_{go}$) require knowledge of the molecular weight at stock tank condition. In order to obtain this property, stock tank densities are to be plugged in equations (4.18a) and (4.18b) to obtain mass composition in the oil phase at stock tank. The mass composition will have to be converted to molar compositions using equations (4.25a) and (4.25b), and then be used in equation (B.22b) to obtain the mixture molecular weight in oil phase.

$$R_{go}\left(\frac{scf}{stb}\right) = \frac{2130\ \rho_{osc}}{MW_{osc}} \tag{C.5}$$

The initial volatilized oil-gas ratio ($R_{vi}$) is measured by taking the ratio of the initial stock tank oil (N) separated to the initial separated gas (G) from the 3-separation system.

$$R_{vi}\left(\frac{stb}{scf}\right) = \frac{N}{G} \tag{C.6}$$

Plugging the values of $R_{go}$ and $R_{vi}$ into equation (C.7) lead to the initial mole fraction of the separator in the gas ($y_{gi}$).

$$y_{gi} = \frac{1}{\left(1 + R_{vi}R_{go}\right)} \tag{C.7}$$

In dry gas reservoirs where oil is not present at the surface wellstream, $R_{go}$ is taken to be zero and thus the initial mole fraction collapses to unity. However, in wet gas and gas-condensate reservoirs, condensate drops out of the main stream at the surface facilities, which is accounted for in the calculation of the gas formation volume factor. Estimating the initial gas formation volume factor ($B_{gi}$) is attained using equation (C.8a). While, the initial condensate formation volume factor ($B_{oi}$) is determined through equation (C.8b)

$$B_{gi}\left(\frac{rcf}{scf}\right) = \frac{0.028269\ T_{res} z_i}{y_{gi}\ p_i} \tag{C.8a}$$

$$B_{oi}\left(\frac{rb}{stb}\right) = \frac{B_{gi}\left(\frac{rcf}{scf}\right)\ /\ 5.615\left(\frac{rcf}{rb}\right)}{R_{vi}\left(\frac{stb}{MMscf}\right) * \left(\frac{MMscf}{1.0e6\ scf}\right)} \tag{C.8b}$$

The general form to calculate original gas in place in (*scf*) and original condensate in place (*stb*) are shown by equations (C.9) and (C.10). Those equations are functions of saturations, formation volume factor of each phase, volatilized oil-gas ratio, and dissolved gas-oil ratio inside the reservoir at initial conditions.

$$OGIP\ (scf) = 43560\ A\ h\ \phi\ \left[\frac{S_{gi}}{B_{gi}} + R_{si}\frac{S_{oi}}{B_{oi}}\right] \tag{C.9}$$

$$OCIP\ (scf) = 43560\ A\ h\ \phi\ \left[\frac{S_{gi}}{B_{gi}} R_{vi} + \frac{S_{oi}}{B_{oi}}\right] \tag{C.10}$$

where: $A$ : area of reservoir, *acres*

$h$ : reservoir thickness, *ft*

$\phi$ : porosity

$S_{fi}$ : initial phase saturation

$R_{vi}$ : initial volatilized oil-gas ratio, $\frac{stb}{MMscf}$

$R_{si}$ : initial dissolved gas-oil ratio, $\frac{scf}{stb}$

In the case of an undersaturated gas reservoir with no condensate present at initial conditions, equations (C.9) and (C.10) collapse to the expressions demonstrated by (C.11) and (C.12).

$$OGIP\ (scf) = 43560\ A\ h\ \phi\ \left[\frac{S_{gi}}{B_{gi}}\right] \tag{C.11}$$

$$OCIP\ (stb) = R_{vi}\ \ OGIP \tag{C.12}$$

**C.2 Productivity analysis**

This section presents gas-condensate reservoir performance by providing detailed productivity analysis using data provided from Constant-Composition-Experiment (CCE) and Constant-Volume-Depletion (CVD) experiments. CCE are performed on gas condensate to simulate the pressure-volume relations of these hydrocarbon systems. It provides information on saturation pressure (dew-point pressure), isothermal compressibility coefficients of the single-phase fluid in excess of saturation pressure, and total hydrocarbon volume as a function of pressure (Relative Volume). While, the CVD experiments are performed to evaluate depletion behavior for reservoirs with compositional variation such as retrograde condensate reservoirs. The test provides a variety of useful data to be used in reservoir engineering calculations; the volume of retrograde liquid, maximum liquid dropout, instantaneous recovery, and cumulative recovery.

Using the experimental reports provided, several Standard PVT Property calculations are carried to obtain formation volume factors for oil and gas, dissolved gas-oil ratio, and volatilized oil-gas ratio for each pressure at and below dew point pressure. The procedures and equation to obtain this valuable information follows the modified procedures of Walsh and Lake (2003).

At first, properties such as the equivalent gas formation volume factor ($B_{ge}$) and the amount of gas equivalent ($G_e$) are estimated at reservoir conditions. These values are essential for the calculations of the total volume at reservoir conditions ($V_T$).

Using pressure data from the CVD test in (*psia*), the equivalent gas formation volume factor at dew point pressure is calculated as:

$$B_{ge_{DP}}\left(\frac{rb}{Mscf}\right) = \frac{5.035\, T_{res} Z}{p} \qquad \text{(C.13)}$$

Commonly, PVT reports consider the wellstream value as the amount of gas equivalent ($G_e$) found in (*Mscf*). With the knowledge of $G_{e,}$ and the sum of the separated gas (G) from the 3-separation system, the initial mole fraction of the separator in the gas ($y_{gi}$) at dew point pressure is determined using equation (C.14).

$$y_{gi_{DP}} = \frac{G(Mscf)}{G_e(Mscf)} \tag{C.14}$$

As a result, the initial gas formation volume factor at dew point pressure is calculated using equation (C.15).

$$B_{gi_{DP}}\left(\frac{rb}{Mscf}\right) = \frac{B_{ge_{DP}}}{y_{gi_{DP}}} \tag{C.15}$$

Now, plugging the results from (C.15) and the value of G into the following expression yield the total volume at reservoir conditions in (*rb*). Total volume ($V_T$) is the reference point to maintain constant volume at the end of each pressure reduction step.

$$V_T(rb) = B_{gi_{DP}} G \tag{C.16}$$

The following procedures are performed at each pressure entry given by the CVD report, where each pressure entry is denoted by "j". The value of j ascends from *1* to $n_e$*-1*, where $n_e$ is the total number of pressure levels.

The oil-phase and gas-phase volumes at each pressure are estimated in (*rb*) as follows:

$$V_{o,j}(rb) = V_T\, v_{o,j} \quad ; \quad j = 1, 2, \ldots\, n_e - 1 \tag{C.17}$$

$$V_{g,j}(rb) = V_T - V_{o,j} \quad ; \quad j = 1, 2, \ldots\, n_e - 1 \tag{C.18}$$

where: $v_{o,j}$ : volume fraction of retrograde liquid given by CVD data

Lower pressure levels allow the fluids to expand in volume. At each recorded pressure level by CVD, where equilibrium is reached, gas will be expelled by an amount that will return the cell volume to its reference point. After the expelled gas is removed, several information can be attained from CVD such as the total moles present ($n_T$), the gas-phase moles remaining ($n_g$), and the moles of gas phase removed ($\Delta n_g$). The follows present the equations to obtain such information:

$$n_{T,j} = \frac{\left({}^{p_j}/_{Z_{2,j}}\right)}{\left({}^{p_1}/_{Z_{2,1}}\right)} \quad ; \quad j = 1, 2, \ldots n_e - 1 \tag{C.19}$$

$$n_{g,j} = \frac{\left(p_j\, Z_1 V_{g,j}\right)}{\left(p_1 Z_j\, V_T\right)} \quad ; \quad j = 1, 2, \ldots n_e - 1 \tag{C.20}$$

$$\Delta n_{g,j} = n_{T,j-1} - n_{T,j} \quad ; \quad j = 1, 2, \ldots n_e - 1 \tag{C.21}$$

where: $n_{T,j}$ total moles present after excess gas removed at the $j^{th}$ pressure level, *moles*

$n_{g,j}$ : gas moles remaining at the $j^{th}$ pressure after excess gas removed, *moles*

$\Delta n_{g,j}$ : moles of gas phase removed at the $j^{th}$ pressure level, *moles*

$p_j$ : pressure at the $j^{th}$ pressure level from CVD data, *psia*

$Z_j$ : Z-factor at the $j^{th}$ pressure level from the depletion study given

$Z_{2,j}$ : two phase Z-factor at the $j^{th}$ pressure level from the depletion study given

Calculating the incremental produced separator fluids is achieved between two pressure levels using equations (C.22) and (C.23) for gas and oil respectively.

$$\Delta G_P(Mscf) = G_{P,j} - G_{P,j-1} \quad ; \quad j = 1, 2, \ldots n_e - 1 \tag{C.22}$$

$$\Delta N_P(stb) = N_{P,j} - N_{P,j-1} \quad ; \quad j = 1, 2, \ldots n_e - 1 \tag{C.23}$$

where:

$$G_P(Mscf) = G_{P_1,j} + G_{P_2,j} + G_{P_3,j} \quad ; \quad j = 1, 2, \ldots n_e - 1 \tag{C.24}$$

$\Delta G_P$ : incremental produced separator gas between pressures *j-1* and *j*, *Mscf*

$\Delta N_P$ : incremental produced separator oil between pressures *j-1* and *j*, *stb*

$G_{P,j}$ : total gas produced from the three separators at the $j^{th}$ pressure, *Mscf*

$N_{P,j}$ : stock tank oil production at the $j^{th}$ pressure, *stb*

With the knowledge of the incremental produced fluids, surface volumes of separator gas (*Mscf*) and stock-tank oil (*stb*) remaining after removing the excessive gas are calculated as follows:

$$G_j(Mscf) = G_{j-1} - \Delta G_{P_j} \quad ; \quad j = 1, 2, \ldots n_e - 1 \tag{C.25}$$

$$N_j(stb) = N_{j-1} - \Delta N_{P_j} \quad ; \quad j = 1, 2, \ldots n_e - 1 \tag{C.26}$$

Furthermore, after the removal of excessive gas and calculating the gas-phase moles, surface volumes remaining in free gas and free oil are calculated using equations (C.27) through (C.30).

$$G_{fg,j}(Mscf) = \frac{n_{g,j}}{\Delta n_{g,j}} \Delta G_{P_j} \quad ; \quad j = 1, 2, \ldots n_e - 1 \tag{C.27}$$

$$N_{fg,j}(stb) = \frac{n_{g,j}}{\Delta n_{g,j}} \Delta N_{P_j} \quad ; \quad j = 1, 2, \ldots n_e - 1 \tag{C.28}$$

$$G_{fo,j}(Mscf) = G_j - G_{fg,j} \quad ; \quad j = 1, 2, \ldots n_e - 1 \tag{C.29}$$

$$N_{fo,j}(stb) = N_j - N_{fg,j} \quad ; \quad j = 1, 2, \ldots n_e - 1 \tag{C.30}$$

where: $G_{fg,j}$ : surface volume of separator gas remaining in free gas, *Mscf*

$N_{fg,j}$ : surface volume of separator oil remaining in free gas, *stb*

$G_{fo,j}$ : surface volume of separator gas remaining in free oil, *Mscf*

$N_{fo,j}$ : surface volume of separator gas remaining in free oil, *stb*

Ultimately, using the productivity analysis retrieved from CCE-CVD and recovery data, Standard PVT Property calculations are carried to obtain formation volume factors for oil and gas, dissolved gas-oil ratio, and volatilized oil-gas ratio. The following calculations are applicable for each pressure level at and below dew point pressure as shown:

$$B_{g,j}\left(\frac{rb}{Mscf}\right) = \frac{V_{g,j}}{G_{fg,j}} \quad ; \quad j = 1, 2, \ldots n_e - 1 \tag{C.31}$$

$$B_{o,j}\left(\frac{rb}{stb}\right) = \frac{V_{o,j}}{N_{fo,j}} \quad ; \quad j = 1, 2, \ldots n_e - 1 \tag{C.32}$$

$$R_{s,j}\left(\frac{scf}{stb}\right) = \frac{G_{fo,j}}{N_{fo,j}} \quad ; \quad j = 1, 2, \ldots n_e - 1 \tag{C.33}$$

$$R_{v,j}\left(\frac{stb}{MMscf}\right) = \frac{N_{fg,j}}{G_{fg,j}} \quad ; \quad j = 1, 2, \ldots n_e - 1 \tag{C.34}$$

where: $B_{g,j}$: gas formation volume factors at $j^{th}$ pressure, $\frac{rb}{Mscf}$

$B_{o,j}$ : oil formation volume factors at $j^{th}$ pressure, $\frac{rb}{stb}$

$R_{s,j}$ : dissolved gas-oil ratio at $j^{th}$ pressure, $\frac{scf}{stb}$

$R_{v,j}$ : volatilized oil-gas ratio at $j^{th}$ pressure, $\frac{stb}{MMscf}$

# Appendix D

# MODIFIED BLACK-OIL MODEL

## D.1 Definition of composition and saturation using mass formulation

Modified black-oil simulators depend on fluids properties at surface conditions such as densities at standard condition, formation volume factors, solution gas-oil ratio, and volatile oil-gas ratio. Reservoir fluid densities and molecular weights are not available to provide mean of calculating molar properties. Thus, the definition of compositions indicated earlier need to be redefined in terms of surface fluid properties. Primarily, fluids' densities will be expressed in terms of densities at standard conditions as shown below (Walsh and Lake, 2003).

$$\rho_o\left(\frac{lbm}{ft^3}\right) = \frac{5.615\left(\frac{scf}{stb}\right)\rho_{osc} + \rho_{gsc}\,R_{so}}{5.615\left(\frac{ft^3}{rb}\right)B_o} \tag{D.1}$$

$$\rho_g\left(\frac{lbm}{ft^3}\right) = \frac{\rho_{gsc} + \rho_{osc}\,R_v\,5.615\left(\frac{scf}{stb}\right)}{5.615\left(\frac{ft^3}{rb}\right)B_g} \tag{D.2}$$

Subsequently, the compositions expressed in equations (4.8a) through (4.8d) will take the following form as $f = (\rho_{osc}, \rho_{gsc}, R_{so}, R_v, B_o, B_g\ )$

$$\omega_{1o} = \frac{Mass\ of\ P_1\ in\ 1\ STB\ of\ oil\left(\frac{lbm}{stb}\right)}{Mass\ of\ liquid\ phase\ in\ 1\ STB\ of\ oil\left(\frac{lbm}{stb}\right)} = \frac{\rho_{gsc}\,R_{so}}{5.615\,\rho_{osc} + \rho_{gsc}\,R_{so}} \tag{D.3a}$$

$$\omega_{2o} = \frac{Mass\ of\ P_2\ in\ 1\ STB\ of\ oil\left(\frac{lbm}{stb}\right)}{Mass\ of\ liquid\ phase\ in\ 1\ STB\ of\ oil\left(\frac{lbm}{stb}\right)} = \frac{\rho_{osc}\,5.615}{5.615\,\rho_{osc} + \rho_{gsc}\,R_{so}} \tag{D.3b}$$

$$\omega_{1g} = \frac{Mass\ of\ P_1\ in\ 1\ SCF\ of\ gas\left(\frac{lbm}{scf}\right)}{Mass\ of\ vapor\ phase\ in\ 1\ SCF\ of\ gas\left(\frac{lbm}{scf}\right)} = \frac{\rho_{gsc}}{\rho_{gsc} + \rho_{osc}\ R_v\ 5.615} \qquad \text{(D.3c)}$$

$$\omega_{2g} = \frac{Mass\ of\ P_2\ in\ 1\ SCF\ of\ gas\left(\frac{lbm}{scf}\right)}{Mass\ of\ vapor\ phase\ in\ 1\ SCF\ of\ gas\left(\frac{lbm}{scf}\right)} = \frac{\rho_{osc}\ R_v\ 5.615}{\rho_{gsc} + \rho_{osc}\ R_v\ 5.615} \qquad \text{(D.3d)}$$

Once all the mass fraction compositions are known, the vapor-liquid equilibrium ratio ($K_m^\omega$) of each component are estimated by equation (D.4). While, the equilibrium mass vapor fraction of the reservoir mixture ($\alpha_g^\omega$) can be calculated using the method of Rachford and Rice (1952) as a function of vapor-liquid equilibrium ratio and compositional mass fraction ($z_m^\omega$). The function of Rachford-Rice for multicomponent as introduced in the PBM is illustrated by equation (D.5a). Warren and Adewumi (1993) extended the summation of Rachford-Rice equation and used mathematical manipulation to present equation (D.5a) for binary, ternary and quaternary systems. Since the focus of this study is binary systems, the equilibrium mass vapor fraction is calculated using the binary representation of the objective function given by equation (D.5b).

$$K_m^\omega = \frac{\omega_{mg}}{\omega_{mo}} \quad ; \quad m = 1, 2 \qquad \text{(D.4)}$$

$$f\left(\alpha_g^\omega\right) = \sum_{m=1}^{n_c} \frac{z_m^\omega (K_m^\omega - 1)}{1 + \alpha_g^\omega (K_m^\omega - 1)} = 0 \qquad \text{(D.5a)}$$

$$f\left(\alpha_g^\omega\right) = -\left[\frac{z_1^\omega}{(K_2^\omega - 1)} + \frac{z_2^\omega}{(K_1^\omega - 1)}\right] \qquad \text{(D.5b)}$$

where:

$$z_m^\omega = \frac{z_m MW_m}{\sum_{m=1}^{n_c} z_m MW_m} \quad ; \quad m = 1,2 \qquad \text{(D.5c)}$$

$$\sum_{m=1}^{n_c} z_m^\omega = 1 \qquad \text{(D.5d)}$$

Properties such as densities at standard conditions will be calculated using the standard PVT property procedures introduced in Appendix C. While, viscosity of each phase can be either provided with PVT data as a function of pressure, or can be calculated using Lohrenz *et al.* (1964) empirical correlation. Using the fluid properties and the equilibrium mass vapor fraction, gas saturation can be calculated by establishing a mass-based relationship similar to the molar relationship shown by equation (4.16n). Equation (D.6a) through equation (D.6j), capture the derivation of a mass-based relationship between saturation and equilibrium mass vapor fraction. Initially, saturations are expressed in specific volume ratios to yield mass fractions.

$$S_g = \frac{V_g}{V_T} = \frac{v_g}{v_T}\frac{m_g}{m_T} = \alpha_g^{\omega}\frac{v_g}{v_T} \tag{D.6a}$$

$$S_o = \frac{V_o}{V_T} = \frac{v_o}{v_T}\frac{n_o}{n_T} = \alpha_o^{\omega}\frac{v_o}{v_T} \tag{D.6b}$$

Substituting the definitions of saturation into equation (4.16b) to simplify the conversion in terms of specific densities and avoid calculating the total specific volume of the mixture.

$$S_o = \frac{\alpha_o^{\omega}\frac{v_o}{v_T}}{\left(\alpha_o^{\omega}\frac{v_o}{v_T} + \alpha_g^{\omega}\frac{v_g}{v_T}\right)}\ (1 - S_w) \tag{D.6c}$$

Eliminating the total specific volume of the mixture by multiplying and dividing the RHS of equation (D.6c) by the total specific volume yields:

$$S_o = \frac{v_T}{v_T}\frac{\alpha_o^{\omega}\frac{v_o}{v_T}}{\left(\alpha_o^{\omega}\frac{v_o}{v_T} + \alpha_g^{\omega}\frac{v_g}{v_T}\right)}\ (1 - S_w) = \frac{\alpha_o^{\omega}v_o}{\left(\alpha_o^{\omega}v_o + \alpha_g^{\omega}v_g\right)}\ (1 - S_w) \tag{D.6d}$$

Since specific volume is the reciprocal of specific density, converting specific volume to specific density shall provide and expression of oil saturation in terms of mass fraction.

$$S_o = \frac{\alpha_o^{\omega} \frac{1}{\rho_o}}{\left(\alpha_o^{\omega} \frac{1}{\rho_o} + \alpha_g^{\omega} \frac{1}{\rho_g}\right)} \ (1 - S_w) \tag{D.6e}$$

Equation (D.6e) is re-arranged by mathematical manipulation as follows:

$$S_o = \frac{\rho_g \rho_o}{\rho_g \rho_o} \frac{\alpha_o^{\omega} \frac{1}{\rho_o}}{\left(\alpha_o^{\omega} \frac{1}{\rho_o} + \alpha_g^{\omega} \frac{1}{\rho_g}\right)} \ (1 - S_w) = \frac{\alpha_o^{\omega} \rho_g}{\left(\alpha_o^{\omega} \rho_g + \alpha_g^{\omega} \rho_o\right)} \ (1 - S_w) \tag{D.6f}$$

The final form of the relationship between saturation and the equilibrium mass fraction is written in terms of fluid densities and mass vapor fraction as shown by equation (D.6g).

$$S_o = \frac{\left(1 - \alpha_g^{\omega}\right)\rho_g}{\left(\left(1 - \alpha_g^{\omega}\right)\rho_g + \alpha_g^{\omega} \rho_o\right)} \ (1 - S_w) \tag{D.6g}$$

Equation (D.6g) can be defined explicitly in terms of $\alpha_g^{\omega}$and $S_g$ with proper handling of variables similar to the previous re-arrangements with the molar vapor fraction and gas saturation. Simply, the relationship between $\alpha_g^{\omega}$ and $S_g$ is represented by the following equations:

$$\alpha_g^{\omega} = \frac{\rho_g S_g}{\rho_o S_o + \rho_g S_g} \tag{D.6h}$$

$$S_g = \frac{\alpha_g^{\omega} \rho_o S_o}{\rho_g (1 - \alpha_g^{\omega})} \tag{D.6i}$$

Substituting the definition of $S_o$ from equation (D.6g) into equation (D.6i) will show $S_g$ in its final form as a function of pressure:

$$S_g = \frac{\frac{\alpha_g^{\omega} \rho_o}{\rho_g - \alpha_g^{\omega} \rho_g}(1 - S_w)}{\left(1 + \frac{\alpha_g^{\omega} \rho_o}{\rho_g - \alpha_g^{\omega} \rho_g}\right)} \tag{D.6j}$$

**D.2 Formulations of fluid-in-place**

In contrast to the formulation of compositional simulators for the original gas and condensate in place, modified black-oil models are designed based on CCE and CVD experiments as presented in Appendix C that provides data in terms of gas and oil. Because the PVT experiments provide data in relation to the phases, the calculations of fluids in place for MBO simulators are limited.

The total amount of fluids in place analysis is carried based on separator experiment and recovery analysis from a typical PVT report as presented in Appendix C. Estimating the fluids in place is possible after evaluating the initial gas formation volume factor ($B_{gi}$) and the initial condensate formation volume factor ($B_{oi}$) in the case of a saturated reservoir. Reservoirs with condensate present at initial conditions require the use of equations (D.7a) and (D.7b) with the consideration of the initial formation volume factor expressions demonstrated in Appendix C.

$$OGIP\ (scf) = 43560\ A\ h\ \phi\ \left[\frac{S_{gi}}{B_{gi}} + R_{si}\frac{S_{oi}}{B_{oi}}\right] \quad ; \quad S_{oi} > 0 \tag{D.7a}$$

$$OCIP\ (stb) = 43560\ A\ h\ \phi\ \left[\frac{S_{gi}}{B_{gi}} R_{vi} + \frac{S_{oi}}{B_{oi}}\right] \quad ; \quad S_{oi} > 0 \tag{D.7b}$$

Reservoirs which are presented in a single gaseous state at initial conditions commonly referred to as undersaturated gas reservoirs, use a collapsed form of equations (D.7a) and (D.7b). Expressions which eliminate the existence of initial condensate saturation in its form as shown below:

$$OGIP\ (scf) = 43560\ A\ h\ \phi\ \left[\frac{S_{gi}}{B_{gi}}\right] \quad ; \quad S_{oi} \leq 0 \tag{D.8a}$$

$$OCIP\ (stb) = R_{vi}\ \ OGIP \quad ; \quad S_{oi} \leq 0 \tag{D.8b}$$

Fluids remaining in place are taken as the difference between original fluids in place and cumulative production shown by equations (D.9a) and (D.9b).

$$GIP\ (scf) = OGIP - G_P \tag{D.9a}$$

$$CIP\ (stb) = OCIP - N_P \tag{D.9b}$$

where:

$$G_P = \int_t q_{sc,g}\, dt \tag{D.9c}$$

$$N_P = \int_t q_{sc,o}\, dt \tag{D.9d}$$

$G_P$: cumulative production of surface gas, *scf*

$N_P$: cumulative production of surface oil, *stb*

$q_{sc,g}$ : gas production at stock tank conditions, *scfD*

$q_{sc,o}$ : oil production at stock tank conditions, *stbD*

Lastly, assessing liquid-rich gas reservoirs production with MBO simulators is achieved through calculating condensate content in gas stream. The initial and current amount of volatilized condensate in the gas phase ($R_{vi}$) and ($R_v$) are determined as displayed previously by equations (4.49) and (4.50).

**D.3 Surface production for MBO**

Genuinely, fluids change volumes through its journey from reservoir conditions at high pressure to a lower pressure condition at surface. The change in volumes are captured with the calculation of formation volume factors, which reflect the ratio of reservoir volume to the volume at stock tank conditions. The ratio of volumes can be expressed as specific volume or molar volume easily, because the volumes reflect the same quantity of mass being transferred from reservoir to surface.

$$B_f\left(\frac{res\ volume}{surface\ volume}\right) = \frac{V_f}{V_{fsc}} = \frac{V_f/m}{V_{fsc}/m} = \frac{v_f}{v_{fsc}} \tag{D.10}$$

Equations (D.11a) and (D.11b) illustrate those definition and shows apparent relationship to the density of each phase respectively.

$$B_g\left(\frac{rb}{scf}\right) = \frac{v_g}{v_{gsc}} = \frac{\rho_{gsc}}{\rho_g \; 5.615 \; \left(\frac{ft^3}{rb}\right)} \tag{D.11a}$$

$$B_o\left(\frac{rb}{stb}\right) = \frac{v_o}{v_{osc}} = \frac{\rho_{osc} \; 5.615 \; \left(\frac{scf}{stb}\right)}{\rho_o \; 5.615 \; \left(\frac{ft^3}{rb}\right)} \tag{D.11b}$$

As presented in Appendix C, the attained volume factors of gas and oil using standard PVT calculations were done at and below dew point pressure. Above dew point pressure, there is only one phase existing in the reservoir meaning formation volume factor of oil is taken as zero. However, the gas formation volume factor is calculated at each pressure level above dew point pressure using equation (D.12).

$$B_{g,j}\left(\frac{rb}{scf}\right) = \frac{\frac{R\,T\,Z}{p\,MW}}{\frac{R\,T_{sc}\,Z_{gsc}}{p_{sc}\,MW}} = \frac{p_{sc}\,T_j\,Z_j}{T_{sc}\,p_j \; 5.615 \; \left(\frac{ft^3}{rb}\right)} \quad ; \quad j = 1, 2, \ldots n_p \tag{D.12}$$

In accordance with the mass formulation of the governing equation presented in equations (4.11b) and (4.11c) for the gas phase, the source term is expressed as:

$$\frac{Q_g^{\omega}}{\rho_{gsc}}\left(\frac{scf}{day}\right) = q_{sc,g} \tag{D.13a}$$

The gas mass rate in (*lbm/day*) at surface is defined using equation (D.13b) by re-arranging terms.

$$Q_g^{\omega}\left(\frac{lbm}{day}\right) = q_{sc,g}\,\rho_{gsc} \tag{D.13b}$$

Using the same analogies, reservoir mass rate is presented in terms of reservoir flow rate and density.

$$Q_g^{\omega}\left(\frac{lbm}{day}\right) = q_{res,g}\,\rho_g\,5.615\left(\frac{ft^3}{rb}\right) \tag{D.13c}$$

The displacement of fluids from reservoir to surface reflects the same quantity of mass; thus, equations of (D.13b) and (D.13c) are equated together to solve for surface gas rate.

$$q_{sc,g}\,\rho_{gsc} = q_{res,g}\,\rho_g\,5.615\left(\frac{ft^3}{rb}\right) \tag{D.13d}$$

$$q_{sc,g}\left(\frac{scf}{day}\right) = \frac{q_{res,g}\,\rho_g\,5.615\left(\frac{ft^3}{rb}\right)}{\rho_{gsc}} \tag{D.13e}$$

Substituting in the definition of gas formation volume factor from equation (D.11a), demonstrate the final form for surface gas rate in the MBO formulation.

$$q_{sc,g}\left(\frac{scf}{day}\right) = \frac{q_{res,g}}{B_g} \tag{D.13f}$$

Likewise, the oil phase source term is illustrated below with respect to the mass formulation of the oil phase of the two-component system presented in equations (4.12b) and (4.12c).

$$\frac{Q_o^{\omega}}{5.615\left(\frac{scf}{stb}\right)\rho_{osc}}\left(\frac{stb}{day}\right) = q_{sc,o} \tag{D.14a}$$

Equation (D.14a) can be expressed in oil mass rate (*lbm/day*) as a function of surface flow rate and density as follows:

$$Q_o^{\omega}\left(\frac{lbm}{day}\right) = q_{sc,o}\,\rho_{osc}5.615\left(\frac{scf}{stb}\right) \tag{D.14b}$$

Oil mass rate can also be presented in terms of reservoir flow rate and density as shown by equation (D.14c)

$$Q_o^{\omega}\left(\frac{stb}{day}\right) = q_{res,o}\,\rho_o\,5.615\,\left(\frac{ft^3}{rb}\right) \qquad \text{(D.14c)}$$

Equating equations (D.14b) and (D.14c) yield the following expression, which represent flow rate of oil at surface conditions:

$$q_{sc,o}\left(\frac{stb}{day}\right) = \frac{q_{res,o}\,\rho_o\,5.615\,\left(\frac{ft^3}{rb}\right)}{\rho_{osc}\,5.615\,\left(\frac{scf}{stb}\right)} \qquad \text{(D.14d)}$$

Substituting in the definition of oil formation volume factor from equation (4.8b), provide the final form for surface oil rate.

$$q_{sc,o}\left(\frac{stb}{day}\right) = \frac{q_{res,o}}{B_o} \qquad if\ \ p_{res} \le p_{dew} \qquad \text{(4.14e)}$$

where $q_{sc,o}\left(\frac{stb}{day}\right) = 0 \qquad if\ \ p_{res} > p_{dew}$

# Appendix E

## RESULT TABLES OF CAPILLARY RELATIONSHIPS

**Table E.1: Higher and lower dew-point for methane 70% - decane 30%**

| | | Higher Pdew* | | | | Lower Pdew** | | | |
|---|---|---|---|---|---|---|---|---|---|
| 1/r (1/nm) | r (nm) | Pcgo (psia) | Pdew (psia) | IFT (dyne/cm) | Pdew Diff (psia) | Pcgo (psia) | Pdew psia | IFT (dyne/cm) | Pdew Diff (psia) |
| 0.00 | ∞ | 0.0000 | 1467.35 | 0.04308 | 0.00 | 0.0000 | 1031.69 | 0.25424 | 0.00 |
| 0.05 | 20.00 | 0.3039 | 1478.57 | 0.03966 | 11.22 | 4.9056 | 986.09 | 0.27938 | -45.60 |
| 0.10 | 10.00 | 0.6077 | 1490.17 | 0.03624 | 22.82 | 9.8111 | 952.30 | 0.29659 | -79.39 |
| 0.15 | 6.67 | 0.9112 | 1502.23 | 0.03281 | 34.88 | 14.7094 | 924.87 | 0.30918 | -106.82 |
| 0.20 | 5.00 | 1.2155 | 1514.94 | 0.02931 | 47.59 | 19.6223 | 901.42 | 0.31861 | -130.27 |
| 0.25 | 4.00 | 1.5194 | 1528.46 | 0.02573 | 61.11 | 24.5279 | 880.86 | 0.32558 | -150.83 |
| 0.30 | 3.33 | 1.8251 | 1543.22 | 0.02196 | 75.87 | 29.4629 | 862.33 | 0.33059 | -169.36 |
| 0.35 | 2.86 | 2.1250 | 1559.42 | 0.01794 | 92.07 | 34.3047 | 845.79 | 0.33383 | -185.90 |

* $P_{gi}^{(n)}$ for the higher dew-point pressure is 1225.4 psia

** $P_{gi}^{(n)}$ for the lower dew-point pressure is 1108 psia

**Table E.2: Effect of changing $P_{gi}^{(n)}$ on dew-point for methane 70% - decane 30%**

| | | Higher Pdew* | | | | Lower Pdew** | | | |
|---|---|---|---|---|---|---|---|---|---|
| 1/r (1/nm) | r (nm) | Pcgo (psia) | Pdew (psia) | IFT (dyne/cm) | Pdew Diff (psia) | Pcgo (psia) | Pdew psia | IFT (dyne/cm) | Pdew Diff (psia) |
| 0.00 | ∞ | 0.0000 | 1467.35 | 0.04308 | 0.00 | 0.0000 | 1031.69 | 0.25424 | 0.00 |
| 0.05 | 20.00 | 0.2162 | 1475.30 | 0.04065 | 7.95 | 6.9310 | 971.14 | 0.28719 | -60.55 |
| 0.10 | 10.00 | 0.4324 | 1483.42 | 0.03822 | 16.07 | 13.8621 | 929.28 | 0.30726 | -102.41 |
| 0.15 | 6.67 | 0.6482 | 1491.75 | 0.03578 | 24.40 | 20.7827 | 896.33 | 0.32046 | -135.36 |
| 0.20 | 5.00 | 0.8647 | 1500.34 | 0.03334 | 32.99 | 27.7242 | 868.64 | 0.32904 | -163.05 |
| 0.25 | 4.00 | 1.0809 | 1509.23 | 0.03087 | 41.88 | 34.6552 | 844.64 | 0.33401 | -187.05 |
| 0.30 | 3.33 | 1.2983 | 1518.53 | 0.02835 | 51.18 | 41.6279 | 823.19 | 0.33595 | -208.50 |
| 0.35 | 2.86 | 1.5117 | 1528.10 | 0.02583 | 60.75 | 48.4688 | 804.14 | 0.33519 | -227.55 |

* $P_{gi}^{(n)}$ for the higher dew-point pressure is 1125.4 psia

** $P_{gi}^{(n)}$ for the lower dew-point pressure is 1208 psia

**Table E.3: Capillary, dew-point pressure, and IFT for methane 85% - butane 15%**

| | T=50 F - Pgi=1677 psia | | | T=70 F - Pgi=1623.9 psia | | | T=100 F - Pgi=1354.9 psia | | |
|---|---|---|---|---|---|---|---|---|---|
| r (nm) | Pcgo (psia) | Pdew (psia) | IFT (dyne/cm) | Pcgo (psia) | Pdew (psia) | IFT (dyne/cm) | Pcgo (psia) | Pdew (psia) | IFT (dyne/cm) |
| ∞ | 0.0000 | 1945.53 | 0.01605 | 0.0000 | 1892.36 | 0.07916 | 0.0000 | 1623.39 | 0.56734 |
| 20.00 | 0.1285 | 1946.87 | 0.01501 | 0.6226 | 1895.54 | 0.07384 | 3.9926 | 1634.29 | 0.52425 |
| 10.00 | 0.2570 | 1948.27 | 0.01392 | 1.2453 | 1898.86 | 0.06828 | 7.9853 | 1645.77 | 0.47961 |
| 6.67 | 0.3853 | 1949.73 | 0.01276 | 1.8669 | 1902.35 | 0.06340 | 11.9719 | 1657.93 | 0.43299 |
| 5.00 | 0.5139 | 1951.28 | 0.01150 | 2.4905 | 1906.06 | 0.05605 | 15.9705 | 1671.04 | 0.38325 |
| 4.00 | 0.6424 | 1952.94 | 0.01009 | 3.1131 | 1910.06 | 0.04900 | 19.9631 | 1685.36 | 0.32897 |
| 3.33 | 0.7717 | 1954.75 | 0.00838 | 3.7395 | 1914.50 | 0.04057 | 23.9797 | 1701.64 | 0.26560 |
| 2.86 | 0.8985 | 1956.82 | 0.00553 | 4.3540 | 1919.59 | 0.02774 | 27.9205 | 1721.28 | 0.17464 |

**Table E.4: Capillary, dew-point pressure, and IFT for methane 70% - butane 30%**

| | T=170 F - Pgi=1285.5 psia | | | |
|---|---|---|---|---|
| r (nm) | Pcgo (psia) | Pdew (psia) | IFT (dyne/cm) | Pdew Diff (psia) |
| ∞ | 0.0000 | 1554.04 | 0.09409 | 0.00 |
| 20.00 | 0.6390 | 1559.59 | 0.08688 | 5.55 |
| 10.00 | 1.2779 | 1565.44 | 0.07943 | 11.40 |
| 6.67 | 1.9160 | 1571.65 | 0.07167 | 17.62 |
| 5.00 | 2.5559 | 1578.35 | 0.06344 | 24.31 |
| 4.00 | 3.1949 | 1585.65 | 0.05454 | 31.62 |
| 3.33 | 3.8377 | 1593.94 | 0.04429 | 39.90 |
| 2.86 | 4.4683 | 1603.79 | 0.03057 | 49.75 |

**Table E.5: Capillary, dew-point pressure, and IFT for methane 60% - butane 40%**

| | T= 200 F - Pgi=1188.5 psia | | | |
|---|---|---|---|---|
| r (nm) | Pcgo (psia) | Pdew (psia) | IFT (dyne/cm) | Pdew Diff (psia) |
| ∞ | 0.0000 | 1457.00 | 0.01682 | 0.00 |
| 20.00 | 0.1080 | 1459.16 | 0.01572 | 2.16 |
| 10.00 | 0.2160 | 1461.43 | 0.01458 | 4.43 |
| 6.67 | 0.3238 | 1463.81 | 0.01340 | 6.81 |
| 5.00 | 0.4319 | 1466.34 | 0.01215 | 9.34 |
| 4.00 | 0.5399 | 1469.04 | 0.01083 | 12.04 |
| 3.33 | 0.6485 | 1472.00 | 0.00937 | 15.00 |
| 2.86 | 0.7551 | 1475.25 | 0.00770 | 18.25 |

**Table E.6: Capillary, dew-point pressure, and IFT for methane 85% - hexane 15%**

| | T=150 F - Pgi=2719.2 psia | | | T=200 F - Pgi=2403.6 psia | | | T=250 F - Pgi=1665.5 psia | | |
|---|---|---|---|---|---|---|---|---|---|
| r (nm) | Pcgo (psia) | Pdew (psia) | IFT (dyne/cm) | Pcgo (psia) | Pdew (psia) | IFT (dyne/cm) | Pcgo (psia) | Pdew (psia) | IFT (dyne/cm) |
| ∞ | 0.0000 | 2990.18 | 0.00158 | 0.0000 | 2674.63 | 0.04411 | 0.0000 | 1936.52 | 0.54994 |
| 20.00 | 0.0157 | 2990.95 | 0.00150 | 0.4173 | 2678.98 | 0.04136 | 4.3640 | 1957.25 | 0.50455 |
| 10.00 | 0.0313 | 2991.74 | 0.00141 | 0.8346 | 2683.52 | 0.03849 | 8.7280 | 1979.09 | 0.45786 |
| 6.67 | 0.0470 | 2992.56 | 0.00132 | 1.2513 | 2688.26 | 0.03548 | 13.0855 | 2002.26 | 0.40947 |
| 5.00 | 0.0627 | 2993.42 | 0.00122 | 1.6692 | 2693.27 | 0.03227 | 17.4561 | 2027.28 | 0.35828 |
| 4.00 | 0.0783 | 2994.31 | 0.00111 | 2.0865 | 2698.59 | 0.02878 | 21.8201 | 2054.75 | 0.30280 |
| 3.33 | 0.0941 | 2995.26 | 0.00099 | 2.5063 | 2704.37 | 0.02481 | 26.2103 | 2086.28 | 0.23831 |
| 2.86 | 0.1096 | 2996.26 | 0.00085 | 2.9182 | 2710.67 | 0.01997 | 30.5176 | 2125.70 | 0.13925 |

**Table E.7: Capillary, dew-point pressure, and IFT for methane 70% - hexane 30%**

| | T=310 F - Pgi=1710.6 psia | | | |
|---|---|---|---|---|
| r (nm) | Pcgo (psia) | Pdew (psia) | IFT (dyne/cm) | Pdew Diff (psia) |
| ∞ | 0.0000 | 1981.61 | 0.00948 | 0.00 |
| 20.00 | 0.0763 | 1983.87 | 0.00887 | 2.26 |
| 10.00 | 0.1526 | 1986.23 | 0.00824 | 4.62 |
| 6.67 | 0.2289 | 1988.70 | 0.00758 | 7.09 |
| 5.00 | 0.3053 | 1991.32 | 0.00688 | 9.71 |
| 4.00 | 0.3816 | 1994.11 | 0.00612 | 12.50 |
| 3.33 | 0.4584 | 1997.14 | 0.00527 | 15.53 |
| 2.86 | 0.5337 | 2000.46 | 0.00425 | 18.85 |

**Table E.8: Capillary, dew-point pressure, and IFT for methane 60% - hexane 40%**

| | T=350 F - Pgi=1478 psia | | | |
|---|---|---|---|---|
| r (nm) | Pcgo (psia) | Pdew (psia) | IFT (dyne/cm) | Pdew Diff (psia) |
| ∞ | 0.0000 | 1624.00 | 0.00278 | 0.00 |
| 20.00 | 0.0209 | 1625.24 | 0.00261 | 1.24 |
| 10.00 | 0.0418 | 1626.52 | 0.00243 | 2.52 |
| 6.67 | 0.0628 | 1627.87 | 0.00224 | 3.87 |
| 5.00 | 0.0837 | 1629.29 | 0.00205 | 5.29 |
| 4.00 | 0.1046 | 1630.80 | 0.00183 | 6.80 |
| 3.33 | 0.1257 | 1632.43 | 0.00160 | 8.43 |
| 2.86 | 0.1463 | 1634.20 | 0.00132 | 10.20 |

**Table E.9: Capillary, dew-point pressure, and IFT for methane 85% - decane 15%**

| | T=450 F - Pgi=2400.9 | | | |
|---|---|---|---|---|
| r (nm) | Pcgo (psia) | Pdew (psia) | IFT (dyne/cm) | Pdew Diff (psia) |
| ∞ | 0.0000 | 2642.88 | 0.05539 | 0.00 |
| 20.00 | 0.5471 | 2650.54 | 0.05270 | 7.66 |
| 10.00 | 1.0942 | 2658.45 | 0.04996 | 15.57 |
| 6.67 | 1.6405 | 2666.62 | 0.04715 | 23.74 |
| 5.00 | 2.1884 | 2675.13 | 0.04424 | 32.25 |
| 4.00 | 2.7355 | 2683.98 | 0.04124 | 41.10 |
| 3.33 | 3.2859 | 2693.30 | 0.03809 | 50.42 |
| 2.86 | 3.8259 | 2702.95 | 0.03482 | 60.07 |

**Table E.10: Capillary, dew-point pressure, and IFT for methane 70% - decane 30%**

| | T=515 F - Pgi=1982.6 | | | T=530 F - Pgi=1744.3 | | | T=540 F - Pgi=1541.2 | | |
|---|---|---|---|---|---|---|---|---|---|
| r (nm) | Pcgo (psia) | Pdew (psia) | IFT (dyne/cm) | Pcgo (psia) | Pdew (psia) | IFT (dyne/cm) | Pcgo (psia) | Pdew (psia) | IFT (dyne/cm) |
| ∞ | 0.0000 | 2224.55 | 0.00002 | 0.0000 | 1986.30 | 0.00117 | 0.0000 | 1783.22 | 0.00681 |
| 20.00 | 0.0002 | 2224.67 | 0.00002 | 0.0101 | 1987.26 | 0.00112 | 0.0551 | 1785.87 | 0.00648 |
| 10.00 | 0.0004 | 2224.79 | 0.00002 | 0.0201 | 1988.24 | 0.00107 | 0.1103 | 1788.60 | 0.00615 |
| 6.67 | 0.0006 | 2224.92 | 0.00002 | 0.0302 | 1989.25 | 0.00102 | 0.1653 | 1791.43 | 0.00580 |
| 5.00 | 0.0008 | 2225.04 | 0.00002 | 0.0402 | 1990.29 | 0.00097 | 0.2206 | 1794.37 | 0.00545 |
| 4.00 | 0.0010 | 2225.18 | 0.00002 | 0.0503 | 1991.37 | 0.00091 | 0.2757 | 1797.43 | 0.00508 |
| 3.33 | 0.0012 | 2225.31 | 0.00002 | 0.0604 | 1992.49 | 0.00086 | 0.3312 | 1800.65 | 0.00469 |
| 2.86 | 0.0014 | 2225.45 | 0.00002 | 0.0703 | 1993.64 | 0.00080 | 0.3856 | 1803.99 | 0.00429 |

**Table E.11: Capillary, dew-point pressure, and IFT for methane 70% - decane 30% (cont.)**

| | T=545 F - Pgi=1410.6 | | | T=550 F - Pgi=1225.4 | | |
|---|---|---|---|---|---|---|
| r (nm) | Pcgo (psia) | Pdew (psia) | IFT (dyne/cm) | Pcgo (psia) | Pdew (psia) | IFT (dyne/cm) |
| ∞ | 0.0000 | 1652.62 | 0.01597 | 0.0000 | 1467.35 | 0.04308 |
| 20.00 | 0.1229 | 1657.29 | 0.01508 | 0.3039 | 1478.57 | 0.03966 |
| 10.00 | 0.2458 | 1662.14 | 0.01417 | 0.6077 | 1490.17 | 0.03624 |
| 6.67 | 0.3688 | 1667.17 | 0.01324 | 0.9112 | 1502.23 | 0.03281 |
| 5.00 | 0.4917 | 1672.44 | 0.01228 | 1.2155 | 1514.94 | 0.02931 |
| 4.00 | 0.6146 | 1677.97 | 0.01130 | 1.5194 | 1528.46 | 0.02573 |
| 3.33 | 0.7383 | 1683.87 | 0.01026 | 1.8251 | 1543.22 | 0.02296 |
| 2.86 | 0.8596 | 1690.06 | 0.00918 | 2.1250 | 1559.42 | 0.01794 |

**Table E.12: Capillary, dew-point pressure, and IFT for methane 60% - decane 40%**

| | T=575 F - Pgi=1094.9 | | | |
|---|---|---|---|---|
| r (nm) | Pcgo (psia) | Pdew (psia) | IFT (dyne/cm) | Pdew Diff (psia) |
| ∞ | 0.0000 | 1336.94 | 0.00403 | 0.00 |
| 20.00 | 0.0263 | 1338.98 | 0.00384 | 2.04 |
| 10.00 | 0.0526 | 1341.08 | 0.00364 | 4.14 |
| 6.67 | 0.0788 | 1343.26 | 0.00343 | 6.32 |
| 5.00 | 0.1052 | 1345.52 | 0.00323 | 8.58 |
| 4.00 | 0.1315 | 1347.88 | 0.00301 | 10.94 |
| 3.33 | 0.1579 | 1350.37 | 0.00279 | 13.43 |
| 2.86 | 0.1839 | 1352.94 | 0.00256 | 16.00 |

**Table E.13: Capillary data for higher dew-point at 10 nm for methane 85% - butane 15%**

| Temp (F) | Pdew w/o Pcgo (psia) | Pgi (psia) | Pcgo (psia) | Pdew w/Pcgo (psia) | IFT (dyne/cm) | Pdew Difference (psia) |
|---|---|---|---|---|---|---|
| 25 | 1920.16 | **1808.46** | 0.0154 | 1920.95 | 0.00055 | 0.79 |
| 30 | 1932.45 | **1820.75** | 0.0357 | 1933.65 | 0.00126 | 1.20 |
| 35 | 1941.25 | **1829.55** | 0.0721 | 1942.98 | 0.00255 | 1.73 |
| 40 | 1946.46 | **1834.76** | 0.1324 | 1948.81 | 0.00467 | 2.35 |
| 50 | 1945.53 | **1833.83** | 0.3674 | 1949.52 | 0.01293 | 3.99 |
| 60 | 1928.20 | **1816.50** | 0.8588 | 1934.52 | 0.03014 | 6.32 |
| 70 | 1892.36 | **1780.66** | 1.8003 | 1901.96 | 0.06306 | 9.60 |
| 80 | 1834.64 | **1722.94** | 3.5205 | 1849.05 | 0.12307 | 14.41 |
| 90 | 1749.11 | **1637.41** | 6.6203 | 1771.11 | 0.23076 | 22.00 |
| 100 | 1623.39 | **1511.69** | 12.3740 | 1659.21 | 0.42812 | 35.82 |
| 110 | 1418.94 | **1307.24** | 24.6670 | 1492.24 | 0.82066 | 73.30 |
| 115 | 1212.60 | **1100.90** | 40.3849 | 1378.79 | 1.13773 | 166.19 |

**Table E.14: Capillary data for lower dew-point at 10 nm for methane 85% - butane 15%**

| Temp (F) | Pdew w/o Pcgo (psia) | Pgi (psia) | Pcgo (psia) | Pdew w/Pcgo (psia) | IFT (dyne/cm) | Pdew Difference (psia) |
|---|---|---|---|---|---|---|
| 115 | 926.06 | **1050.00** | 181.0702 | 703.16 | 4.90515 | -222.90 |
| 114 | 868.29 | **992.23** | 208.5308 | 665.92 | 5.17365 | -202.37 |
| 113 | 824.67 | **948.61** | 232.1370 | 635.2000 | 5.40946 | -189.47 |
| 112 | 788.42 | **912.36** | 253.9948 | 608.2900 | 5.62565 | -180.13 |
| 111 | 756.93 | **880.87** | 274.9061 | 584.0500 | 5.82772 | -172.88 |
| 110 | 728.85 | **852.79** | 295.3082 | 561.8300 | 6.01882 | -167.02 |

**Table E.15: Capillary data for higher dew-point at 10 nm for methane 85% - hexane 15%**

| Temp (F) | Pdew w/o Pcgo (psia) | Pgi (psia) | Pcgo (psia) | Pdew w/Pcgo (psia) | IFT (dyne/cm) | Pdew Difference (psia) |
|---|---|---|---|---|---|---|
| 125 | 3051.56 | **2920.94** | 0.0018 | 3051.96 | 0.00006 | 0.40 |
| 150 | 2990.18 | **2859.56** | 0.0383 | 2992.10 | 0.00137 | 1.92 |
| 175 | 2867.62 | **2737.00** | 0.2510 | 2872.76 | 0.00889 | 5.14 |
| 200 | 2674.63 | **2544.01** | 1.0474 | 2685.91 | 0.03697 | 11.28 |
| 225 | 2389.16 | **2258.54** | 3.5755 | 2412.89 | 0.12597 | 23.73 |
| 250 | 1936.52 | **1805.90** | 12.0646 | 1996.69 | 0.42101 | 60.17 |
| 260 | 1617.22 | **1486.60** | 22.2011 | 1742.19 | 0.73247 | 124.97 |
| 262 | 1512.66 | **1382.04** | 26.3288 | 1680.63 | 0.82247 | 167.97 |
| 263 | 1440.62 | **1310.00** | 29.3949 | 1651.38 | 0.86314 | 210.76 |

**Table E.16: Capillary data for lower dew-point at 10 nm for methane 85% - hexane 15%**

| Temp (F) | Pdew w/o Pcgo (psia) | Pgi (psia) | Pcgo (psia) | Pdew w/Pcgo (psia) | IFT (dyne/cm) | Pdew Difference (psia) |
|---|---|---|---|---|---|---|
| 262 | 1025.28 | **1110.28** | 117.1828 | 814.4200 | 3.54220 | -210.86 |
| 260 | 936.17 | **1021.17** | 138.4244 | 753.4500 | 3.84587 | -182.72 |
| 258 | 869.86 | **954.86** | 157.0806 | 704.0900 | 4.11490 | -165.77 |
| 256 | 815.57 | **900.57** | 174.6254 | 661.7400 | 4.36265 | -153.83 |
| 254 | 769.04 | **854.04** | 191.6480 | 624.3100 | 4.59519 | -144.73 |
| 252 | 728.08 | **813.08** | 208.4569 | 590.6200 | 4.81591 | -137.46 |
| 250 | 691.37 | **776.37** | 225.2495 | 559.9000 | 5.02702 | -131.47 |

**Table E.17: Capillary data for higher dew-point at 10 nm for methane 70% - decane 30%**

| Temp (F) | Pdew w/o Pcgo (psia) | Pgi (psia) | Pcgo (psia) | Pdew w/Pcgo (psia) | IFT (dyne/cm) | Pdew Difference (psia) |
|---|---|---|---|---|---|---|
| 515 | 2224.55 | **1982.55** | 0.0004 | 2224.79 | 0.00002 | 0.24 |
| 520 | 2151.00 | **1909.00** | 0.0021 | 2151.58 | 0.00011 | 0.58 |
| 530 | 1986.30 | **1744.30** | 0.0201 | 1988.24 | 0.00107 | 1.94 |
| 540 | 1783.22 | **1541.22** | 0.1103 | 1788.60 | 0.00615 | 5.38 |
| 545 | 1652.62 | **1410.62** | 0.2458 | 1662.14 | 0.01417 | 9.52 |
| 547 | 1589.16 | **1347.16** | 0.3441 | 1601.75 | 0.02013 | 12.59 |
| 549 | 1513.38 | **1271.38** | 0.4955 | 1531.36 | 0.02942 | 17.98 |
| 550 | 1467.35 | **1225.35** | 0.6077 | 1490.17 | 0.03624 | 22.82 |

**Table E.18: Capillary data for lower dew-point at 10 nm for methane 70% - decane 30%**

| Temp (F) | Pdew w/o Pcgo (psia) | Pgi (psia) | Pcgo (psia) | Pdew w/Pcgo (psia) | IFT (dyne/cm) | Pdew Difference (psia) |
|---|---|---|---|---|---|---|
| 550 | 1031.69 | **1108.00** | 9.8112 | 952.30 | 0.29659 | -79.39 |
| 545 | 881.81 | **958.12** | 17.0283 | 820.08 | 0.44969 | -61.73 |
| 540 | 786.30 | **862.61** | 23.9895 | 731.13 | 0.58885 | -55.17 |
| 520 | 555.74 | **632.05** | 55.6470 | 510.13 | 1.11789 | -45.61 |
| 500 | 417.20 | **493.51** | 97.8782 | 374.89 | 1.63267 | -42.31 |

**Table E.19: Searching for single-phase temp. at 10 nm for methane 85% - butane 15%**

| Pg (psia) | Tdew w/o Pcgo (psia) | Ti (F) | Pcgo (psia) | Tdew w/Pcgo (F) | IFT (dyne/cm) | Tdew Difference (F) |
|---|---|---|---|---|---|---|
| 1400 | 110.65 | **95.65** | 40.3072 | 114.50 | 1.057443366 | 3.85 |
| 1350 | 112.17 | **97.17** | 46.4735 | 116.16 | 1.219449486 | 3.99 |
| 1300 | 113.42 | **98.42** | 53.1433 | 117.56 | 1.394891402 | 4.14 |
| 1250 | 114.42 | **99.42** | 60.3357 | 118.71 | 1.584528612 | 4.29 |
| 1200 | 115.17 | **100.17** | 68.0826 | 119.62 | 1.789080000 | 4.45 |
| 1150 | 115.68 | **100.68** | 76.4096 | 120.29 | 2.009549737 | 4.61 |
| 1100 | 115.95 | **100.95** | 85.3508 | 120.72 | 2.246971925 | 4.77 |
| 1050 | 115.99 | **100.99** | 94.9321 | 120.91 | 2.502479517 | 4.92 |
| 1000 | 115.78 | **100.78** | 105.2097 | 120.86 | 2.777156247 | 5.08 |
| 950 | 115.32 | **100.32** | 116.2245 | 120.57 | 3.072198308 | 5.25 |
| 900 | 114.60 | **99.60** | 128.0302 | 120.01 | 3.389926263 | 5.41 |
| 850 | 113.61 | **98.61** | 140.6850 | 119.20 | 3.730998067 | 5.59 |
| 800 | 112.34 | **97.34** | 154.2509 | 118.10 | 4.098433676 | 5.76 |
| 750 | 110.77 | **95.77** | 168.8082 | 116.69 | 4.494737955 | 5.92 |
| 700 | 108.87 | **93.87** | 184.4591 | 114.97 | 4.921666047 | 6.10 |

**Table E.20: Searching for single-phase temp. at 10 nm for methane 85% - hexane 15%**

| Pg (psia) | Tdew w/o Pcgo (psia) | Ti (F) | Pcgo (psia) | Tdew w/Pcgo (F) | IFT (dyne/cm) | Tdew Difference (F) |
|---|---|---|---|---|---|---|
| 1650 | 259.25 | **255.00** | 29.8877 | 263.10 | 0.863162288 | 3.85 |
| 1600 | 260.38 | **256.13** | 32.8955 | 264.36 | 0.950044201 | 3.98 |
| 1550 | 261.36 | **257.11** | 36.1262 | 265.47 | 1.043495046 | 4.11 |
| 1500 | 262.20 | **257.95** | 39.5858 | 266.44 | 1.143704127 | 4.24 |
| 1450 | 262.89 | **258.64** | 43.2924 | 267.26 | 1.251240166 | 4.37 |
| 1400 | 263.43 | **259.18** | 47.2585 | 267.93 | 1.366509739 | 4.50 |
| 1350 | 263.81 | **259.56** | 51.5045 | 268.45 | 1.489909946 | 4.64 |
| 1300 | 264.02 | **259.77** | 56.0522 | 268.80 | 1.622354811 | 4.78 |
| 1250 | 264.07 | **259.82** | 60.9089 | 268.99 | 1.764103885 | 4.92 |
| 1200 | 263.95 | **259.70** | 66.0975 | 269.00 | 1.916172948 | 5.05 |
| 1150 | 263.64 | **259.39** | 71.6511 | 268.84 | 2.078784268 | 5.20 |
| 1100 | 263.14 | **258.89** | 77.5878 | 268.48 | 2.253378496 | 5.34 |
| 1050 | 262.43 | **258.18** | 83.9444 | 267.93 | 2.440240972 | 5.50 |
| 1000 | 261.51 | **257.26** | 90.7413 | 267.16 | 2.640975398 | 5.65 |
| 950 | 260.37 | **256.12** | 98.0093 | 266.16 | 2.856641549 | 5.79 |
| 900 | 258.97 | **254.72** | 105.8116 | 264.92 | 3.088270974 | 5.95 |
| 850 | 257.31 | **253.06** | 114.1745 | 263.42 | 3.337429658 | 6.11 |
| 800 | 255.37 | **251.12** | 123.1463 | 261.63 | 3.606118726 | 6.26 |
| 750 | 254.00 | **249.75** | 132.1401 | 259.50 | 3.899005409 | 5.50 |

**Table E.21: Searching for single-phase temp. at 10 nm for methane 70% - decane 30%**

| Pg (psia) | Tdew w/o Pcgo (psia) | Ti (F) | Pcgo (psia) | Tdew w/Pcgo (F) | IFT (dyne/cm) | Tdew Difference (F) |
|---|---|---|---|---|---|---|
| 1500 | 549.31 | **545.06** | 1.0819 | 550.19 | 0.032526323 | 0.88 |
| 1450 | 550.34 | **546.09** | 1.3806 | 551.32 | 0.041493043 | 0.98 |
| 1400 | 551.16 | **546.91** | 1.7430 | 552.24 | 0.05239508 | 1.08 |
| 1350 | 551.77 | **547.52** | 2.1780 | 552.97 | 0.065414574 | 1.20 |
| 1300 | 552.17 | **547.92** | 2.6951 | 553.47 | 0.081024212 | 1.30 |
| 1250 | 552.33 | **548.08** | 3.3097 | 553.76 | 0.099442019 | 1.43 |
| 1200 | 552.25 | **548.00** | 4.0337 | 553.80 | 0.121246238 | 1.55 |
| 1150 | 551.91 | **547.66** | 4.8840 | 553.60 | 0.146769571 | 1.69 |
| 1100 | 551.30 | **547.05** | 5.8771 | 553.13 | 0.176644378 | 1.83 |
| 1050 | 550.41 | **546.16** | 7.0308 | 552.37 | 0.211513769 | 1.96 |
| 1000 | 549.21 | **544.96** | 8.3699 | 551.32 | 0.251902109 | 2.11 |
| 950 | 547.67 | **543.42** | 9.9217 | 549.94 | 0.298737097 | 2.27 |
| 900 | 545.79 | **541.54** | 11.7076 | 548.22 | 0.352775889 | 2.43 |

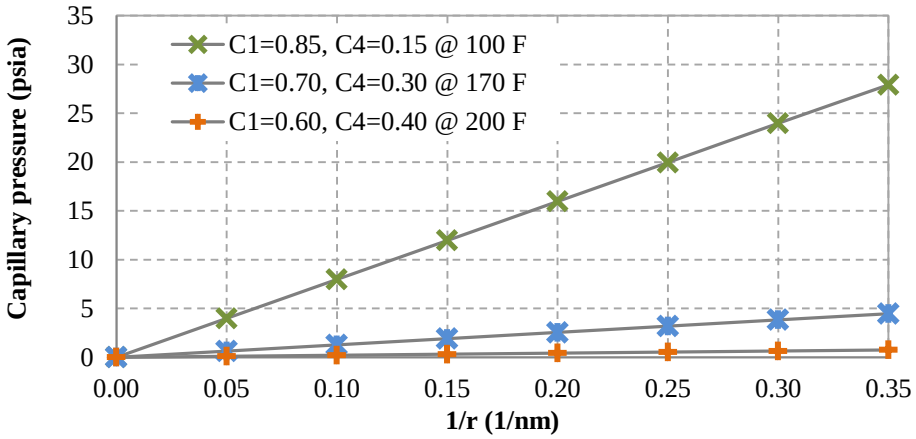


**Figure E.1: Capillary pressure of methane-butane: different concentrations**

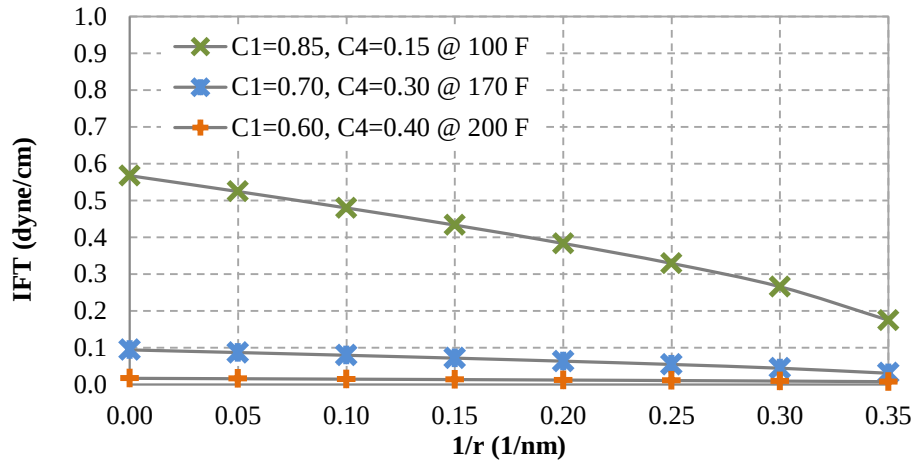


**Figure E.2: Interfacial tension of methane-butane: different concentrations**

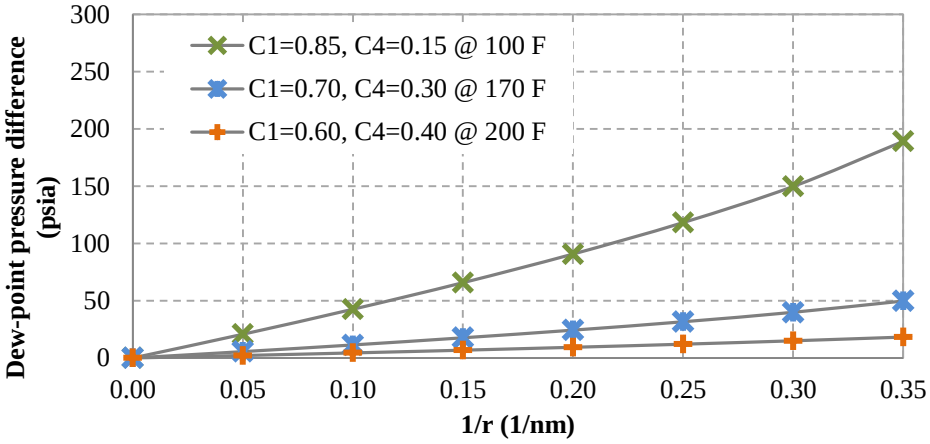


**Figure E.3: Dew-point pressure differences of methane-butane: different concentrations**

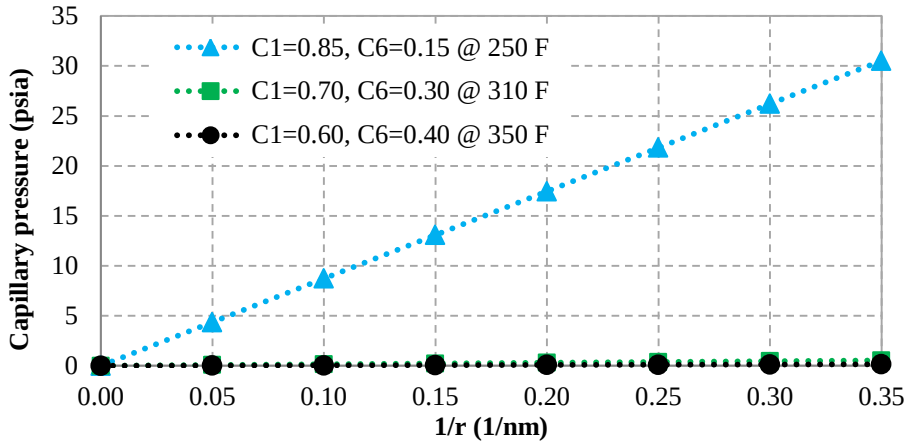


**Figure E.4: Capillary pressure of methane-hexane: different concentrations**

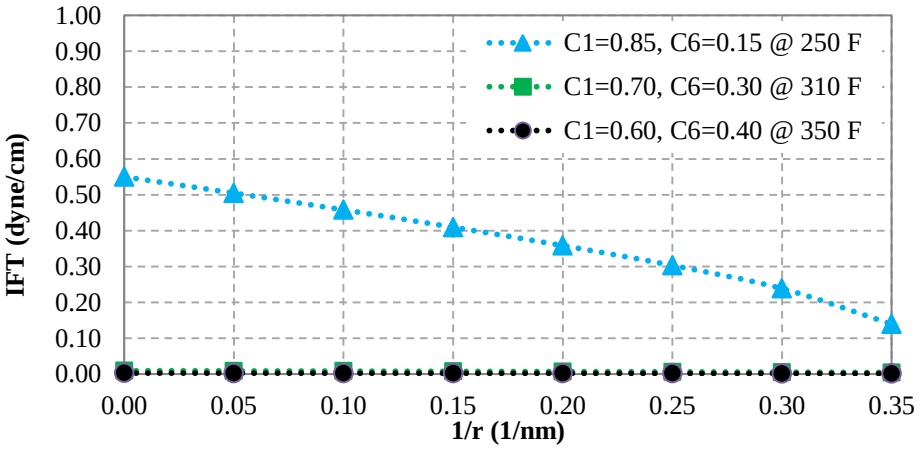


**Figure E.5: Interfacial tension of methane-hexane: different concentrations**

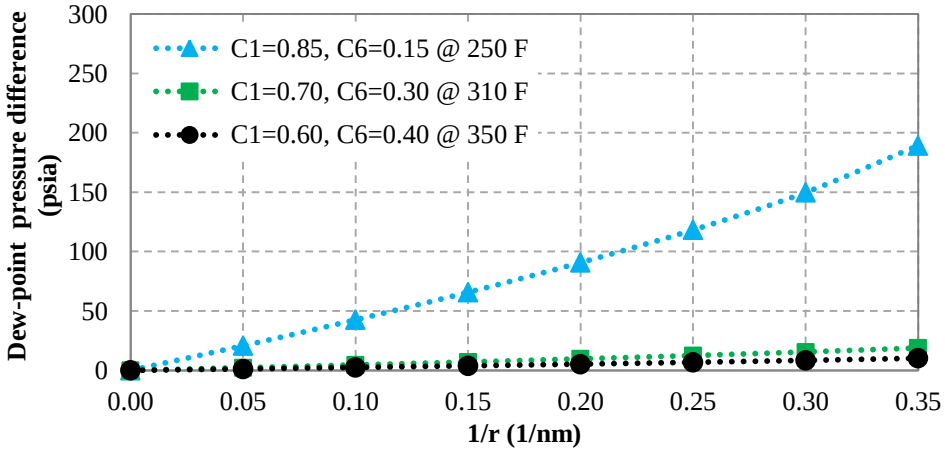


**Figure E.6: Dew-point pressure differences of methane-hexane: different concentrations**

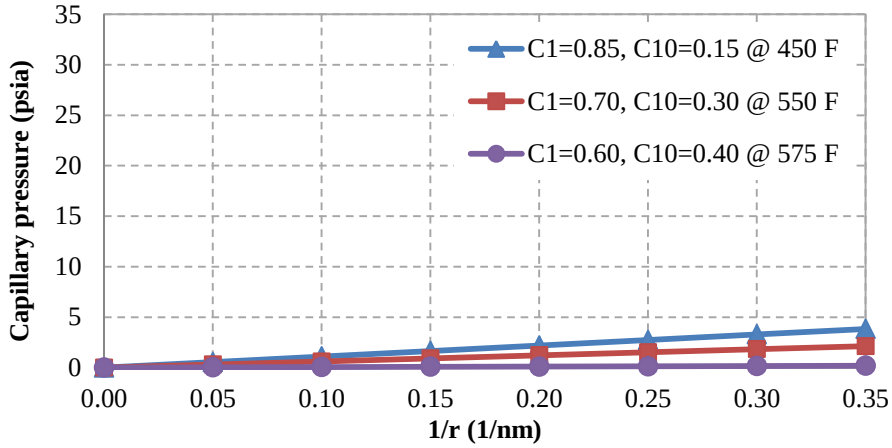


**Figure E.7: Capillary pressure of methane-decane: different concentrations**

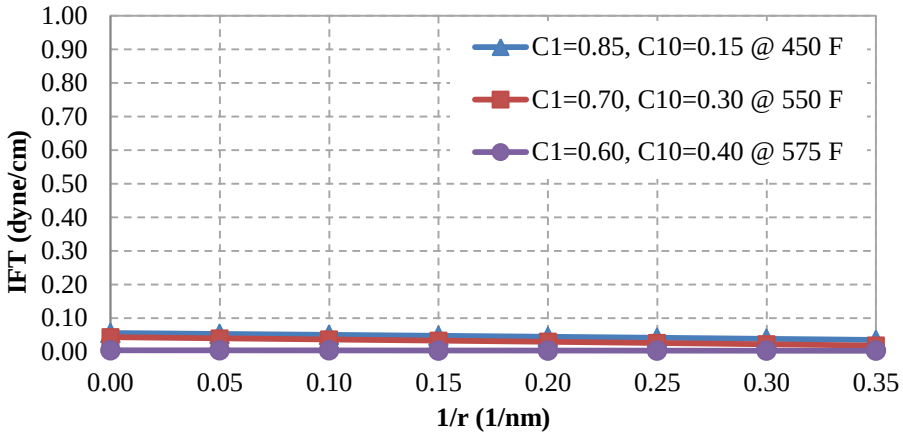


**Figure E.8: Interfacial tension of methane-decane: different concentrations**

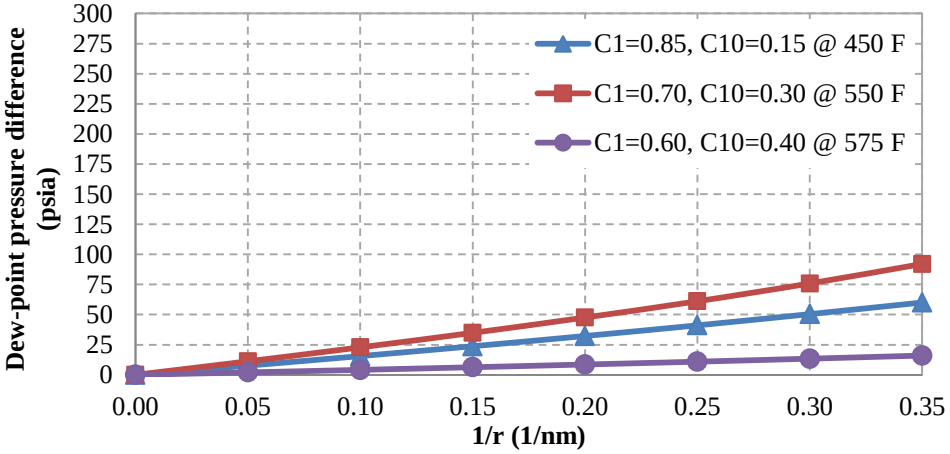


**Figure E.9: Dew-point pressure differences of methane-decane: different concentrations**

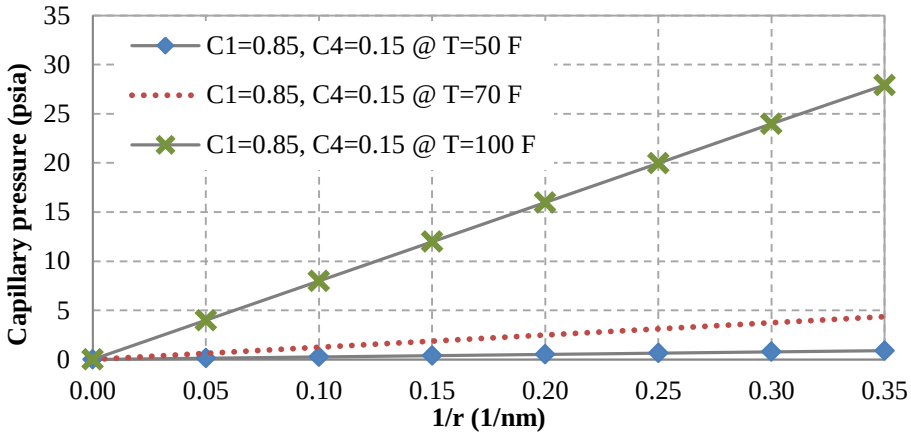


**Figure E.10: Capillary pressure of methane-butane: different temperatures**

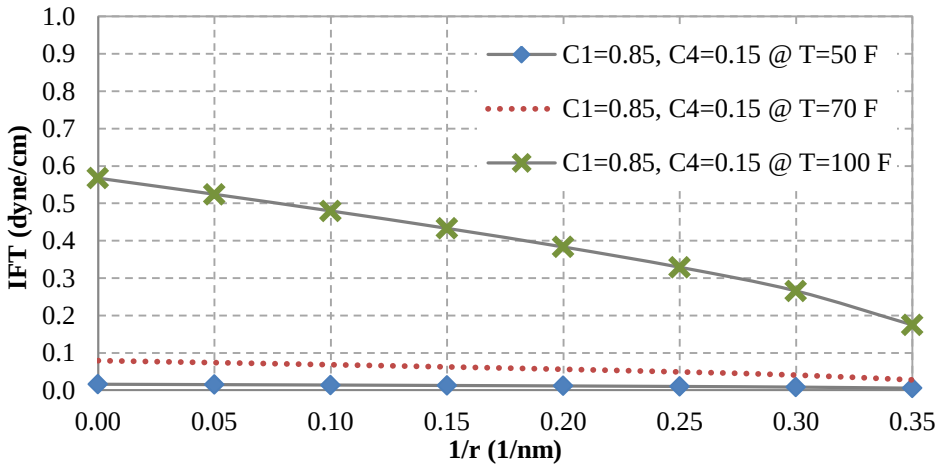


**Figure E.11: Interfacial tension of methane-butane: different temperatures**

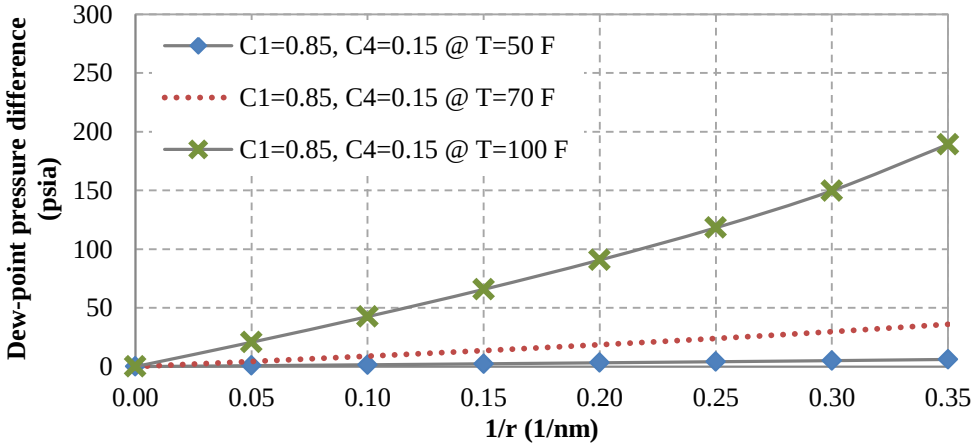


**Figure E.12: Dew-point pressure differences of methane-butane: different temperatures**

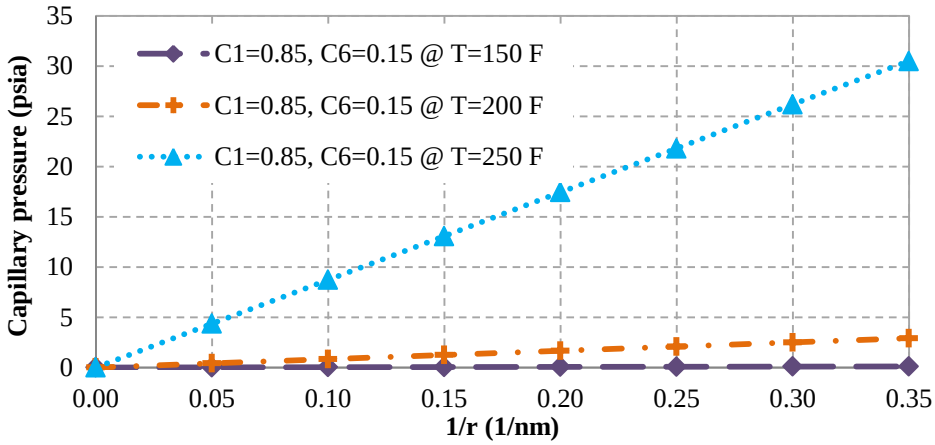


**Figure E.13: Capillary pressure of methane-hexane: different temperatures**

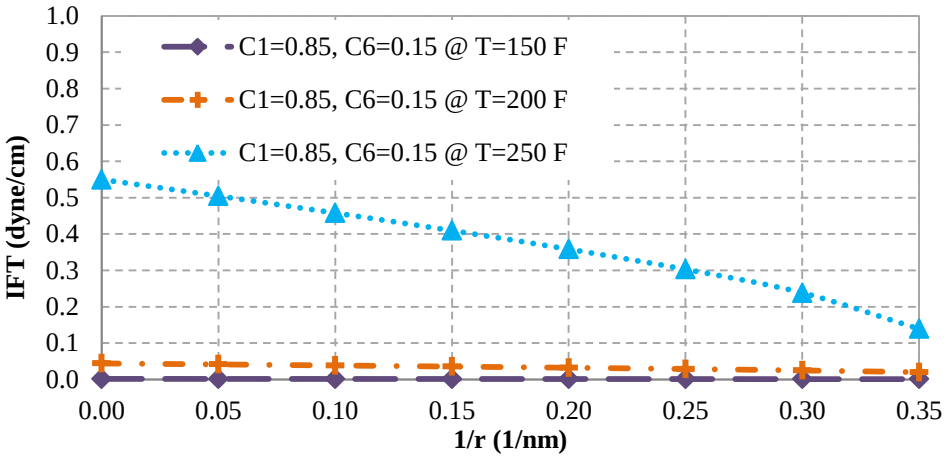


**Figure E.14: Interfacial tension of methane-hexane: different temperatures**

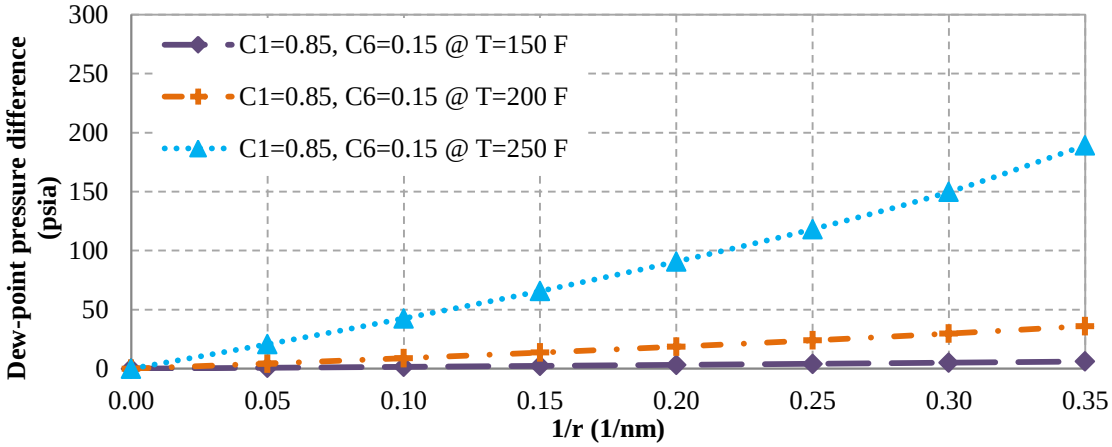


**Figure E.15: Dew-point pressure differences of methane-hexane: different temperatures**

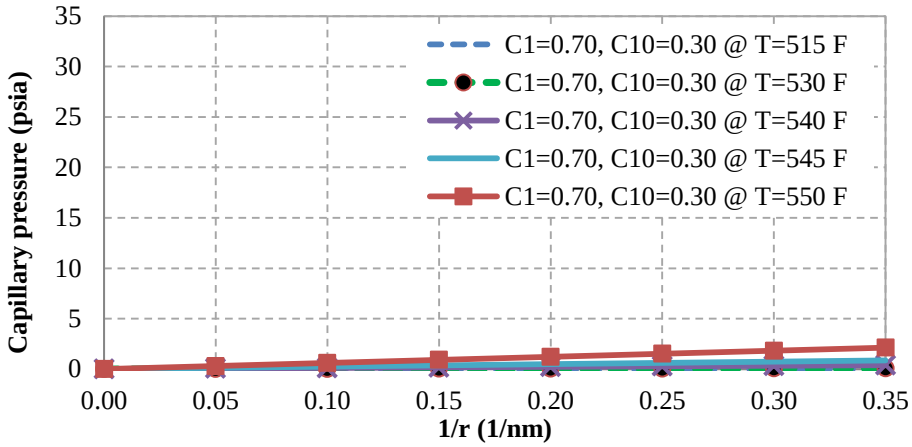


**Figure E.16: Capillary pressure of methane-decane: different temperatures**

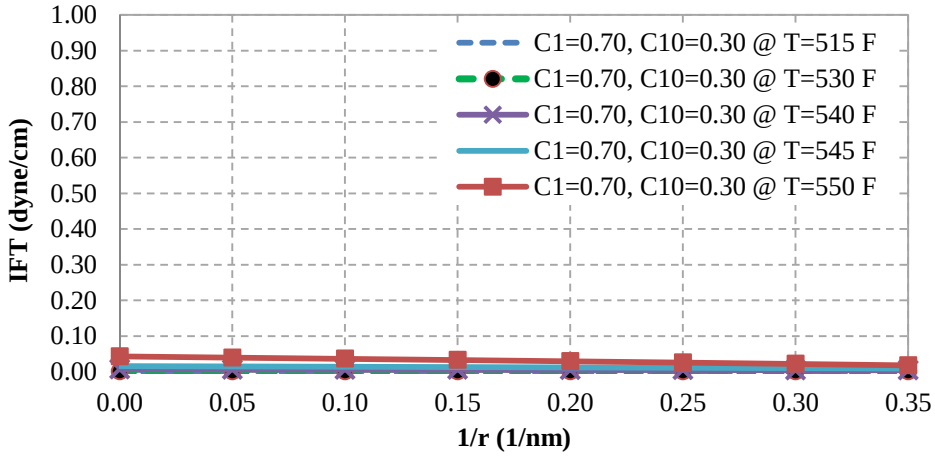


**Figure E.17: Interfacial tension of methane-decane: different temperatures**

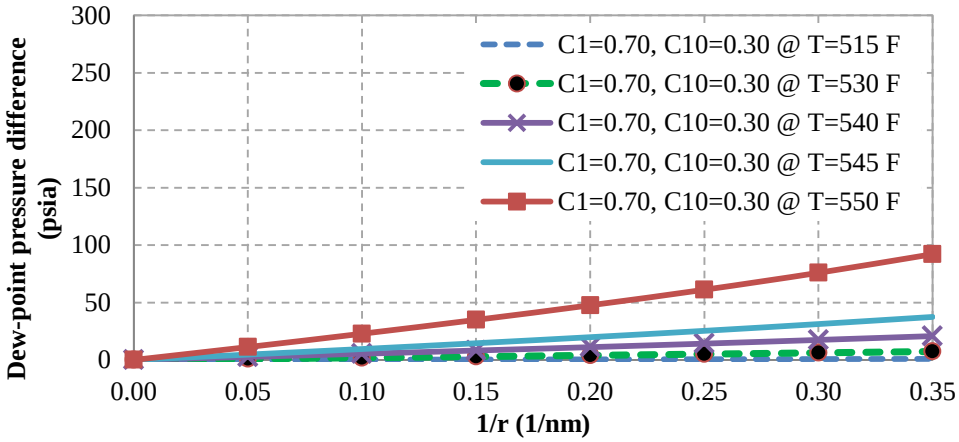


**Figure E.18: Dew-point pressure differences of methane-decane: different temperatures**

# VITA

## Bander Nasser Al Ghamdi

Bander Nasser Al Ghamdi was born on April 27, 1980 in Saudi Arabia. In Dhahran, he attended King Abdulaziz Elementary, Middle School, and High school, which he graduated from in 1998. In the summer of 1998, he was accepted by Saudi Aramco as a participant in the College Degree Program for Non-Employees. After one year of intensive college preparation program, Mr. Al Ghamdi was sponsored to pursue his Bachelor's degree in Petroleum Engineering. He attended Montana Tech of the University of Montana in 1999, and graduated with a Bachelor of Science in May 2003. Upon the completion of his degree, Al Ghamdi joined Saudi Aramco in June 2003 as a Simulation Engineer. With the reservoir simulation division, he was focused in gas reservoir studies with emphasis on gas-condensate compositional simulation. In the fall of 2008, Bander joined the Pennsylvania State University as a graduate student in the Energy and Mineral Engineering Department. He graduated in December 2009 with a Master of Science in energy and mineral engineering with option in petroleum and natural gas engineering. In January 2010, he returned to his former job as a simulation engineer. Few months after his return, he was awarded the title SPE Certified Petroleum Engineer by the Society of Petroleum Engineers. Al Ghamdi had presented technical papers in his field of specialty and participated as a technical committee and co-chairperson in regional venues. In August 2012, Bander joined Pennsylvania State University to pursue a doctorate degree in energy and mineral engineering with option in petroleum and natural gas engineering. During his studies, Bander participated as a Teaching Assistant for graduate-level classes, Phase Relation in Reservoir Engineering, and Natural Gas Engineering.